8-14-2013 12:00 AM

New Mineralogical and Geochemical Characterization of Martian Meteorites: Implications for Habitability and Astrobiological Exploration of Mars

Jared N. Shivak, *The University of Western Ontario*

Supervisor: Roberta L. Flemming, *The University of Western Ontario*
Joint Supervisor: Neil R. Banerjee, *The University of Western Ontario*
A thesis submitted in partial fulfillment of the requirements for the Master of Science degree in Planetary Science

NEW MINERALOGICAL AND GEOCHEMICAL CHARACTERIZATION OF MARTIAN METEORITES: IMPLICATIONS FOR HABITABILITY AND ASTROBIOLOGICAL EXPLORATION OF MARS

(Thesis format: Monograph)

by

Jared N. Shivak

Graduate Program in Geology & Planetary Science

A thesis submitted in partial fulfillment
of the requirements for the degree of
Master of Science

The School of Graduate and Postdoctoral Studies
The University of Western Ontario
London, Ontario, Canada

Abstract

Mars is thought to have shared many similarities with the Earth during its history, leading to extensive research into the potential for life to arise on Mars. Here, a thorough mineralogical and geochemical characterization of primary and secondary phases in Martian meteorites Los Angeles, Zagami, and Nakhla was performed. This novel approach assesses their potential to host life and build on previous studies that focused on either astrobiological or geological factors. These meteorites were found to contain abundant iron-rich phases that can act as microbial substrates. Investigation of alteration phases in Nakhla allowed for the identification of a new secondary alteration assemblage and allowed for a reevaluation of aqueous environmental conditions. The subsurface horizons from which these meteorites are sourced represent potentially habitable substrates for microbial colonization, if aqueous environmental conditions were present. The methodologies developed here can be used to guide future Martian exploration and Mars sample return missions.

Keywords

Mars, SNC Meteorites, Shergottites, Nakhlites, Astrobiology, Habitability, Exploration, Mineralogy, Geochemistry, Aqueous Alteration

Dedication

This thesis is dedicated to my late grandfather, Stanley (Sonny) Shivak. I am proud to carry his family name, and I hope that he would be proud to see me reaching for the stars.

Acknowledgments

Firstly, I must thank my supervisors at the University of Western Ontario: Dr. Neil Banerjee and Dr. Roberta Flemming. When I came to Western I was a freshly minted engineer with no idea of what direction I was heading, other than knowing that I wanted to work with rocks from space. Without your help, this project wouldn't have been possible. The advice, guidance, and mentoring that you gave me has been invaluable in both my personal and professional growth. From all the field trips and conferences to the graduation parties and impromptu thesis meetings at the coffee shop, you have instilled in me your passion for what we do. Thank you both for keeping me on track and for somehow managing to turn me into a scientist (which was no small task, I'm sure).

I would like to acknowledge the various groups who provided funding that was integral to the success of this work: the Natural Sciences and Engineering Research Council of Canada, the Canadian Astrobiology Training Program (part of NSERC CREATE), the National Aeronautics and Space Administration, the Canadian Space Agency, the Mineralogical Association of Canada, the Meteoritical Society, the UWO Graduate Thesis Research Fund, and the UWO Department of Earth Sciences. This project would not have been possible without the extraordinary generosity of the individuals and organizations that loaned and donated meteorites to me for analysis. These are: Robert Verish of the Meteorite Recovery Lab, Dr. David Deamer of UC Santa Cruz, Dr. Tim McCoy at the Smithsonian Institution Department of Mineral Sciences, and Dr. Carl Agee of the Institute of Meteoritics at the University of New Mexico.

It takes a village to raise a child, and in a very similar way it takes many people to mentor a graduate student. I would like to thank Dr. Phil McCausland of UWO and Dr. Alexander Pavlov of NASA Goddard for their guidance and mentorship, and for treating me as if I was one of their own students even while I was off doing my own thing. I owe my success in no small part to the unique perspectives that you offered me. I would also like to thank Dr. Ron Peterson of Queen's University, Dr. Gordon Osinski of UWO, Dr. Livio Tornabene of UWO, Lisa Munro of UWO, and Dr. Gordon Southam (formerly of UWO) for the help and advice that they offered me along the journey.

I would also like to extend my sincere gratitude to everyone who helped me with carrying out my instrumental analyses and data acquisition: Ivan Barker of UWO ZAPLab (SEM), Sergei Matveev of the University of Alberta (EPMA), Mary Jane Walzak of Surface Science Western (Raman), Stephen Wood of UWO (thin section preparation), and Tim Goldhawk & Todd Simpson of Western Nanofabrication Facility (SEM). Without your help, this thesis would just be a bunch of words on a page.

Thank you to all of the administrative staff in the Department of Earth Sciences and the Centre for Planetary Science & Exploration for all of their logistical help, Claire Mortera for helping me with innumerable things over the course of the last few years, and Barry Price for poster making and technical help.

Thank you to **all** of my friends, both near and far (especially those from UWO). Your friendship and support kept me sane and made sure that I spent the last three years of my life smiling, which is perhaps the most important thing of all.

Thank you to my family (particularly my mother, father, and brother). To say that I am here because of you would be a gross understatement. Thank you, mom and dad, for giving me so many books about the planets and for taking me to the museum over and over so that I could look at the T-Rex bones for the hundredth time. You always cultivated an amazing sense of wonder in me, and I owe you so much. I'm not sure where I'll end up in the future, but I hope you'll be proud of it.

Finally, thank you to anyone that I may have forgotten. It has been an incredible journey to go from being an undergrad who just thought rocks were cool to where I am now, and there are more people who have made an impact in my life than I can count.

Table of Contents

List of Figures

List of Tables

Chapter 1.0 Introduction & Background

1.1 Purpose of this Study

The purpose of this study is to perform a full mineralogical and geochemical characterization of a suite of Martian meteorites from an astrobiological perspective that has not been heavily documented in the past, and to use this information (along with the published literature) to evaluate and assess the astrobiological potential of these rocks and the factors influencing whether they may represent viable Martian habitats for microbial life that may have evolved on Mars. In the context of this study, habitability is defined as conditions similar to those in analogous terrestrial environments (such as subaqueous basaltic rocks) that are known to host microbial life. The major aim of this work is to better reconcile astrobiological knowledge about planetary habitability and the survival of microorganisms in terrestrial environments with geological information about Martian rocks and environments.

Past work on habitability represented by Martian meteorites has largely focused on geochemical indicators of past environmental conditions. However, direct analysis of mineralogy is a powerful tool for understanding environmental conditions in the geologic past. We focus on techniques that provide direct mineralogical information (such as X-Ray diffraction) and obtain a more precise understanding of the mineral assemblages present in these environments. From this, new mineralogical insights can be drawn toward the potential habitability of Martian rocks. This approach also informs the

methodologies and tools which can be used in the future to probe planetary samples for evidence of habitability.

In order to assess the environmental conditions that microbial life would be exposed to in the subsurface crust represented by these Martian meteorites, characterization of the potential mineral substrates must be carried out. An understanding of the minerals present in a rock is necessary for an evaluation of the types of metabolisms that might be available to microbes. Therefore, the mineral phases present in the rocks (both primary and secondary) were identified and fully characterized mineralogically and geochemically using a variety of techniques. Once this was completed, a more thorough study of the potential energy and nutrient sources in these rocks could be done. Potential energy and nutrient sources in Martian meteorites have been discussed in the past (Fisk et al., 1999), but never following a full characterization of Martian samples. Our *in situ* mineralogical investigation of alteration assemblages in the Nakhla meteorite allowed for a reassessment of the minerals deposited by secondary alteration processes. Minerals deposited by aqueous activity provide information on the fluid environment, and the re-evaluation here of the mineral phases present in this alteration material has large implications for the ability of microbes to inhabit these rocks in the Martian subsurface. This study provides new insights into the metabolic and nutrient pathways available to potential microorganisms living in the Martian crust and the fluid environment that they would be exposed to in the subsurface.

This information will allow for an assessment of the environment of emplacement, evolution and alteration of these meteorite samples and for an evaluation of their potential

to represent possible habitats for microbial life on Mars and relative attractiveness of targets for future exploration missions. The laboratory characterization of the suite of Martian meteorites performed in this study can be considered as analogous to what might be conceived for an "unknown" sample of the Martian crust returned by a future sample return mission. Therefore, the methodologies developed here will provide a framework for the approach that should be taken during the evaluation of the potential habitability represented by a Martian returned sample in order to help guide future sample return and *in situ* exploration missions to the surface.

1.2 Context for this Work

The study of the habitability of Mars has been a motivating factor for expanding on the past history of the planet with consideration of the various factors influencing its ability to host life that may have arisen (Cockell, 2007). The Curiosity rover, launched in November 2011 and landing on Mars in August 2012, has as an overall scientific goal to "explore and quantitatively assess a local region on Mars' surface as a potential habitat for life, past or present" (Grotzinger et al., 2012). Curiosity carries an extensive suite of instrumentation (e.g., Grotzinger et al., 2012; Mahaffy et al., 2012), similar to the instrumentation available to terrestrial scientists working in tandem with the rover. These instruments can be used to assess the potential of the Martian surface as a habitat for life that may have evolved on Mars in the past or present. In large part, this will consist of mineralogical and geochemical analyses of near-surface materials that the rover encounters on Mars. The work presented here complements this *in situ* work done by rovers on the surface of Mars and provides information only obtainable from meteorite

samples. Future exploration missions over the next several decades will likely aim to return samples of the Martian crust back to the Earth in order to allow for more extensive instrumental analyses than are possible with a robotic exploration mission on the surface (McLennan et al., 2011).

Observations made by rovers and orbiters have been supported by the study of Martian meteorites and the information provided by the phases and textures they contain, leading to a greatly improved understanding of the evolution of the planet and its potential for harbouring life (McCoy et al., 2011). Many studies have focused on particular details in isolation, such as alteration textures that resemble terrestrial bioalteration or mineral phases suspected of being biological in origin (e.g., McKay et al., 1996; McKay et al., 2001; Fisk et al., 2006). Other work has focused on the characterization of specific Martian meteorites, but without any consideration being given to the astrobiological potential of these studies (e.g. McCoy et al., 1992; Warren et al., 2004; Papike et al., 2009). These studies would benefit from an improved methodology and framework for conducting a thorough characterization of meteorites with the intent of providing a solid foundation from which to evaluate their potential habitability, which this work provides. Microbial life in the terrestrial geosphere subsists in part on chemical products derived from minerals and solid phases within the rocks hosting their communities (e.g., Lunine, 2005). Therefore, a full understanding of the mineralogical substrates and chemical resources available for any hypothetical biosphere is required in order to evaluate whether a subsurface environment on Mars represents a potentially habitable setting for any microbial life that may have existed on the planet.

1.3 SNC Meteorites

Meteorites sourced from Mars form a group known as the SNC meteorites. The SNCs are named for the type specimens of the three Martian meteorite groups (Shergotty, Nakhla, and Chassigny, respectively) and comprise all but two of the currently known Martian samples (e.g., Bridges et al., 2006; Chennaoui Aoudjehane et al., 2012; Agee et al., 2013). The SNC meteorites are all igneous in character and represent samples of the Martian crust; the group contains both volcanic and plutonic rocks, and a range of crystallization ages sampling the early portion of Mars' history to the recent past (e.g., Weisberg et al., 2006).

Many of the samples of SNC meteorites were discovered many decades ago, but their Martian origin was not recognized until more recently (e.g., McSween, 1984). Early workers identified that the SNC meteorites must have originated on a large, differentiated body and an asteroidal origin was favoured for many decades (e.g., Vickery et al., 1983). The final evidence confirming a Martian origin came when trapped gases within melt pockets in several SNC meteorites were correlated with Martian atmospheric composition at measured by the Viking landers in 1976 (e.g., Marti et al., 1995), and their Martian origin is largely undisputed in the current literature.

Meteorites are grouped in order to align similar meteorites with each other and provide information about the differences in solar system processes that they represent (Weisberg et al., 2006). A large number of techniques are used to group meteorites, including mineralogy, petrology, geochemistry, and oxygen isotopic systematics (e.g., Scott et al.,

1975; Clayton et al., 1976); groupings from each of these methods are not always in agreement with each other, and the existence of many ungrouped meteorites further complicates classification systems. At the highest level, stony meteorites are divided into two distinct groups (the chondrites and the achondrites). This distinction is made based on the presence or absence of chondrules in a meteorite (Scott et al., 1974; Weisberg et al., 2006). Many other subtypes are observed within these two major groupings, but are not strictly relevant here.

The achondrites are subdivided into the primitive (undifferentiated) and the differentiated achondrites. The primitive achondrites contain no chondrules but have not undergone the complex processes that erase their primitive textures and compositions; they likely represent partial melts or melt residues from local heating events during impacts or the early formation of asteroids or planetary bodies (McSween, 1989). The differentiated achondrites are sourced from large planetary bodies, such as the asteroid 4 Vesta, the Moon, or Mars. These originated during the evolution of magmas and planetary components on large differentiated bodies and provide a record of the geology at various depths on these bodies (e.g., McSween et al., 2011). Due to the complex processes of differentiation and volcanism taking place on Mars throughout its history, the SNC meteorites represent some of the youngest meteorite types currently known (e.g., Nyquist et al., 2001).

The basaltic shergottites are mafic igneous rocks and represent products of tholeiitic lava flows (Lorand et al., 2005) The thickness of these basaltic lava flows cannot be determined precisely, but is known to have been significantly greater than 10 m (McCoy

et al., 1999; Nyquist et al., 2001). The basaltic shergottites are significantly enriched in iron when compared to terrestrial basalts (e.g., McSween, 1994; Nyquist et al., 2001; Warren et al., 2004). The overall FeO content of Zagami and Los Angeles is approximately 20 wt%, whereas terrestrial ocean floor basalts have typical values of <10 wt% (Bridges et al., 2006). Aluminum content of basaltic shergottites is lower than that of comparable terrestrial basaltic rocks (McSween, 1994; Nyquist et al., 2001).

The nakhlites are cumulate rocks derived from thick lava flows, and the chassignites may represent mafic intrusions at shallow depths (Nyquist et al., 2001; McSween, 1994; Treiman, 2005). The nakhlites (in addition to the chassignites) are among the SNC meteorites displaying definitively cumulate textures, as contrasted with the shergottites (representing a mixture of cumulate and primary textures) (e.g., Bridges et al., 2006; Szymanski et al., 2010).

The nakhlites, including Nakhla, are known to contain relatively high amounts of organic matter thought to be preterrestrial in origin, representing organic matter from the Martian system (e.g., Jull et al., 2000). This organic matter includes amino acids (Glavin et al., 1999) and high molecular weight organics having some similarities to the organic matter found in other meteorites such as carbonaceous chondrites (Sephton et al., 2002). The nakhlites are also among the most notable Martian meteorites because they contain significant evidence of having been altered by aqueous fluids while on Mars, prior to ejection and transport to the Earth (e.g., Changela et al., 2011; Leshin et al., 2006). This evidence is primarily mineralogical, with secondary phases precipitated and primary

phases altered due to the action of aqueous brines on Mars (e.g., Bridges et al., 2001; Gooding et al., 1991).

1.3.1 Los Angeles

The Los Angeles meteorite was the fourteenth Martian meteorite to be discovered. It was found in 1999, as part of the private rock collection of Robert Verish of the Meteorite Recovery Lab in California. Two stones were found, partially covered in fusion crust. Stone 1 had a total original weight of 452.6 g and stone 2 (of interest to this work) had a total original weight of 245.4 g (Rubin et al., 2000). These stones were identified as Martian meteorites after some time in a private rock collection, so their exact find date and locality cannot be determined. The most accurate estimate is that they were recovered some time in the late 1980s to mid 1990s in the Mohave Desert near Los Angeles (Rubin et al., 2000). The crystallization age of Los Angeles 002 has been determined to be approximately 175 +/- 8 Ma, with an ejection age (determined by its exposure to cosmic rays) of approximately 3.10 +/- 0.20 Ma (Nyquist et al., 2001).

Los Angeles is the most differentiated basaltic shergottite yet discovered, both mineralogically and in its geochemical composition (Rubin et al., 2000). This meteorite is among the most iron and REE rich shergottites yet discovered (Rubin et al., 2000; Xirouchakis et al., 2002). LA 002 is representative of a late-stage rock from a lava flow related to crystallization of rocks of other types of SNC meteorites, such as Nakhla and Shergotty (Xirouchakis et al., 2002). It is enriched in incompatible elements and late-forming components (such as phosphates and large areas of pyroxferroite), and likely

derived from a part of the upper and later forming parts of the hierarchy of melt products from which Martian meteorites are sourced (Borg et al., 2003).

Shock effects such as maskelynization of plagioclase and minor mosaicity of pyroxenes are observed in the Los Angeles meteorite, indicating that it has undergone significant shock during its ejection and subsequent fall (Warren et al., 2004). The shock processes that Los Angeles, Zagami, and Nakhla underwent during ejection, transport and impact on Earth are not strictly relevant to an assessment of its potential habitability in the Martian subsurface; although the effects of shock must be taken into account in order to ascertain the condition of the rocks as part of the Martian crust, the processes of impact and shock will not be a focus of this work.

1.3.2 Zagami

The Zagami meteorite was the second meteorite found to contain a significant amount of trapped Martian atmosphere within shocked glassy material, aiding in the identification of a Martian origin for the SNC meteorites (Marti et al., 1995). It was observed to fall in 1962 near Zagami Rock in Nigeria. Its original main total mass was approximately 18 kg, making it the largest single Martian meteorite ever discovered (Bridges et al., 2006). The crystallization age of Zagami has been determined to be approximately 177 +/- 3 Ma, with an ejection age (determined by its exposure to cosmic rays) of approximately 2.92 +/- 0.15 Ma (Nyquist et al., 2011).

Zagami has been determined to have crystallized over a period of a few weeks to months (Lentz et al., 2000). Based on its two distinct textural morphologies (coarser and finer grained, respectively), Zagami is believed to have crystallized in a two-step process with initial pyroxene crystallization followed by entrainment of these crystals in an extruded lava flow and subsequent crystallization of other phases (e.g., Bridges et al., 2006; McCoy et al., 1992; Nyquist et al., 2001).

Zagami has experienced severe shock during the process of transport from Mars to the Earth (McCoy et al., 1992). In addition to an almost completely maskelynized plagioclase phase, pyroxene crystals are heavily fractured and display significant mosaicity (McCoy et al., 1992). Large scale first order fractures filled with black impact melt produced during shock are also present throughout the Zagami meteorite (e.g., Marti et al., 1995), including the materials studied in this work.

1.3.3 Nakhla

The Nakhla meteorite is the type meteorite of the nakhlite class of SNC meteorites. It was observed to fall near the city of El Nakhla al Baharia, Egypt on the morning of June 28th, 1911 (McBride et al., 2011). A common legend says that one fragment of the meteorite struck a dog upon impacting the Earth, although this story is considered apocryphal. Nakhla is a substantial meteorite discovery, with over 10 kg of material recovered from various fragments in the area of the fall (Grady, 2000). The crystallization age of Nakhla has been reported as approximately 1.27 +/- 0.01 Ga, with subsequent processing on Mars

and impact ejection age of approximately 10.75 +/- 0.4 Ma (Eugster et al., 1997; Nyquist et al., 2001).

The nakhlites are all grouped and originate from a single ejection event ~11 million years ago (Eugster et al., 1997). The nakhlite parent magma was more oxidized than the parent magma of the shergottites, suggesting a different magma source either by differentiation in the crust or a differing source region (Szymanski et al., 2010). Similar ejection ages of many shergottites with the nakhlites (and the chassignites) suggest that the impact event that ejected the nakhlites and chassignites may also have been one of the up to 7 shergottite ejection events (e.g., Eugster et a, 1997).

Significant depth of emplacement is required to produce the mineralogical and textural characteristics observed in a rock formed in a slowly cooling accumulating flow (such as Nakhla) (e.g., Bridges et al., 2006; Changela et al., 2011). Nakhla is believed to have formed in the intermediate zone of the nakhlite pile, based on exsolution in olivine as well as the proportion of olivine to aqueous alteration and oxide phases when compared to the other nakhlites (Bridges et al., 2006). Nakhla has many similarities to the augite-rich igneous cumulate rocks of the Abitibi greenstone belt in North America that comprise the lower half of a thick flow 125 m in thickness (Nyquist et al., 2001).

Nakhla is unbrecciated, contains only one lithology, and displays a characteristic cumulate texture across almost the entirety of its mass (Treiman, 2005). It is thought to be most likely sourced from a basaltic cumulate flow, displaying subcumulate to cumulate textures, although a shallow intrusive origin has also been proposed by some workers

(Friedman-Lentz et al., 1999; Harvey et al., 1992). Nakhla most probably represents the accumulating products of a flowing basaltic body and the later forming phases that crystallized and quenched once this "crystal mush" had been entrained at the surface (e.g., Treiman, 2005). Amino acids and heavy organic matter has been described in Nakhla; these are commonly present in fractures associated with clays and secondary alteration phases (e.g., Sephton et al., 2002; Jull et al., 2000).

Alteration assemblages in Nakhla comprise veins of hydrated "iddingsite", as well as halides, carbonates and sulfates (Bridges et al., 2001; Changela et al., 2011). Due to the seemingly pervasive nature of alteration throughout the rock, it has been suggested that Nakhla underwent a prolonged period of exposure to aqueous fluids on Mars (Leshin et al., 2006). It is thought that this alteration occurred between 500-700 my in the past, and it provides a mineralogical record of the nature of the aqueous fluids that acted on Nakhla and the conditions under which it underwent aqueous alteration in the Martian subsurface (Leshin et al., 2006).

Chief among these alteration phases is the "iddingsite" material primarily resulting from the alteration of olivine grains (e.g., Gooding et al., 1991). This alteration material in nakhlites has been seen in some cases to occur along grain boundaries between olivine and augite, and where large areas of mesostasis have been subjected to extensive aqueous alteration (Treiman, 2005). "Iddingsite" is a rust-colored assemblage that forms in fractures and veins in olivine grains, and if pervasive can completely replace olivine crystals. It is often found associated with other secondary minerals such as serpentine and clays. It is highly variable in composition due to its being made up of multiple phases

(Delvigne et al., 1979), although some workers have previously identified “iddingsite” material in Nakhla as being a monomineralic or amorphous phase (Bunch et al., 1975). Due to the variable composition of “iddingsite” and the qualitative nature of this term, it is useful to discontinue the use of “iddingsite” in favour of more descriptive language. This work will refer to the rust-coloured alteration assemblage in Nakhla as vein alteration material, and attempts to quantify the precise mineral assemblage. Veins containing alteration material in Nakhla are offset along fractures and are melted near fusion crust material, indicating that it is preterrestrial in origin (Gooding et al., 1991). It is thought to have formed through low temperature alteration of mafic primary minerals within the rock (Delvigne, 1998; Smith et al., 1987).

Vein alteration material in Nakhla has been described in the past as “reddish-brown staining primarily along fractures in olivine” (Bunch et al., 1975), “mixed-phase silicate alteration product (Ashworth et al., 1975) “rust”, and “iron-rich siliceous material” Gooding, 1991). Previous work has determined that the vein alteration material in Nakhla is mineralogically comprised of iron oxy-hydroxides, smectites or other phyllosilicates, and minor amounts of other phases such as salts and carbonates (e.g., Gooding et al., 1991; Bridges et al., 2000; Leshin et al., 2006). Geochemical mass balancing has suggested that smectites and/or illite may be present in the vein alteration material (Gooding, 1991), and previous studies have performed thorough reconnaissance of the textures and phase groupings of other nakhlite meteorites (Changela et al., 2011). However, an adequate identification of the specific minerals within Nakhla vein alteration material has not been carried out. A clear picture of the mineral phases present in this aqueous alteration material is necessary for an increased understanding of the conditions

of alteration to which Nakhla was subjected on Mars and the history of aqueous activity in the subsurface following emplacement.

Nakhla has experienced significant shock during its transport to the Earth (Bunch et al., 1975). However, plagioclase crystals are present in Nakhla with their crystal lattice intact, and no mosaicity is observed in pyroxene or olivine grains. This suggests that the levels of shock that it experienced were much lower than those experienced by other Martian meteorites, such as many shergottites (e.g., Treiman, 2005).

1.4 Relevance of Mars to Astrobiology

Mars has long been thought to be a prime candidate for the existence of life elsewhere in the solar system (e.g., Grady, 2007). The similarities to the Earth that Mars has shared throughout its history have prompted extensive research into its potential to host life, both currently and in its past (Veronique et al., 2012). A widely publicized paper in the early days of NASA's Mars Exploration Program claimed to have discovered relict biogenic activity in the Martian meteorite ALH84001 (McKay et al., 1996). However, more recent work has led to this finding being disputed on both methodological grounds as well as interpretation of the features observed in ALH84001 (Gibson et al., 2001). Similarly, a large body of work has been published demonstrating possible abiotic origins for many of the claimed biogenic features (e.g., Martel et al., 2012; Treiman, 2003). Overall, the existence of direct evidence of life preserved in Martian meteorites remains inconclusive at best and wide consensus is that no fossilized Martian life has been discovered in meteoritic samples to date.

Despite this, the possibility remains that crustal igneous rocks on Mars (similar to those represented by the SNC meteorites) are theoretically a potential habitat to be considered for possible Martian life that may have arisen in its history. The fundamental general requirements for microbial life on a planetary body as currently understood can be summarized succinctly: energy sources, a supply of nutrients, adequate substrate material, appropriate environmental conditions (temperature, pressure, radiation, etc.), and the presence of liquid water (e.g., Southam et al., 2007a). The nature of these factors of the Earth through its history (both during its early history at the origin of life and at the present day) is well described. It is possible that Mars may have hosted some or all of these conditions at some point during its history, potentially to the present day (e.g., Banin et al., 1992; Boston et al, 1992; Carr, 1996; Newsom et al., 1997; Shock et al., 1998).

Evidence suggesting the presence of liquid water at the surface and near subsurface has been well established through geomorphological formations, the presence of aqueously deposited rock strata and minerals and the action of aqueous brines on the present-day surface (Grady, 2007). Liquid water may be possible in the regolith of Mars at present under transient conditions and in extremely limited quantities (e.g., Haberle et al., 2001; Mohlmann, 2005), but it is clear that widespread aqueous activity is unlikely at present. Although the surface of Mars at present is not within the stability field of liquid water, it is thought that Mars may have been able to support liquid water during its past (e.g. Jakosky et al., 2007; Squyres et al, 1994; Ehlmann et al., 2011).

The Phoenix mission has led to an increased understanding of the near-surface inventory of water in the Martian regolith (e.g., Stillman et al., 2011). Recent work has also suggested that impact events and their associated hydrothermal systems may provide habitable environments for microbial colonization on the Earth and elsewhere, though the nature of these active surficial impact hydrothermal-related systems is poorly constrained and not well understood at present (e.g., Osinski et al., 2001; Cockell et al., 2002; 2003; Osinski, 2005; 2013). These discoveries have lead to an increased scientific consensus that Mars was, during its past, a planet with much higher potential to host life than was once thought (Cockell, 2007). It is important to note that the aqueous conditions on Mars during its past and present are likely to have varied widely both temporally and spatially, both on local and regional scales. Therefore, the detailed habitability potential of a specific region on Mars is likely to depend on extremely variable local conditions as well as on large-scale conclusions that can be derived from the study of Martian meteorites (e.g., McCoy et al., 2011).

Due to its relatively thin atmosphere, cold temperatures, and low surface pressures, the Martian surface is thought to be largely inhospitable to known forms of life (Boston et al., 1992; Parnell et al., 2010). The harsh UV radiation exposure that the surface is subjected to is thought to be prohibitive to cellular survival in the long term and would limit the growth of microbial life on the surface of Mars (e.g., Boston et al., 1992; Cockell et al., 2004; Kerney et al., 2011). Laboratory experiments show that terrestrial bacteria in simulated surficial Martian regolith environments exposed to Martian UV conditions do not grow at their normal rate and find it difficult to survive the radiation (Kerney et al., 2011). It is thought that some terrestrial bacteria may be able to survive in the shallow

subsurface if protected by an adequate covering of regolith material (Pavlov et al., 2010), but due to the ubiquitous nature of subsurface endolithic life on Earth it is clear that the subsurface lithosphere is a more attractive environment for microbial colonization on Mars (Southam et al., 2007a; Reith, 2011).

1.5 Geological History of Mars

The surface crust of Mars can be generally divided into two terrain types, broadly delineated along the two hemispheres of the planet; these are the southern highlands and the northern lowlands, with the southern highlands being generally older than the northern lowlands (Carr, 2006; Werner et al., 2011). These two terrains are differentiated based on their elevation (with a difference of 5.5 km in average height), crustal thickness (averaging 30 km in the northern hemisphere and 60 km in the southern hemisphere) and a crater density in the southern hemisphere (Carr, 2006). The large and abrupt break between these two regions is known as the crustal dichotomy (Carr, 2006; Werner et al., 2011). This large dichotomy most likely formed early in Mars' history, but the exact mechanism of its formation is poorly constrained. It may be due to an underlying endogenic process such as mantle convection (Neumann et al., 2004), or a large oblique impact early in Mars' history (Marinova et al., 2008). A map of the Martian surface showing this crustal dichotomy is shown below in Figure 1.1.

The majority of the surface of Mars is thought to be covered in volcanic rocks or weathering products of primary volcanic mineralogies (Carr, 2006; Taylor et al., 2008). Volcanism on Mars includes large shield volcanoes (such as the Tharsis province), low-

lying highland Paterae (Williams et al., 2009), smaller volcanic constructs such as Tholi (e.g., Hauber et al., 2005), and large areas covered by lava flows of variable morphology. Mars displays a variety of tectonic structures, both compressional (e.g., wrinkle ridges and lobate scarps (Watters, 2004)) and extensional (e.g., dyke swarms, strike-slip movement, and grabens (e.g., Ernst et al., 2001)). Despite this, there is no conclusive evidence of plate tectonics on Mars and it is widely accepted that the bulk of the two hemispheres on Mars are similar in age (Taylor et al., 2009). Mars likely differentiated into a crust-mantle-core system very early in its history, within the first few tens of millions of years (e.g., Foley et al., 2005). Based on geothermal modeling through the crust, volcanism was probably very active early on and then declined over time (Robbins et al., 2011).

Following this extremely early period of Mars' accretion and formation (largely lost in the rock record), the geological history of the planet has been subdivided into three age groups (Scott et al., 1978). These are comparable to eons in the terrestrial timescale, but are necessarily much more coarsely delineated based on the limited information regarding absolute chronology of Martian events (Scott et al., 1978). These three major subdivisions have been determined based on intersection relationships of major features on Mars and changes in cratering chronology of different terrains (Carr et al., 2010); although other chronological divisions have been proposed based on alteration mineralogy and changes in geochemical cycles through Martian time (Bibring et al., 2006), these are less widely adopted and less applicable to general discussion of Martian geological processes through time.

The three generally accepted periods of Mars history are the Noachian, Hesperian , and Amazonian (e.g., Scott et al., 1978; Carr, 2006). These follow the established terrestrial practice of naming geological periods after type localities, namely the Noachis region, Hesperia Planum, and Amazonis Planitia (Hartmann et al., 2001). The Noachian has a poorly defined start date but is widely agreed to begin with the formation of the Hellas basin at approximately 4.1 Ga and is considered to end at 3.7 Ga (Scott et al., 1978). The Hesperian period ranged from 3.7 Ga to 3.0 Ga, and the Amazonian covers the majority of Martian history from the end of the Hesperian to the present day (Scott et al., 1978). Each of these periods is defined by distinct geological units with widespread implications for the evolution of the planet throughout time. The general geological timescale of Mars, contrasted with that of the Earth, is shown below in Figure 1.2.

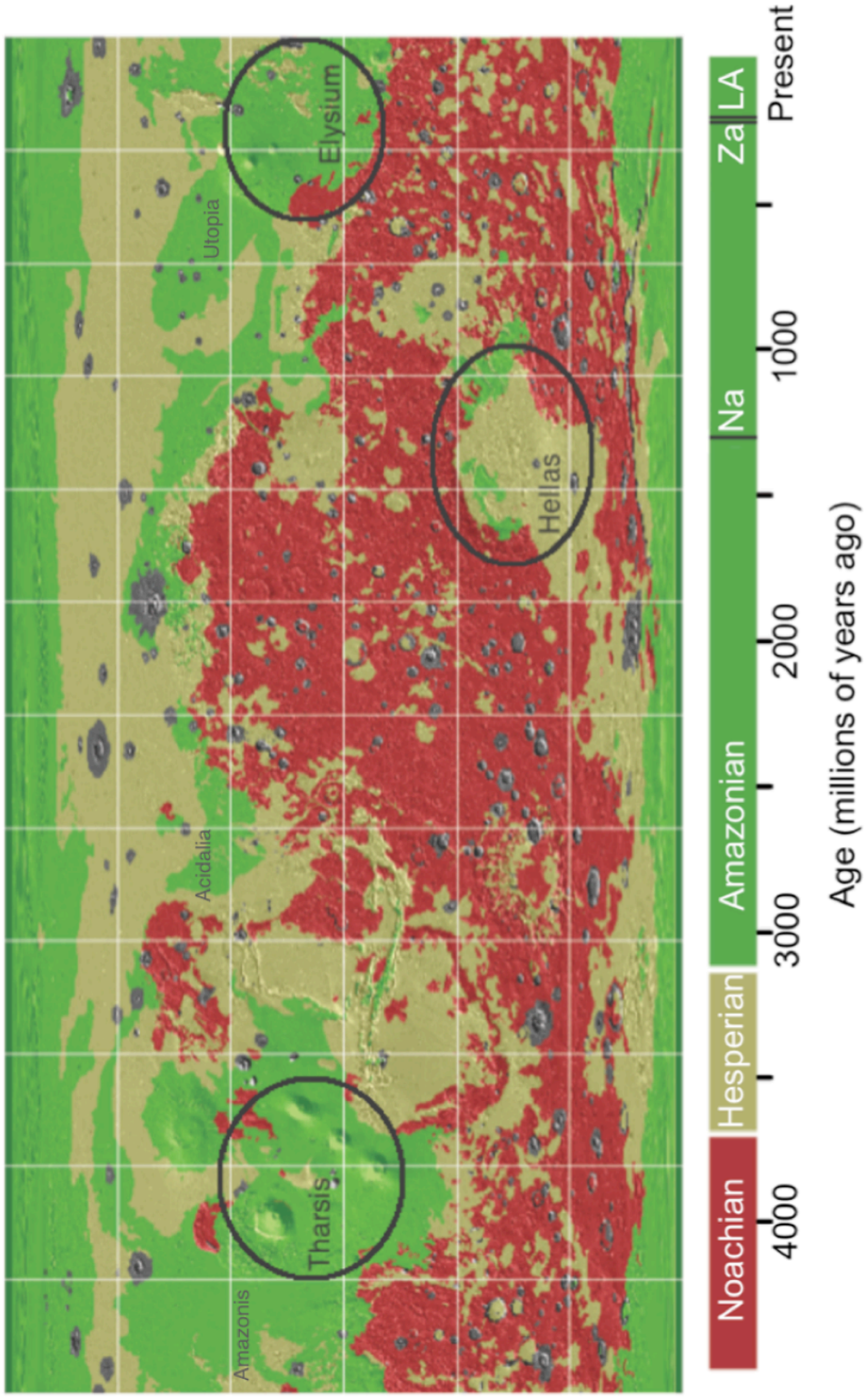

Figure 1.1: Chronostratigraphic map of the Martian surface. Several notable regions are indicated. Units are colour-coded by associated time period. Note crystallization ages of LA 002, Zagami, and Nakhla meteorites on scale. Adapted from Rossi et al., 2010.

The Noachian period is characterized by high rates of erosion, cratering, and valley formation. The SNC meteorite ALH84001 crystallized during the Noachian period on Mars (Gibson et al., 2001). Volcanism in the Noachian was dominated by the creation of the Tharsis bulge, and weathering of these primary materials was widespread across the globe. During the Noachian period, Mars held a much thicker (but still carbon dioxide rich) atmosphere than at the present day (Kasting, 1991). This had profound effects on the climate and hydrosphere of the planet. The secondary mineralogical and geomorphological evidence for warm (and therefore likely wet) conditions in the Noachian period is convincing (e.g., Ming et al., 2008). This includes aqueous minerals (such as gypsum, carbonates, hematite, and sulfate) as well as gullies and outflow channels (Carr, 2006). The environmental conditions to support large standing bodies of water across swaths of the Martian surface would have been present in large part during the Noachian, if such a widespread hydrosphere was available (Carr et al., 2010). Depending on the quantity of water available to the system, topographical lows may have been filled with at least local bodies of water (Carr et al., 2010).

Much of the Noachian terrain on Mars is dissected by valley networks that drain into locally constrained lows, and several valleys running lengths of thousands of kilometres are present in the Noachian (Carr, 2006). These are thought to have formed from the flow of liquid water across the planet. This suggests that precipitation, followed by surface runoff and groundwater recharge, occurred at least episodically in the Noachian (Ming et al., 2008).

Noachian-aged rocks form a large part of the southern highlands of the Martian crust. The majority of rocks forming the southern highlands are most likely primary volcanic materials or volcanics that have been reworked by impact (such as breccia flows) (Taylor et al., 2008). The Noachian was a time of high global volcanic output (e.g., Werner, 2009). Volcanism during this period is dominated by Ca-rich basaltic effusive flows (e.g., Lang et al., 2009). Most of the volcanism during the Noachian was concentrated in the Tharsis region. Tharsis is a large volcanic edifice composed of a number of large basaltic shield volcanoes and voluminous flows (e.g., Wise et al., 1979).

This large volcanic pile had largely accumulated by the end of the Noachian and the rate of volcanism slowed considerably into the Hesperian and Amazonian (Phillips et al., 2001). Although much of the crust had differentiated and volcanism had been widespread across the globe by the beginning of the Noachian, this period was a time of significant building of crustal volcanic packages (e.g., Scott et al., 1981). While most of the Noachian record is visible only in the southern highlands, the younger northern lowlands deposits are likely underlain by extensive volcanic flows of Noachian origin (Johnson et al., 2005).

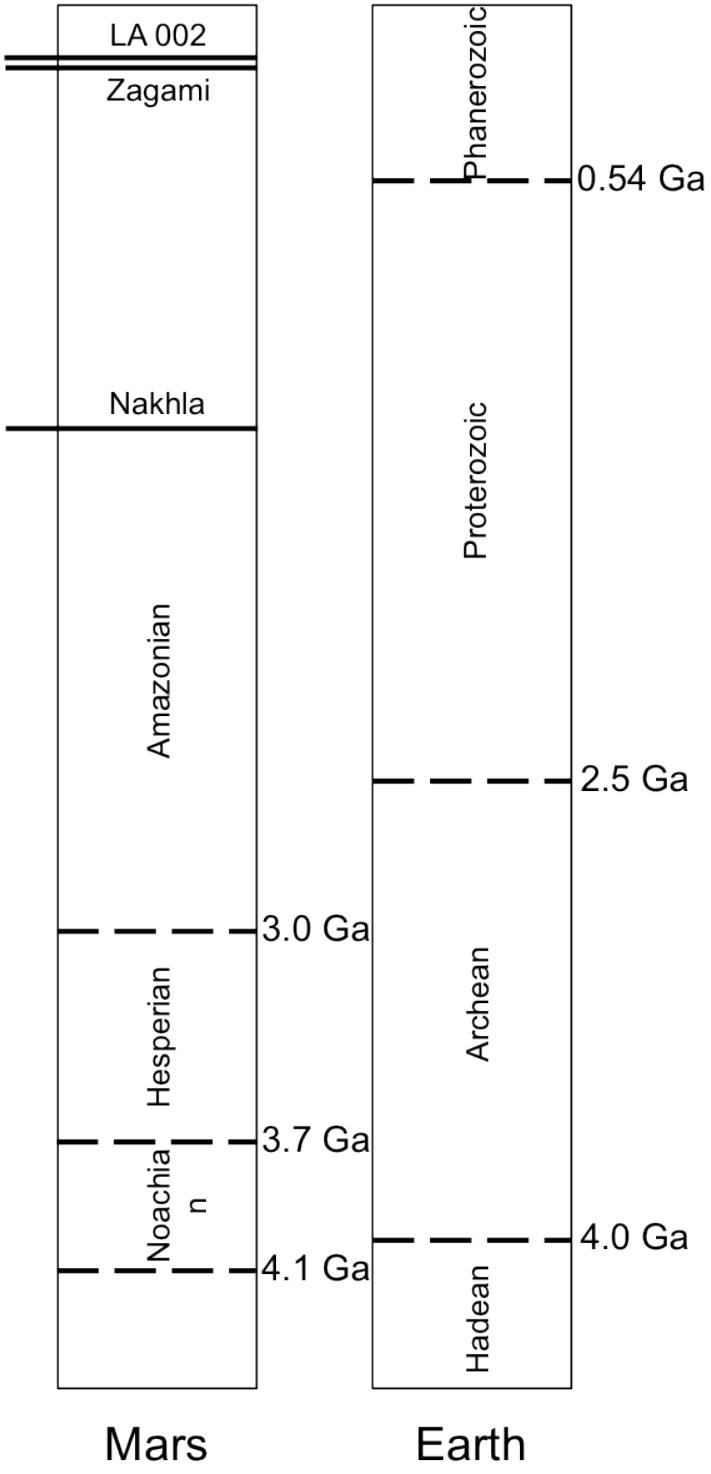

Figure 1.2: Generalized geological timescale of Mars. Terrestrial timescale is provided for comparison. Note that pre-Noachian period is poorly constrained and not well described. Absolute ages of LA 002, Zagami, and Nakhla meteorites have been indicated. Adapted from Carr et al., 2010.

The Noachian was a period of widespread formation of phyllosilicate mineral phases, including smectites and Fe-chlorite (Newsom, 2005). These are all known to be aqueous alteration products of basaltic rocks, and represent extensive interactions of Noachian volcanic rocks with fluids both on the surface and at depth (Ehlmann et al., 2011). The presence of these phyllosilicates suggests that the Martian hydrosphere during the Noachian was much more active than at present, and was interconnected across the subsurface-surface-atmospheric range (Ming et al., 2008). Noachian phyllosilicates are largely observed in areas of stratigraphic exposure, rather than as surficial deposits. They are overlain with a package of olivine rich volcanic rocks that preserve their primary mineralogy and have not been significantly weathered (Mustard et al., 2007). This suggests that conditions favoured phyllosilicate formation for much of the Noachian, but conditions changed at the end of the period. Following the Noachian, there was negligible hydrous weathering for the rest of Martian history (Mustard et al., 2007).

The Hesperian period is characterized by continued volcanism, low rates of erosion, formation of canyons and large outflow channels, and a shift from phyllosilicate alteration to sulfate deposition (Carr, 2006). The transition from the Noachian to the Hesperian was a major change on a global scale; impact frequency and erosional rates declined dramatically, volcanic resurfacing covered approximately 30% of the planet, and the intensity of large valley formation steeply declined (Carr et al., 2010). Notably, conditions at and near the surface changed from erosional (favouring phyllosilicate formation from weathering of silicates) to depositional (favouring the deposition of large quantities of sulfate minerals) (e.g., Bibring et al., 2006). Abundant sulfates have been observed in Hesperian terranes, including all of the surface landing sites visited up until

the Phoenix mission. Climate change at the end of the Noachian caused the growth of a large global cryosphere that persists to the present (Carr et al., 2010).

Despite lower rates of erosion, large outflow channels of Hesperian age are observed and are primarily suggestive of a fluvial origin (Carr, 2006). The likely source of these large channels is attributed to the rapid release of large volumes of stored water, rather then sustained drainage (Carr et al., 2010). While the mechanism for the storing and release of this water is not well constrained, saturated groundwater aquifers, moderately-sized lakes, and bodies of ice are potential intermediate sinks for large volumes of water if the Hesperian hydrosphere was widespread enough to allow for their formation (e.g., Ghatan et al., 2005; Harrison et al., 2008; Hovius et al., 2008). The short-term flow of such large volumes of water has the potential to create oceans or large standing bodies of water, but currently understood sinks do not appear to be large enough to compensate for the removal of an oceanic volume of water between the Hesperian and Amazonian (Carr et al., 2010). Valles Marineris formed during the Hesperian period (or late Noachian), and is thought to represent a combination of crustal movement along faults radial to Tharsis (e.g., Blasius et al., 1977) and the action of aqueous fluids (e.g., Harrison et al., 2008).

Volcanism during the Hesperian period is present mainly as ridged plains and low-lying volcanic edifices called Paterae (Greeley et al., 1981). Hesperian volcanics are observed in large areas of the northern lowlands and some regions of the southern highlands, and also likely underlie younger Amazonian volcanism in many areas such as Tharsis and Elysium (e.g., Platz et al., 2011). Based on orbital spectra, Hesperian volcanism is largely basaltic with some andesitic volcanism observed (Crisp, 2004). This andesite may be a

primary volcanic product, but it is thought that it may be a product of the alteration rind on basaltic rocks (Carr et al., 2010). The primary mineralogy of Hesperian volcanism has been largely retained due to low erosion and weathering rates, but some alteration is possible due to interactions at low water/rock ratios (e.g., Greeley et al., 1981). Volcanic flows during the Hesperian resurfaced a third of the planet and likely contributed significantly to the subsurface volcanic rocks now present at depth on Mars (Greeley et al., 1981).

The Amazonian period encompasses two thirds of the history of Mars, but surface geomorphological changes are overall modest compared with earlier periods (Taylor et al., 2009). The extremely low erosion and weathering rates from the Hesperian period continued into the Amazonian, where the effects of wind and mid- to high-latitude ice are more prevalent (Balme et al., 2006). Dunes are evident in almost all settings on Mars, and storms and dust devils are widespread (Balme et al., 2006). Primary eolian weathering of bedrock during the Amazonian appears to be relatively minor, with wind-driven reworking of poorly coherent previously fragmented materials dominating (e.g., Balme et al., 2006; Marquez et al., 2004). Some younger outflow channels formed during the Amazonian, but fluvial activity in the last 3 Ga has been minor and is largely restricted to localized groundwater flow (Gallagher et al., 2011; Mangold, 2012). Gullies are by far the most common fluvial features during Amazonian time, although the actual quantity of water present during the formation of these features is unclear (e.g., Malin et al., 2001; Gallagher et al., 2011). Much of the ice present at the poles appears to have accumulated during the late Amazonian, and thicker ice-rich deposits (such as lobate debris aprons) occur at lower latitudes (e.g., Carr, 2001; Marquez et al., 2004).

Volcanism in the Amazonian was largely in the Tharsis and Elysium volcanic terranes and their peripheries; this volcanic activity is believed to have continued into the very recent past or present day (e.g., Dohm et al., 2008). The average effusion rates at these sites during the Amazonian was much lower than in the past, with a decrease of up to an order of magnitude (e.g., Hartmann et al., 2001). Volcanism during the Amazonian was likely highly episodic. Mars is likely still volcanically active in these large volcanic centres, with low rates of effusion and periodicity on the order of hundreds of millions of years (e.g., McSween, 2002).

Much of the volcanic and hydrological activity on Mars was concentrated in the Noachian and Hesperian periods, with a significant amount of both in the early (pre-Noachian) history of Mars (Werner, 2009). The majority of Mars' history (during the Amazonian period) has been characterized by a lack of aqueous activity and sporadic primary volcanism (Carr et al., 2010). As all but one of the known Martian meteorites formed during the Amazonian period, it is clear that our direct knowledge of the oldest parts of Martian history is lacking due to meteoritical sampling bias. These early periods are also the time when Mars was most hospitable for life as currently understood; extensive volcanism, a thick atmosphere, and an active hydrosphere provided temperatures and water that may have made the surface and subsurface of Mars a relatively attractive environment for a sustained microbiosphere (e.g., Jakosky et al., 2007).

1.6 Terrestrial Endolithic Microorganisms

Life on Earth is extremely diverse, with three major domains recognized. These are the bacteria, archaea, and eukarya (Lehto, 2007). While the opinion of the scientific community has varied through time, the current astrobiological consensus is that complex eukaryotic multicellular life is not expected to have arisen on Mars (Grady, 2007). If evidence of extinct or extant Martian life is to be found, it will most likely take the form of microorganisms similar to the bacteria and archaea of Earth (e.g., McKay, 1986; Thomas et al., 1992; Schulze-Makuch et al., 2008).

Terrestrial bacteria and archaea are prokaryotic organisms lacking cell nuclei (Stan-Lotter, 2007). They are typically on the order of several microns in size, significantly smaller than eukaryotic cells (Caldwell, 2000). Most exist on their own as single cells, although many bacteria form groupings such as diploid pairs. Despite phylogenetic similarities within these two domains, the morphology and structure of bacteria and archaea is highly variable (Lehto, 2007). The bacteria and archaea form two distinct phylogenetic groupings but are both considered to be potential archetypes for possible Martian life (Schulze-Makuch et al., 2008). Many terrestrial bacteria and archaea are extremophiles, able to survive in extreme conditions (such as high temperatures, pressures, salinity, or aridity) comparable to those that might be found on extraterrestrial planetary bodies (Stan-Lotter, 2007).

There are three primary nutritional types in microbiological metabolism. These are the phototrophs, lithotrophs, and organotrophs (Bennett et al., 2007). Phototrophs derive their

primary energy from sunlight. Lithotrophs obtain energy and nutrients from the metabolism of inorganic chemical compounds, such as minerals. Organotrophs derive energy and nutrients from the breakdown of organic compounds (Caldwell, 2000). Most microorganisms that derive energy from these sources are autotrophs. Autotrophs produce complex organic compounds required for their cellular activity from materials present in their surroundings, although some organotrophs are also heterotrophic and cannot fix carbon on their own (Caldwell, 2000). Typically, autotrophs use environmental carbon dioxide as their primary energy source (e.g., Caldwell, 2000; Lehto, 2007).

The primary nutritional type thought to be a potential archetype for Martian life is lithotrophy, the use of inorganic mineral substrates to obtain energy and nutrients (Jepsen, 2007). The two primary types of lithotrophs are photolithotrophs and chemolithotrophs. Both use inorganic compounds in their environment for respiration, but differ in the source of energy used in their metabolism; photolithotrophs derive this energy from sunlight, while chemolithotrophs use the inorganic substrate itself (Bennett et al., 2007). Due to the adverse conditions at the surface of Mars during much of its history, chemolithotrophy is likely the most attractive nutritional mode for microbial life on Mars. As a complex heterotrophic biosphere is unlikely to have arisen on Mars, chemolithoautotrophs (microorganisms able to survive using inorganic mineral substrates and carbon dioxide for all of their cellular activity) are the most likely "blueprint" for the forms of life we might expect to detect in the Martian subsurface (e.g., Schulze-Makuch et al., 2008). These may take the form of endolithic microbes living within their rocky substrates in the crust (e.g., Herrera et al., 2009).

The primary metabolic component that lithotrophs derive from rocky materials is a source of energy in the form of electron donors and terminal electron acceptors (e.g., Cardace et al., 2009; Shock, 2009; Southam et al., 2007b). Almost all deep lithospheric environments are anaerobic. Some of the primary energy sources in terrestrial basaltic habitats are H_2 gas and methane, with CO_2 acting as an electron acceptor (Pederson, 2000). While there is some evidence that methane may be produced on Mars in measurable quantities, it is unknown at present if this methane would be available in the appreciable quantities required for metabolism (Formisano et al., 2004; Mumma et al., 2009). Therefore, it is more likely that lithoautotrophic organisms on Mars would derive their energy from their rocky substrate directly (e.g., Weber et al., 2006).

Of particular interest to astrobiological investigation of the Martian subsurface is the success of terrestrial endolithic microorganisms that inhabit glassy substrates in volcanic rocks (e.g., Thorseth et al., 2001). The suitability of basaltic glasses to microbial colonization has long been recognized (Ross et al., 1986; Thorseth et al., 1992), due to their energetically unstable nature in the presence of water and the ease at which they can be processed by microbes. Endolithic microbes mediate the dissolution of volcanic glasses in the presence of water, leading to pitting and eventual tunneling into the glass in the process (Staudigel et al., 1998). Such endolithic bioalteration of glassy volcanic substrates is common in current day suboceanic and ophiolitic rocks, and has been described in rocks dating back to up to 3.5 Ga (Staudigel et al., 2008). Martian volcanic rocks contain glassy materials and any volcanic products erupted in the presence of water on Mars might be expected to form similarly suitable substrates for metabolic processes (Nelson et al., 2005).

Although chemolithoautotrophy within rocky substrates in the subsurface of Mars represents an attractive subject of astrobiological investigation, the large number of unknowns regarding the potential evolution of life on Mars makes this conclusion far from authoritative. However, it provides a foundation for evaluating the potential habitability of Martian rocks to inform future exploration of the planet.

Chapter 2.0 General Materials & Methods

2.1 Study Materials

Two basaltic shergottites (Los Angeles 002 and Zagami) and one nakhlite (Nakhla) were studied in this work. Bulk materials of each were analyzed, as well as thin sections of the meteorites. These specimens are believed to adequately represent the meteorites as a whole for the purposes of this study.

Samples of the Los Angeles 002 meteorite were acquired through the donation and loan of two specimens from Mr. Robert Verish of the Meteorite Recovery Lab. This meteorite is very friable when compared to the other Martian meteorites examined in this study. A slab weighing 11.353 g was loaned to us for the duration of this study, and a slice of material weighing 3.034 g was donated for the purposes of this work. These are shown below in Figures 2.1a and 2.1b, respectively.

The slab weighing 11.353 g was used for non-destructive measurements with micro X-Ray diffraction (μXRD). The slice weighing 3.034 g was used for all research purposes, destructive or otherwise. From this slice, a thin section was cut and an epoxy probe mount were made, allowing for optical microscopy, electron microscopy and Electron Probe Microanalysis (EPMA) geochemistry to be carried out with this meteorite. This slice was also used for μXRD analysis.

The thin section of Zagami is designated UNM 992. Specimens of the Zagami meteorite were acquired from Dr. Carl Agee of the Institute of Meteoritics at the University of New Mexico. A chip of material weighing 0.72 g (Fig. 2.1c) was loaned to us for the duration of this study, as was a thin section. Both of these Zagami specimens, the 0.72 g chip and thin section UNM 992, were utilized for all necessary analytical methods outlined in this work when possible.

Two thin sections of Nakhla, designated USNM 426-2 and USNM 426-6, were loaned by Dr. Tim McCoy from the Meteorite Collection at the Department of Mineral Sciences of the Smithsonian National Museum of Natural History. These two thin sections were chosen specifically due to their close proximity to the cut location of a thin section used in a notable past astrobiological study of Nakhla (Fisk et al., 2006).

A thin section of Nakhla was donated by Dr. David Deamer of the Department of Chemistry at UC Santa Cruz. These samples were part of the original allocation of Nakhla given to academic researchers by NASA. In addition, a chip of material weighing 0.58 g was donated (Fig. 2.1d).

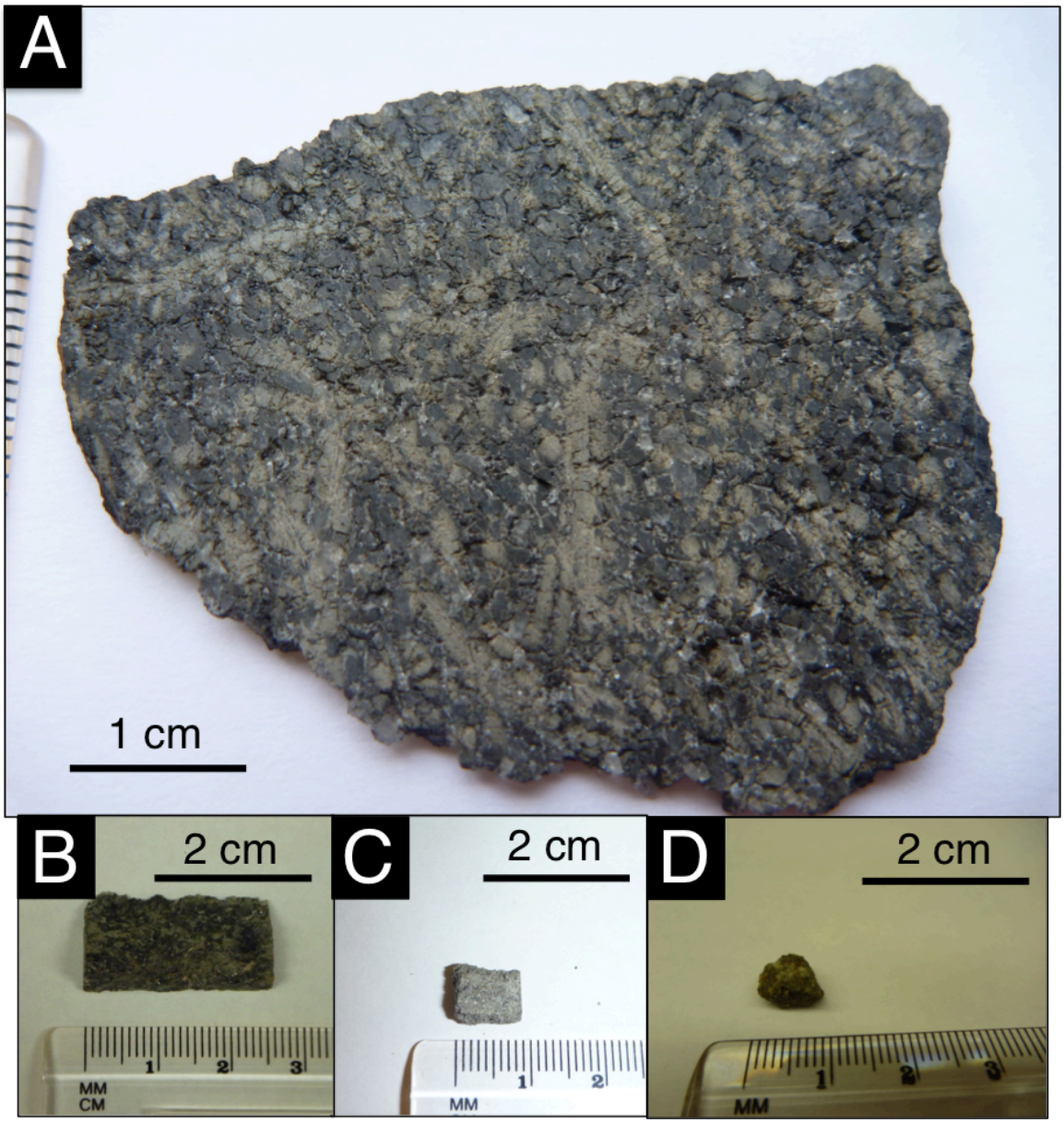

Figure 2.1: Primary bulk samples used in this study. A) Large 11.353 g slab of the Los Angeles 002 meteorite. B) Small 3.034 g slice of the Los Angeles 002 meteorite. C) 0.72 g chip of the Zagami meteorite. D) 0.58 g chip of the Nakhla meteorite.

2.2 Experimental Rationale

Martian meteorites represent the only *ex situ* samples of the Martian crust currently available, and allow for the study of the Martian lithosphere in terrestrial laboratory settings. The SNC meteorites have been key components of the study of astrobiology and the search for life in the solar system for decades (e.g., McKay et al., 1996; Fisk et al., 2006). Rightly or wrongly, these studies have propelled the exploration of Mars and contributed greatly to the field of astrobiology. However, many of the astrobiological studies of Martian meteorites have been called into question based on issues of methodology or interpretation of results (e.g., Martel et al., 2012; Treiman, 2003). It is critical to quantify what is known about the potential habitability presented by SNC meteorites before any significant conclusions can be drawn regarding the evidence for or against life in these rocks and elsewhere on Mars. An understanding of the range of inorganic materials available to possible microbial life on Mars can be accomplished through the study of the mineral make up of Martian meteorites. This study aims to characterize a suite of Martian meteorites from a geological (mineralogical and geochemical) perspective, and to use this as a starting point to attempt an assessment of the potential habitability of the Martian subsurface as represented by these meteorites.

These three meteorites represent a varied selection of the Martian meteorite collection and provide diverse materials that have experienced diverse processes during their formation and evolution. Los Angeles 002 and Zagami are basaltic shergottites, and have been chosen for this study because they represent rock types that are analogous to the basaltic rocks extruded on the terrestrial seafloor. Terrestrial basalts are known to be prolific

microbial habitats and substrates, and their counterparts on Mars are promising candidates for characterization and habitability evaluation. Los Angeles 002 is a relatively differentiated basaltic rock containing a higher proportion of calcium-aluminum rich phases, while Zagami has been shocked to a higher degree than Los Angeles 002. Together they provide two contrasting lithological types within the shergottite family. Nakhla is a clinopyroxenitic nakhlite and has been chosen for this study because it represents a more olivine-rich lithology than the shergottites, providing unique habitability factors to be considered. Nakhla is rich in iron- and magnesium-rich phases and has been heavily altered by aqueous processes while on Mars, making it a good candidate for an evaluation of aqueous processes on Mars and with an emphasis on the habitability of the planet.

Particularly, the fine-grained nature of the vein alteration material in Nakhla has historically impeded intensive study of its mineralogical composition (e.g., Ashworth et al., 1975; Gooding et al., 1991). Polishing during preparation of a thin section may cause much of the soft, altered material within fractures to be removed. Most of what remains is present as coatings and infrequent deposits in fractures with complex geometry that penetrate at various depth into the section. As a result, access to this material is difficult to achieve with many analytical techniques. Obtaining adequate amounts of this material for pulverization and analysis using traditional mass spectrometry or power X-ray diffraction techniques is impractical. The majority of fractures do not contain enough coherent alteration material to make this approach feasible, and acquiring this material would involve destroying or damaging the section. Given the valuable nature of Martian meteorites, this is not an ideal approach. However, the presence of alteration material as

coatings and infrequent deposits within fractures makes them well-suited to analysis by the *in situ* nondestructive techniques used in this study.

2.3 Instrumental Methods

2.3.1 Optical Microscopy

Primary optical microscopy was carried out in the Earth and Planetary Materials Imaging and Analysis Laboratory at Western University, using a Nikon Eclipse LV100POL compound petrographic microscopes fitted with Nikon DS-Ri1 (12.7 Mpx) and Nikon DS-Fi1 (5Mpx) digital cameras. Polarized light is passed through samples in polished section and interaction of the crystal lattice with the beam produces diagnostic interference colours. Optical photomicrographs of meteorite polished sections were taken in both plane- and cross-polarized light. Optical microscopy allowed for the identification of mineral phases and for the study of textural features (such as alteration of primary phases).

2.3.2 Backscattered & Secondary Electron Imaging

Primary backscattered electron (BSE) images and reconnaissance secondary electron imaging of the Nakhla, Los Angeles, and Zagami meteorites were acquired using the Hitachi SU6600 FEG-SEM of the Zircon and Accessory Phase Laboratory (ZAPLab) at Western University. The JEOL 8900 and CAMECA SX100 electron microprobes of the Electron Microprobe Laboratory at the University of Alberta are also equipped to perform electron microscopy and were used for imaging of sites during microprobe analysis. These BSE images provide two-dimensional representations of the general composition

of a sample, as materials with a high atomic weight are displayed with a higher brightness. This allows for textural mapping of meteorite thin sections.

2.3.3 *In Situ* Micro X-Ray Diffraction (μXRD)

Micro X-Ray Diffraction (μXRD) measurements were made using the Bruker-AXS D8 Discover micro-X ray diffractometer at Westerrn University, using the techniques outlined by Flemming (2007). Co Kα radiation (with a wavelength of 1.7889 angstroms) was used, with a beam size of 300 or 100 μm depending on the analytical requirements. An XYZ sample stage allowed equipped with a laser sight and optical microscope allowed for targeting of specific locations of interest on meteorite samples. A Hi-STAR 2D detector using general area detector diffraction system (GADDS) software was used to detect diffracted X-rays. Omega scans, in which the detector and X-ray source rotate in an arc around the sample, were used in this work with a full scan 2θ angle of 2-86^{o}.

X-rays of a known wavelength are directed at a sample and the crystal lattice planes within the mineral specimen are diffracted at diagnostic angles. This allows for characterization of mineral species present in a sample by their crystal structure, where characteristic interplanar lattice spacing is measured by diffraction angle (2θ) using Bragg's Law ($n\lambda = 2d\sin\theta$). Due to the nature of *in situ* micro X-ray diffraction (in which samples are not powdered), it is possible that some crystallographic orientations may not be observed by the beam (as not all lattice planes will satisfy Bragg's Law) and therefore that some expected peaks may not be detected. Amorphous materials do not diffract electromagnetic radiation and cannot be characterized directly using this technique.

Standard count times were 20 minutes per frame per target location; for more detailed analysis, such as identification of secondary alteration phases, count times were increased to one hour and three hours as needed. Due to the *in situ* nature of this technique, both thin sections and whole rock samples were analyzed using μXRD. Some contributions from surrounding phases are present due to the large beam size as compared to the grain size, but these can be accounted for during processing. Conventional intensity versus 2θ XRD patterns are generated by integration of two GADDS frames of acquired data and have been background subtracted. XRD data were analyzed using the BrukerAXS EVA software package. The International Centre for Diffraction Data (ICDD) PDF-4 database was used to identify mineral phases. ICDD cards for reference mineral species were compared with the observed diffraction pattern and the relative contribution of different phases was considered.

2.3.4 Laser Raman Spectroscopy

Laser Raman spectroscopy was performed at Surface Science Western using a Renishaw Model 2000 Raman spectrometer. A beam with wavelength of 633 nm was used in the analyses, and provided an area of excitation approximately 1-2 μm in diameter. This allowed for analysis of small regions of interest within fractures of the Nakhla meteorite. Raman spectroscopy provides information on the nature of chemical bonds in a sample due to induced vibrational energy transfer from Raman shifts in electronic energy states, and can therefore be used to identify the mineral phases present in a mineral phase. Peak contributions were identified using the RRUFF mineral database and published literature on mineral identification by Raman spectroscopy.

Targets for Raman spectroscopy (alteration) were chosen to be fractures within olivine grains that contain a high concentration of vein alteration material. In order to reduce beam scattering and lower signal to noise ratio, the best targets were thick fractures extending approximately vertically into the section with relatively simple geometries.. Subtraction of the baseline epoxy spectrum has been performed, due to the likelihood of contributions from epoxy that may be present in fractures following thin section preparation Mineral contributions to Raman spectra were identified following Hanesch (2009), Rull et al. (2004), Edwards (1999), and references contained therein. The RRUFF database of Raman spectra managed by the Department of Geosciences at the University of Arizona was also used for comparison of mineralogical standards against the observed spectra.

Several of the observed peaks, such as those at 1500 cm^{-1} and 1860 cm^{-1}, can be attributed to contributions by epoxy present in the fractures. Fluorescence caused by the instrumental source creates interference with the spectra at low wavenumbers, impeding the ability to discern peaks from the background signal. Similarly, the geometry of the fractures and scattering of the beam before it is picked up by the detector serves to greatly decrease the signal to noise ratio. Although epoxy pattern subtraction was performed on the spectra, limitations of the algorithm used cause some contributions to remain. Large, broad peaks such as that observed at wavenumber 1670 cm^{-1} can be attributed to the presence of organic carbon due to small patches of carbon coating applied during section preparation unable to be completely removed during diamond polishing. A peak at 3080 cm^{-1} can be attributed to cosmic ray interaction with the instrumental detector; it has not been removed for purposes of data integrity.

2.3.5 Electron Probe Microanalysis (EPMA)

Electron probe microanalysis (EPMA) was used to determine the chemical compositions of major and minor elements in selected targeted phases in the Nakhla, Los Angeles, and Zagami meteorites. These analyses were carried out on the JEOL 8900 and CAMECA SX100 electron microprobes of the Electron Microprobe Laboratory at the University of Alberta. These are both equipped with 5-channel wavelength-dispersive spectrometers with a beam size of approximately 5 μm, and an accelerating voltage of 15 keV was used for analysis. Natural mineral standards provided by the Smithsonian Institution Department of Mineral Sciences were used (Jarosewich, 2002). These were: orthoclase (K), albite (Na), diopside (Ca, Si), hematite (Fe), rutile (Ti), forsterite (Mg), apatite (P, F), pyrope (Al), willemite (Mn), chromite (Cr), and tugtupite (Cl). Data reduction was carried out using standard oxide reduction, as described by Armstrong (1995).

Weight percent oxide totals for all spot analyses presented here total approximately 100%, providing high confidence in the elemental compositions reported. However, weight percent oxide totals for alteration material spot analyses were below 100% due to the presence of abundant hydrated phases. For example, smectites (such as nontronite and saponite) can be expected to lose their approximately 15-20 wt% of volatiles through heating and volatilization during microprobe analysis. Samples analyzed by EPMA were meteorite polished sections. Those provided by the Smithsonian Institution were carbon coated prior to EPMA analysis, and all other samples were osmium coated at the Nanofabrication Facility at Western University.

Chapter 3.0 Results

3.1 Texture and Petrography

Table 3.1 below shows the ideal chemical formulas for all mineral phases discussed in the following sections. The mineral phases described in Section 3.1 were identified and characterized using optical microscopy, backscattered electron imaging, micro-X ray diffraction, and EPMA elemental mapping. These data will be presented in later sections following a textural and petrographic description of all relevant phases.

Table 3.1: Ideal formulas for described mineral phases (from www.mindat.org).

Mineral Phase	Chemical Formula
Augite	$(Ca,Na)(Mg,Fe,Al,Ti)(Si,Al)_2O_6$
Pigeonite	$(Mg,Fe,Ca)(Mg,Fe)(Si)_2O_6$
Olivine	$(Fe,Mg)_2SiO_4$
Hedenbergite	$CaFeSi_2O_6$
Silica	SiO_2
Anorthite	$CaAl_2Si_2O_8$
Albite	$NaAlSi_3O_8$
Merrillite	$Ca_{18}Na_2Mg_2(PO_4)_{14}$
Pyrrhotite	$Fe_{1-x}S$ (x=0-0.17)
Titanomagnetite	$(Fe,Ti)_3O_4$
Ilmenite	$FeTiO_3$

3.1.1 Los Angeles 002

LA 002 is a basaltic shergottite composed of 40% maskelynite regions enclosing 35% coarse-grained pyroxene crystals. Optical photomicrographs of the LA 002 meteorite in polished section are shown in Figure 3.1a-d. Backscattered electron micrographs of

representative regions of LA 002 are shown in Figure 3.2a-d. These images display the textural relationships characteristic of this meteorite.

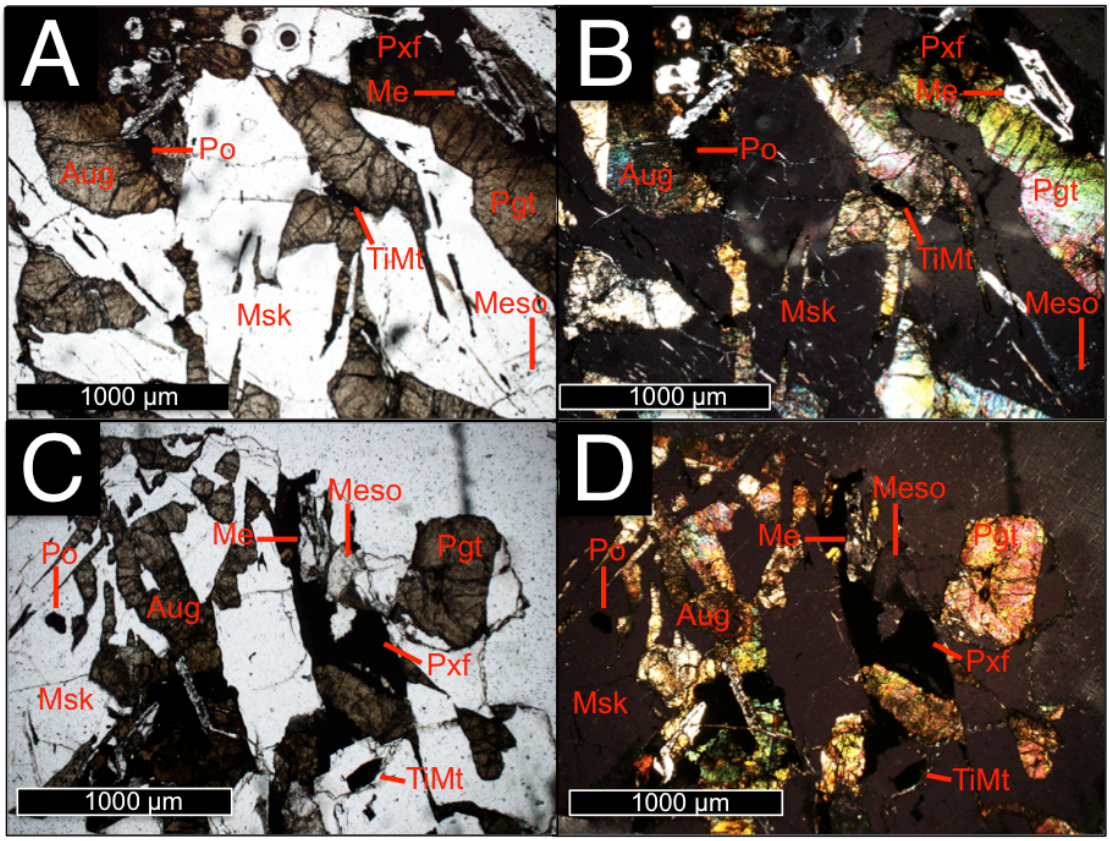

Figure 3.1: Optical photomicrographs of the Los Angeles 002 meteorite in polished section. Major phases have been labeled [Aug = augite, Pgt = pigeonite, Pxf = pyroxferroite, Msk = maskelynite, Meso = mesostasis, Me = merrillite, TiMt = titanomagnetite, Po = pyrrhotite] A) Plane light, subophitic texture with maskelynite regions infilling between pyroxene grains is visible. B) Same region in cross-polarized light, note association of minor phases with pyroxene. C) Plane light, note maskelynite displaying original plagioclase crystal habit. D) Same region in cross-polarized light, slight mosaicism in pyroxene birefringence and extinction due to shock.

The proportion of maskelynite-plagioclase material in this rock is up to twice that of most shergottites. Maskelynite in LA 002 is interconnected across the meteorite and forms a subophitic texture (Winter, 2001). Maskelynite is a diaplectic glass formed when plagioclase feldspars are shocked during impact. Zones of maskelynite in LA 002

preserve in large part their original crystal forms and form a framework intergrown with large pyroxenes. Volcanic mesostasis (late forming glassy material and fine grained phases) is present in patches between larger

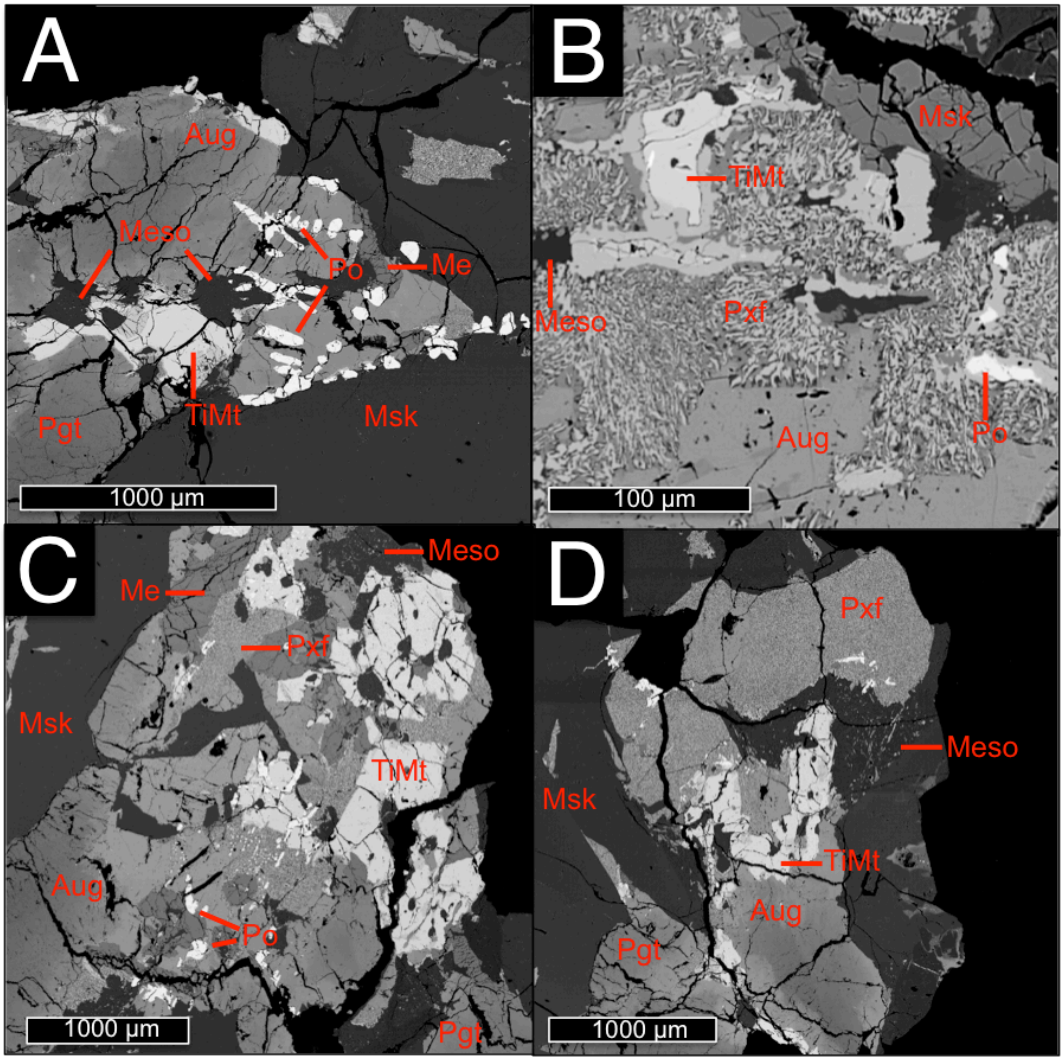

Figure 3.2: Backscattered electron SEM images of the Los Angeles 002 meteorite in polished section. Phases with higher atomic weight appear brighter when imaged. Major phases have been labeled [Aug = augite, Pgt = pigeonite, Pxf = pyroxferroite, Msk = maskelynite, Meso = mesostasis, Me = merrillite, TiMt = titanomagnetite, Po = pyrrhotite] A) Note slight zoning of pyroxenes and association of blebs of sulfide and oxide minerals with other phases. B) Distinct components of pyroxferroite breakdown material can be easily seen on this scale. White = silica, light grey = olivine, dark grey = hedenbergite. C) Note moderate fracture system due to friability of meteorite. D) Note mottled texture of pyroxferroite breakdown material and relationship to pyroxene grains.

crystals. Minor phosphates, oxides and sulfides, are present throughout the rock. Some phases, such as pyroxene, are heavily fractured. The minor phases are associated with spaces between larger pyroxene grains, and commonly with areas of mesostasis. However, there are no continuous pervasive fractures or veins present in the samples of this meteorite that were examined, due to shock or otherwise. Small fractures in LA 002 appear to be largely unaltered, and what little secondary alteration is present in fractures is likely terrestrial in origin.

Large domains of pyroxferroite breakdown material are present in this rock, associated with pyroxene crystals. These appear to be composed of finely-intergrown zones of three separate interfingering phases. Pyroxferroite is a calcium-iron pyroxene and is unstable at low temperatures and pressures, and has been previously reported in LA 002 (Rubin et al., 2000; Rost et al., 2009). The breakdown of metastable pyroxferroite into hedenbergite, fayalite and silica is well documented (Rubin et al., 2000). These three phases form discrete domains clearly distinguishable within the pyroxferroite in LA 002 (as seen in Figure 3.2b).

Both augite and pigeonite are present in LA 002 in similar abundances. Pyroxenes in this meteorite are approximately 2-4 mm in length and up to 1 mm in width. They form prismatic crystals, subhedral to euhedral in form. Pyroxenes are typically tan to dark brown, and display some pleochroism and high birefringence. The interference colours in pyroxene have been augmented due to impact shock that has strained the crystal lattice, and some mottled extinction is observed in pyroxene due to strain (seen in Figures 3.1b and 3.1d). Pyroxferroite breakdown material is visible in LA 002 as dark brown to black

patches associated with pyroxene grains. It is dark (most often opaque), and is visible in Figures 3.2b and 3.2d as a mottled texture.

Maskelynite is present as large 2-4 mm subhedral zones of diaplectic glass formed from original plagioclase during shock. Maskelynite is mostly colourless in plane light and isotropic under cross-polarized light. Mesostasis in this meteorite forms small patches of quenched glass (shown in Figure 3.2a-d), with associated minor mineralization such as fayalite and silica present as rims and blebs. The phosphate phase in LA 002, merrillite, is present as small 0.5-1 mm irregular crystals associated with pyroxene prisms. Colourless in plane light and grey in cross-polarized light (Figure 3.1a-b), it displays no pleochroism and up to first-order grey birefringence. Titanomagnetite is present in LA 002 as anhedral to subhedral opaque intergrowth crystals of several mm most often associated with pyroxenes (see Figures 3.2a and 3.2c). Pyrrhotite is present as an accessory phase as small, approximately 0.5 mm anhedral to subhedral opaque crystals throughout the rock (best seen in Figure 3.2a). These accessory phases can be clearly discerned from other phases optically in plane- and cross-polarized light, as in Figure 3.1.

3.1.2 Zagami

Zagami is a shergottite and displays a fine-grained texture, with well-defined subhedral to euhedral pyroxene crystals forming a framework around zones of maskelynite commonly preserving plagioclase crystal forms. Figure 3.3a-d shows several optical photomicrographs of the Zagami meteorite in polished section. Figure 3.4a-d shows

backscattered electron micrographs of representative regions of Zagami, displaying the characteristic textures of this rock.

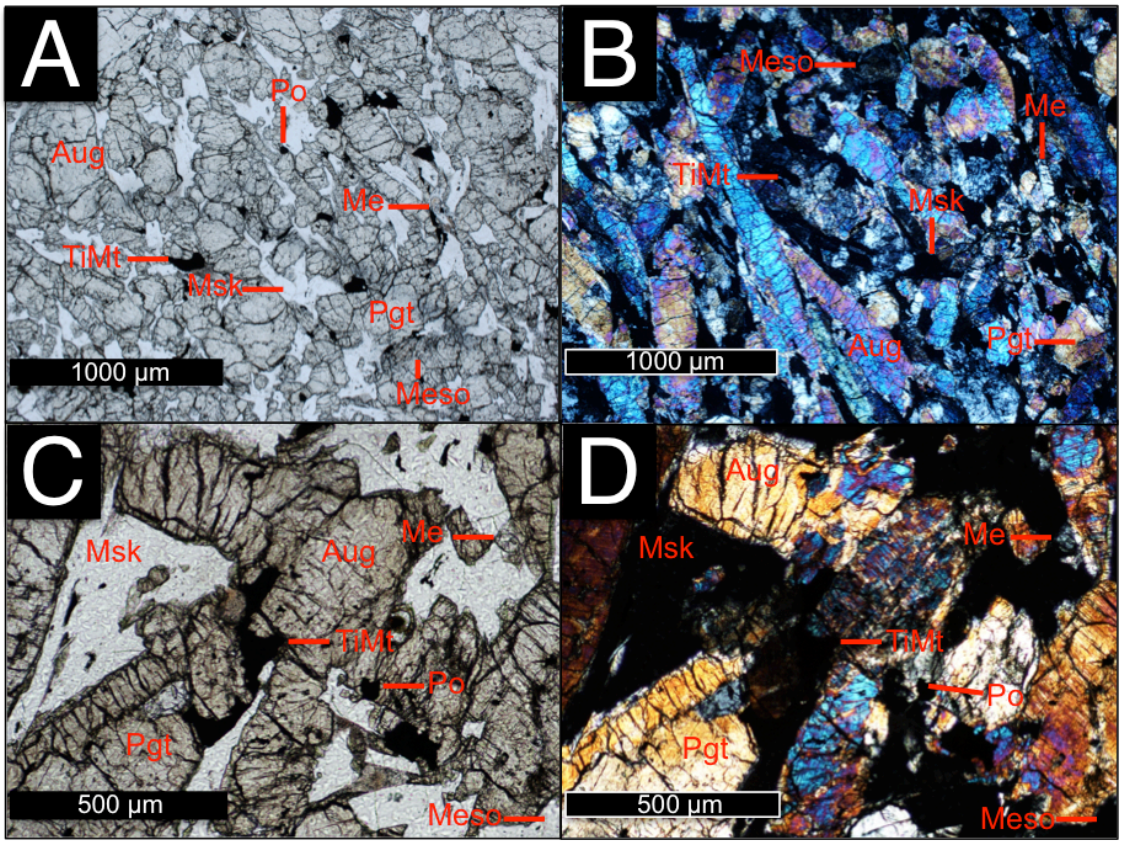

Figure 3.3: Optical photomicrographs of the Zagami meteorite in polished section. Major phases have been labeled [Aug = augite, Pgt = pigeonite, Pxf = pyroxferroite, Msk = maskelynite, Meso = mesostasis, Me = merrillite, TiMt = titanomagnetite, Po = pyrrhotite] A) Plane light, note ophitic texture with small maskelynite zones between pyroxene grains. B) Cross-polarized light, note moderate mosaicity in pyroxene due to shock. C) Plane light, note associated of minor phases with pyroxene D) Same region in cross-polarized light, note moderate retention of original crystal habit by maskelynite zones.

Maskelynite domains are somewhat interconnected and likely represent growth of plagioclase crystals both during and following pyroxene formation. Pyroxene grains form the majority of this meteorite (~70%) and small domains of maskelynite have grown between pyroxenes, forming an ophitic texture (Winter, 2001) Two generations of related

pyroxene growth can be observed. In addition to the pyroxene framework grains, some regions also display a finer-grained texture of smaller pyroxene crystals. Variation in

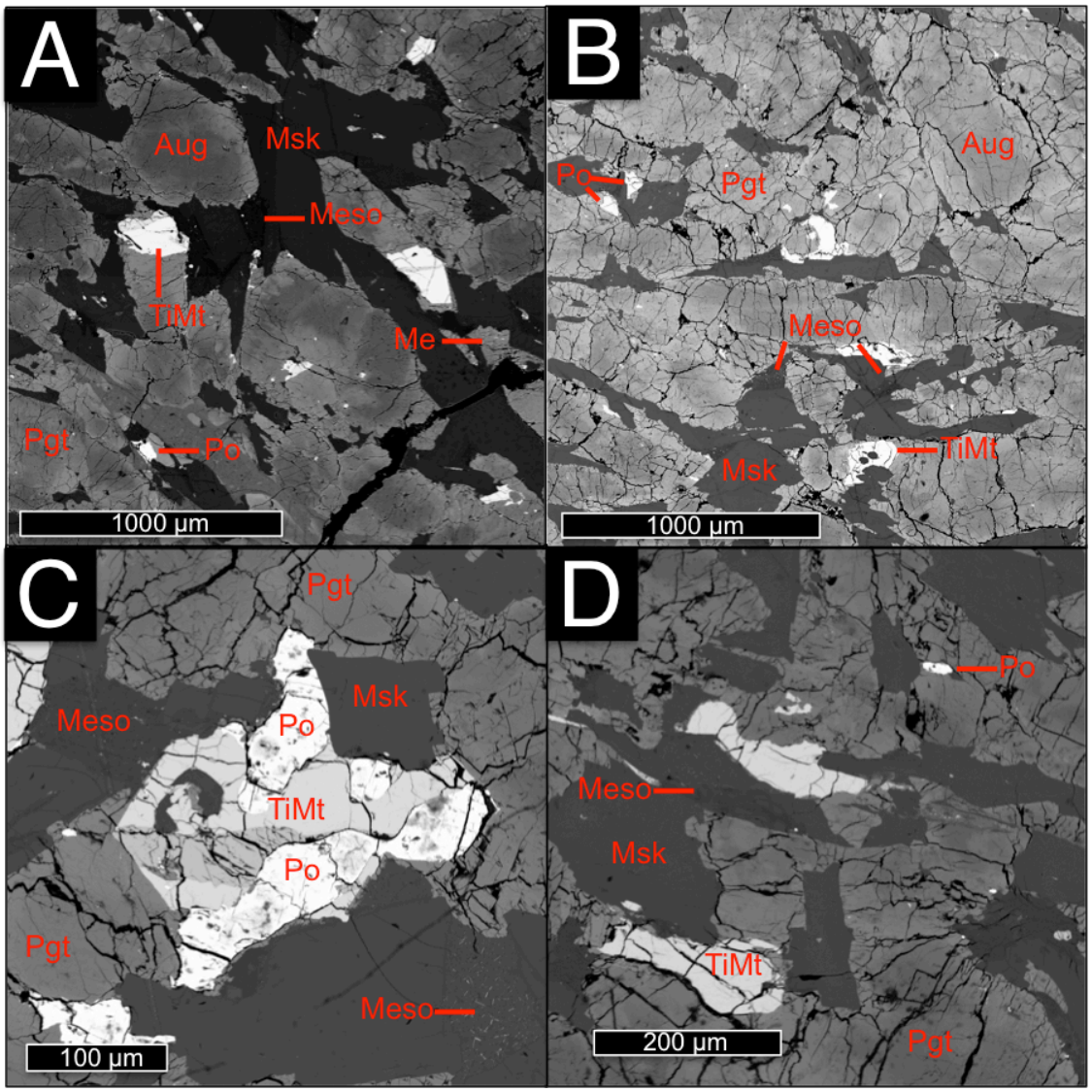

Figure 3.4: Backscattered electron SEM images of the Zagami meteorite in polished section. Phases with higher atomic weight appear brighter when imaged. Major phases have been labeled [Aug = augite, Pgt = pigeonite, Pxf = pyroxferroite, Msk = maskelynite, Meso = mesostasis, Me = merrillite, TiMt = titanomagnetite, Po = pyrrhotite] A) Note patchy nature of maskelynite zones. B) Note association of minor phases with pyroxene grains. C) Note interfingering of oxide and sulfide phases and mottled appearance of mesostasis due to presence of quenched constituents. D) Note bleb-like nature of oxide and sulfide phases.

grain size in Zagami pyroxenes can be on the order of centimetres. A general foliation of aligned pyroxene crystals and maskelynite laths has been previously reported in Zagami on a whole-rock scale (McCoy et al., 1992), and was observed here as seen in Figure 3.3a-b. Fractures in Zagami appear to be largely unaltered, and minor alteration is likely terrestrial in origin. Patches of quenched mesostasis material are present throughout the rock within the pyroxene crystal framework. Minor phases, such as phosphates, oxides and sulfides are present as accessory phases throughout the rock (described below). They are associated with spaces between pyroxene grains, and often with patches of mesostasis material.

Augite and pigeonite are both present in Zagami, in approximately equal abundances. Pyroxenes in Zagami form two distinct size fractions, the first being approximately 2-3 mm in length and up to 1 mm in width, and the second being under 1 mm in all dimensions. They form subhedral to euhedral prismatic grains, and are generally colourless to light tan in plane-polarized light. Pyroxenes in Zagami display strong birefringence, and some mosaicism due to shock effects. Maskelynite forms small, irregularly shaped zones of diaplectic feldspathic glass intergrown between larger grains of pyroxene. These are largely transparent in plane-polarized light and isotropic in cross-polarized light.

Volcanic mesostasis is present in Zagami as small irregularly shaped intergranular zones of late-forming glass and fine grained material, up to approximately 0.5 mm in size (best seen in Figure 3.4b-d). These are sometimes associated with other late forming phases such as small amounts of SiO_2 (McCoy et al., 1992). Merrillite is present as small

anhedral crystals, up to 0.5 mm in size. These are transparent in plane light, display up to first order grey birefringence, and are commonly associated with pyroxene crystals. Titanomagnetite forms anhedral to subhedral opaque intergrowths of up to 1-2 mm in size. These are typically located between larger pyroxene crystals. Pyrrhotite is present as small opaque subhedral accessory crystals < 1mm in size throughout the meteorite.

3.1.3 Nakhla

Nakhla is a clinopyroxenite, with the majority (>70%) of the rock made up of augite and pigeonite. Olivine is a major phase (15%), as well as mesostasis comprising glassy material and plagioclase (10%), with minor Fe-Ti oxides, sulfides, carbonates and hydrated alteration phases also present (described below). Coarse euhedral and subhedral pyroxene and olivine grains are set in a matrix of fine-grained mesostasis. Figure 3.5a-e shows optical photomicrographs of the Nakhla meteorite in thin section. Figure 3.6a-c shows backscattered electron micrographs of representative regions of Nakhla, displaying the textural relationships characteristic of this meteorite.

The primary texture in Nakhla is composed of large augite crystals with other phases interspersed throughout, forming a subcumulate texture. Large olivine grains are much less common than augite crystals but also form one component of this framework. In between these large crystals is late-forming mesostasis material. This comprises phases that are much more fine-grained than the dominant ferromagnesian minerals. Glassy material and plagioclase laths are the dominant constituents of the mesostasis. Other fine grained minor oxide and sulfide phases (primarily titanomagnetite and pyrrhotite)

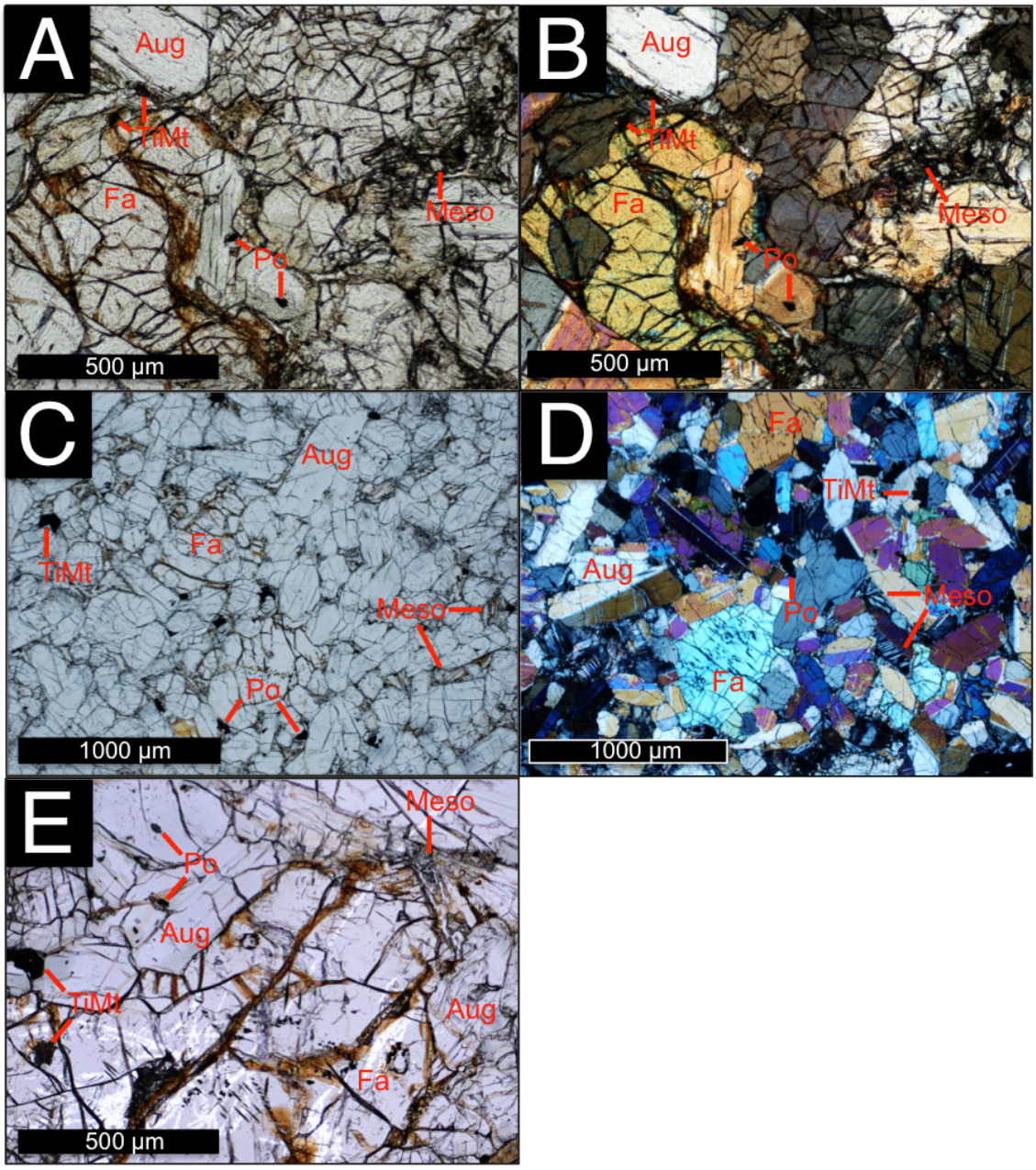

Figure 3.5: Optical photomicrographs of the Nakhla meteorite in polished section. Major phases have been labeled [Aug = augite, Fa = olivine (fayalitic), Meso = mesostasis, Me = merrillite, TiMt = titanomagnetite, Po = pyrrhotite] A) Plane light image showing subcumulate texture with interlocking pyroxene and olivine grains with intercumulus mesostasis and secondary phases. B) Same region in cross-polarized light, note twinning in pyroxene and high variability in mesostasis appearance. C) Plane light, note variation in pyroxene size and reggish-brown alteration of mesostasis as well as olivine. D) Cross-polarized light, note association of minor phases with mesostasis and small exsolution crystallite of augite and magnetite within olivine. E) Plane light image showing rusty nature of alteration of olivine grains and mesostasis.

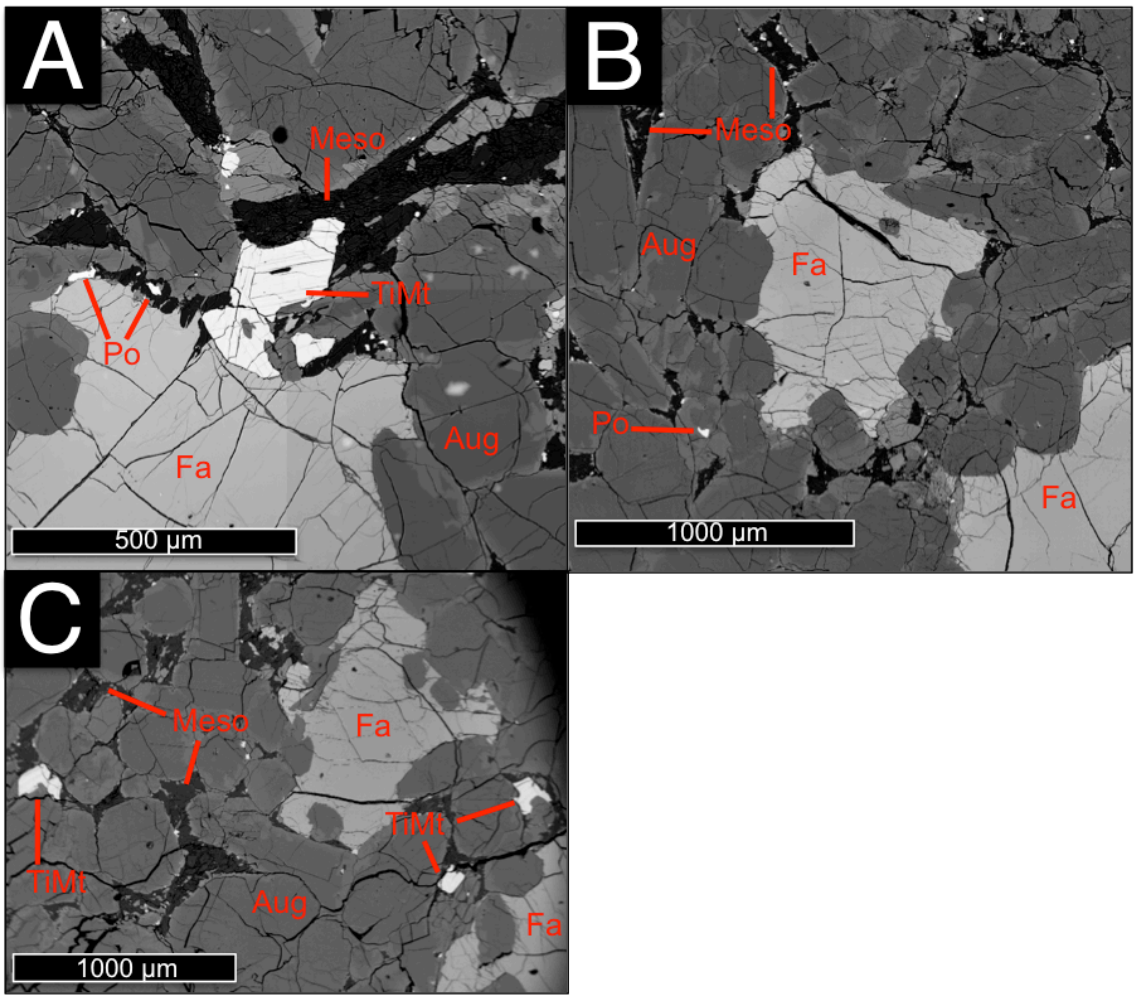

Figure 3.6: Backscattered electron SEM images of the Nakhla meteorite in polished section. Phases with higher atomic weight appear brighter when imaged. Major phases have been labeled [Aug = augite, Fa = olivine (fayalitic), Meso = mesostasis, Me = merrillite, TiMt = titanomagnetite, Po = pyrrhotite] A) Note infilling of fractures in olivine and slight zoning in pyroxenes. B) Note interlocking pyroxene texture, melt inclusion in olivine grain, and association of small sulfide blebs with mesostasis. C) Note crystalline nature of some mesostasis region and glassy nature of others, as well as infiltration of alteration material into olivine grain.

are also present in the rock. These are typically associated with the mesostasis zones, but can be found throughout.

Augite is the dominant mineral in Nakhla (approximately 70% of this rock). Augite is occurs as greenish-brown transparent prisms in plane light approximately 0.5-1 mm in length, with some slightly coarser areas and many grains display minor deformation twinning due to shock and pronounced cleavage. Olivine forms the other dominant phase in this rock, as large phenocrysts throughout the rock. These are approximately 1 mm in width, euhedral, and greenish-brown. Many olivine crystals in Nakhla display symplectitic exsolution of small augite and magnetite crystals (Treiman, 2005), and some contain small magmatic inclusions.

Volcanic mesostasis comprises most of the remaining volume of the meteorite, present as irregular patches of around 0.5 mm or less in size; this late-forming material has filled in the gaps between the interlocking augite and olivine crystals. This is composed of glassy, fine-grained material as well as plagioclase laths of approximately 100 μm at their greatest length. This material has a mottled texture in thin section, and can be highly birefringent depending on its composition. Plagioclase laths present in mesostasis display albite twinning. Potassium feldspar has been reported in some areas of mesostasis elsewhere in Nakhla (e.g., Treiman, 2005), but none was directly observed in this study.

Associated with this mesostasis are other minor phases, such as sulfides and oxides. The primary oxide present in this rock is titanomagnetite, although many grains of this iron oxide phase are compositionally closer to Ti-rich magnetite or ilmenite than true titanomagnetite; both have been reported in the literature (e.g., Bridges et al., 2006). Titanomagnetite is present in Nakhla as irregular, subhedral opaque crystals of approximately 0.5 mm in size. Pyrrhotite is the primary sulfide phase in this meteorite,

although pyrite is present in some locations and it is likely that a continuum exists in the sulfide phase of Nakhla. Pyrrhotite is present as irregular, anhedral opaque crystals of typically <0.5 mm in size. These oxides and sulfides are generally associated with mesostasis, but can also be found independently throughout Nakhla.

Olivine crystals in Nakhla are transected by a pervasive system of fractures approximately 5-10 μm in thickness. This can be seen in Figure 3.7a. Similarly, olivine crystals commonly contain fractures that appear to originate from adjacent phases or from larger fractures between the olivine grain and other phases, typically pyroxene grains. This can be seen in Figure 3.7b, with fractures extending into an olivine grain from an adjacent pyroxene grain. Fractures extending from adjacent grains commonly intersect the pervasive fracture system within the interior of the olivine grain. Mineralogical interfaces with vein alteration material are typically with olivine and/or pyroxene.

Fractures in Nakhla olivine crystals are filled with vein alteration material. It should be noted that “iddingsite” is a primary alteration product of olivine, and never occurs as secondarily precipitated material in pores and cracks (Delvigne et al., 1979). The variation in concentration of “iddingsite” can be seen in Figure 3.7a, as a relative color change across different fractures in the same grain. This vein alteration material appears reddish-brown in plane-polarized light, with slight pleochroism from lighter to darker shades. Many fractures appear darker and opaque in their core and lighten as they move outward, as demonstrated by Figure 3.7b. The opacity of a fracture is likely due in part to the amount of material present in the fracture, as well as its composition. In cross-polarized light, vein alteration material is highly birefringent with colours up to

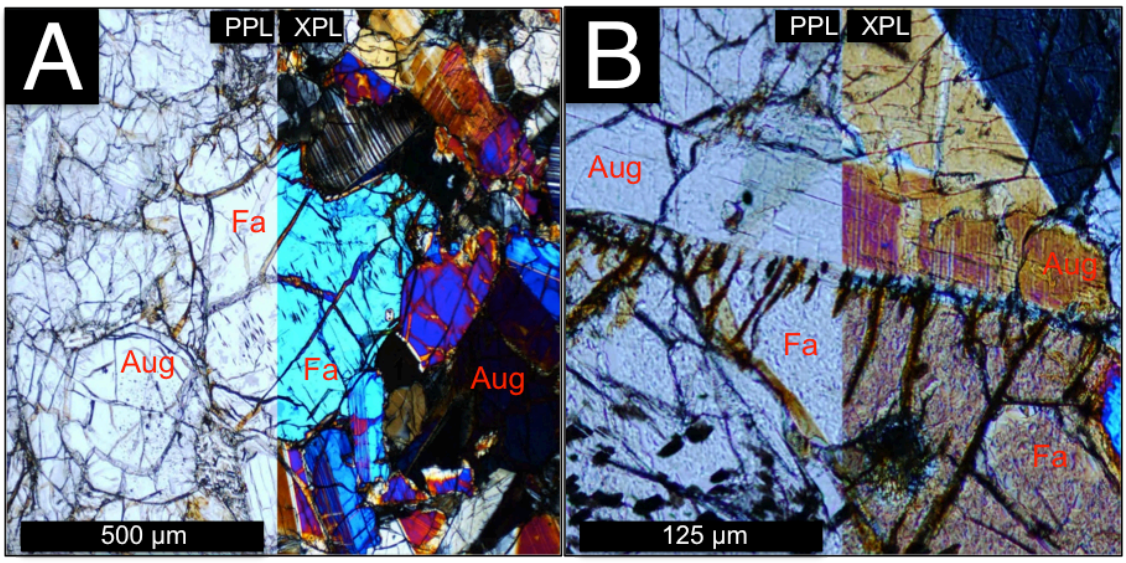

Figure 3.7: Optical photomicrographs of olivine grains in the Nakhla meteorite showing alteration. Major phases have been labeled [Aug = augite, Fa = olivine (fayalitic)] A) Note pervasive nature of fracture system and lack of crystallographic control on fractures. B) Note fractures radiating into olivine grain from Aug-Fa boundary and mottled nature of fracture filling material in cross-polarized light.

second and third order across different sections of alteration. Alteration material within the fractures is micro- or crypto- crystalline and individual crystals cannot be discerned by petrographic microscopy, although platy morphology can be observed in some fractures and discrete coarse grained crystals have been reported in other nakhlites such as Lafayette (Treiman et al., 1993; Treiman, 2005). Nakhla alteration veins have also been suggested to contain an amorphous phase, typically in the center of the veins, that has been described as a gel (Changela et al., 2010).

Backscattered electron imaging (BSE) of fractures in olivine grains shows that the material filling the fractures is significantly lighter in average atomic weight than the host olivine. Alteration domains within fractures are typically coherent, but in some locations

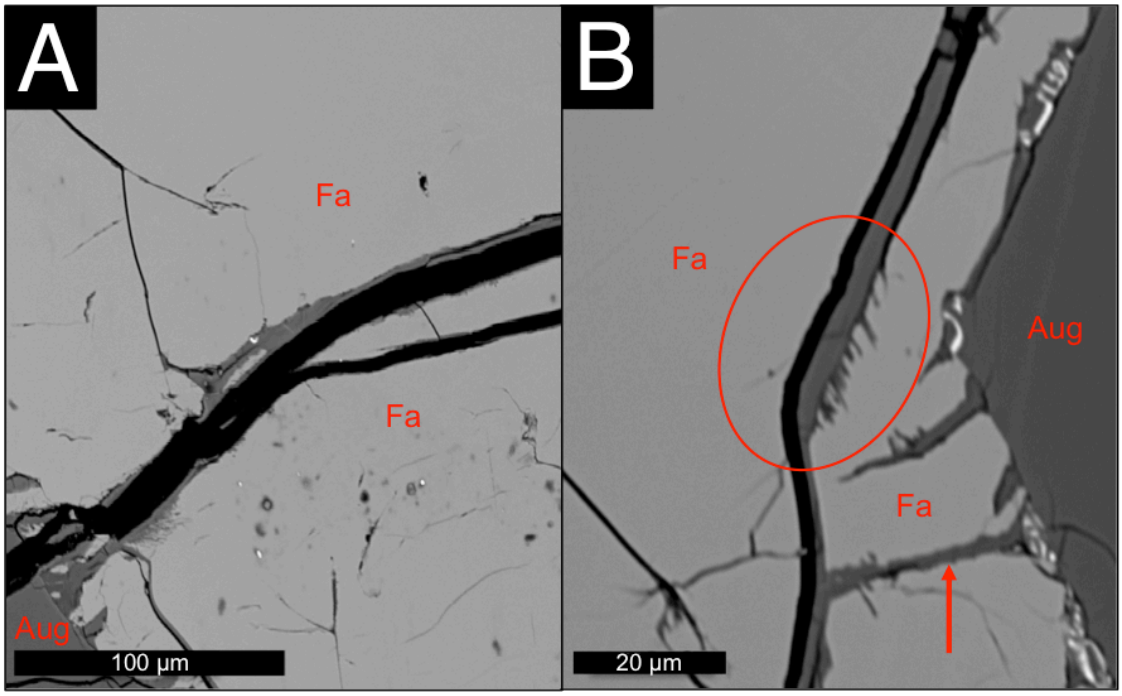

Figure 3.8: Backscattered electron SEM images of vein alteration material in olivine in the Nakhla meteorite. Major phases have been labeled [Aug = augite, Fa = olivine (fayalitic)] and black colour is epoxy filling the fracture in polished section. A) Note that fracture filling material appears darker due to a decrease in average atomic weight of constituent elements during alteration. B) Note infiltration texture of alteration material into olivine grain (circled region) and extension of fracture into Aug-Fa grain boundary (as shown by arrow).

are fractured and broken into multiple discrete domains. Alteration not only occurs in large primary fractures, but also in smaller secondary fractures. The relationship between fracture-filling alteration material and the host olivine can be seen in Figure 3.8a-b. The walls of fractures are typically smooth, indicating that they formed *in situ* and have been altered *in situ*. Alteration material usually adheres to the perimeter of fractures, although some fractures contain vein alteration material in their interior as well. Alteration of the host olivine grains is pervasive and extends, in many locations, away from the originating fracture and into the pristine olivine material (as shown in Figure 3.8b). This suggests that

the vein alteration material has formed from *in situ* alteration of the olivine rather than from deposition of minerals from allochthonous sources.

3.2 Micro X-Ray Diffraction

3.2.1 Los Angeles 002

Context images of several *in situ* micro targets are shown in Figure 3.9a-e. The corresponding diffraction patterns obtained from these spots are shown in Figure 3.10a-e, with ICDD cards for the highlighted contributing phase overlain.

The diffraction pattern of augite in LA 002 is shown in Figure 3.10a and the diffraction pattern of pigeonite in LA 002 is shown in Figure 3.10b. The large beam size compared to the grain size of pyroxenes in LA 002 contributes to some additional signal in these patterns, but the primary peaks can all be identified using the ICDD cards. Although there is some contribution from both pyroxenes in these patterns, the primary phase is clearly discernable by its higher peak intensity.

The diffraction contribution of merrillite, a phosphate phase, is shown in Figure 3.10c. This phase has been identified using other techniques in this work and by comparison to the published literature (e.g., Warren et al., 2004; Bridges et al., 2006). While there is no ICDD pattern for merrillite in the PDF-4 database used here for mineral identification, merrillite is the name for extraterrestrial occurrences of whitlockite and thus the whitlockite reference pattern is sufficient for the identification of merrillite in LA 002.

The diffraction pattern contribution of titanomagnetite, the primary oxide phase in the LA 002 meteorite (e.g., Herd, 2008), is presented in Figure 3.10d. This ICDD card is an excellent match to the observed diffraction pattern due to the acquisition of almost all titanomagnetite peaks in the experimental pattern.

The diffraction contribution of pyrrhotite, the primary sulfide phase present in the LA 002 meteorite (e.g., Lorand et al., 2005), is presented in Figure 3.10e. The geometry of the sample during analysis, contributions from surrounding phases that overprint the minor pyrrhotite peaks, and wide variations in pyrrhotite chemistry make this pattern unable to be unambiguously matched. However, the ICDD card shown is sufficient to allow for the identification of pyrrhotite in this pattern due to the fit of the experimental pattern.

The mineral assemblage of Los Angeles 002 observed here by micro X-ray diffraction confirms the previously reported assemblage by Papike et al. (2009), Warren et al. (2004), and Xirouchakis et al. (2002). The presence of ilmenite as one component of the iron-oxide phase of this meteorite has also been reported (Warren et al., 2004), although it was not found here. Micro X-Ray diffraction analyses have not been previously reported for this meteorite. These results confirm mineral identification by chemical analyses.

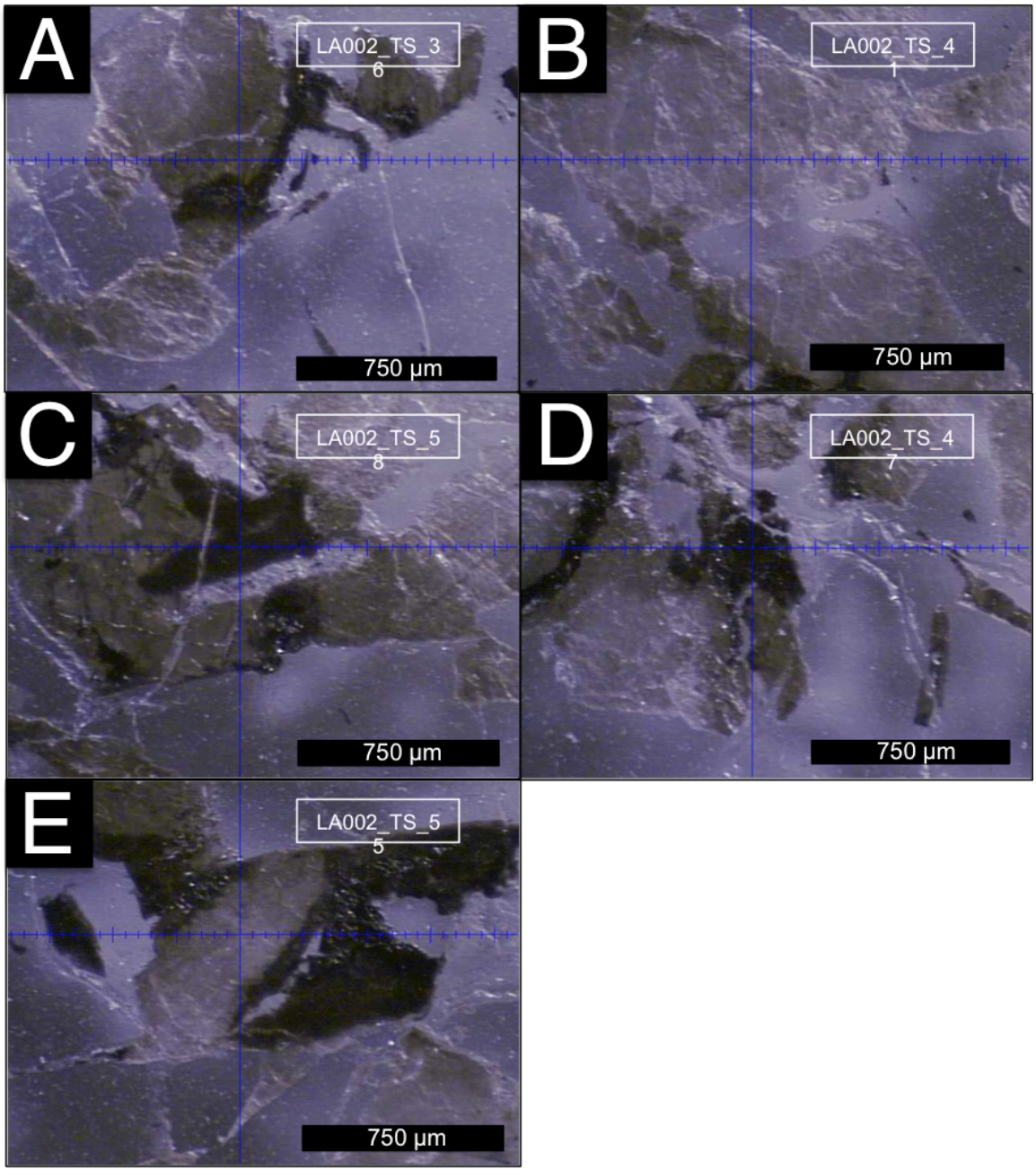

Figure 3.9: Context images of Los Angeles 002 XRD analysis sites in thin section. Crosshairs show the centre of the X-Ray beam, which is nominally 300 µm. Small ticks on crosshairs represent 50 µm.

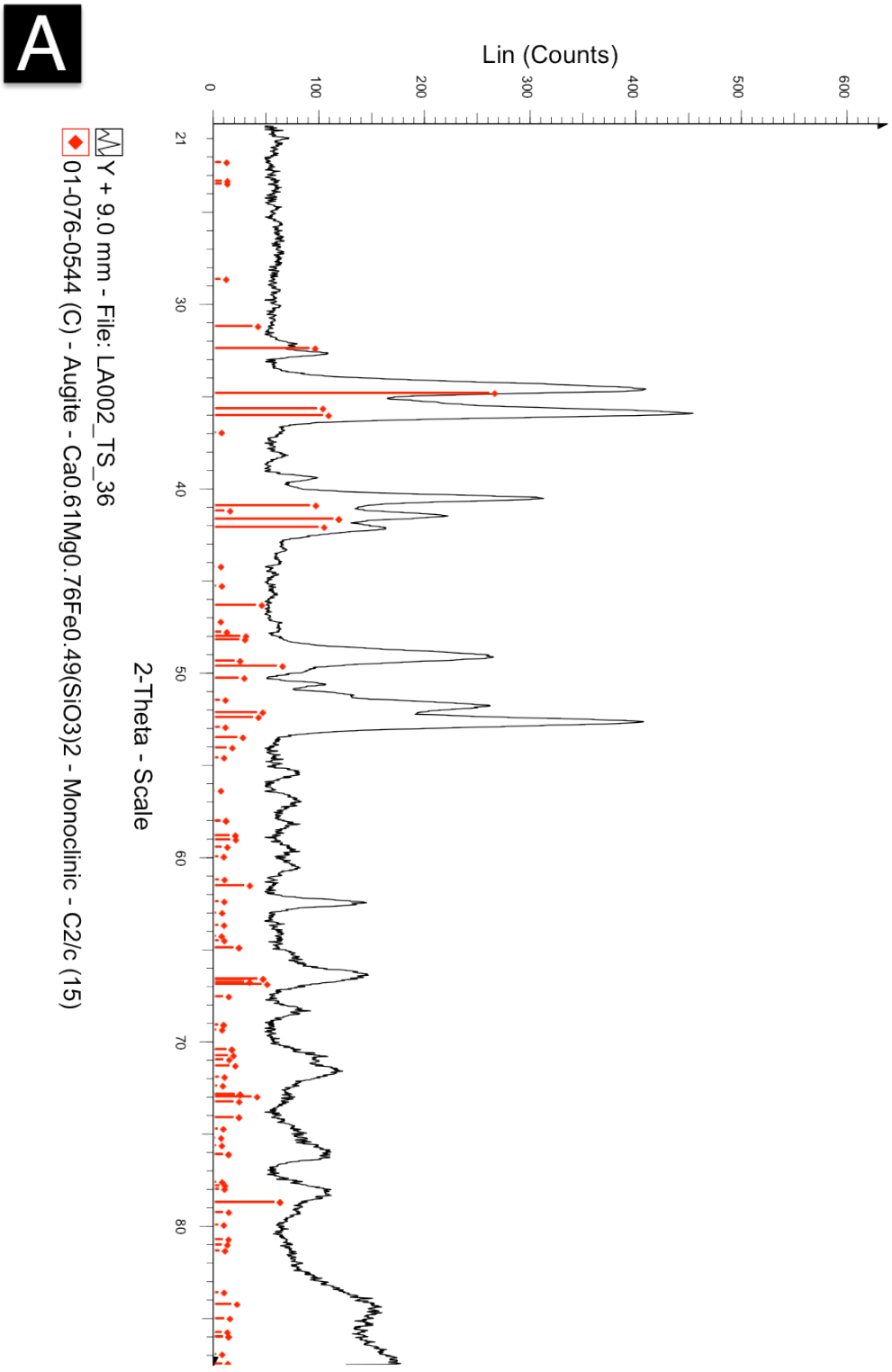

Figure 3.10: XRD patterns acquired at Los Angeles 002 sites A-E. Detected counts are plotted versus progressive 2-theta value. Detected counts are plotted versus 2-theta value. Plot has been background subtracted. ICDD reference pattern sticks corresponding to matching mineral phase have been plotted alongside measured pattern.

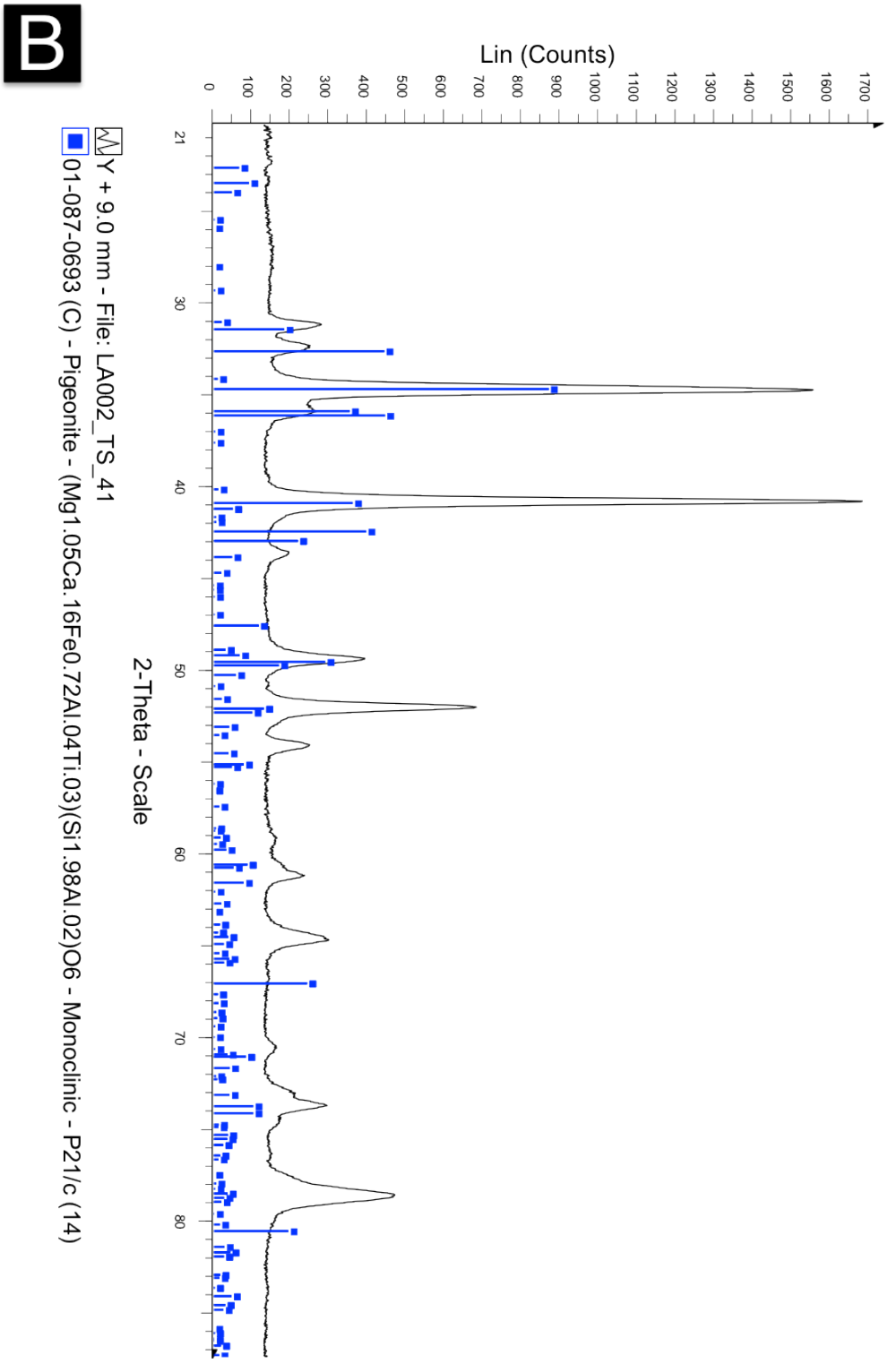
B
Lin (Counts)
0
100
200
300
400
500
600
700
800
900
1000
1100
1200
1300
1400
1500
1600
1700
21
30
40
50
60
70
80
2-Theta - Scale
Y + 9.0 mm - File: LA002_TS_41
01-087-0693 (C) - Pigeonite - (Mg1.05Ca.16Fe0.72Al.04Ti.03)(Si1.98Al.02)O6 - Monoclinic - P21/c (14)

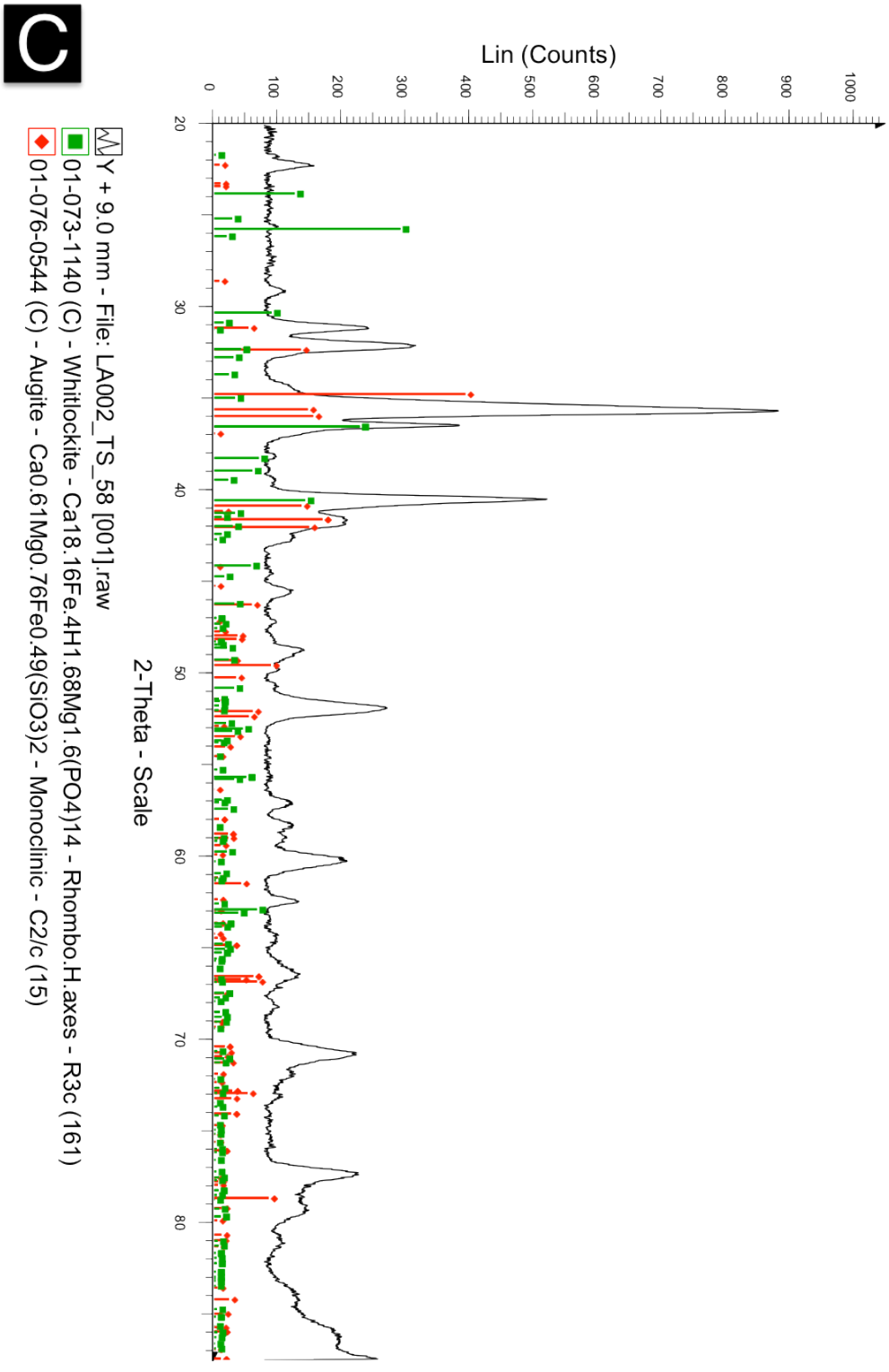
C
Lin (Counts)
0
100
200
300
400
500
600
700
800
900
1000
20
30
40
50
60
70
80
2-Theta - Scale
Y + 9.0 mm - File: LA002_TS_58 [001].raw
01-073-1140 (C) - Whitlockite - Ca18.16Fe.4H1.68Mg1.6(PO4)14 - Rhombo.H.axes - R3c (161)
01-076-0544 (C) - Augite - Ca0.61Mg0.76Fe0.49(SiO3)2 - Monoclinic - C2/c (15)

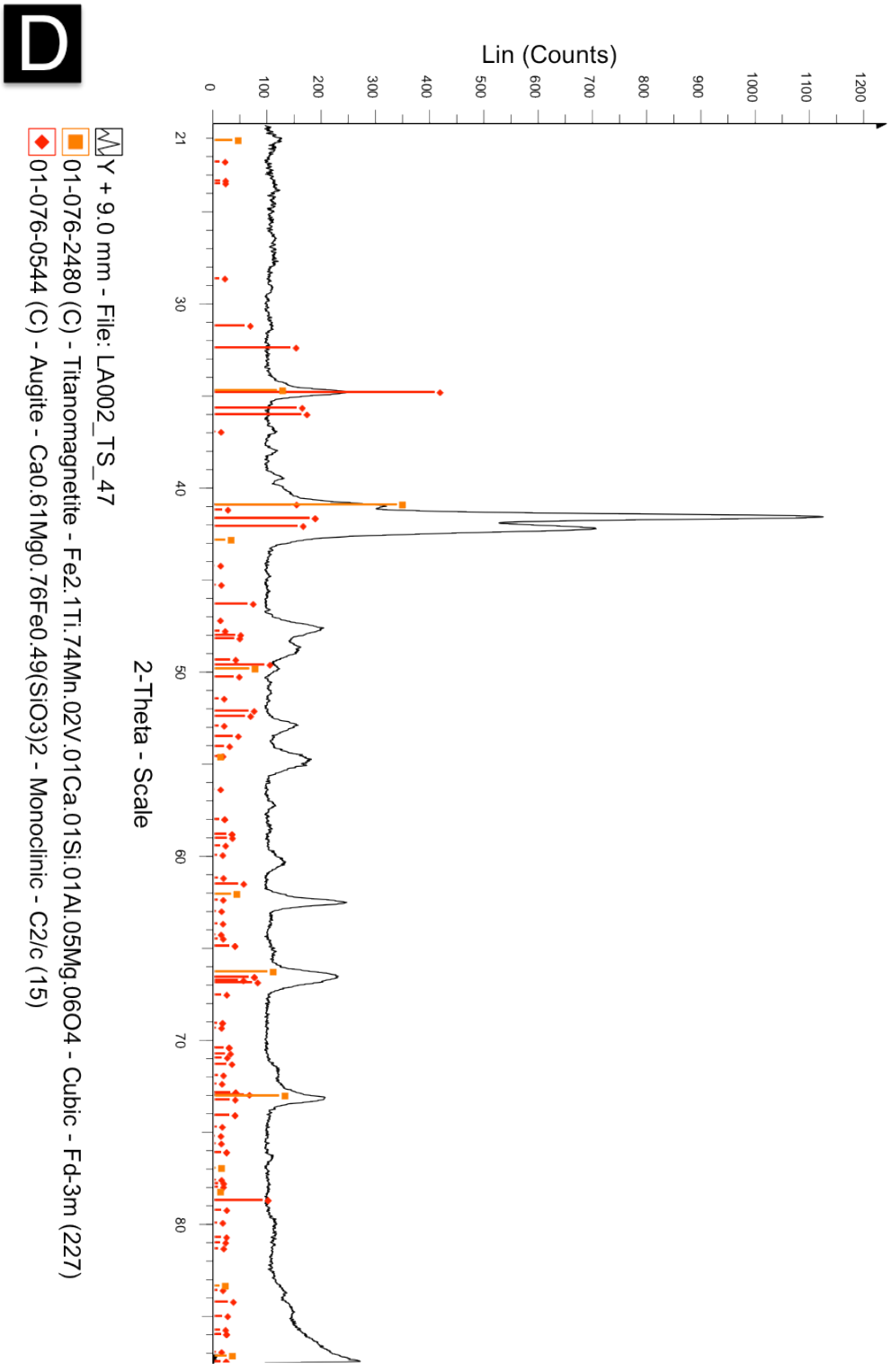
D
Lin (Counts)
0
100
200
300
400
500
600
700
800
900
1000
1100
1200
21
30
40
50
60
70
80
2-Theta - Scale
Y + 9.0 mm - File: LA002_TS_47
01-076-2480 (C) - Titanomagnetite - Fe2.1Ti.74Mn.02V.01Ca.01Si.01Al.05Mg.06O4 - Cubic - Fd-3m (227)
01-076-0544 (C) - Augite - Ca0.61Mg0.76Fe0.49(SiO3)2 - Monoclinic - C2/c (15)

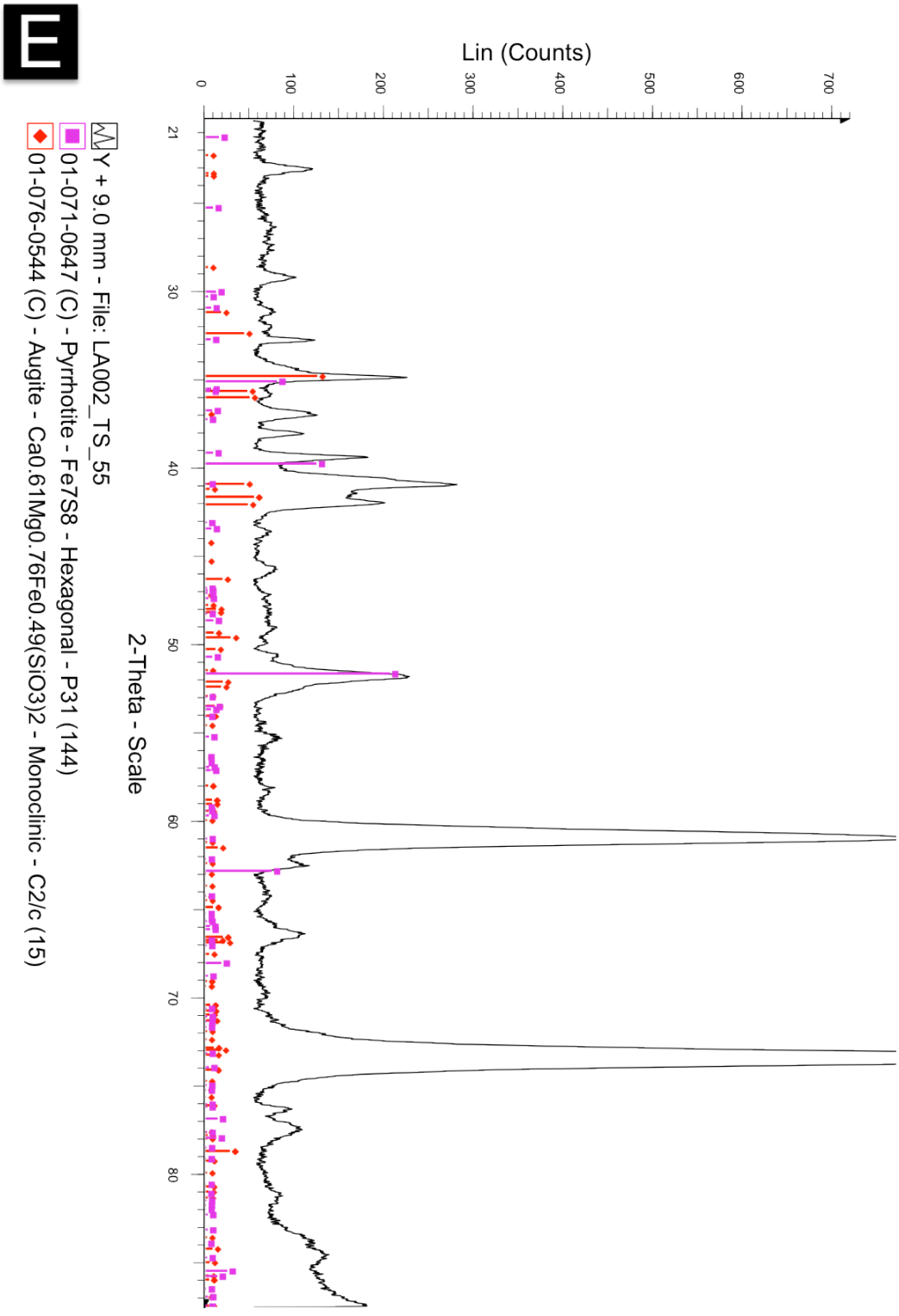
Lin (Counts)
0
100
200
300
400
500
600
700
21
30
40
50
60
70
80
2-Theta - Scale
Y + 9.0 mm - File: LA002_TS_55
01-071-0647 (C) - Pyrrhotite - Fe7S8 - Hexagonal - P31 (144)
01-076-0544 (C) - Augite - Ca0.61Mg0.76Fe0.49(SiO3)2 - Monoclinic - C2/c (15)

3.2.2 Zagami

Context images of several *in situ* micro XRD targets are shown in Figure 3.11a-d. The corresponding diffraction patterns obtained from these spots are shown in Figure 3.12a-d, with ICDD cards for the highlighted contributing phase overlain.

The contributing diffraction patterns of augite and pigeonite in Zagami are shown in Figure 3.12a. These two distinct pyroxenes are present in the Zagami meteorite in similar quantities, and their ICDD patterns are similar but unique enough that contributions from both can be identified. The small grain size in Zagami within the large beam size of the diffractometer (~300 μm) results in contributions from both pyroxenes being present in the XRD patterns. Both phases appear to contribute approximately equally to the observed pattern.

The diffraction contribution of the phosphate phase in the Zagami meteorite is shown in Figure 3.12b. Through other techniques in this work as well as comparison with the literature, this phosphate phase has been identified as merrillite (e.g., McCoy et al., 1992; Papike et al., 2009). While there is no ICDD pattern for merrillite in the PDF-4 database used here for mineral identification, merrillite is the name for extraterrestrial occurrences of whitlockite and so whitlockite reference pattern is sufficient for the identification of merrillite in Zagami.

The diffraction pattern contribution of titanomagnetite, the primary oxide phase in the Zagami meteorite, is presented in Figure 3.12c. The diffraction contribution of pyrrhotite

is shown in Figure 3.12d; this is the primary sulfide phase present in the Zagami meteorite, as identified from the ICDD database. *In situ,* context sensitive micro X-Ray diffraction analyses have not been previously reported for this meteorite. The mineral assemblage of Zagami observed here by micro X-ray diffraction confirms the previously reported assemblage by Papike et al. (2009), McCoy et al. (1992), and McCoy et al. (1999) from chemical analyses and powder X-Ray diffraction.

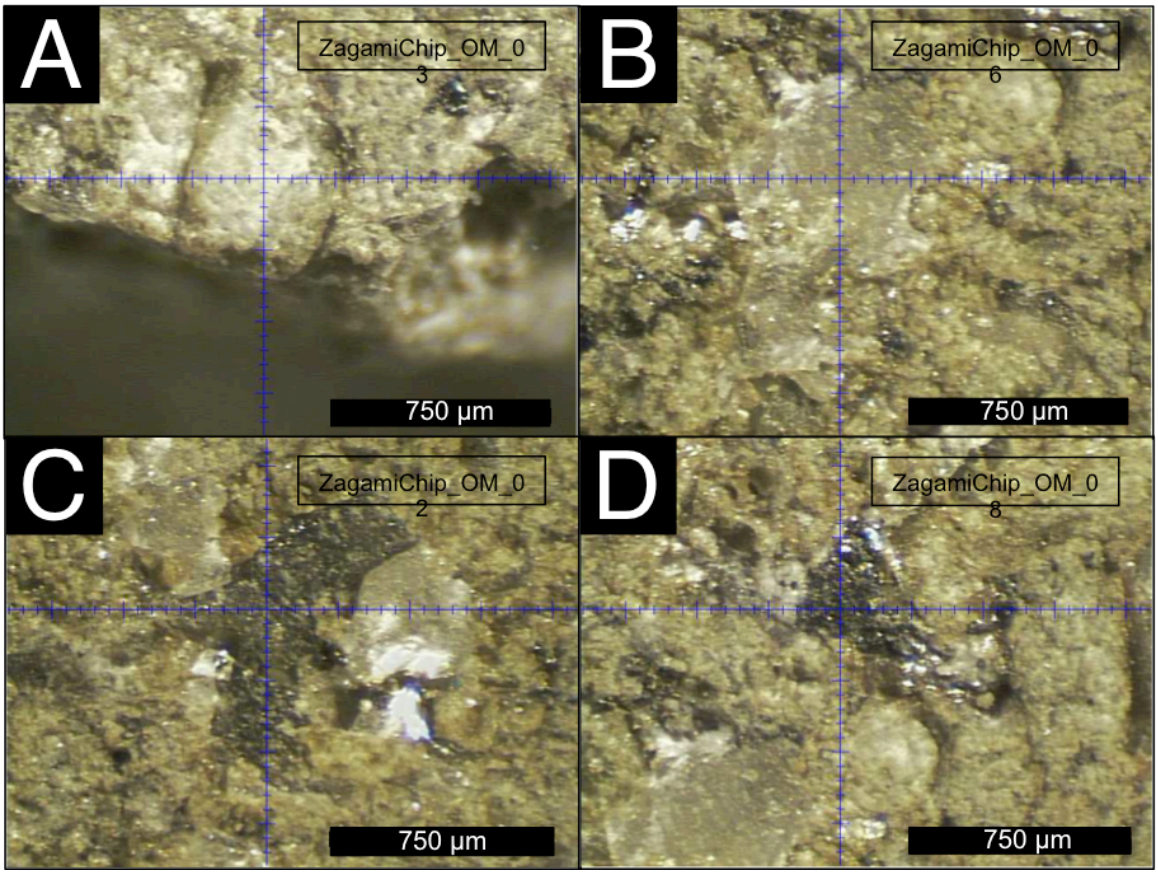

Figure 3.11: Context images of Zagami XRD analysis sites in thin section. Crosshairs show the centre of the X-Ray beam, which is nominally 300 µm. Small ticks on crosshairs represent 50 µm.

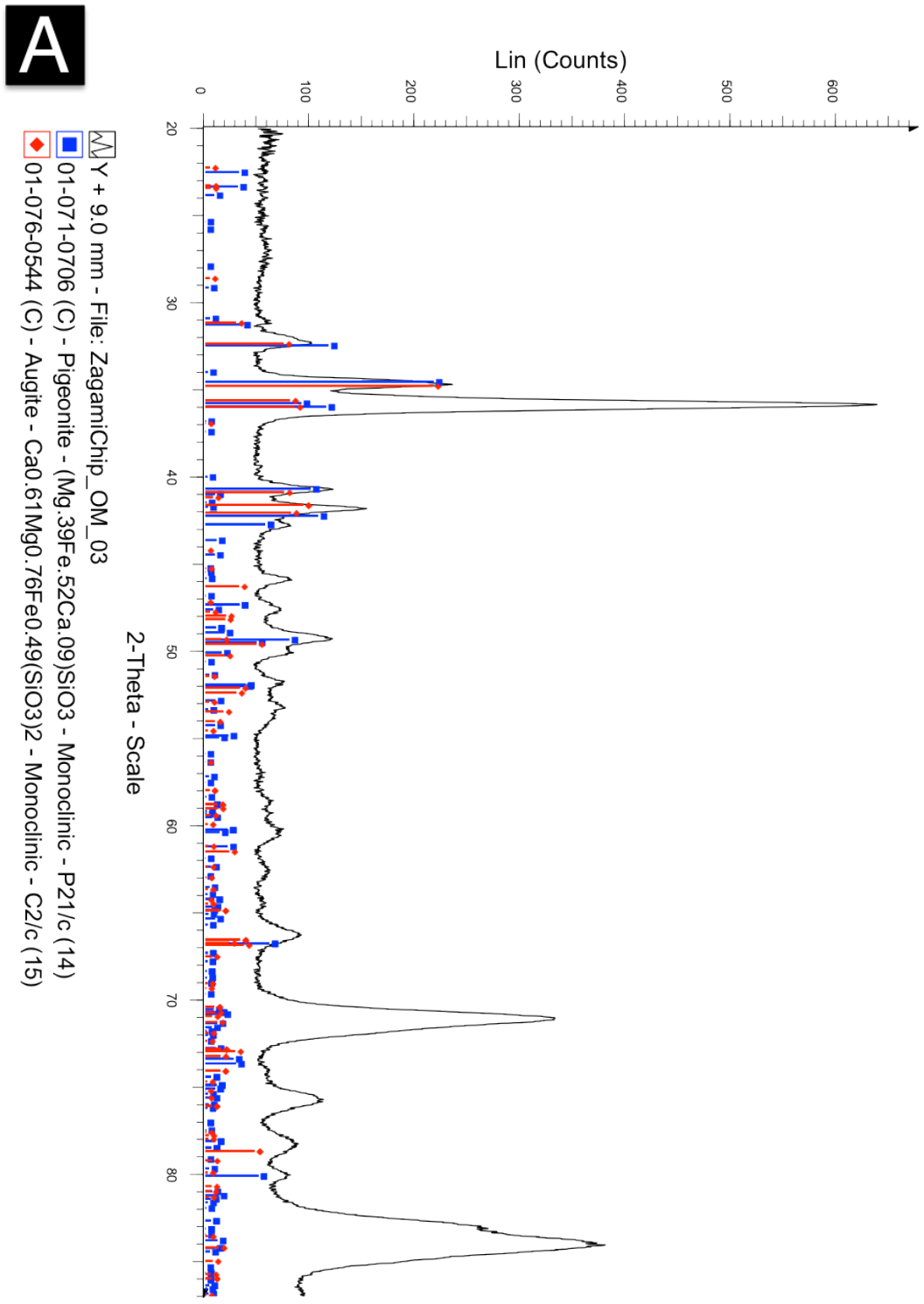

Figure 3.12: XRD patterns acquired at Zagami sites A-D. Detected counts are plotted versus 2-theta value. Plot has been background subtracted. ICDD reference pattern sticks corresponding to matching mineral phase have been plotted alongside measured pattern.

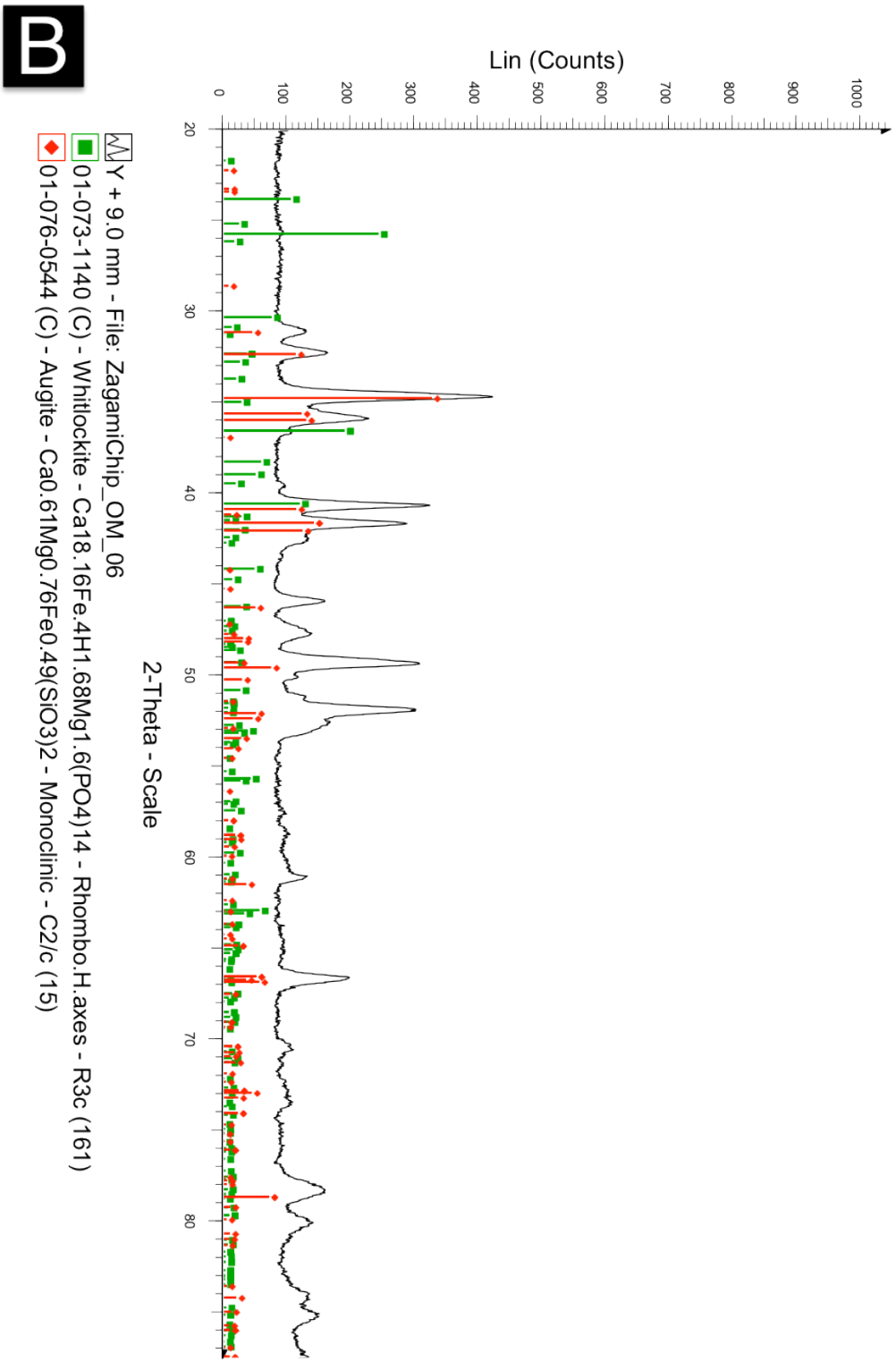
B
Lin (Counts)
0
100
200
300
400
500
600
700
800
900
1000
20
30
40
50
60
70
80
2-Theta - Scale
Y + 9.0 mm - File: ZagamiChip_OM_06
01-073-1140 (C) - Whitlockite - Ca18.16Fe.4H1.68Mg1.6(PO4)14 - Rhombo.H.axes - R3c (161)
01-076-0544 (C) - Augite - Ca0.61Mg0.76Fe0.49(SiO3)2 - Monoclinic - C2/c (15)

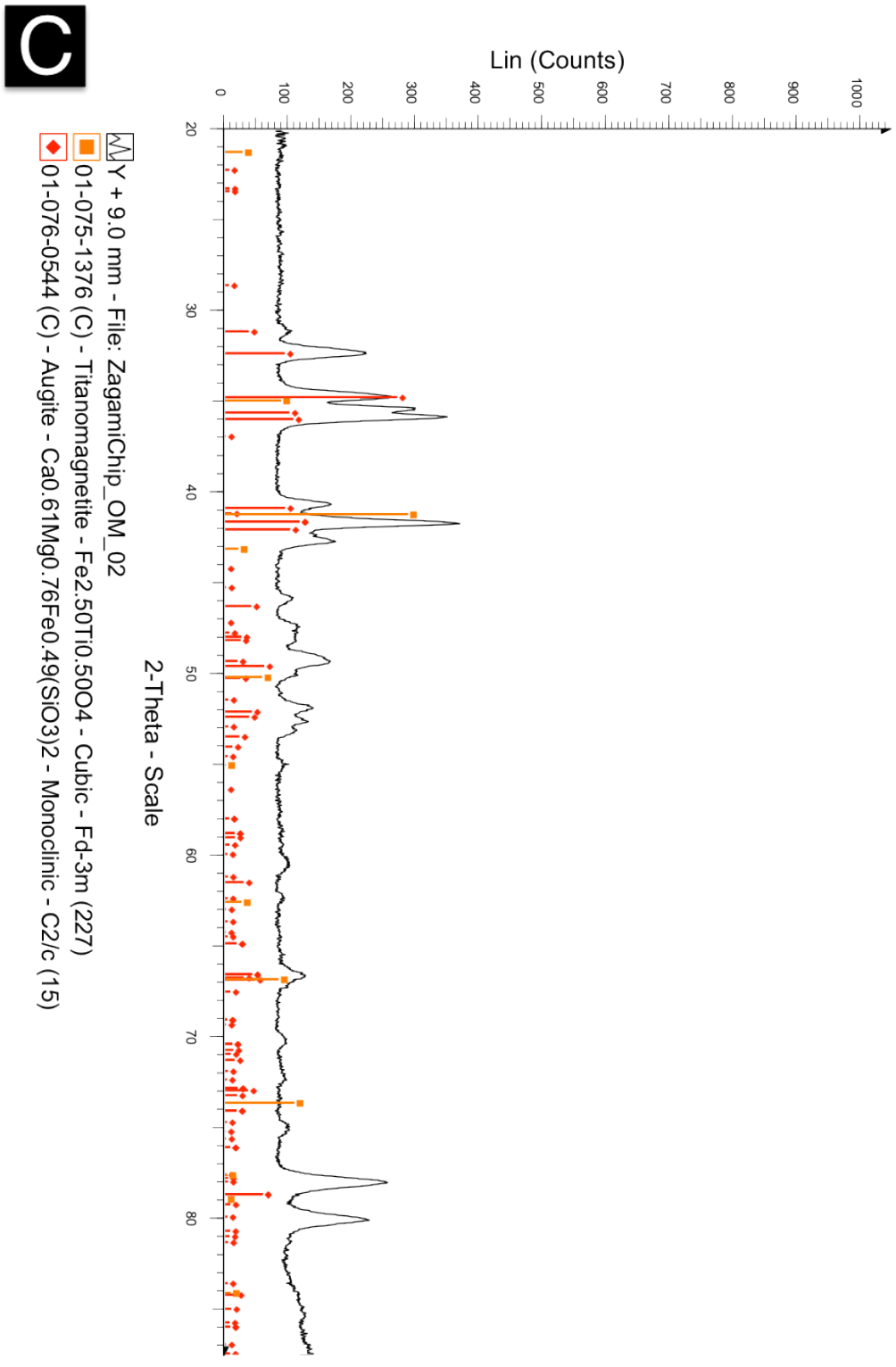
C
Lin (Counts)
0
100
200
300
400
500
600
700
800
900
1000
20
30
40
50
60
70
80
2-Theta - Scale
Y + 9.0 mm - File: ZagamiChip_OM_02
01-075-1376 (C) - Titanomagnetite - Fe2.50Ti0.50O4 - Cubic - Fd-3m (227)
01-076-0544 (C) - Augite - Ca0.61Mg0.76Fe0.49(SiO3)2 - Monoclinic - C2/c (15)

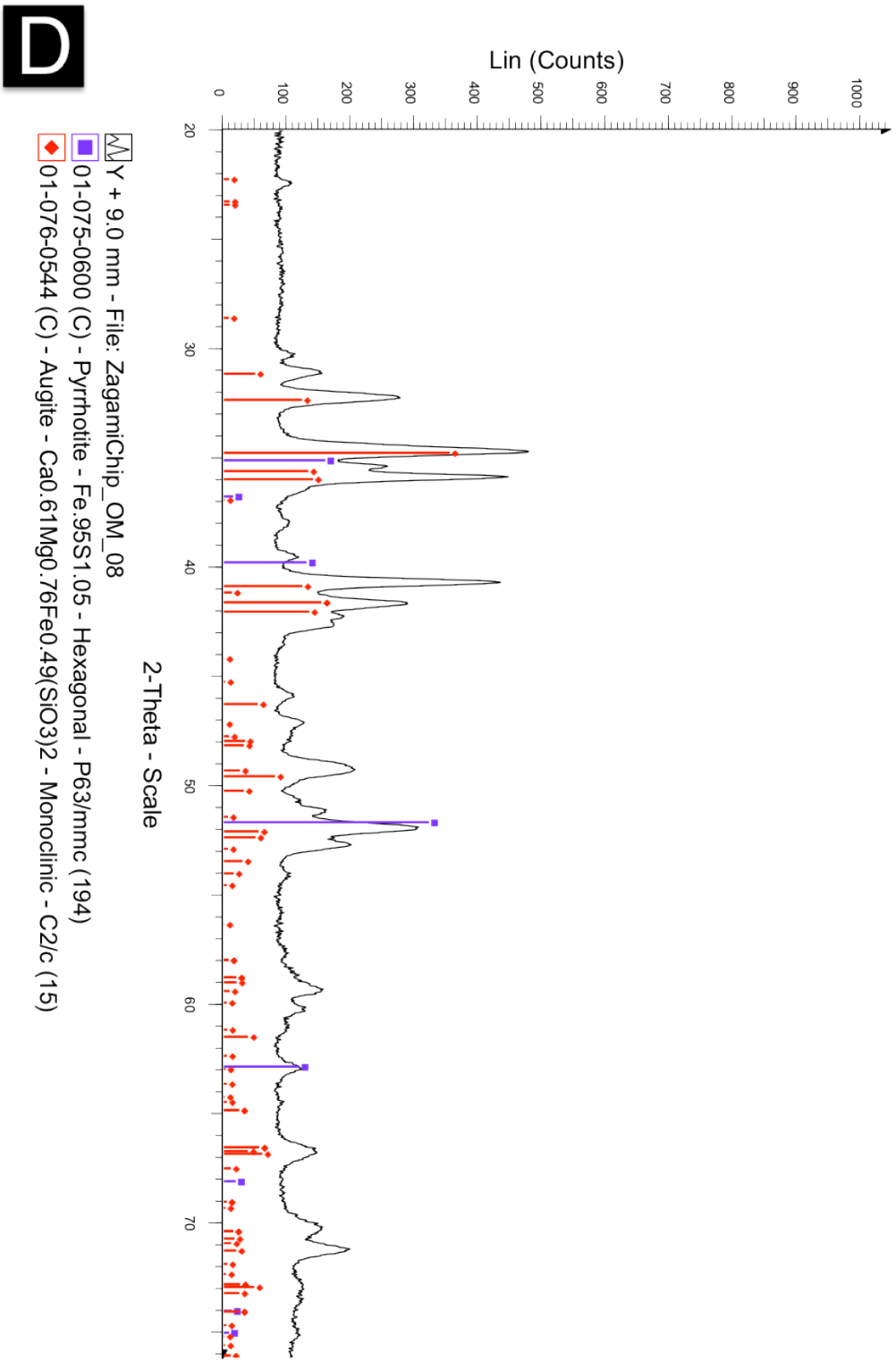
D
Lin (Counts)
0
100
200
300
400
500
600
700
800
900
1000
20
30
40
50
60
70
2-Theta - Scale
Y + 9.0 mm - File: ZagamiChip_OM_08
01-075-0600 (C) - Pyrrhotite - Fe.95S1.05 - Hexagonal - P63/mmc (194)
01-076-0544 (C) - Augite - Ca0.61Mg0.76Fe0.49(SiO3)2 - Monoclinic - C2/c (15)

3.2.3 Nakhla

Context images of several *in situ* micro XRD targets are shown in Figure 3.13a-d. The corresponding diffraction patterns obtained from these spots are shown in Figure 3.14a-d, with ICDD cards for all phases overlain.

The diffraction pattern of augite in Nakhla is shown in Figure 3.14a. This pyroxene phase makes up the majority of the crystalline component in Nakhla and is the dominant mineral in the meteorite. Figure 3.14b shows the diffraction contribution of representative olivine as identified in Nakhla. The large beam size and geometry of the thin section dictates that a significant contribution from surrounding pyroxenes is present in this pattern. However, the peak contributions from olivine can be easily discerned due to their high peak intensity.

The diffraction pattern of titanomagnetite in Nakhla is shown in Figure 3.14c. This is the primary oxide phase present in the meteorite. The diffraction pattern of plagioclase in a feldspathic region of mesostasis in Nakhla is presented in Figure 3.14d. This target was selected as an area of mesostasis in which distinct laths of plagioclase were clearly visible.

In situ, context sensitive micro X-Ray diffraction analyses have not been previously reported for this meteorite .The mineral assemblage of Nakhla observed here by micro X-ray diffraction confirms the previously reported assemblage by Papike et al. (2009),

Bridges et al. (2006), and Treiman (2005) by chemical analyses and powder X-Ray diffraction.

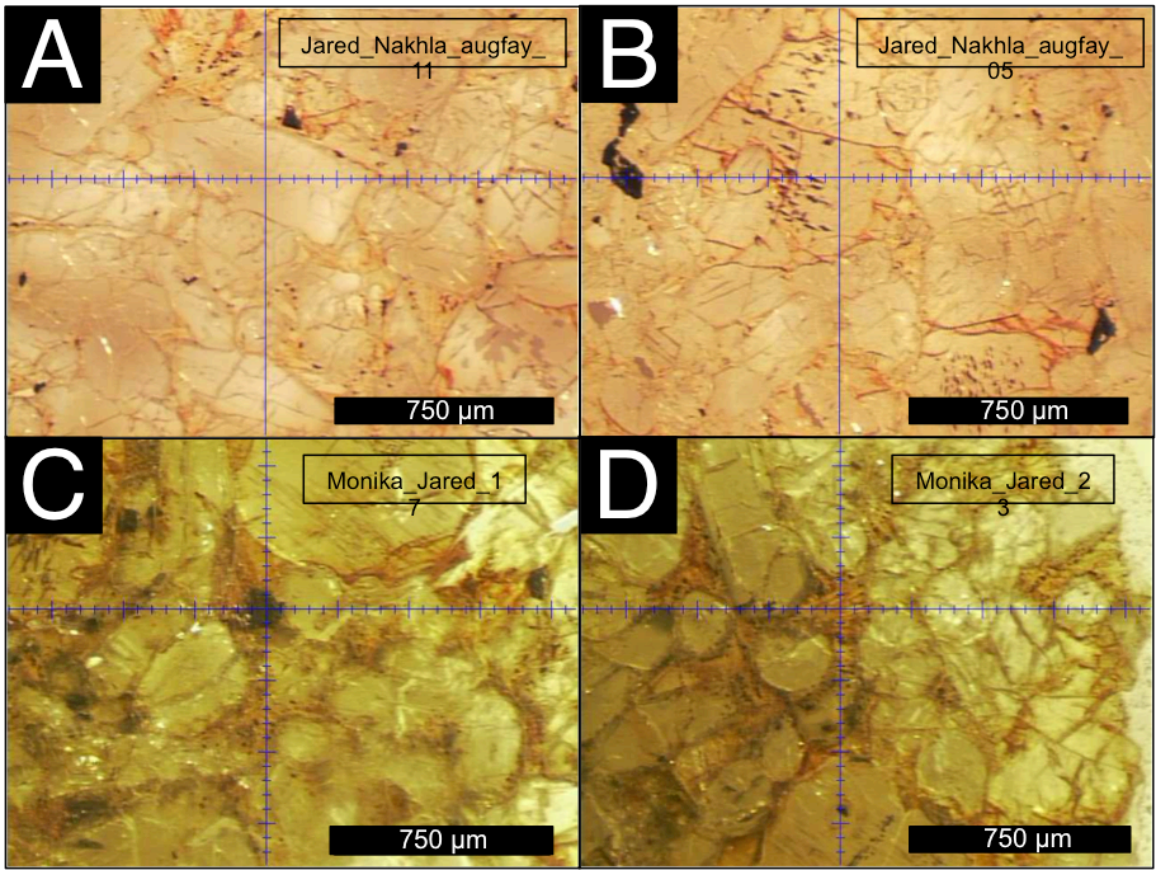

Figure 3.13: Context images of Nakhla XRD analysis sites in thin section. Crosshairs show the centre of the X-Ray beam, which is nominally 300 µm. Small ticks on crosshairs represent 50 µm.

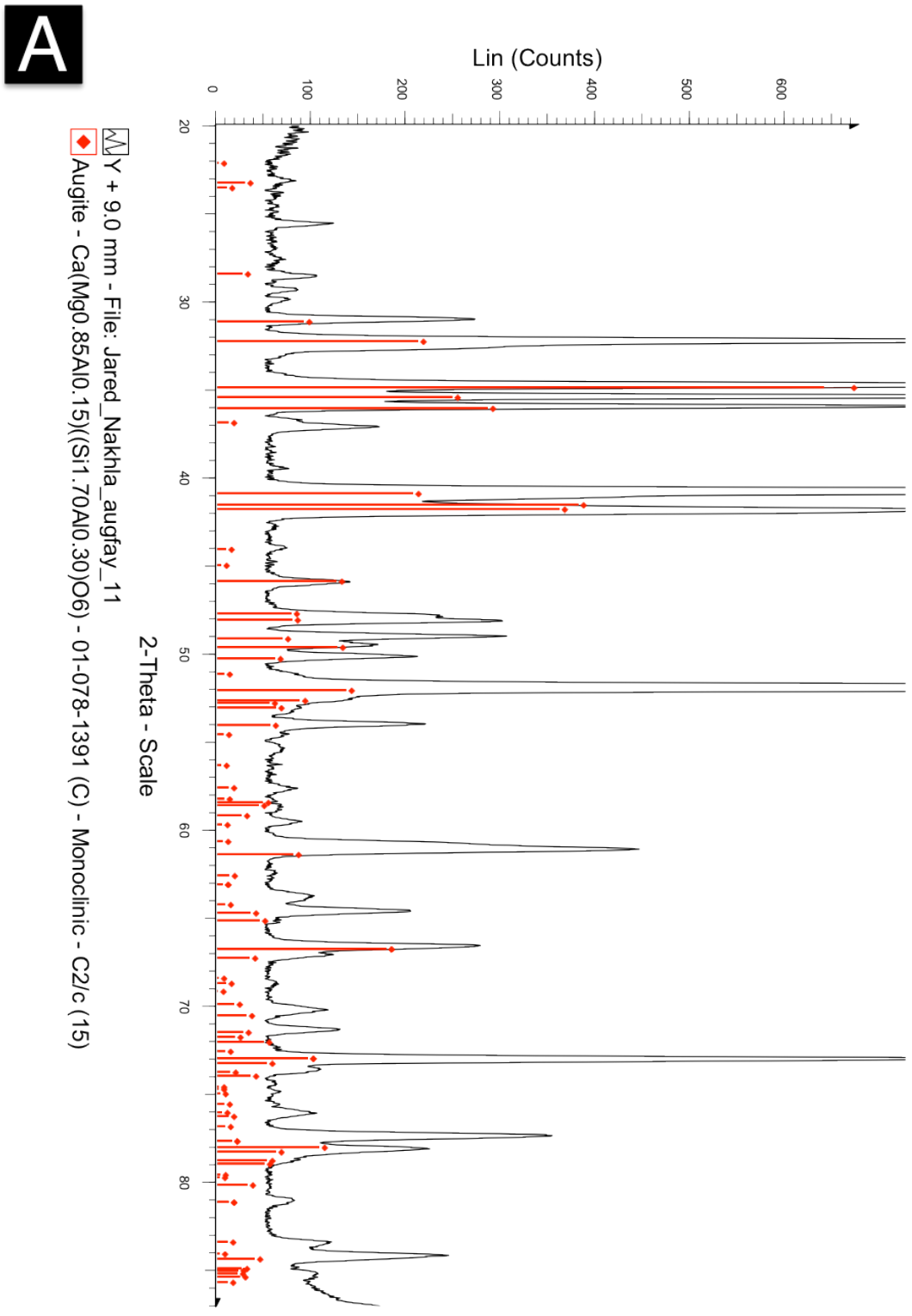

Figure 3.14: XRD patterns acquired at Nakhla sites A-D. Detected counts are plotted versus 2-theta value. Plot has been background subtracted. ICDD reference pattern sticks corresponding to matching mineral phase have been plotted alongside measured pattern.

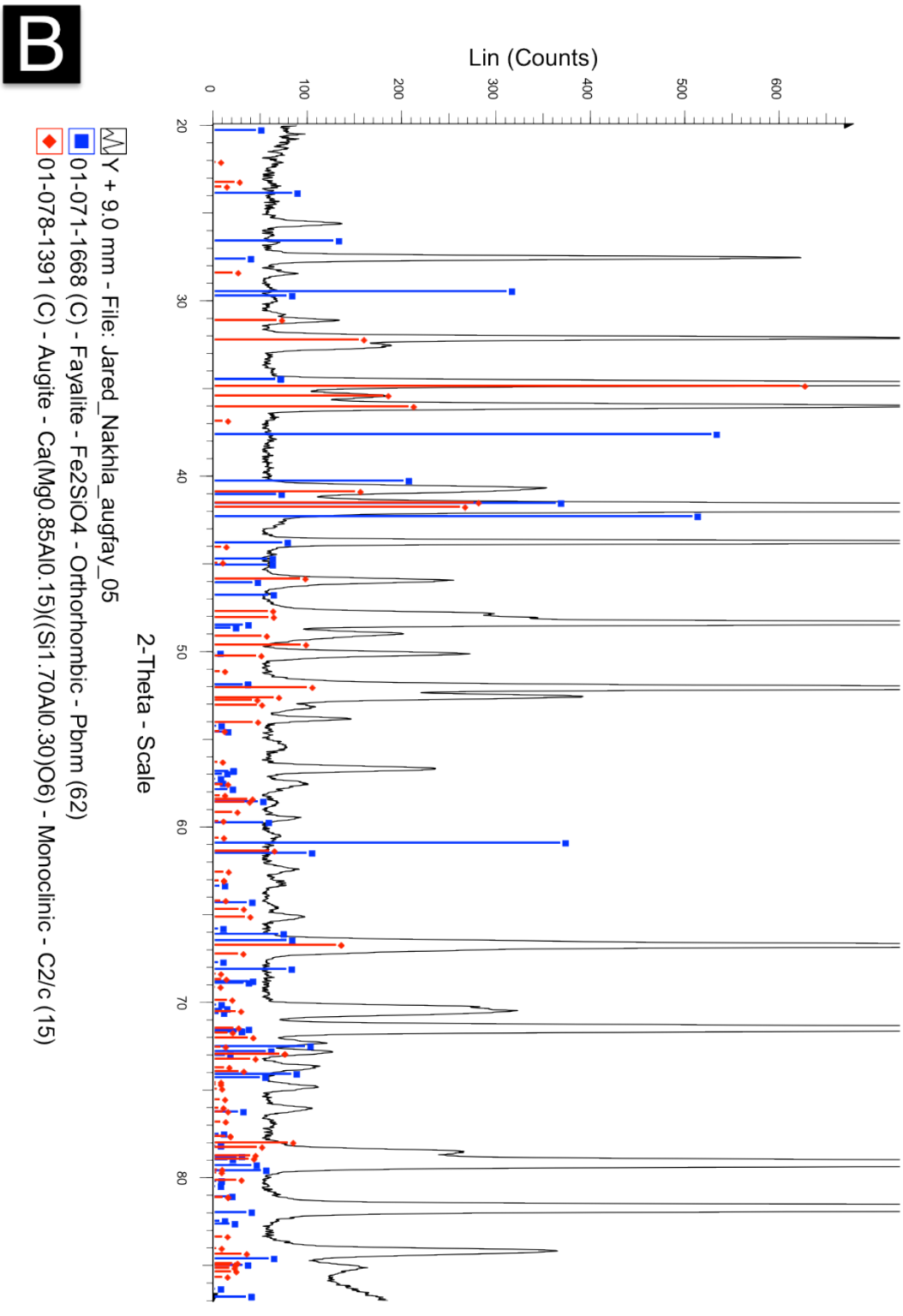
B
Lin (Counts)
0
100
200
300
400
500
600
20
30
40
50
60
70
80
2-Theta - Scale
Y + 9.0 mm - File: Jared_Nakhla_augfay_05
01-071-1668 (C) - Fayalite - Fe2SiO4 - Orthorhombic - Pbnm (62)
01-078-1391 (C) - Augite - Ca(Mg0.85Al0.15)((Si1.70Al0.30)O6) - Monoclinic - C2/c (15)

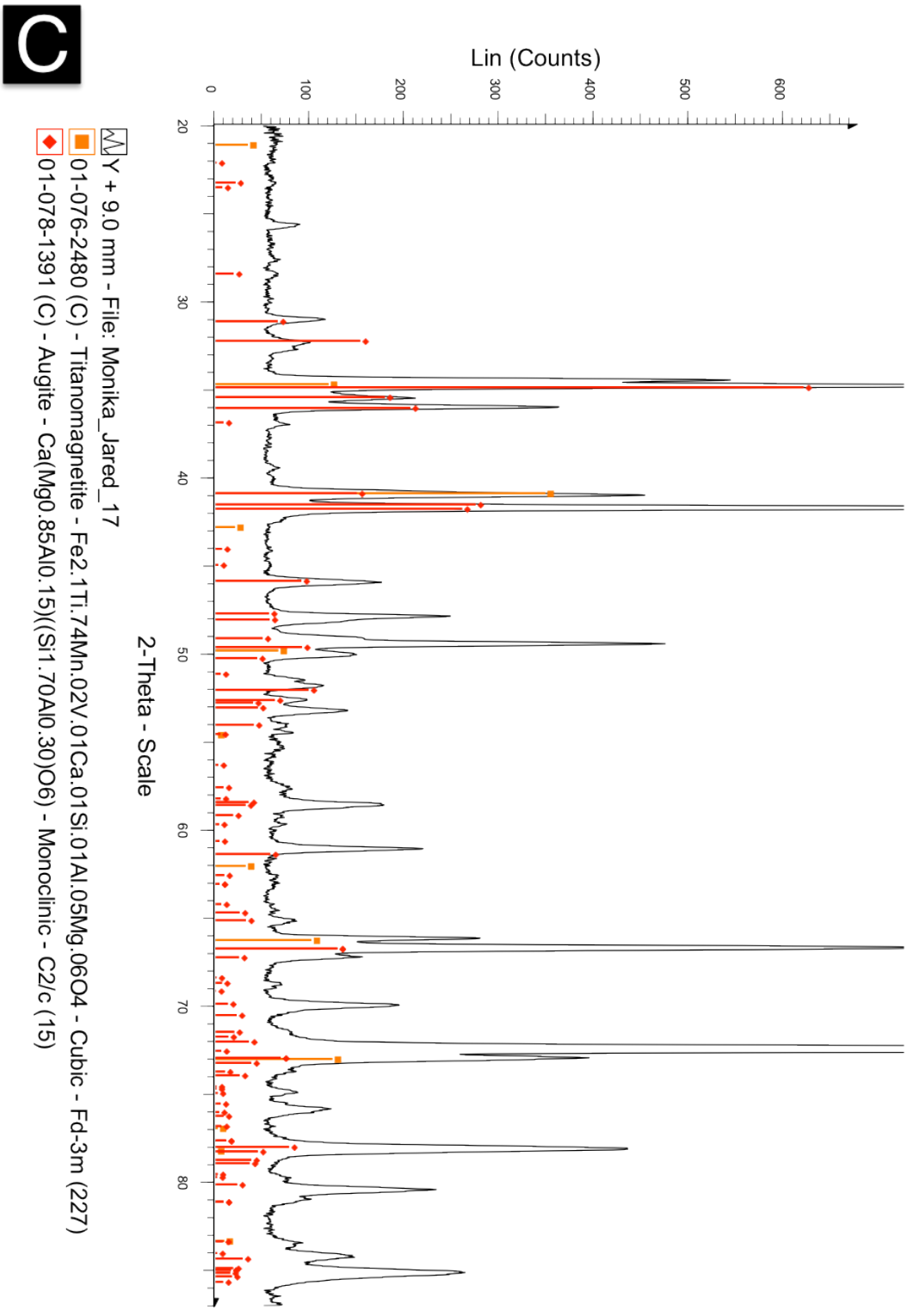
C
Lin (Counts)
0
100
200
300
400
500
600
20
30
40
50
60
70
80
2-Theta - Scale
Y + 9.0 mm - File: Monika_Jared_17
01-076-2480 (C) - Titanomagnetite - Fe2.1Ti.74Mn.02V.01Ca.01Si.01Al.05Mg.06O4 - Cubic - Fd-3m (227)
01-078-1391 (C) - Augite - Ca(Mg0.85Al0.15)((Si1.70Al0.30)O6) - Monoclinic - C2/c (15)

D

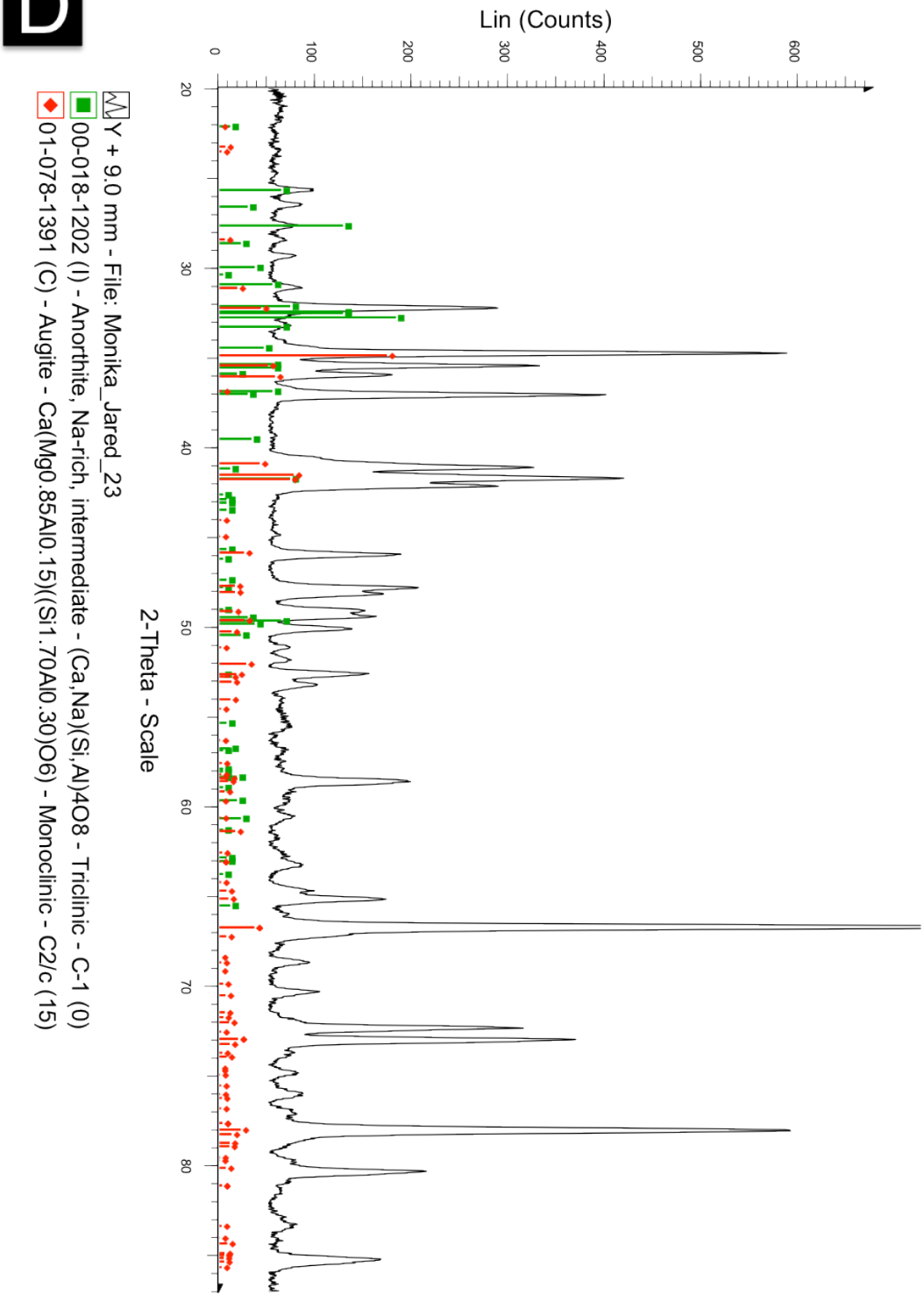
Lin (Counts)
0
100
200
300
400
500
600
20
30
40
50
60
70
80
2-Theta - Scale
Y + 9.0 mm - File: Monika_Jared_23
00-018-1202 (I) - Anorthite, Na-rich, intermediate - (Ca,Na)(Si,Al)4O8 - Triclinic - C-1 (0)
01-078-1391 (C) - Augite - Ca(Mg0.85Al0.15)((Si1.70Al0.30)O6) - Monoclinic - C2/c (15)

3.2.4 Nakhla Aqueous Vein Alteration

Context images of several alteration micro XRD targets and GADDS data collected at each site are shown in Figure 3.15a-c, while Figure 3.16 shows the corresponding X-Ray diffraction patterns with ICDD cards for identified mineral phases overlain.

GADDS data provide textural information about the phases analyzed by *in* situ micro X-Ray diffraction. Points on GADDS images represent crystal lattice diffractions, streaks represent strained mineral phases, and rings represent fine-grained or poorly crystalline material (e.g., Flemming, 2007). The micro X-Ray diffraction patterns collected at these sites comprise contributions from the surrounding minerals augite and olivine that have been slightly strained during impact (points and streaks on GADDS images) and the fine grained alteration phases (diffraction rings on GADDS images).

The mineral phases making up the vein alteration alteration assemblage observed here are highly different from assemblages previously reported for Nakhla by Gooding et al. (1991), Bridges et al. (2001), and Changela et al. (2011). Notably, we have identified smectites, serpentine group, and iron oxide minerals in the alteration material of Nakhla. The mineral assemblage of vein alteration material in Nakhla by micro X-Ray diffraction analysis has not been previously reported. The ability of micro X-Ray diffraction in this study to provide new *in situ* identification of the minerals present in the alteration material allows for a re-evaluation of the precise mineral assemblage and the conditions of alteration.

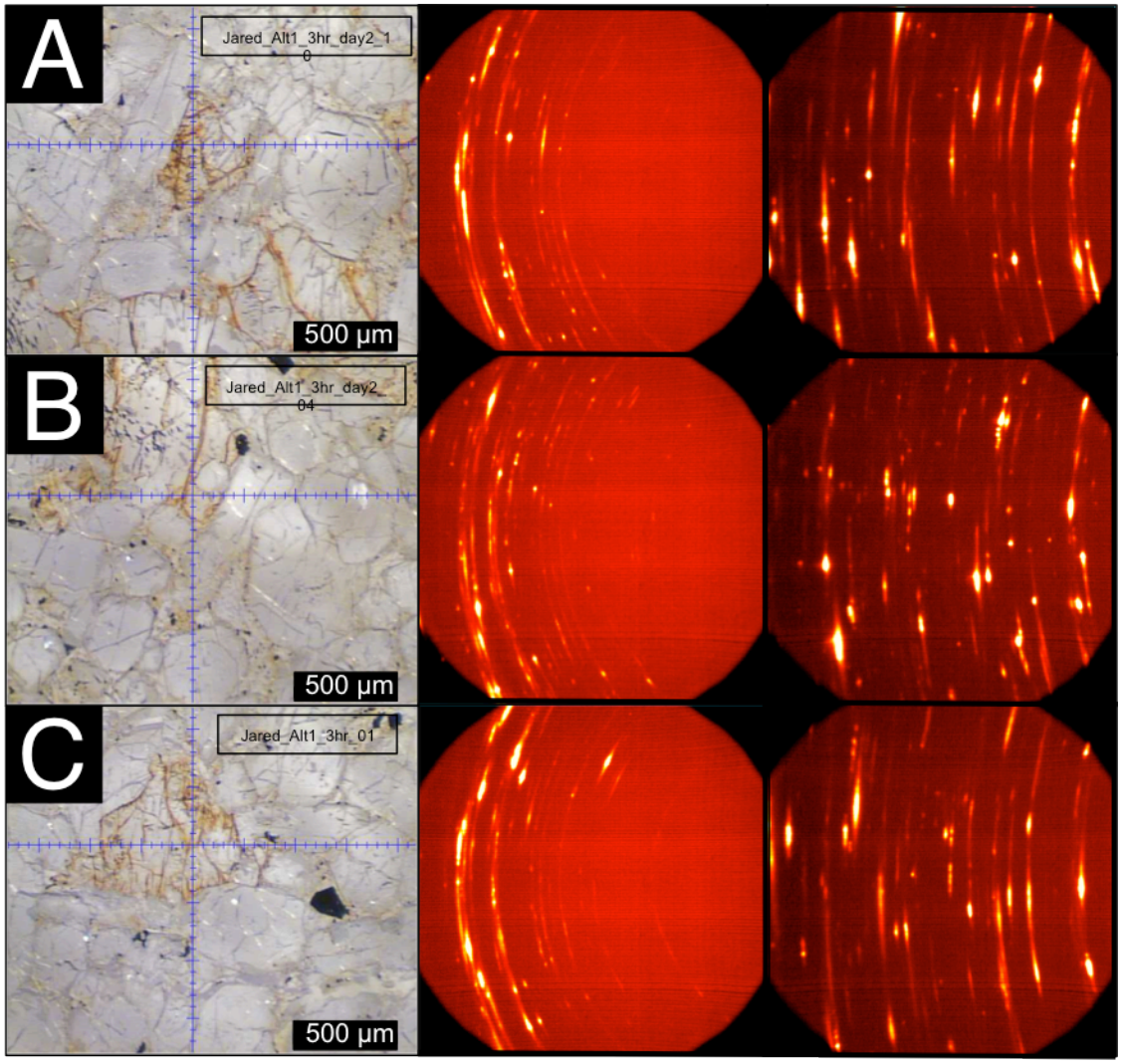

Figure 3.15: Context images of Nakhla aqueous vein alteration XRD analysis sites in USNM 426-6 polished section and GADDS data collected at each site. Targeted areas include extensively fractured region within olivine grains. Crosshairs show the centre of the X-Ray beam, which is nominally 300 µm. Small ticks on crosshairs represent 50 µm. Points on GADDS image represent crystal lattice diffractions, streaks represent strained mineral phases, and rings represent fine-grained or poorly crystalline material.

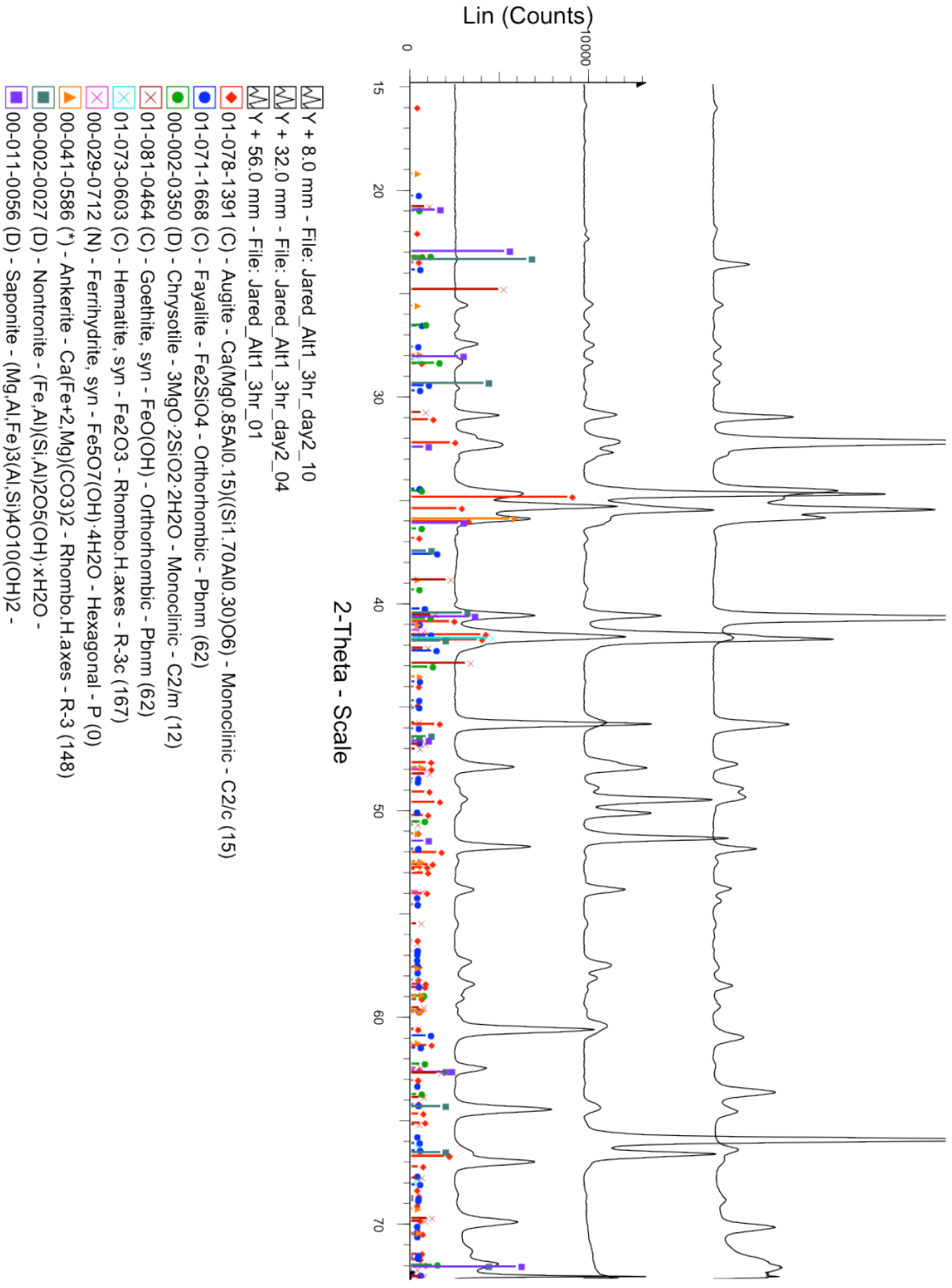

Figure 3.16: XRD patterns acquired at Nakhla Aqueous Vein Alteration sites A-C. Patterns have been stacked to show similarities in identified mineral assemblage across different sampling locations.

3.3 EPMA Geochemistry

3.3.1 Shergottites

Representative compositions of both major and minor phases in the Los Angeles 002 meteorite are shown below in Table 3.2. Representative compositions of both major and minor phases in the Zagami meteorite are shown below in Table 3.3.

Table 3.2: Representative compositions of major phases in the LA 002 meteorite (wt%).

Mineral Phase	Na_2O	MgO	Al_2O_3	SiO_2	CaO	TiO_2	MnO	FeO	NiO	Cr_2O_3	K_2O	P_2O_5	Total
Augite rim	0.23	6.92	0.79	48.61	10.78	0.61	0.85	32.53	BD	BD	BD	BD	101.34
Augite rim	0.12	1.95	0.72	47.07	11.18	0.52	0.81	38.67	BD	BD	BD	BD	101.09
Augite core	0.17	10.41	0.80	50.11	11.83	0.43	0.77	26.19	BD	BD	BD	BD	100.78
Augite core	0.17	10.54	1.08	50.52	14.47	0.43	0.66	23.01	BD	BD	BD	BD	100.94
Pigeonite rim	0.05	1.74	0.25	45.92	5.51	0.29	1.17	45.18	BD	BD	BD	BD	100.12
Pigeonite rim	BD	1.60	0.29	46.30	5.97	0.28	1.22	44.53	BD	BD	BD	BD	100.29
Pigeonite core	0.10	1.53	0.62	52.69	8.81	0.38	0.75	34.24	BD	BD	0.05	0.24	99.41
Pigeonite core	0.12	9.76	0.61	48.06	6.61	0.36	0.88	33.06	BD	BD	BD	BD	99.49
Maskelynite	4.86	0.08	28.08	54.51	10.97	BD	BD	0.56	BD	BD	0.18	BD	99.29
Maskelynite	4.57	0.05	26.72	58.14	8.96	0.05	BD	0.64	BD	BD	0.37	BD	99.55
Maskelynite	4.86	0.05	27.89	53.62	10.74	BD	BD	0.61	BD	BD	0.33	BD	98.18
Maskelynite	3.01	0.11	28.33	55.16	11.27	BD	BD	0.54	BD	BD	0.14	BD	98.64
Merrillite	1.21	0.99	0.05	0.07	46.23	BD	0.20	4.92	BD	BD	0.06	46.43	100.17
Merrillite	1.15	0.92	BD	0.07	46.26	BD	0.16	5.08	BD	BD	0.05	46.46	100.20
Merrillite	1.16	0.83	BD	0.09	46.34	BD	0.16	5.14	BD	BD	0.06	46.14	100.00
Titanomagnetite	0.08	0.15	1.66	0.08	BD	25.42	0.52	71.79	BD	BD	BD	BD	99.76
Titanomagnetite	0.09	0.12	1.52	0.07	BD	25.17	0.49	72.50	BD	BD	BD	BD	100.03
Ilmenite	0.08	0.26	0.11	BD	BD	52.38	0.58	48.22	BD	BD	BD	BD	101.66
Mesostasis	2.30	BD	12.92	74.47	1.28	0.46	BD	1.27	BD	BD	4.90	0.08	97.65
Mesostasis	1.40	BD	12.12	75.28	0.93	0.24	BD	0.44	BD	BD	6.29	0.49	97.19
Mesostasis	1.85	BD	12.75	76.38	1.02	0.15	BD	1.46	BD	BD	4.49	0.05	98.25
Olivine	BD	1.61	0.05	29.80	0.30	0.49	1.32	66.58	BD	BD	BD	BD	100.25
Olivine	BD	1.53	BD	29.49	0.43	0.07	1.33	67.16	BD	BD	BD	0.19	100.31
Olivine	BD	1.57	BD	29.49	0.31	0.25	1.34	67.06	BD	BD	BD	BD	100.12

*Associated error = 0.02, detection limit = 0.05 wt%, BD = below detection limit.

Table 3.3: Representative compositions of major phases in the Zagami meteorite (wt%).

Mineral Phase	K_2O	Na_2O	CaO	SiO_2	FeO	TiO_2	MgO	P_2O_5	Al_2O_3	MnO	Cr_2O_3	Total
Augite rim	BD	0.28	9.75	50.24	26.83	0.44	12.01	BD	0.78	0.69	0.27	101.32
Augite rim	BD	0.37	10.95	49.07	27.98	0.63	10.05	BD	0.72	0.71	BD	100.55
Augite core	BD	0.31	15.98	50.29	20.73	0.60	10.99	BD	1.09	0.55	0.32	100.89
Augite core	BD	0.31	16.12	50.44	13.84	0.21	15.23	BD	0.96	0.48	0.68	98.28
Pigeonite rim	BD	0.27	6.25	49.06	31.94	0.53	11.08	BD	0.59	0.81	0.08	100.63
Pigeonite rim	0.07	0.34	6.18	48.33	33.10	1.41	9.14	BD	0.60	0.82	0.11	100.14
Pigeonite core	BD	0.19	4.69	52.45	20.08	0.14	21.63	BD	0.63	0.66	0.37	100.88
Pigeonite core	BD	0.21	6.47	51.97	18.78	0.14	20.61	BD	0.80	0.65	0.50	100.13
Maskelynite	0.30	4.70	11.15	55.68	0.75	0.10	0.09	BD	28.42	BD	BD	101.28
Maskelynite	0.65	5.12	9.14	57.12	0.72	0.07	0.07	BD	26.41	BD	BD	99.35
Maskelynite	0.29	5.04	10.55	55.96	0.93	BD	0.10	BD	27.64	BD	BD	100.61
Maskelynite	0.73	5.28	8.67	57.89	0.73	0.09	BD	0.05	26.25	BD	BD	99.73
Merrillite	0.09	1.63	46.71	0.12	3.22	BD	2.14	44.50	BD	0.13	BD	98.60
Merrillite	0.11	1.68	46.87	0.11	2.53	0.06	2.62	45.12	BD	0.11	BD	99.28
Merrillite	0.11	1.44	47.31	0.12	2.88	0.10	2.71	44.72	BD	0.15	0.07	99.63
Titanomagnetite	BD	0.06	BD	0.16	73.04	22.91	0.40	BD	1.89	0.62	0.58	99.66
Titanomagnetite	BD	0.26	BD	0.14	72.12	22.98	0.59	BD	1.84	0.48	1.15	99.59
Ilmenite	BD	0.13	BD	BD	47.99	50.86	0.73	BD	0.09	0.70	0.05	100.62
Mesostasis	BD	0.57	0.14	98.57	0.13	0.25	BD	BD	1.44	BD	BD	101.12
Mesostasis	0.44	2.36	3.16	80.51	0.43	0.20	BD	BD	12.97	BD	BD	100.16
Mesostasis	6.34	1.51	0.99	77.96	0.49	0.33	BD	0.07	11.87	0.04	BD	99.64

*Associated error = 0.02, detection limit = 0.05 wt%, BD = below detection limit.

The Los Angles meteorite mineral chemistry data in Table 3.2 confirm the compositional ranges previously reported by Papike et al. (2009), Rubin et al. (2000), and Warren et al. (2004). The Zagami meteorite mineral chemistry data in Table 3.3 confirm the compositional ranges previously reported by Papike et al. (2009), Bridges et al. (2006), and McCoy et al. (1992).

A ternary diagram comparing the composition of pyroxenes in the Zagami and LA 002 meteorites is shown below in Figure 3.17. Data have been plotted as normalized mol % showing proportional Ca-Fe-Mg composition of each pyroxene analysis. Warren et al.

(2004) present a well-defined compositional field for pyroxene (both augite and pigeonite) in Los Angeles 002, and the results reported here are in good agreement. McCoy et al. (1999) define a compositional range for pyroxenes (both augite and pigeonite) in Zagami, in broad agreement with the compositions reported here; several of the outlying iron-rich data points reported here likely correlate to pyroxenes described as a "dark mottled lithology" by those workers (the second phase of fractional crystallization during the formation of Zagami). Bridges et al. (2006) defined a compositional range for pyroxenes in both Los Angeles and Zagami, in agreement with the results presented here.

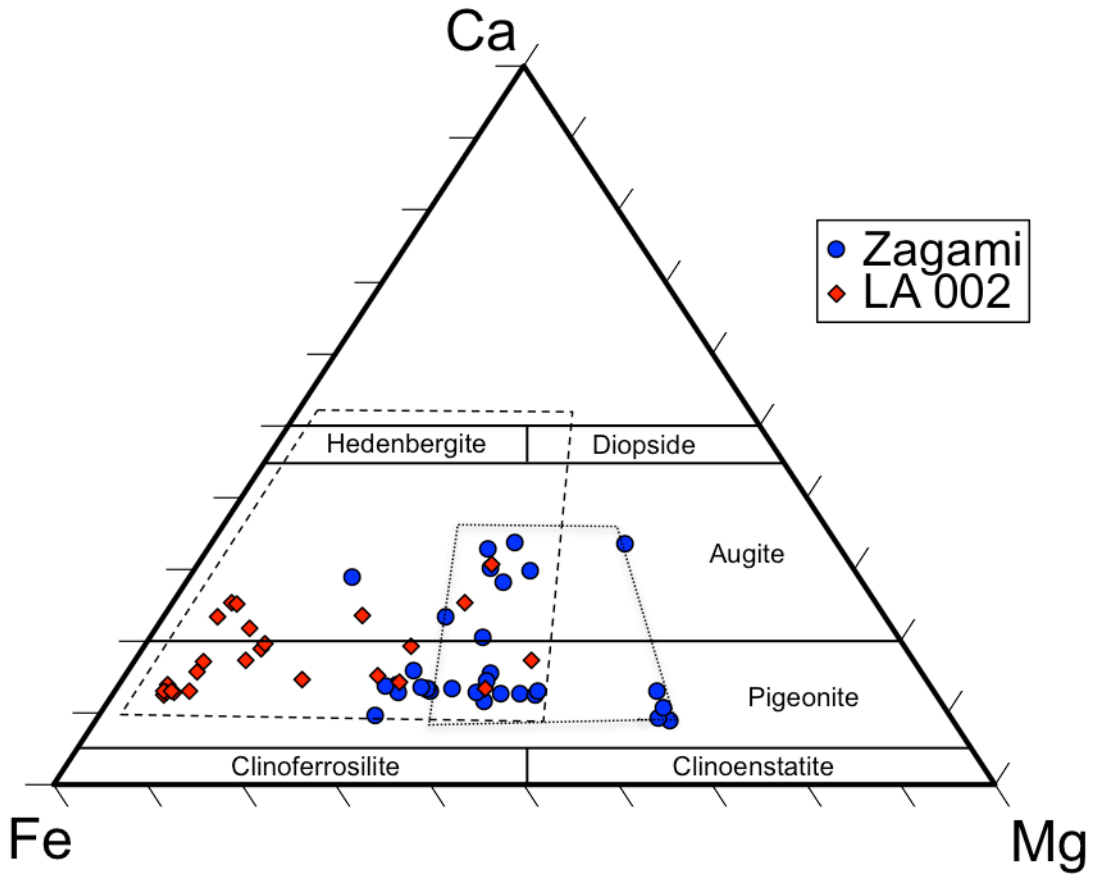

Figure 3.17: Ternary composition diagram comparing pyroxenes in LA 002 and Zagami. Ideal pyroxene domains have been shown for reference. Heavy dotted line for LA 002 is from Warren et al. (2004). Light dotted line for Zagami is from McCoy et al. (1999).

A ternary diagram comparing the compositions of maskelynite in the Zagami and LA 002 meteorites is shown in Figure 3.18. Data have been plotted in normalized mol % showing proportional Ca-K-Na composition of each maskelynite analysis. The compositional range for plagioclase-glass (maskelynite) in Los Angeles 002 defined by Warren et al. (2004) is in good agreement with many of the data points reported here. However, this study has measured a group of plagioclase compositions that are slightly more anorthitic in original composition than those reported by Warren et al. (2004).

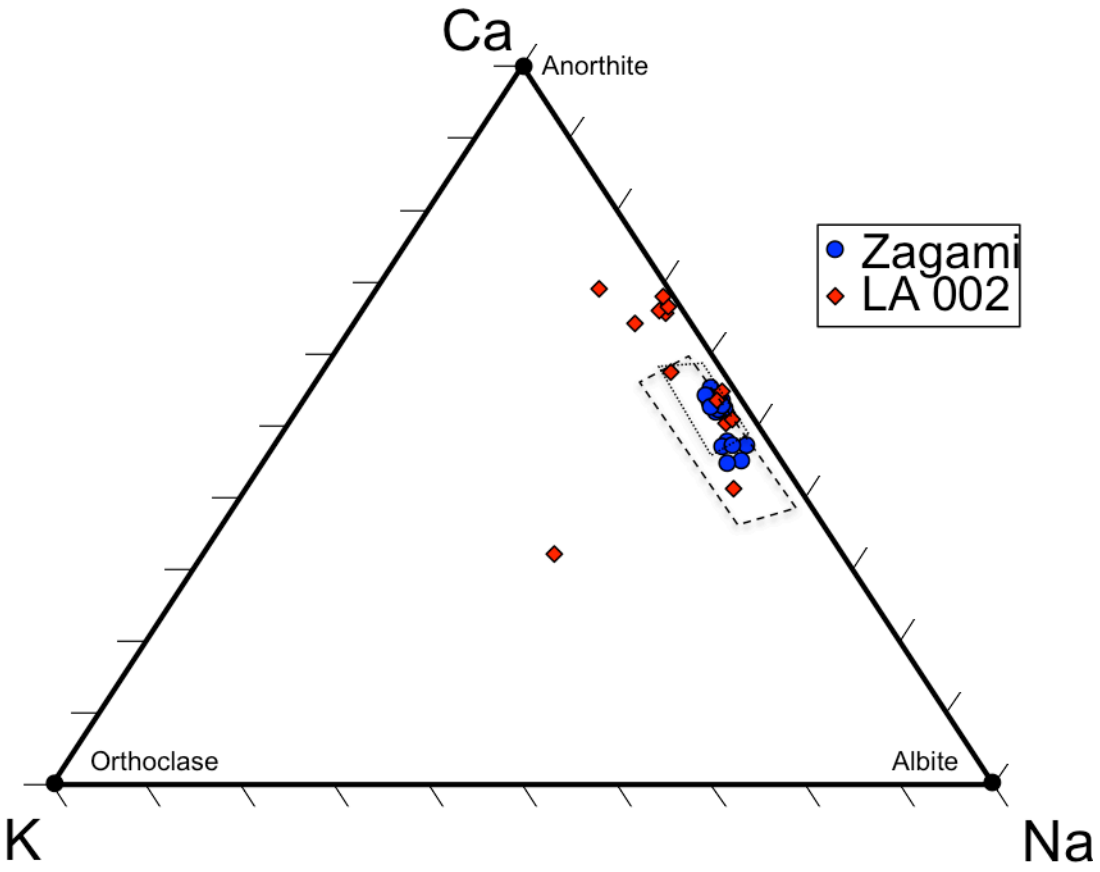

Figure 3.18: Ternary composition diagram comparing maskelynite in LA 002 and Zagami. Ideal feldspar compositions have been plotted for reference. Heavy dotted line for LA 002 is from Warren et al. (2004). Light dotted line for Zagami is from McCoy et al. (1999).

The maskelynite composition from Zagami reported by McCoy et al. (1999) is in broad agreement with the data presented here, although their composition was slightly more sodic.

A ternary diagram comparing the composition of titanomagnetite in the Zagami and LA 002 meteorites is shown in Figure 3.19. Data have been plotted in normalized mol % showing proportional Al-Fe-Ti composition of each titanomagnetite analysis. McCoy et al. (1999) present a representative composition for titanomagnetite from Zagami, consistent with the compositional range defined by the data reported here. Warren et al. (2004) present representative compositions for the iron-oxide phase in Los Angeles 002, in agreement with the data reported here (including the somewhat bimodal compositional space). Some oxides in LA 002 were identified as ilmenite by Warren et al. (2004), and several compositional points presented in Figure 3.19 may represent ilmenite.

The measured compositions of pyrrhotite grains in the Zagami meteorite are shown below in Table 3.4. Due to calibration limitations, data from non-oxygen bearing phases in LA 002 were unable to be collected. However, the composition of pyrrhotites in LA 002 are similar enough to those in Zagami to allow for similar conclusions to be drawn between the two meteorites. The pyrrhotite composition shown here confirms the composition reported by Lorand (2005) within 2% of their reported values.

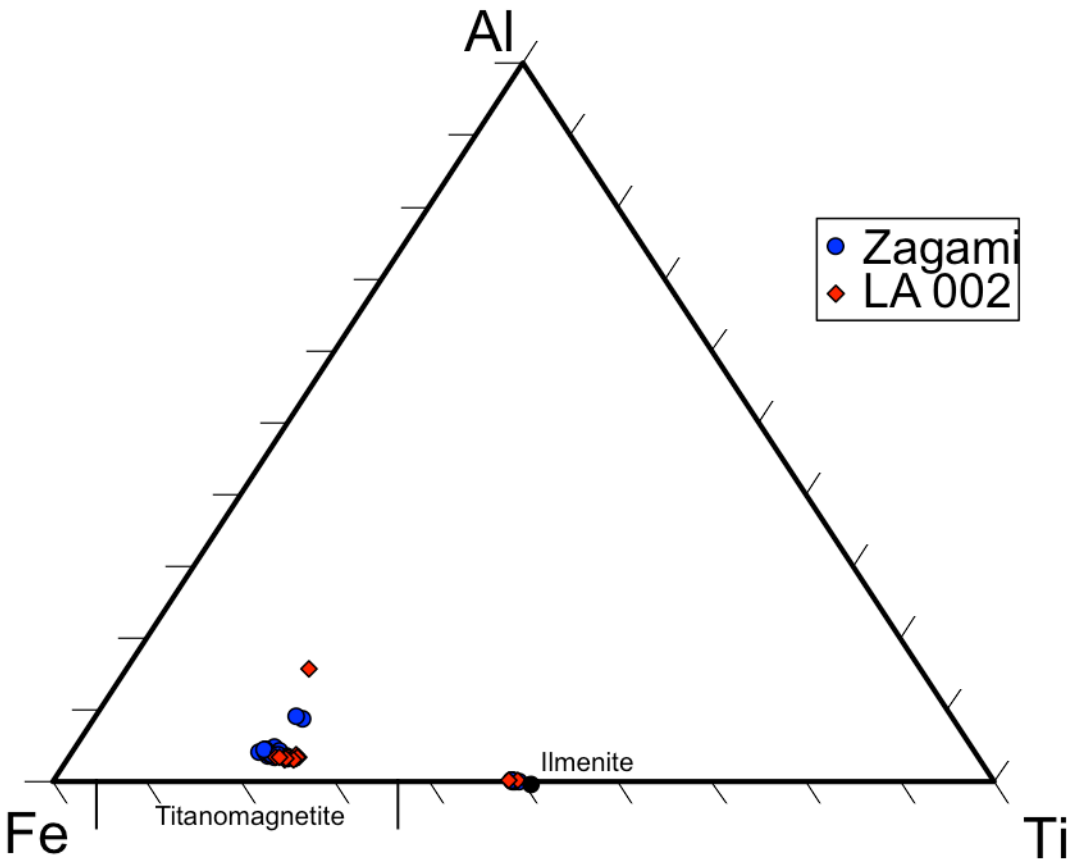

Figure 3.19: Ternary composition diagram comparing titanomagnetite in LA 002 and Zagami. Ideal titanomagnetite and ilmenite compositions have been shown for reference.

Table 3.4: Elemental composition of Zagami pyrrhotite grains.

No.	Fe	Co	S	Cu	Ni	Pb	Si	Total
1	59.29	0.10	36.41	0.07	0.30	0.14	BD	96.31
2	59.42	0.13	36.90	BD	0.36	0.03	0.06	96.9
3	59.53	0.10	37.12	BD	0.43	0.12	0.07	97.37
4	58.46	0.10	35.02	BD	0.33	0.06	0.36	94.33

*Associated error = 0.02, detection limit = 0.05 wt%, BD = below detection limit.

Representative compositions of pyroxferroite domains in the Los Angeles 002 meteorite are shown in Table 3.5. As pyroxferroite domains in this meteorite comprise small

regions of several distinct mineral phases, targets were selected to sample material from each different phase within the pyroxferroite. Rost et al. (2009) reported representative compositions of each component of the pyroxferroite breakdown material in LA 002, and the compositions reported here are in excellent agreement with their results. The bulk composition of the three components of pyroxferroite breakdown material reported here is in broad agreement with that of Warren et al. (2004), although that study reported an aggregated composition for all three components rather than discrete compositions for each component.

Table 3.5: Representative composition of LA 002 pyroxferroite (wt%).

Mineral Phase	Na_2O	MgO	Al_2O_3	SiO_2	CaO	TiO_2	MnO	FeO	NiO	Cr_2O_3	K_2O	P_2O_5	Total
Pyroxferroite (iron poor)	0.09	1.61	1.01	46.53	6.47	0.24	0.95	43.59	BD	BD	BD	BD	100.54
Pyroxferroite (iron rich)	0.08	1.60	0.16	32.95	0.88	0.14	1.28	63.67	BD	BD	BD	BD	100.81
Pyroxferroite (silicon rich)	0.35	BD	2.25	95.09	0.35	0.17	BD	0.72	BD	BD	0.75	BD	99.72

*Associated error = 0.02, detection limit = 0.05 wt%, BD = below detection limit.

The compositions of pyroxferroite and pyroxene in LA 002 meteorite are plotted for comparison in Figure 3.20. Data have been plotted in normalized mol % showing proportional Ca-Fe-Mg composition of each analysis. The compositional range for pyroxferroite defined here is in agreement with those of Warren et al. (2004) and Rost et al. (2009).

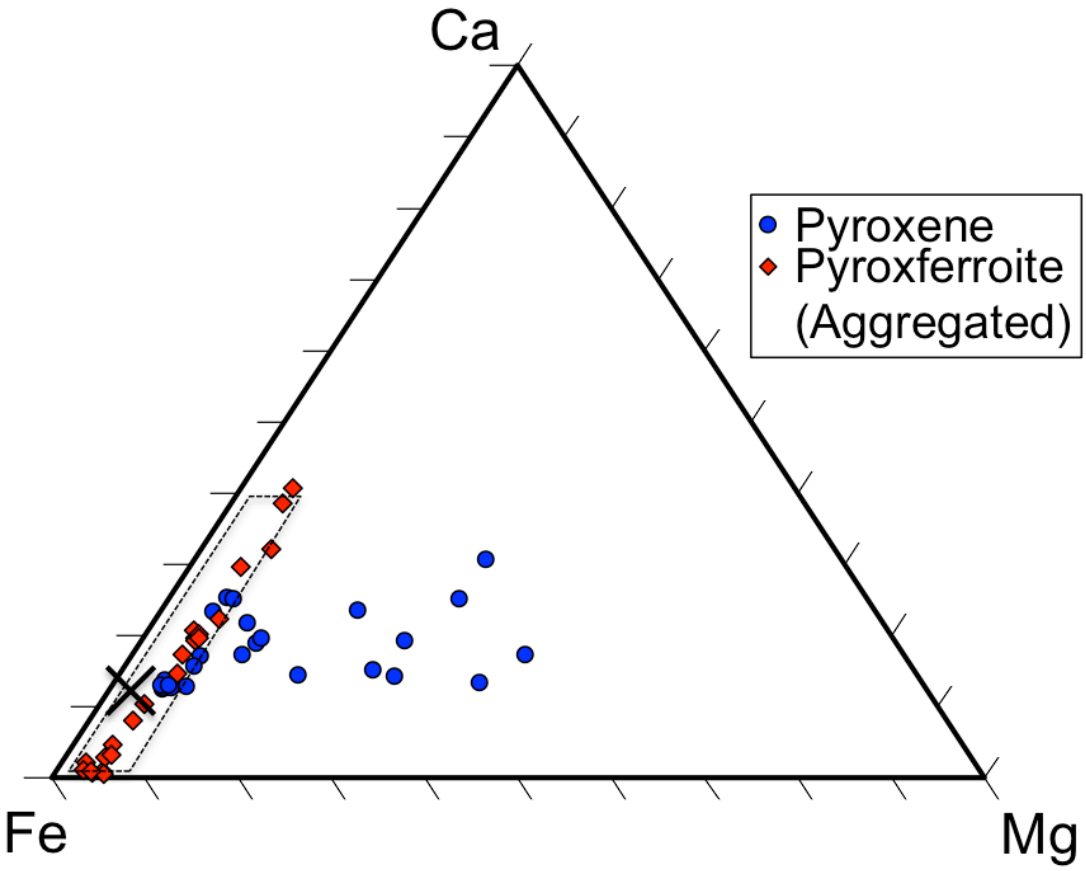

Figure 3.20: Ternary composition diagram comparing pyroxenes and pyroxferroite breakdown material in LA 002. Dotted line represents compositional field from Rost et al. (2009). Black X is average pyroxferroite breakdown material composition from Warren et al. (2004).

3.3.2 Nakhla

Representative compositions of major and minor phases in the Nahkla meteorite are shown below in Table 3.6. These confirm the compositional ranges reported previously in Papike et al. (2009), Bridges et al. (2006), and Treiman (2005).

Table 3.6: Representative compositions of major phases in the Nakhla meteorite (wt%).

Mineral Phase	Na_2O	MgO	Al_2O_3	SiO_2	CaO	TiO_2	MnO	FeO	NiO	Cr_2O_3	K_2O	Total
Augite rim	0.28	8.66	1.97	49.93	17.16	0.55	0.58	21.97	BD	0.12	BD	101.23
Augite rim	0.26	9.45	1.47	49.06	17.75	0.39	0.55	20.18	BD	0.09	BD	99.22
Augite core	0.20	13.38	0.87	51.92	18.47	0.30	0.42	14.77	BD	0.48	BD	100.83
Augite core	0.21	13.24	0.53	52.30	18.32	0.16	0.44	14.50	BD	0.41	BD	100.13
Olivine	BD	17.27	BD	33.22	0.44	BD	0.97	48.94	BD	BD	BD	100.89
Olivine	BD	14.98	BD	32.59	0.42	BD	0.99	51.35	BD	0.03	BD	100.41
Olivine	BD	13.11	BD	32.10	0.36	BD	1.07	53.51	BD	BD	BD	100.20
Olivine	BD	12.85	BD	30.83	0.43	BD	1.04	55.03	BD	BD	BD	100.30
Titanomagnetite	BD	0.40	1.51	BD	0.09	16.61	0.49	73.45	BD	6.00	BD	98.58
Titanomagnetite	BD	0.40	0.94	0.05	0.07	21.55	0.47	73.16	BD	1.22	BD	97.87
Titanomagnetite	BD	0.39	1.69	0.07	BD	15.06	0.41	78.53	BD	0.79	BD	96.96
Meso. (Glassy)	1.72	4.70	7.45	70.84	0.37	0.17	0.10	4.93	BD	BD	4.01	94.32
Meso. (Glassy)	6.09	1.62	20.57	56.13	5.55	BD	0.05	5.73	BD	BD	0.59	96.36
Meso. (Glassy)	5.82	0.58	23.11	61.32	6.11	0.05	BD	1.41	BD	BD	0.89	99.30
Meso. (Feldspathic)	7.42	BD	24.05	60.76	6.50	BD	BD	0.85	BD	0.01	0.75	100.43
Meso. (Feldspathic)	7.72	BD	24.26	60.67	6.60	0.06	BD	0.93	BD	BD	0.67	100.94
Meso. (Feldspathic)	7.29	BD	24.33	59.13	8.01	0.06	BD	0.88	BD	BD	0.52	100.28

*Associated error = 0.02, detection limit = 0.05 wt%, BD = below detection limit.

A ternary plot of measured augite composition in Nakhla is shown below in Figure 3.21. Data have been plotted in normalized mol % showing proportional Ca-Fe-Mg composition of each pyroxene analysis. This field of augite composition is in excellent agreement with the compositional domain reported in Treiman (2005) and Bridges et al. (2006).

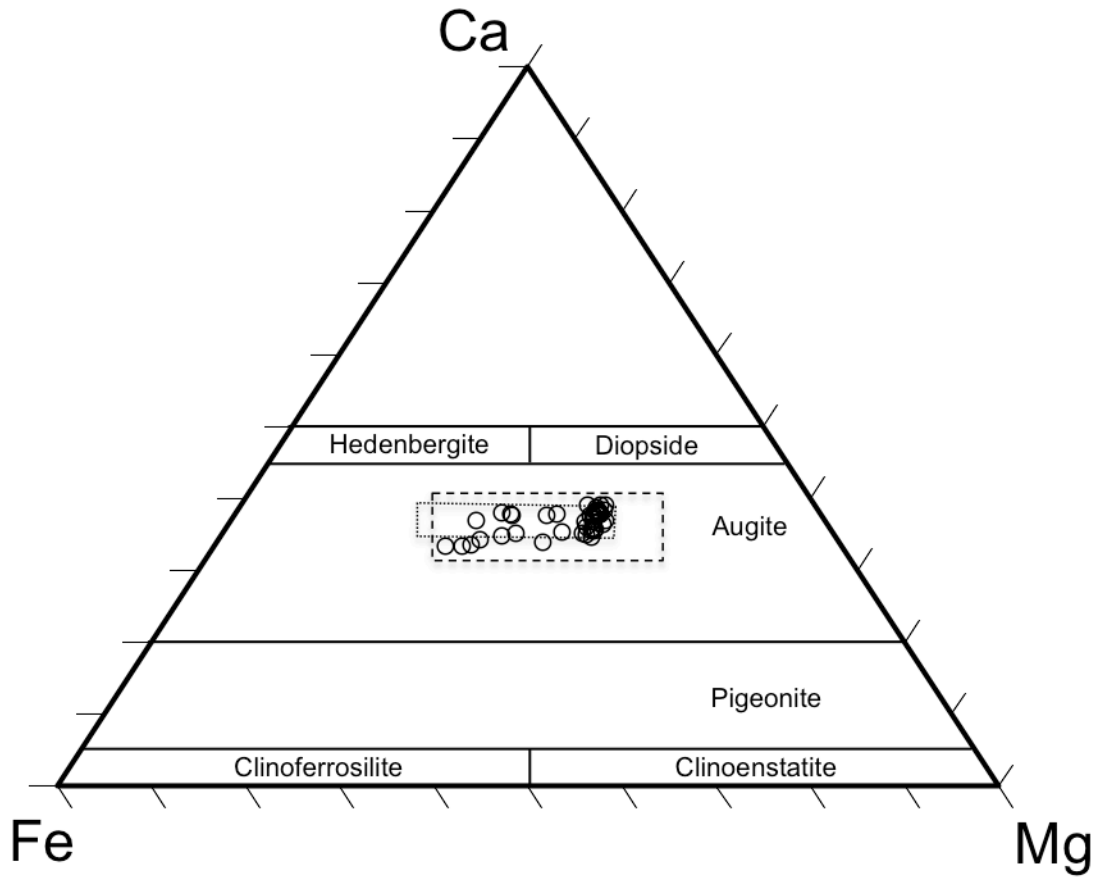

Figure 3.21: Ternary composition diagram showing composition of augite in Nakhla. Ideal pyroxene domains have been shown for reference. Heavy dashed line is from Treiman (2005). Light dashed line is from Harvey et al. (1992).

Measured olivine compositions in Nakhla are plotted below in Figure 3.22. Data have been plotted in normalized mol % showing proportional Fe-Mg-Si composition of each olivine analysis. The olivine composition reported here is in broad agreement with that presented by Harvey et al. (1992), among others.

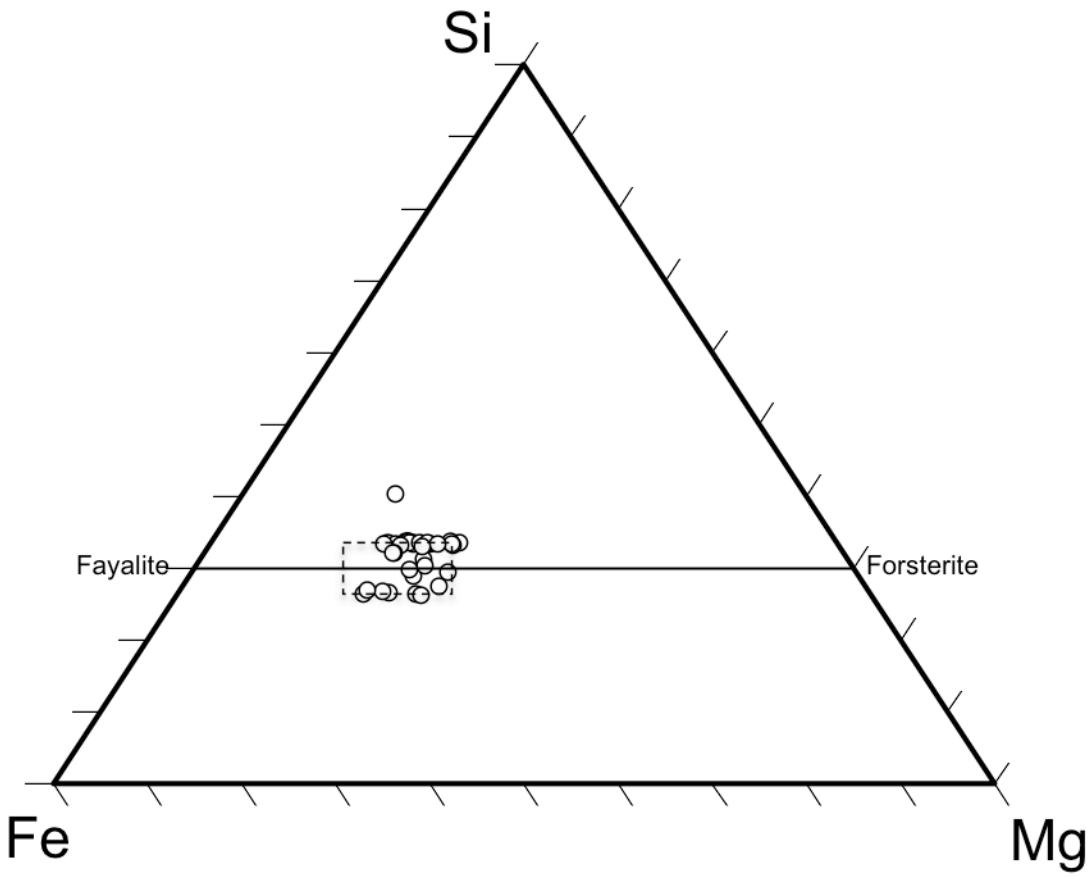

Figure 3.22: Ternary composition diagram showing composition of olivine in Nakhla. Ideal olivine compositions have been plotted for reference. Dotted line represents compositional field from Harvey et al. (1992).

A ternary plot of measured mesostasis composition in Nakhla is shown below in Figure 3.23. Data have been plotted in normalized mol % showing proportional Al-Alkali-Ferromagnesian composition of each analysis. The composition of the plagioclase component of this mesostasis material is in good agreement with that presented in Treiman (2005), but with a larger compositional field.

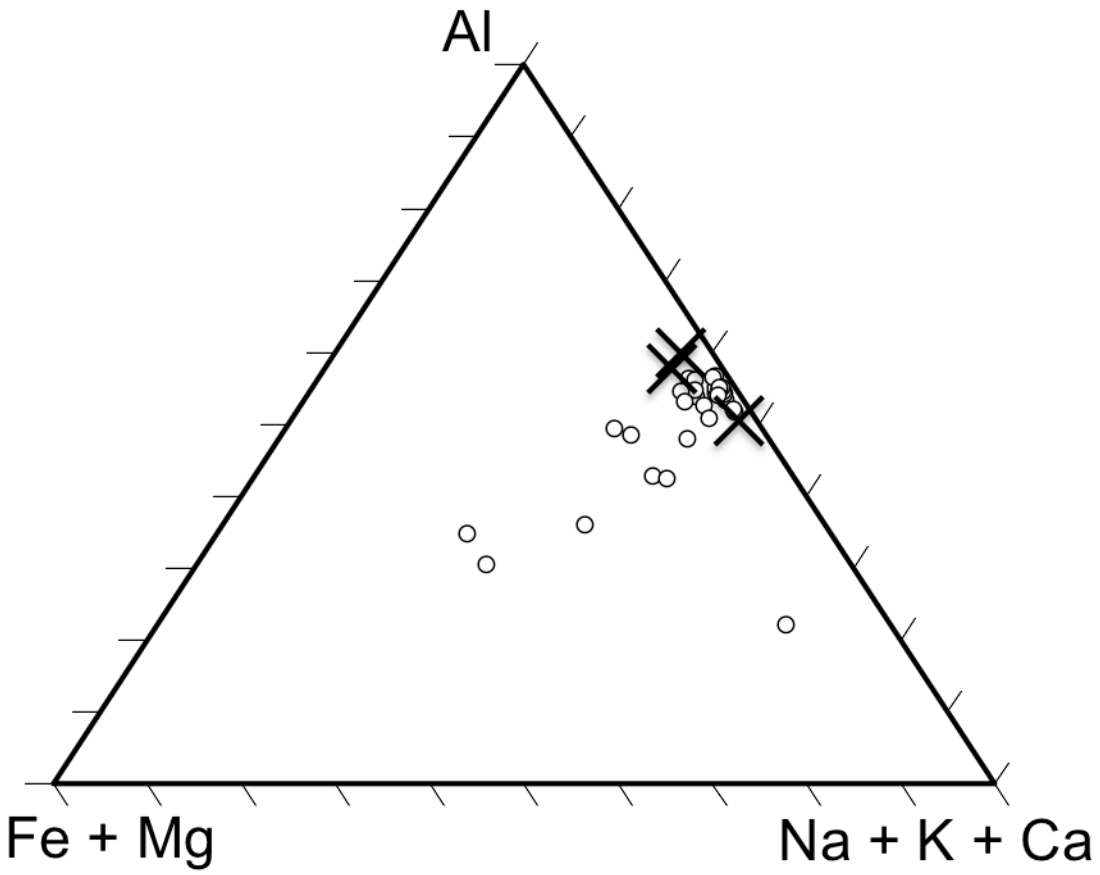

Figure 3.23: Ternary composition diagram showing composition of mesostasis in Nakhla. Large X are from Treiman (2005).

Comparative geochemical data for olivine grains and alteration material are shown in Tables 3.7 and 3.8. Both olivine and alteration material data were normalized to four oxygen atoms for purposes of comparison and equivalency. Several olivine analyses have slightly low totals (<99%); these analyses were likely not taken in ideal target locations, and as such the integrity of these data may not be as high as for other analyses. They have been reported here for completeness. Similarly, alteration material analyses have low totals due to the presence of abundant hydrated phases and the loss of these volatiles on analysis. Quantitative values cannot be discerned due to these low totals, but the

compositions reported here are adequate for comparison with olivine. Several alteration material analyses have anomalously low totals (49-62%); these have been reported here only for data completeness, but have not been included in interpretation of our results.

Table 3.7: Composition of Nakhla olivine associated with vein alteration material (wt%).

No.	FeO*	MgO*	MnO*	CaO*	Na_2O*	K_2O*	Al_2O_3*	SiO_2*	Total
1	48.94	17.27	0.97	0.44	BD	BD	BD	33.22	100.87
2	50.89	15.36	1.00	0.37	BD	BD	BD	32.82	100.46
3	53.51	13.11	1.07	0.36	BD	BD	BD	32.10	100.18
4	51.35	14.98	0.99	0.42	BD	BD	BD	32.59	100.36
5	49.35	17.09	0.94	0.43	BD	BD	BD	34.00	101.82
6	51.70	15.26	1.02	0.36	BD	BD	BD	33.29	101.66
7	49.40	17.33	0.94	0.35	BD	BD	BD	33.75	101.81
8	54.30	13.33	1.02	0.43	BD	BD	0.06	23.67	92.81
9	50.47	16.07	0.98	0.47	BD	BD	BD	33.19	101.22
10	45.56	9.48	0.82	0.25	0.14	0.29	0.08	35.35	91.96
11	54.95	12.95	1.02	0.42	BD	BD	BD	30.91	100.26
12	51.59	15.27	0.97	1.09	BD	BD	0.08	30.07	99.07
13	54.90	12.86	1.05	0.28	BD	BD	BD	23.81	92.91
14	51.66	15.14	0.96	0.40	BD	BD	BD	23.61	91.79
15	55.16	11.31	1.07	0.22	BD	BD	BD	22.72	90.50
16	51.38	15.59	0.98	0.36	BD	BD	BD	23.56	91.93
17	52.71	14.84	1.03	0.43	BD	BD	BD	27.04	96.08
18	49.66	16.77	0.94	0.34	BD	BD	BD	25.24	92.98
19	56.05	11.75	1.09	0.23	BD	BD	BD	23.78	92.89
20	55.03	12.85	1.04	0.43	BD	BD	BD	30.83	100.24
21	51.49	14.80	1.02	0.51	0.14	BD	0.41	32.26	100.64
22	49.41	17.43	0.94	0.37	BD	BD	BD	28.06	96.25
23	51.87	15.62	1.05	0.40	BD	BD	BD	29.08	98.06
24	53.69	14.64	1.09	0.28	0.05	BD	BD	28.48	98.25

*Associated error = 0.02, detection limit = 0.05 wt%, BD = below detection limit.

Table 3.8: Composition of Nakhla vein alteration material (wt%).

No.	FeO*	MgO*	MnO*	CaO*	Na_2O*	K_2O*	Al_2O_3*	SiO_2*	Total
1	34.21	6.79	0.39	BD	BD	0.67	0.07	44.25	86.44
2	35.08	6.27	0.43	BD	0.13	0.64	0.08	44.07	86.72
3	34.38	5.93	0.42	BD	0.09	0.50	0.22	44.32	85.90
4	30.76	6.42	0.39	1.74	0.09	0.51	0.57	44.07	84.55
5	33.40	5.72	0.43	1.35	0.08	0.43	0.11	43.27	84.79
6	34.52	6.41	0.41	0.10	0.09	0.61	0.16	45.16	87.46
7	30.38	4.03	0.46	0.35	0.31	0.30	0.13	13.30	49.26
8	30.14	4.21	0.53	0.20	0.08	0.25	0.13	15.10	50.63
9	30.82	4.93	0.40	BD	0.06	0.39	0.04	26.00	62.69
10	13.57	10.86	0.29	20.59	0.13	0.04	0.74	48.03	94.25
11	35.03	7.72	0.82	4.38	0.06	0.22	0.09	33.06	81.39
12	32.94	6.44	0.46	0.23	0.06	0.20	0.07	40.11	80.51
13	32.87	6.20	0.46	0.11	0.06	0.28	0.22	41.42	81.61
14	34.97	6.11	0.45	0.07	0.08	0.36	0.12	43.72	85.87
15	30.94	6.14	0.32	0.07	0.10	0.59	0.63	45.09	83.88
16	35.01	6.02	0.45	0.26	0.14	0.80	0.21	45.81	88.70
17	32.94	7.13	0.48	1.13	0.21	0.87	0.18	40.63	83.57
18	33.97	6.55	0.38	0.24	0.18	0.40	0.17	42.31	84.20
19	34.11	5.91	0.45	BD	0.08	0.49	0.12	42.50	83.69
20	36.20	5.64	0.49	0.15	0.15	0.47	0.09	42.79	85.98
21	37.07	6.25	0.63	0.66	0.28	0.78	0.09	43.81	89.57
22	34.90	5.81	0.46	BD	0.09	0.66	0.10	42.37	84.42
23	39.72	7.51	0.62	0.09	0.05	0.36	0.10	37.07	85.54

*Associated error = 0.02, detection limit = 0.05 wt%, BD = below detection limit.

Relative proportions of Fe-Si-Mg for both olivine grains and alteration material were plotted for comparison on a ternary diagram, in Figure 3.24. The geochemical compositions of this vein alteration material presented here are in rough agreement with those reported in Gooding et al. (1991), Bridges et al. (2001), and Changela et al. (2011).

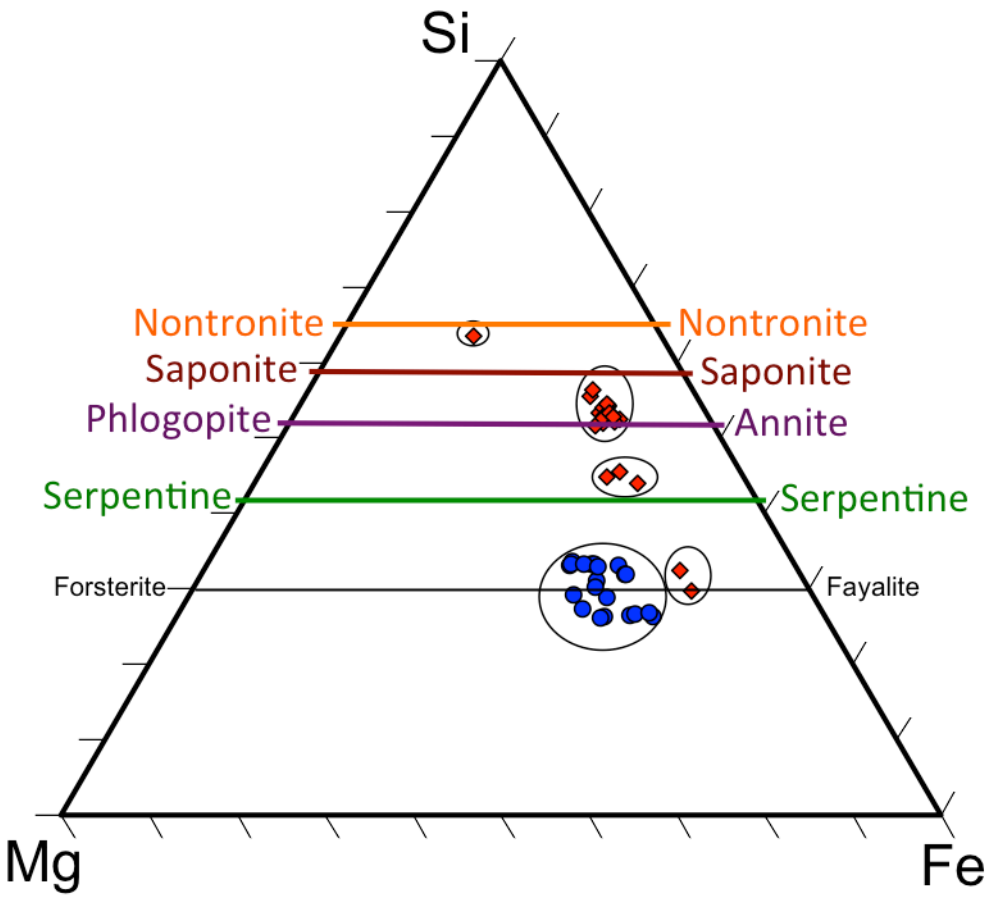

Figure 3.24: Ternary composition comparison diagram for Nakhla olivine and alteration material. Measurements obtained by EPMA spot analysis. Values in cation per formula unit. Ideal mineral compositions have been plotted for reference. Blue points represent data from olivine analyses spots, while red points represent alteration material.

3.4 Raman Spectroscopy

3.4.1 Nakhla Aqueous Vein Alteration

Optical photomicrographs of several laser Raman spectroscopy target regions are shown in Figure 3.25a-c, while the corresponding spectra with peaks labeled by location in wavenumber space are shown in Figure 3.26a-c. Contributing minerals identified in these Raman spectra are summarized below in Tables 3.9, 3.10, and 3.11.

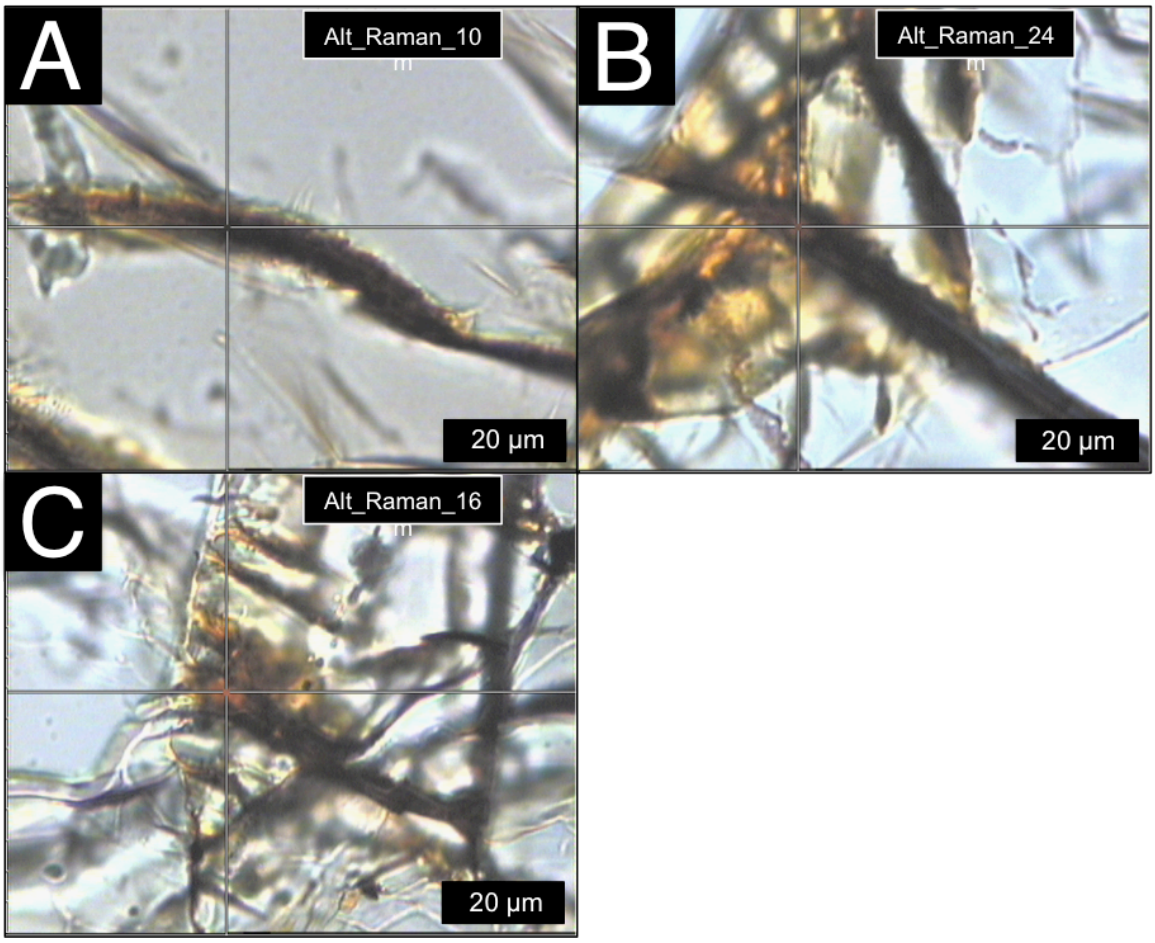

Figure 3.25: Context images of Nakhla aqueous vein alteration Raman spectroscopy analysis sites in USNM 426-6 polished section. Crosshairs show centre of ~1 µm analysis spot. A) Single thick fracture is present in olivine grain and shows infilling by opaque material. B) Extensively fractured region within olivine grain is shown, and a dark infilled fracture was chosen for analysis. C) Extensively fractured region within olivine grain is shown, and a dark infilled fracture intersection area was chosen for analysis.

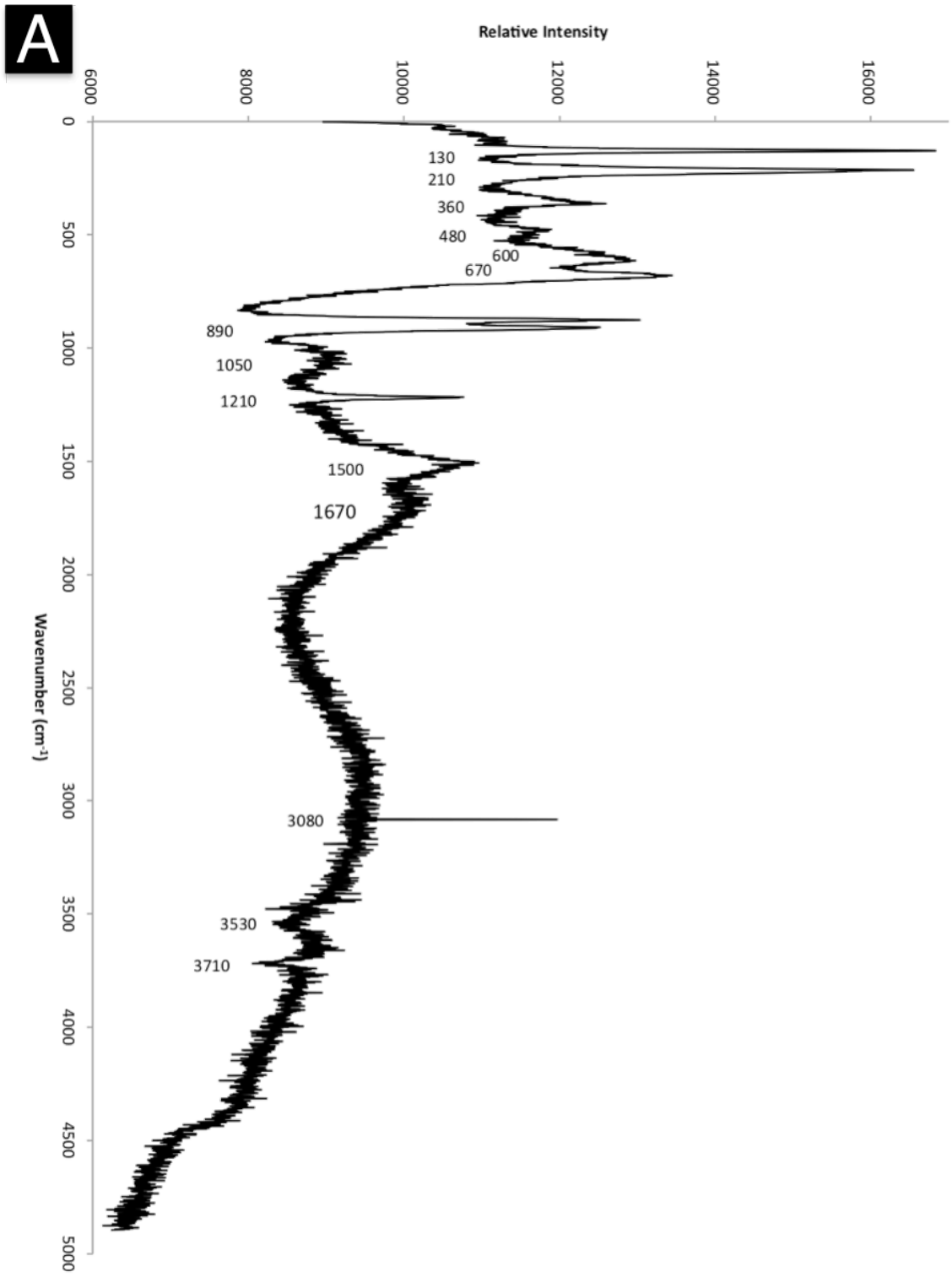

Figure 3.26: Raman spectra of fracture filling alteration material acquired at Nakhla Aqueous Vein Alteration Raman sites A-C. Relative intensity of signal is plotted versus wavenumber. Plot has been background corrected and subtracted.

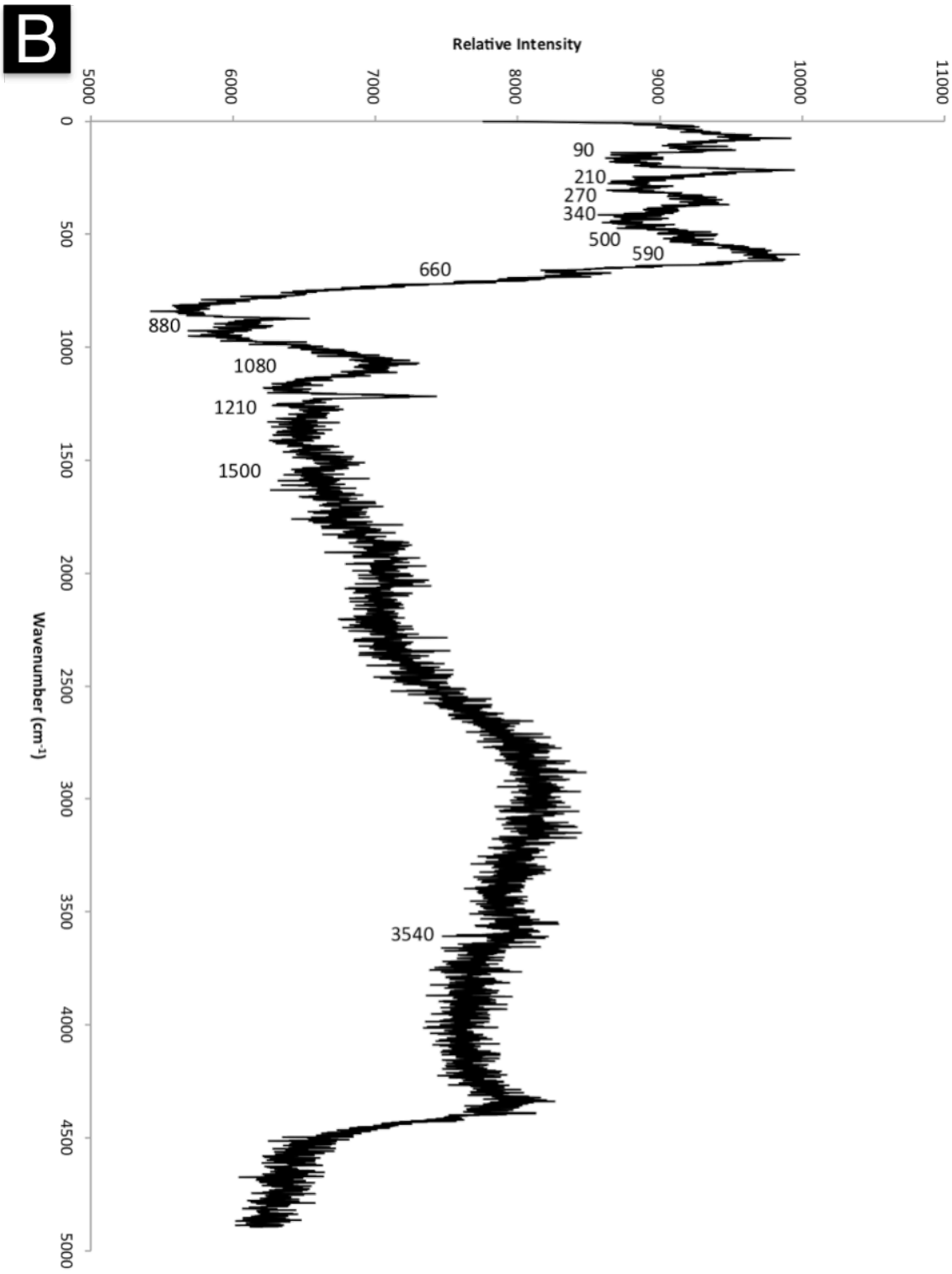
B
Relative Intensity
5000
6000
7000
8000
9000
10000
11000
0
500
1000
1500
2000
2500
3000
3500
4000
4500
5000
Wavenumber (cm-1)
90
210
270
340
500
590
660
880
1080
1210
1500
3540

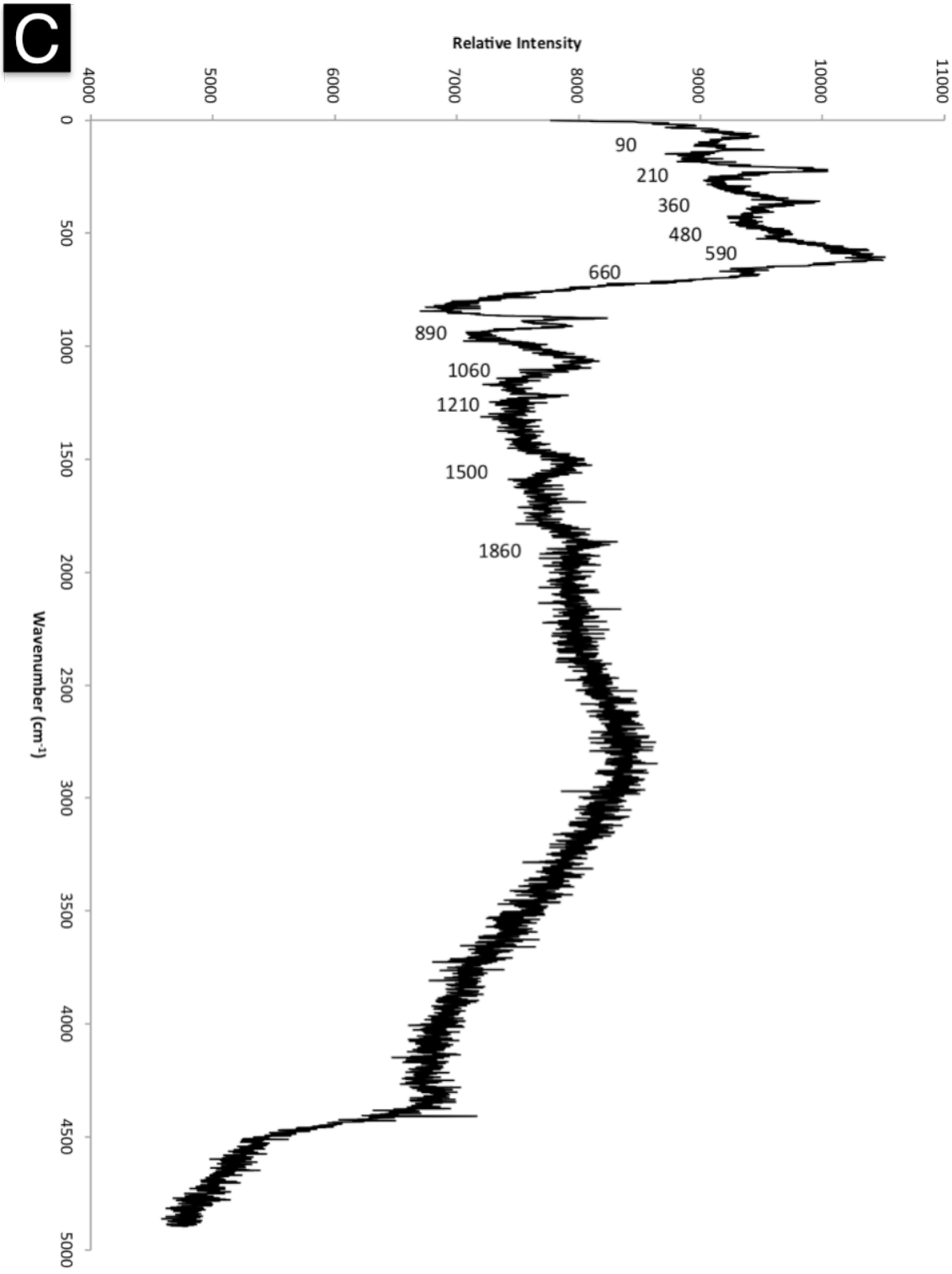
C
Relative Intensity
4000
5000
6000
7000
8000
9000
10000
11000
Wavenumber (cm-1)
0
500
1000
1500
2000
2500
3000
3500
4000
4500
5000
90
210
360
480
590
660
890
1060
1210
1500
1860

Table 3.9: Mineral and spectral contributions identified in Raman spectrum A.

Peak Wavenumber (cm^{-1})	Olivine	Serpentine	Goethite	Siderite	Smectite	Other Contribution
130	◆				◆	
210	◆	◆	◆	◆		
360	◆	◆	◆	◆		
480			◆	◆		
600		◆				
670		◆	◆	◆		
890	◆					
1050				◆		
1210					◆	
1500						Epoxy
1670						Carbon Coating
3080						CR Interaction
3530					◆	
3710					◆	

Table 3.10: Mineral and spectral contributions identified in Raman spectrum B.

Peak Wavenumber (cm^{-1})	Olivine	Serpentine	Goethite	Siderite	Smectite	Other Contribution
90					◆	
210	◆	◆	◆	◆		
270				◆		
340	◆	◆	◆	◆		
500			◆	◆		
590		◆				
660		◆	◆	◆		
880	◆					
1080				◆		
1210					◆	
1500						Epoxy
3540					◆	

Table 3.11: Mineral and spectral contributions identified in Raman spectrum C.

Peak Wavenumber (cm^{-1})	Olivine	Serpentine	Goethite	Siderite	Smectite	Other Contribution
90					◆	
210	◆	◆	◆	◆		
360	◆	◆	◆	◆		
480			◆	◆		
590		◆				
660		◆	◆	◆		
890	◆					
1060				◆		
1210					◆	
1500						Epoxy
1860						Epoxy

The alteration phases identified here by Raman analysis are in agreement with those identified by *in situ* micro XRD and EPMA elsewhere in this study. The mineral phases making up the vein alteration alteration assemblage observed here by Raman Spectroscopy are also largely consistent with the assemblages previously reported by Gooding et al. (1991), Bridges et al. (2001), and Changela et al. (2011) using other techniques. However, these three studies did not report Raman spectral data and did not report the presence of smectite mineral phases, although it was reported in alteration of the Lafayette meteorite (a similar nakhlite). Raman analyses of carbonates and iron oxides in Nakhla have been previously reported by Rull et al. (2004).

Chapter 4.0 Discussion

4.1 Discussion of Results

4.1.1 Shergottites

Compositionally, and despite much overlap, the pyroxenes from the two shergottites plot in fields with two distinct centres. On a Ca-Fe-Mg ternary plot (shown in Figure 3.17), both shergottites display significant variation in the composition of their pyroxenes with large fields covered by these analyses. Both low calcium (pigeonite) and high calcium (augite) pyroxenes can be distinguished using these data. A continuous range of compositions spans the usual miscibility gap. The compositional difference between the augite and pigeonite phases appears to be more pronounced in the pyroxenes in Zagami than those in LA 002. On average, pyroxenes in LA 002 are lower in calcium than those in Zagami, although some LA 002 pyroxenes are quite calcium rich. Notably, pyroxenes in LA 002 are significantly enriched in iron compared to those of Zagami, with more than half of LA 002 augite and pigeonite plotting in the upper third of the ternary in Fe space. BSE mapping (as presented in Figures 3.2 and 3.4) shows that pyroxenes in both LA 002 and Zagami display significant compositional zoning, with Fe-rich exteriors and Mg-rich interiors. This zoning is more pronounced in LA 002 pyroxenes than in those of Zagami. This likely represents two stages of pyroxene growth, one at depth directly out of melt and one following emplacement at lower temperatures forming exterior rims (Bridges et al., 2006).

Data plotted in Figure 3.20 as “aggregated pyroxferroite” show a continuum between the iron rich and iron poor phases comprising the pyroxferroite. Clear differences can be seen between the composition of pyroxferroite domains in LA 002 and the distinct pyroxene phases. Pyroxferroite in LA 002 is Mg poor (particularly when compared with the augite and pigeonite in the rock) with approximately constant Mg composition (as shown in Figure 3.20). The iron rich phase of the pyroxferroite is significantly enriched in iron when compared with the pyroxenes in LA 002, and the iron poor phase of pyroxferroite is significantly lower in iron content to the majority of pyroxene analyses (Figure 3.20). Notably, all pyroxferroite analyses appear to plot on a mixing line, reflecting that they shared an initial metastable starting pyroxene composition.

Three separate phases within the pyroxferroite breakdown material were identified from these data. The first is the iron poor phase, the second is the iron rich phase, and the third is silicon rich. This segregation results from the breakdown of the metastable iron-rich pyroxferroite phase in the rock upon emplacement in the Martian subsurface at lower pressures than those at which the pyroxferroite is stable and relatively rapid cooling (Bridges et al., 2006). The iron poor phase is identified as hedenbergite, an iron and calcium rich pyroxene endmember. The iron rich phase is fayalite. The silicon rich phase is likely silica with minor impurities resulting from the breakdown and migration of components of the starting composition (Rost et al., 2009). These iron rich, iron poor and silica rich phases are all present in extremely close proximity, intermixed with one another on the micron scale (as shown in Figure 3.2b).

Maskelynite in both shergottites is relatively low in potassium; one outlier point may represent an area of potassium concentration during maskelynitzation of the original feldspar. Despite much overlap between maskelynite composition in LA 002 and Zagami, two distinct compositional domains can be identified. The maskelynite in LA 002 is much more compositionally variable than that of Zagami. LA 002 maskelynite is grouped into two regions, one of approximately equal calcium and sodium contributions and one enriched in calcium. Maskelynite in Zagami is closely grouped around an approximately equal anorthite-albite composition. LA 002 likely originally contained two distinct plagioclase compositions, reflecting fractional crystallization of feldspar following pyroxene crystallization on Mars (e.g., Rubin et al., 2000).

Merrillite analyses in both shergottites are relatively similar. Calcium, potassium and sodium contents in both meteorites are approximately equal when allowing for error. Merrillite in LA 002 is slightly enriched in potassium when compared to that of Zagami. Quenched mesostasis (as shown in Figure 3.2 and 3.4) compositions in both meteorites are relatively equivalent. LA 002 mesostasis is slightly enriched in silica and depleted in aluminum when compared to that of Zagami. Mesostasis in Zagami is also slightly enriched in both iron and alkali content in relation to LA 002. Notably, fayalite rims associated with mesostasis material in LA 002 could be identified using the microprobe and analyzed here. This fayalite material is extremely iron rich, with an average cationic composition of Fa_{96}.

Comparison of the iron and sulfur content of the pyrrhotite analyses from Zagami presented here in Table 3.4 provides an average composition of $Fe_{0.935}S$. This is relatively

iron rich and approaches the ideal FeS troilite endmember composition. The sulfide phase in Zagami and LA 002 is iron-rich and relatively free of impurities such as nickel or lead. Overall, there is much similarity between the titanomagnetite compositions in these two shergottites. Most are iron-rich, with iron-titanium ratios of approximately 3:1. Several anomalous analyses show a relatively high amount of aluminum contamination within the iron oxide phase. However, there is a small grouping of grains in both meteorites that contain a significantly higher proportion of titanium, in approximately equal amounts to that of iron in these titanomagnetites. These grains may represent ilmenite mineralization. Herd (2008) demonstrated that the iron and titanium content of the iron oxide phases in igneous rocks such as Martian meteorites can be used as an oxybarometer to provide information about the redox state of the rock at the time of crystallization. However, iron and titanium exchange continues during cooling so this may not be a strictly accurate method of determining redox state (Herd, 2008). Still, the data presented by Herd (2008) suggest that it is possible to conclude that the two groupings of oxide composition in LA 002 and Zagami reflect the redox conditions during the emplacement of these rocks.

Despite being heavily fractured, Los Angeles and Zagami show little evidence of aqueous alteration. Alhough the shergottites contained a large proportion of water in their original mantle-derived melt (potentially up to several wt. %), there is very little evidence of any interactions with water after their crystallization and emplacement (Bridges et al., 2006). They also show no evidence of thermal alteration or any significant interaction with the Martian atmosphere. Although the early history of Mars was a time of significant clay formation due to the actions of hydrothermal fluids on crustal rocks, there are no

preterrestrial clays present in any fractures or pore spaces of basaltic shergottites such as Los Angeles and Zagami (Ehlmann et al., 2011).

4.1.2 Nakhla

Nakhla is a clinopyroxenite. Augite in Nakhla is rich in calcium and iron with slightly lesser magnesium content. It contains minimal sodium, aluminum and titanium cation substitution, approximately an order of magnitude lower than the primary constituents. This average augite composition is richer in iron and poorer in magnesium than typical terrestrial augites, as iron and magnesium substitution are inversely related (Anthony et al., 1995). All augite analyses have broadly similar calcium contents; this suggests that the distribution of calcium in the early melt was homogenous, as augite was the first phase to crystallize. Augite in Nakhla is slightly zoned, with Fe rich material in the rims, but not to the extent of other SNC meteorites such as many shergottites (e.g., Bridges et al., 2006).

Olivine in Nakhla is iron-rich, particularly when contrasted with similar terrestrial basaltic olivines (McSween, 1994; Bridges et al., 2006). It has an average composition of $Fa_{65.5}$. This supports the prevailing view that the Martian crust is more enriched in iron than that of the Earth (McSween et al., 2010). It has a manganese content of about 1 wt.%, toward the higher end of expected values for terrestrial basaltic olivine but within the expected range for Martian basaltic rocks (Anthony, 1995). Some grains of titanomagnetite in Nakhla show evidence of ilmenite exsolution, as seen in Figure 3.6a. The mesostasis in Nakhla contains glassy material and plagioclase laths, alongside minor

phases such as sulfides and oxides. As such, it is rich in both iron and alkali elements. Most of the sodium and potassium in Nakhla has been partitioned into the mesostasis phase, both in the plagioclase crystals and the glassy material. Magnesium is the primary component substituting for iron in the olivine structure, with an average composition of $Fo_{32.4}$, less than what would be expected from similar olivines in terrestrial settings. Manganese and calcium make up the remainder of cation substitution in Nakhla olivine; manganese substitutes for iron at approximately one percent of atomic sites, in addition to minor (<1%) amounts of calcium substitution. Minimal variation in chemistry, relatively homogenous appearance of olivine grains lacking major zoning, and the association of olivine grains within the larger subcumulate sugite texture suggests that olivine crystallization in Nakhla occurred approximately simultaneously with augite formation (e.g., Treiman, 2005).

The mesostasis data in Figure 3.23 plot in two distinct regions. The first is a cluster of analyses at low (<10%) Fe + Mg contents. The second is a diffuse region of points that can be differentiated from this cluster by their varying ferromagnesian and alkali contents. The cluster of points with low Fe + Mg values appear to be enriched in aluminum and alkali elements such as Na, K, and Ca. This cluster likely represents the plagioclase laths that form a significant component of mesostasis in Nakhla. These display minimal compositional variation in alkali and aluminum space; their non-zero iron and magnesium contents are likely artifacts due to the contribution of surrounding and interstitial fine grained materials containing iron. Compositionally this cluster of points appears to be slightly anorthitic based on the ratio of aluminum to alkali elements, due to the ideal formulas for anorthite ($CaAl_2Si_2O_8$) and albite ($NaAlSi_3O_8$). Due to the

partitioning of all alkali elements into the mesostasis and the presence of plagioclase within the mesostasis as the primary alkali phase in this rock, this feldspar is likely of an intermediate composition.

The remaining diffuse region of points appears to be largely enriched in iron and magnesium when contrasted with the plagioclase cluster. These analyses likely represent the glassy, fine-grained material that was quenched and makes up much of the mesostasis present in between plagioclase laths. This fine-grained, glassy mesostasis appears to be highly heterogenous in its composition. It is enriched in iron, magnesium and alkali elements to varying degrees in varying regions throughout the meteorite. The glassy mesostasis material most often interfaces with pyroxene or olivine crystals at irregular boundaries and usually abuts many crystals in one region. This material is distributed throughout the meteorite and phase crystal boundaries with the ferromagnesian minerals across the entire rock.

Although Nakhla has experienced relatively minor shock when compared to most other Martian meteorites (Eugster et al., 1997), it contains a moderate fracture system. Olivine grains have been extensively fractured and pyroxene grains show some fracturing as well, creating a somewhat interconnected fracture system throughout the rock. These fractures have a relatively large opening, up to 10-20 μm in width in some locations, creating a significant amount of pore space similar to many terrestrial igneous rocks.

4.1.3 Nakhla Aqueous Vein Alteration

Olivine can be identified in the Raman spectra presented here by its characteristic peak doublet at a wave number of approximately 890 cm^{-1}. Smectites are found in all observed Raman spectra, with characteristic peaks at wavenumbers of approximately 90-135 cm^{-1}, 1200 cm^{-1}, 3500 cm^{-1} and 3700 cm^{-1}. These peaks contain minimal contribution from overlap due to other mineral phases. These peaks most likely correspond to the presence of nontronite in the vein alteration material, although it may represent saponite contribution due to some similarities in the spectra of the two minerals. Serpentine can be identified due to a characteristic peak at approximately wavenumber 600 cm^{-1} and several other diagnostic peaks at approximately 210 cm^{-1}, 360 cm^{-1} and 670 cm^{-1}.

One of the primary components of the vein alteration material present in Nakhla is an iron oxide phase. The observed Raman spectra show a large contribution by goethite. Magnetite shares several Raman peaks with goethite, suggesting that there may be a slight contribution from magnetite; this contribution is likely not significant, but the presence of magnetite could be expected due to the importance of magnetite formation in the serpentinization process due to the liberation of iron from olivine (Gahlan et al., 2006; Janecky et al., 1986). Previous studies have identified the presence of hematite and/or ferrihydrite (Treiman, 2005). However, the Raman spectra of both hematite and ferrihydrite contain a diagnostic peak at wavenumber of approximately 1300 cm^{-1}. The observed Raman spectra from Nakhla do not present any peaks at 1300 cm^{-1}, and therefore there is likely no significant contribution from hematite and ferrihydrite.

Notably, the observed Raman spectra display a peak at approximately wavenumber 1050-1080 cm^{-1}. This peak is a diagnostic carbonate peak, and indicates the presence of a carbonate phase in the vein alteration material. The Raman spectrum of siderite is an excellent match with the observed spectra, with all characteristic peaks present. Other Ca-Fe-Mg carbonate minerals have similar Raman spectra, although several of their diagnostic Raman peaks are not present here. It can be concluded on the basis of these Raman data that the carbonate phase contributing to the Raman spectra is most likely siderite. This is supported by the presence of siderite elsewhere in the Nakhla meteorite and outside of vein alteration (e.g., Bridges et al., 2000).

Augite was identified from the X-ray diffraction patterns as the primary contributing pyroxene phase. Fayalitic olivine was identified as the best match for the contributing olivine phase. These two "host" minerals have complex diffraction signatures and contribute many peaks and overlap with the other phases requiring identification in the alteration material. Serpentine group minerals (lizardite, antigorite and chrysotile) initially provided promising matches for the observed XRD patterns. Of these, chrysotile provides the best match containing most of its diagnostic peaks and is identified as the contributing serpentine group mineral in all observed patterns.

Ankerite is identified as the carbonate phase contributing to the observed XRD patterns, matching a number of strong experimental peaks. Ankerite is a member of the dolomitic Ca-Fe-Mg carbonate system (Chang et al., 1996), and it is the best Ca-Fe-Mg carbonate fit for the XRD data here. A carbonate identified as siderite containing significant amounts of calcium and magnesium has been previously identified in aqueous vein

alteration in the Nakhla meteorite (Bridges et al., 2000). It can be concluded based on the XRD and Raman data presented here that both siderite and ankerite are present in this alteration material.

Iron oxide XRD patterns are a significant contributor to the experimental peaks, and delineation of the iron oxide minerals present is a key aspect of understanding the mineralogical composition of the vein alteration material. The primary iron oxide, an excellent match to the observed patterns, is goethite. Almost all peaks within goethite standard patterns are accounted for within expected deviation, and many of these peaks are excluded from the augite and olivine patterns that interfere with the alteration material signal. The fit between hematite and the experimental peaks is good and a contribution from hematite is identified. Hematite is likely not as significant as goethite in the iron oxide phase of the vein alteration material, but may be present in small amounts related to other iron oxides. Ferrihydrite is an excellent match to most observed patterns, with all of its ICDD card peaks taken up by the experimental peaks. It may be present as a transitional phase between Goethite and other iron oxide minerals.

Many unique peaks in the observed XRD patterns are matches to minerals in the smectite group. The best match for the observed patterns is nontronite. It is an excellent match with many of its diagnostic peaks and is likely the primary contributing smectite mineral. Saponite is also a good match to many of the observed experimental peaks, and is likely present in the vein alteration material, although in a smaller amount than nontronite.

Notably, vein alteration material in Nakhla is enriched in iron in comparison to pristine olivine grains. This suggests the possibility of addition of iron into the system by aqueous fluids, and the enrichment of iron by precipitation of iron rich phases such as iron oxides. Similarly, alteration material is proportionally deficient in magnesium and manganese when compared to initial olivine values. This mobilization and removal of magnesium is known to occur during "iddingsite" formation (Delvigne et al., 1979). Remobilized magnesium during alteration is a possible magnesium input for the precipitation of serpentine group minerals in the fractures. The vein alteration material is enriched in aluminum, with several spots highly anomalous in aluminum content. This suggests the formation of phyllosilicate minerals during olivine alteration, such as smectites, that are highly enriched in aluminum. Smectite group minerals typically do not contain appreciable amounts of potassium, although they may incorporate it into their structure if there is excess potassium present in the system. However, many similar phyllosilicate minerals such as illite contain potassium. The data precision that can be obtained from the complex fracture systems in Nakhla is not sufficient for discrimination of phyllosilicate phases in the vein alteration material based on geochemistry.

Iron, magnesium and silicon are the primary components of olivine and are important constituents of the vein alteration material, and have been plotted in ternary space in Figure 3.24. Olivine compositions plot in one group in the lower third of the silicon scale, and notably plot toward the Fe-rich side of the diagram. Four mineral fields have been plotted based on silicon content (as in Changela et al., 2011) on Figure 3.24 with corresponding lines based on their ideal chemical formula and the spread allowed by

variations in iron and magnesium content, one each for serpentine, phlogopite-biotite, saponite, and nontronite.

The majority of the groupings of alteration material compositions plot relatively near these mineral lines, with one grouping corresponding to serpentine, one grouping corresponding to saponite or less hydrated phyllosilicate phases, and one point corresponding to nontronite. These results are consistent with similar ternary analysis done with alteration phyllosilicates from the nakhlite Lafayette (Changela et al., 2011). Biotitie is not likely to be stable under the conditions expected here, and has been included to provide a broad spectrum of phyllosilicate structures. While quantitative identification of mineralogical phases is not possible due to the difficulties with signal acquisition in poorly-formed vein alteration material, these data suggest groupings of alteration material with similar compositions to phases that might be expected in the vein alteration material and have been confirmed using other techniques.

4.2 Refinement of Nakhla Vein Alteration Mineral Assemblage and Subsurface Environmental Conditions of Alteration

“Iddingsite” in terrestrial settings has long been known to be a primary alteration product formed by the weathering of olivine, containing a mixture of cryptocrystalline goethite and a phyllosilicate phase of varying composition (e.g., Delvigne et al., 1979). Aqueous vein alteration material in the Nakhla meteorite was initially described as reddish-brown staining along fractures, composed of iron-rich siliceous material, carbonates, and an unidentified phyllosilicate phase (e.g.. Gooding et al., 1991). Later work refined the

known assemblage to contain a sub-micron mixture of smectite clay, iron oxy-hydroxides such as hematite, and secondary minerals such as carbonates, halides, and sulfates (e.g., Bridges et al., 2000; Bridges et al., 2001; Fisk et al., 2006; McKay et al., 2001; Treiman, 2005). Notably, clay minerals in vein alteration material have been described as being common among the nakhlites (Leshin et al., 2006).

In a recent study by Changela et al. (2011), aqueous alteration in the nakhlite group of meteorites was described in extensive detail. Vein alteration material in Nakhla was found to contain crystalline siderite with significant substitution of calcium and magnesium, patches of gypsum, and largely amorphous iron-silicate gel (Changela et al., 2011). No phyllosilicates or significant iron oxy-hydroxides were described (Changela et al., 2011). However, extensive layers of phyllosilicate minerals were found in the veins of Lafayette, another nakhlite. Veins in Lafeyette were found to contain smectite crystals of up to 100 μm in size (Treiman, 2005; Changela et al., 2011). Mineral identification in these past studies was largely carried out using Transmission Electron Microscopy (TEM). TEM does not provide information on the crystal structure of a mineral, the critical component used to quantitatively identify a phase. Therefore, the use of micro X-Ray diffraction this work allows for more quantitative identification of specific minerals in the alteration material and can identify phases that TEM is not able to detect. f

The results of this study indicate the presence of smectites, serpentine, iron oxides, and carbonates in altered veins, based on laser Raman spectroscopy, micro X-ray diffraction and EPMA geochemistry. The smectite phases identified are nontronite and saponite. Chrysotile is the serpentine phase, and both siderite and ankerite were identified as the

carbonate phases. Goethite is the primary iron oxide phase present, although hematite may be present in small amounts. Ferrihydrite is likely present as a transitional phase between goethite and other iron oxides. It is believed that iron oxides and smectites comprise a significant proportion of the alteration material present in veins in Nakhla. Gypsum may be present within veins elsewhere in the Nakhla meteorite, but was likely not sampled here due to its sporadic and patchy nature.

This mineral assemblage differs from recent work (e.g., Changela et al., 2011), notably by the presence of smectites (nontronite, saponite), the identification of ankerite in the carbonate assemblage, and by the identification of iron oxides (goethite, hematite). This places the alteration assemblage, and thus the conditions of alteration, closer to that shown by other nakhlites that contain extensive iron oxides and phyllosilicates (especially Lafayette) than was previously thought. The alteration conditions of Nakhla should therefore be re-evaluated. The identification of phyllosilicates in vein alteration in this work places Nakhla lower in the proposed stratigraphy of the volcanic nakhlite source flow than was previously considered by Changela et al. (2011).

The possible environmental conditions of alteration in the nakhlites have been discussed extensively in the past, focusing on the assemblage of carbonates, sulphates, and halides elsewhere in the meteorite (Changela et al., 2011). The alteration assemblages observed here are significantly enriched in Fe and Mg, with minimal amounts of phases containing volatile elements. This may be due to the high Fe and Mg content of the starting material (olivine) that was altered by aqueous fluids. Additionally, serpentine formation (such as the chrysotile observed here) involves the uptake of magnesium and does not incorporate

significant amounts of iron into its structure (Janecky et al., 1986). This may have increased the relative iron content of the remaining alteration phases (iron oxides and phyllosilicates) without any significant influx of iron into the alteration interface. However, the formation of "iddingsite" has been shown experimentally to require the addition of ferric iron and is commonly associated with some removal of magnesium from the system (Delvigne et al., 1979). This experimentally suggested high Fe/Mg fluid ratio is consistent with the geochemistry of Nakhla vein alteration material reported here, suggesting that primary altering fluids may have been slightly iron rich and relatively magnesium depleted.

The presence of both ankerite and siderite in this alteration assemblage suggests that hydrothermal modification by Mg-enriched fluids has taken place following the initial alteration of the Nakhla meteorite, with Ca and Mg replacing Fe in the carbonate structure. Hydrothermal dolomitization of calcite, with Ca replacement by Mg, is well documented (Warren, 2000; Machel, 2004). Ankerite is chemically and morphologically similar to siderite, but structurally distinct. In this setting, it can only be differentiated using *in situ* mineralogical techniques that measure the crystal lattice of mineral species, such as micro X-Ray diffraction. Therefore, it is possible that past studies such as those by Bridges et al. (2001) and Changela et al. (2011) did not detect ankerite despite its presence in the alteration assemblage. This study reports the first direct detection of ankerite in the vein alteration of Nakhla.

Carbonates in the nakhlites along with the other minerals present in this assemblage are suggested to have formed from aqueous fluids at temperatures well below 150^{o}C, and are

potentially consistent with temperatures as low as 10-25^{o}C (Bridges et al., 2000; Herut et al., 1990). The observation in the assemblage here of iron carbonates such as siderite and ankerite, containing Fe^{2+}, suggests alteration fluids of pH near 7 (e.g., Changela et al., 2011). The presence of Ca-Fe-Mg carbonates suggests pCO_2 conditions of >50-100 mbar, significantly higher than the current pCO_2 of ~6 mbar at the surface of Mars (Catling, 1999; Changela et al., 2011).

The identification here of smectites and iron oxides in Nakhla vein alteration material suggests that a re-evaluation of the environmental conditions of alteration may be required. Formation temperatures for iron bearing smectites such as those identified in this study are variable and can range up to ~250^{o}C (Tosca et al., 2008). However, Ca-Fe-Mg carbonates in the veins suggests lower formation temperatures, below 150^{o}C (e.g., Bridges et al., 2000). The presence of phyllosilicates that precipitated after siderite in Nakhla indicates that temperatures were warm during alteration of olivine, slightly below or approaching 150^{o}C.

An assemblage including Ca-Fe-Mg carbonates in altered veins are thought to represent alteration fluids that were slightly reducing in order to allow for adequate mobility of Fe^{2+} (Chevrier et al., 2007). Smectites, such as nontronite and saponite (identified in this work), are precipitated in reducing conditions with pH above 7 (Chevrier et al., 2007). Iron oxides, such as goethite and hematite, require oxidizing conditions during their formation (e.g., Bridges et al., 2000). The refined mineral assemblage identified in this study suggests that the altering fluids in Nakhla were significantly reduced at first, after which they became oxidized once primary alteration had taken place. Some iron oxide

formation may also have occurred in part due to oxidation of iron-bearing carbonates within veins (e.g., Bridges et al., 2001). Smectites such are known to precipitate at significantly lower pCO_2 conditions than carbonates (closer to ~50 mbar) (Catling, 1999). This reducing-oxidizing transition may have been caused by pulses of aqueous altering fluids persisting in the subsurface rather than extensive, long-lived hydrothermal systems (e.g., Bridges et al., 2001; Changela et al., 2011).

4.3 Implications for Habitability of the Martian Subsurface

In order for metabolic reactions to take place, endolithic microbes such as chemoautolithotrophs require an energy source that can be derived from their rock substrate. This takes the form of an electron donor and acceptor pair through which the microbe can facilitate a preferred transfer of energy from one state to another, typically through some form of disequilibrium within the system (Schulte et al., 2006). Microbial life on Earth is known to utilize numerous and varied metabolic pathways as sources of energy in lithospheric settings (e.g., Benzerara et al., 2009; Colwell et al., 1997; Liu et al., 2012; Jorgensen et al., 2007; Mortimer et al., 1997; Stetter et al., 1990). Some of these are summarized below in Table 4.1. A notable potential source of energy on Mars (supported by the identification in this work of serpentine minerals in Nakhla) is methane produced by serpentinization and its associated products (e.g., Adhikari et al., 2010; Bonch-Osmolovskaya, 2010; Chi Fru, 2009; Stevens et al., 1995; Thomsen et al., 2001).

Potential substrates for metabolic activity are abundant in basaltic rocks colonized by microbes in terrestrial settings (e.g.. Engelen et al., 2008; Peckman et al., 2008; Walton,

2008). For microbes living in basaltic rocks on the Earth, the primary inorganic energy source is iron (e.g., Thorseth et al., 2003). Ferromagnesian minerals and basaltic glass provide excellent substrates for boring and metabolic activity (e.g., Banerjee et al., 2003; 2006; 2008; Furnes et al., 2004; 2009; Eickmann, 2009; Herrera et al., 2009; Muehlenbachs et al., 2009).

Table 4.1: Potential metabolic pathways on Mars (adapted from Boston et al, 1991).

Metabolic Pathway	Relevant Chemical Reaction
Methanogenesis	$CO_2 + 4H_2 \rightarrow CH_4 + 2H_2O$
	$CO + 3H_2 \rightarrow CH_4 + H_2O$
	$4CO + 2H_2O \rightarrow CH_4 + 3CO_2$
Acetogenesis	$2CO_2 + 4H_2 \rightarrow CH_3COOH + 2H_2O$
Sulfate reduction	$H_2SO_4 + 4H_2 \rightarrow H_2S + 4H_2O$
Sulfur reduction	$S^o + H_2 \rightarrow H_2S$
Thionic denitrification	$H_2S + NO_3^- \rightarrow SO_4^{2-} + H_2O$
	$S^o + NO_3^- \rightarrow SO_4^{2-}$
Iron reduction	$2Fe^{3+} + H_2 \rightarrow 2Fe^{2+} + 2H^+$

The reduction and oxidation of iron, as well as similar elements such as manganese, form a significant source of energy for microbes metabolizing the solid phase of basaltic rocks on the Earth (e.g., Amend et al., 2005; Varnes et al., 2003; Weber et al., 2006). Through oxidation and reduction of this iron and the use of CO_2 or O_2 from the environment as an electron acceptor, microorganisms can derive efficient and extensive energy from iron hosted in volcanic minerals and glass (Cockell et al., 2010). The oxidation of iron sulfides is also an extremely effective energy source for endolithic microorganisms (Edwards et al., 2003; Mielke et al., 2003). Olivine and pyroxene can be metabolized directly by some microorganisms in Earth's basaltic environments. *Pseudomonas* sp. HerB uses ferrous

iron from olivine as an electron donor, using O_2 or NO_3^- as an electron acceptor (Popa et al., 2012).

Los Angeles and Zagami contain large amounts of iron, in significant excess to similar terrestrial rocks (Bridges et al., 2006). Los Angeles is the most iron rich Martian meteorite, and therefore represents some of the most iron rich differentiated crustal material sourced from another planetary body currently known (Rubin et al., 2000). Sulfides, oxides and ferromagnesium phases are intergrown with fine-grained textures and extensive mineral interfaces throughout these rocks. Both Los Angeles and Zagami contain patches of mafic glassy material, a large potential source for energy for microbes (e.g., Thorseth et al., 2001; Furnes et al., 2004; Banerjee et al., 2009; Izawa et al., 2010). The presence of iron rich pyroxenes in Los Angeles and Zagami would be an excellent source of energy, as microbes obtaining their energy from ferromagnesian minerals directly rather than from more energetically unstable sources such as glasses have been documented (e.g., Popa et al., 2012). The iron rich sulfides (pyrrhotite) in Los Angeles and Zagami are similarly highly productive energy sources for any potential microbes (e.g., Mielke et al., 2003). Of particular note is the presence of large areas of pyroxferroite breakdown material in Los Angeles. This is composed of small regions of an extremely iron rich phase (fayalite), an intermediately iron rich phase (hedenbergite) and an iron deficient phase (silica) intermixed with each other in close proximity on a small scale.

Nakhla is a unique rock in that it is mineralogically distinct from the typical basalts forming the majority of mafic endolithic habitats on the Earth (as well as the basaltic shergottites), yet its heavy alteration by aqueous fluids makes it among the most attractive

crustal rocks for microbial colonization yet known from Mars (e.g., Haberle et al., 2001). Nakhla is dominantly composed of ferromagnesian mineral phases; in the absence of any (as of yet) clearly defined major methane or hydrogen gas source, the primary energy source for metabolic reactions is likely to be these iron-bearing phases. Olivine in Nakhla is very iron-rich and is heavily fractured with evidence of extensive aqueous activity within these fractures. These heavily-fractured iron-rich olivine grains are likely to be the most attractive substrate within these rocks for microbial colonization due to their interaction with aqueous fluids and easily accessible iron rich material.

The mesostasis in Nakhla has localized enrichments in both Fe/Mg and alkali elements. Despite its low proportions in contrast to the ferromagnesian mineral phases, this glassy and fine grained material is likely to be a major controlling factor on both the localization and extent of any potential biomass to be supported by Nakhla type rocks in the Martian subsurface. The presence of such substrates along with the levels of organic matter reported in Nakhla suggests that this rock would provide all of the necessary components for microbial metabolism in the Martian subsurface (e.g., Jull et al., 2000).

Sulfide minerals in Los Angeles, Zagami, and Nakhla display evidence that post magmatic oxidation occurred following their emplacement in the Martian subsurface (Lorand et al., 2005). The fact that oxidation was energetically favoured during their residence time in the subsurface suggests that these iron rich phases would provide plentiful energy for metabolic reactions.

With the exception of extremely arid and water limited environments (e.g., Navarro-Gonzalez et al., 2003), the limiting factor in most lithospheric microbial habitats appears

to be the aqueous flux and what (if any) sources of energy and nutrients this provides. Los Angeles and Zagami display many extremely attractive characteristics for the colonization of these rocks in the subsurface by any potential microorganisms present on Mars through its history. The presence of liquid water, in addition to all of the other features present in these rocks, may create habitable environmental niches in the subsurface. However, the absence of any evidence of interaction with aqueous fluids during their time in the Martian subsurface suggests that despite any other considerations, the rocks represented by Los Angeles and Zagami were not strictly habitable under these conditions. While microbial communities may persist with periodic wetting by extremely low amounts of water (Bagshaw et al., 2011), the lack of aqueous phases observed in this work suggest that the subsurface horizons sampled by Los Angeles and Zagami likely never interacted with groundwater on Mars.

Nakhla shows extensive evidence of aqueous alteration, and it is likely that mobile fluids were present in the environment into which it was emplaced for a significant period of time. The inorganic components necessary for the support of microbial colonization are all present in the solid phase of Nakhla, and it shares many similarities with basaltic rocks on the Earth that are extensively colonized by microorganisms. However, despite Nakhla's alteration by aqueous fluids, it is clear that the influx of water into this rock was not as extensive as that experienced by environments such as submarine basalts on the Earth. As basaltic rocks are ineffective at retaining fluids when contrasted with materials such as salts or sediments, these environments need a constant influx of water in order to remain aqueously active and provide the necessary conditions for life (Jepsen et al., 2007). Therefore, any organisms surviving in Nakhla-type rocks in the subsurface are

likely to spend much of their time in dormant "maintenance" modes between periods of wetting and active groundwater flow (e.g., Jepsen et al., 2007).

In this study, the fluids that interacted with the subsurface during alteration of Nakhla have been found to be similar to those supporting terrestrial subsurface endolithic communities based on fluid chemistry, pH, pressure, and temperature (e.g., Engelen et al., 2008; Peckman et al., 2008; Walton, 2008; Thorseth et al., 2003). These terrestrial settings are known to be excellent habitats for microbial growth and colonization (e.g., Cockell et al., 2010; Cowen et al., 2003; Engelen et al., 2008). It can be concluded that the aqueous fluids that were present in the rocks represented by the Nakhla meteorite provided adequate energy sources and environmental conditions to support a biosphere of microorganisms similar to those known to inhabit such systems on the Earth. It is unclear whether the nutrient load provided by these aqueous fluids would be adequate to support biological activity, although there is evidence to suggest that it was capable of providing the required organic nutrients (Kate, 2010; Mahaffy et al., 2012).

These aqueous habitable conditions are extremely dependent on the aqueous conditions of the site in question, and are likely to be highly variable on both a local and regional scale. The full spatial and temporal extent and activity of any potential Martian hydrosphere is, at present, unconstrained and poorly understood. These subsurface environments may be habitable if the aqueous conditions are sustained for an adequate period of time to allow for the emergence and survival of microorganisms, or if periods of intense arid conditions are periodically assuaged by frequent wetting from meteoric or groundwater influx.

4.4 Implications for Future Astrobiological Mars Exploration and Applicability to Mars Sample Return

The lack of appreciable water interaction evidenced in the Los Angeles and Zagami meteorites make it difficult to compare them favourably to habitable terrestrial basaltic settings. However, the rocks represented by Los Angeles and Zagami display many characteristics in common with terrestrial lithospheric habitats. This suggests that they have a high habitability potential if aqueous conditions were present in the subsurface where they were emplaced (e.g., Southam et al., 2007b; Veronique et al., 2012). Mineralogical and geochemical evidence reported in this study suggests that Nakhla displays evidence of higher levels of interaction with fluids, but it is unclear whether these aqueous conditions were sustained over a period of time adequate for supporting a microbial colony (should one have arisen over the evolutionary history of Mars).

Although liquid water is unstable at the surface of Mars and no liquid water has yet been definitively observed directly in the subsurface, it is believed that the subsurface of Mars could be a water rich environment (McCoy et al., 2011). These fluids likely take the form of brines that have interacted heavily with the rock through which they flow (Bridges et al., 2012). Deep subsurface hydrothermal fluid systems would likely have been present across much of Mars during its early history. These may have persisted to the present day, although likely on a much smaller scale and perhaps at greater depth (Ehlmann et al., 2011). These hydrothermal systems are likely to have been well preserved at depth on Mars in the rock record (Ehlmann et al., 2011).

Some Martian meteorites show evidence of having been altered by neutral to alkaline brines, and studies have suggested that these fluids may have represented habitable conditions (e.g., Bridges et al., 2012). It can be assumed that on Mars, reasonably similar fluids would have been the most likely candidates for aqueous alteration of rocks like Los Angeles and Zagami in the subsurface. Therefore, subsurface locations on Mars where the conditions include aqueous fluids and basaltic rocks similar to the Los Angeles, Zagami, and Nakhla meteorites would be attractive targets for astrobiological investigation. The geological substrates represented by these meteorites are likely good targets for subsurface exploration, although the hydrological history of the site is a large limiting factor on the possible detection of past habitability or evidence of life.

It has long been thought that both extant and extinct life on Mars are possible and their investigation should be high priority targets for planetary exploration missions (e.g., Davila et al., 2010; Klein, 1996). Many exploration probes, orbiters, landers and rovers have been sent to Mars in the past in an attempt to ascertain evidence of Martian life or to constrain the possibility of a habitable planet. Most recently, NASA's Curiosity rover was sent to Gale Crater on Mars (thought to have undergone extensive aqueous activity in its past) (e.g., Arvidson et al., 2010; Arvidson et al., 2011; Grotzinger et al., 2012; Rossi et al., 2010; Stillman et al., 2011). If life occurs elsewhere in the solar system, there is thought to be a strong chance that it occurs in a deep biosphere far below the planetary surface (Parnell et al., 2010). Life in terrestrial sites that are analogous to Mars is not always detectable on a planetary scale, yet it can be detected when looking in specific niches with enhanced habitability (Davila et al., 2010). Clay minerals, as well as smectites and other Fe-Mg phyllosilicates, are thought to help in the preservation of

organic material, microbial remains, and potential chemical biosignatures (Cady et al., 2003). The aqueous subsurface environment that led to the precipitation of phyllosilicate minerals, as represented by the Nakhla meteorite, is an excellent candidate for the preservation of evidence of biological activity that may have taken place in the past on Mars (e.g., Bridges et al., 2012). Subsurface environments on Mars where igneous rocks interact with aqueous fluids enriched in iron and other energy sources and nutrients are favourable environments for possible microbial activity and a high chance of preservation thereof (e.g., Bridges et al., 2012).

The precise source location of the Martian meteorites, such as an individual impact crater or group of craters, cannot be determined with our limited understanding of impact processes and basins on Mars (McSween, 1994). However, likely source regions can be determined based on the geology of the Martian meteorites and the surface of Mars. Based on their basaltic composition and relatively young crystallization ages, the northern lowlands of Mars are the most likely source region for these rocks (Bridges et al., 2006). Tharsis (as well as similar regions such as Elysium and Amazonis Planitia) is a young volcanic terrane with lava flows of similar age to shergottite crystallization dates and appropriate thickness for the formation of both the basaltic shergottites and the nakhlites (McCoy et al., 1992). The Tharsis Montes region of Mars is therefore thought to be the most probably source region for the shergottites (McCoy et al., 1992).

Tornabene et al. (2006) identified seven large rayed craters on Mars in the Tharsis and Elysium regions. A high velocity was likely required for the ejection of meteorite material from the Martian crust into space (Artemieva et al., 2004); rays, such as those present at

these craters, are physical products of the high velocity imparted to ejecta during impact (Tornabene et al., 2006). Rayed craters in the Tharsis and Elysium regions on Mars are therefore thought to be the most likely source mechanisms for the ejection of the SNC meteorites (Tornabene et al., 2006). As these meteorites show no evidence of alteration by hydrothermal fluids, it is likely that they formed in a region proximal to Tharsis to allow for the emplacement of lava flows but not in a zone of the crust with significant interaction with any subsurface hydrosphere (Ehlmann et al., 2011; Bridges et al., 2006). Settings within the Tharsis terrane showing evidence of hydrothermal alteration by aqueous fluids flowing through the subsurface are the best locations for astrobiological investigation of SNC meteorite-like subsurface rocks.

Rover and orbital exploration of Mars has confirmed that potential host rocks in the form of basaltic flows are abundant in the Tharsis-Elysium region, and volcanism in the area has persisted up to the recent past (e.g., Carr et al., 2010). These rocks are likely to be extremely similar to the Los Angeles and Zagami meteorites in their composition at moderate depth (e.g., Carr, 2006). However, it is unclear to what extent the Martian hydrosphere (if it is active in this region) has interacted with these rocks at depth and near the surface. It is of critical importance to develop the capacity to recognize and identify locations in this region that have interacted with any potential hydrothermal fluids during the evolution of the planet (Arvidson et al., 2010).

It is possible that exploration at great depth may be required in order to discover any relict hydrosphere in the subsurface. The ExoMars mission has been proposed to fly with a small drill to core small samples of regolith soil material, but in order to detect habitable

conditions for endolithic life a larger drill able to collect rock samples from depth will likely be required. Impact craters increase the porosity of their target rocks, and it has been suggested that impacts into crystalline rocks create a good potential habitat for microbial colonization in terrestrial and other planetary settings (Cockell et al., 2004; Pontrefact et al., 2012). Impact craters into Tharsis-aged basaltic lava flow terranes (of which there are many) may also represent attractive astrobiological targets, if there is evidence of hydrothermal or other aqueous activity within them at depth. The identification of surface features indicating potential habitable environments in the subsurface lithosphere, such as hydrothermal mineral deposits and thick basaltic flows, is critical to allow for the effective selection of sites for future exploratory and sample return missions to Mars.

The results from this study show that the Martian meteorites examined here (Los Angeles, Zagami, and Nakhla) represent moderate analogues to similar rocks in terrestrial settings that are known to host microbial communities. The two shergottites show no evidence of interaction with aqueous fluids, and the nakhlite shows evidence of significant interaction with fluids. However, it is unclear how sustained these aqueous conditons were and how extensive the hydrosphere which supported this alteration was in both spatial and temporal range. This suggests that the shergottite class of SNC meteorites do not necessarily represent astrobiologically “interesting” candidate horizons for follow-up life and habitability detection, and that the nakhlites are moderately attractive candidates for these searches. It is possible that other lithologies exist in the Martian subsurface that may have higher likelihoods to host evidence of past or extant life (such as clay rich sediments or carbonate horizons), but these do not appear to have been sampled by meteorite

delivery. However, the results of this study show that endolithic colonization of Martian volcanic rocks is viable under amenable conditions that are conceivable based on the past history of Mars. Therefore, the search for evidence of (past or present) endolithic chemoautolithotrophic life should be considered a priority for astrobiological investigations of Mars. Intense geological and astrobiological scrutiny of all currently held Martian meteorites (particularly the water-rich, highly brecciated NWA 7034) and any samples that may be obtained in the future from Mars will be required to obtain a fuller picture of the potential habitability of subsurface lithological horizons.

Notably, in recent years Mars Sample Return has been proposed as a mission objective for missions in the near future (e.g., McLennan et al., 2011). This study aimed to develop a methodology for the characterization of a Martian rock sample and a preliminary evaluation of the potential habitability of its subsurface source horizon using techniques common to geology departments at universities and institutions around the world. This framework for thorough sample characterization can easily be applied to unknown samples returned from the surface of Mars. It is unlikely that the initial group of rocks returned from Mars will contain definitive evidence of life or habitable conditions, as they will be influenced by engineering and logistical constraints of what can be safely returned to Earth. However, a novel methodological approach to characterization of the potential habitability represented by these samples can be applied to help guide the next phase of surface exploration (and sample return). Studies such as this one, applied to unknown returned samples, can be used to prioritize samples for follow-up and help "vector" future exploration missions towards areas representing high potential for the detection of habitable conditions and evidence of life (or any other mission objectives of interest).

Chapter 5.0 Summary, Conclusions, and Future Studies

5.1 Summary & General Conclusions

Mars has been the subject of much scrutiny in the study of the possible existence of life elsewhere in the universe, and Martian meteorites represent the only samples of the Martian crust directly available for study. Here, a methodology was developed for the evaluation of astrobiologically interesting samples to help guide future exploration work. This was achieved using a variety of techniques widely used in the assessment of geological materials in terrestrial laboratories (including optical microscopy, scanning electron microscopy, *in situ* micro X-Ray diffraction, electron probe microanalysis, and Raman spectroscopy).

This consisted of the mineralogical and geochemical characterization of a suite of Martian meteorites from an astrobiology perspective. Once a thorough reconnaissance study was carried out to characterize the mineral species present in these Martian meteorites, a more in depth investigation of their environmental characteristics and potential habitability could be done. The results from the study of mineral substrates present in the rocks and the alteration conditions that they were exposed to allowed for an evaluation of the potentially habitable environments they represent.

Los Angeles is a coarse-grained basaltic shergottite displaying a subophitic texture. It is more differentiated than most other Martian rocks, found to be composed of 40% large maskelynite regions enclosing 35% coarse-grained pyroxene crystals. Pyroxferrroite

breakdown material is present throughout the meteorite, as a symplectic hedenbergite-fayalite-silica assemblage resulting from the metastable breakdown of an iron-rich pyroxene phase. The Zagami meteorite is a basaltic shergottite. It is fine-grained and less differentiated when contrasted with the Los Angeles meteorite, with an ophitic texture and slight pyroxene foliation. Quenched glassy mesostasis was found in both shergottites, and minor phosphates (merrillite), sulfides (pyrrhotite), and oxides (titanomagnetite with some ilmenite) are present as accessory phases. Nakhla is a clinopyroxenite (nakhlite) displaying a subcumulate texture. The majority of the rock is made up of augite crystals. Olivine, associated mesostasis (glassy and feldspathic), and minor oxides (primarily titanomagentite), sulfides (pyrrhotite), and aqueous secondary minerals are also present in Nakhla.

Micro X-Ray diffraction was shown to be an effective technique for the *in situ* identification of mineral species. It requires minimal sample preparation and does no damage to the sample. It allowed for identification of all major mineral species in these three meteorites. Targeted micro X-Ray diffraction analysis of alteration material in the Nakhla meteorite provided a detailed mineral assemblage present within alteration veins. This material is composed primarily of iron oxides (including goethite and hematite) and smectites (including saponite and nontronite), with some serpentine and the carbonates ankerite and siderite. Targeted *in situ* Raman spectroscopy of Nakhla alteration material was also able to provide information on the mineral assemblage present in altered veins. These spectra allowed for the identification of iron oxides, smectites, and carbonates, confirming the assemblage obtained from μXRD.

EPMA geochemical analyses provided *in situ* compositional information on the mineral phases present in the meteorites with minimal damage to the samples. The major ferromagnesian phase in all three of these meteorites is pyroxene. Augite and pigeonite make up equal proportions of Los Angeles and Zagami, while augite is the pyroxene present in Nakhla. Los Angeles and Zagami have much more variation in their pyroxene composition than Nakhla, showing considerable zoning with iron-rich pyroxene rims. Pyroxferroite in Los Angeles was found to be enriched in iron when compared to the two stable pyroxene phases. Los Angeles is the most iron rich meteorite studied here; the iron content of primary ferromagnesian (pyroxene) phases in Los Angeles (33-39 wt%) were found to be significantly higher than that of Zagami (22-28 wt%), with Nakhla pyroxenes (16 wt%) being iron-poor compared to the two shergottites.

Nakhla contains fayalitic olivine that is significantly enriched in iron content (52 wt%) compared to similar volcanic olivines on Earth, with an average composition of $Fa_{65.5}$. Maskelynite in Los Angeles was found to be slightly more anorthitic than that of Zagami, with both shergottites containing minimal potassium in their feldspathic phases. Pyrrhotite in the shergottites was found to be very iron-rich, with an average composition of $Fe_{0.935}S$. Mesostasis in LA and Zagami is glassy and silicon-rich, while mesostasis in Nakhla is composed of coarse anorthitic feldspar laths and silica-rich glassy material with iron enrichment in some areas.

The alteration mineral assemblage identified here using mineralogical techniques (micro X-Ray diffraction and Raman spectroscopy) differs from previously reported assemblages in Nakhla, by the identification of iron oxides and smectites. This allows for a

reevaluation of the environment of alteration. The assemblage reported here suggests a relatively high Fe/Mg fluid ratio, temperatures of slightly below or approaching 150^{o}C, fluid pCO_2 conditions of >50-100 mbar, and circumneutral fluids pH transitioning from reducing to oxidizing. The presence of siderite and ankerite in the alteration products suggests hydrothermal reworking of carbonates by aqueous fluids.

Endolithic microbes in terrestrial environments require an energy source for metabolism to take place (e.g., Benzerara et al., 2009; Colwell et al., 1997; Liu et al., 2012; Jorgensen et al., 2007; Mortimer et al., 1997; Stetter et al., 1990). Serpentine identified here in Nakhla suggests methane may be a potential energy source. Reduction and oxidation of iron is the major metabolic pathway used by endolithic microorganisms in terrestrial settings (e.g., Thorseth et al., 2003). Los Angeles, Zagami and Nakhla contain large amounts of iron in their primary phases, in significant excess to similar terrestrial rocks (Bridges et al., 2006). Iron-rich sulfides, oxides, and ferromagnesian phases are intergrown with fine-grained textures and extensive mineral interfaces throughout these rocks. These three meteorites also contain patches of mafic glassy material, a large potential source for energy for microbes (e.g., Thorseth et al., 2001; Furnes et al., 2004; Banerjee et al., 2009; Izawa et al., 2010). Olivine in Nakhla is very iron-rich and is heavily fractured with evidence of extensive aqueous activity within fractures.

The limiting factor in most lithospheric microbial habitats appears to be the aqueous flux and what (if any) sources of energy and nutrients this provides. Los Angeles and Zagami show no evidence of interaction with any fluids, while Nakhla displays evidence of interaction with aqueous fluids in the Martian subsurface. These fluids were found to be

similar to those supporting terrestrial subsurface endolithic communities based on fluid chemistry, pH, pressure, and temperature (e.g., Engelen et al., 2008; Peckman et al., 2008; Walton, 2008; Thorseth et al., 2003). This suggests that the subsurface horizons represented by Los Angeles and Zagami would be attractive microbial substrates if aqueous environmental conditions were present, and that Nakhla was a potential substrate for microbial colonization (though the extent of the aqueous hydrosphere at depth is poorly understood).

The results reported here show that iron-rich basaltic rocks (such as the subsurface Martian rocks represented by the Los Angeles, Zagami, and Nakhla meteorites) are attractive astrobiological targets where they occur in settings with evidence of aqueous activity at depth. Rocks in the Tharsis region that have interacted with fluids (such as those in hydrothermal environments) are high priority targets in the search for endolithic basaltic habitats on Mars. This study developed a methodology for investigating Martian rocks with consideration of their potential to act as microbial substrates in the Martian subsurface. This work will help to understand how best to guide future exploration missions on the Martian surface. Studies such as this are critical in preparation for Martian sample return during future exploration to allow for effective sample selection during these missions.

5.2 Suggestions for Future Studies

The instrumental techniques used in this study were provided data that allowed for a thorough characterization of the potential habitability of the crustal rocks represented by a

suite of Martian meteorites. However, these techniques were far from exhaustive. Many other instrumental techniques, commonly used to characterize terrestrial rocks, would provide useful information for such astrobiological characterization of Martian meteorites. Many of these, such as alpha particle X-Ray spectroscopy and stable carbon and oxygen isotopic analyses, have been sent to study Mars directly as part of the instrument package on the Curisoity rover. Others, such as UV-VIS-IR spectroscopy, provide habitability information on Martian rocks that cannot be obtained from the MSL mission.

Future investigations on these samples should focus on an increased understanding of the aqueous vein alteration mineral assemblage in Nakhla. Focused ion beam milling of small samples for analysis by transmitted electron microscopy can be used to provide increased textural and mineralogical information at a fine scale (as has been done by many past workers, including Changela et al. (2011)). Further biological investigation of the similarities between terrestrial bioalteration and the alteration seen in Nakhla, as was done by Fisk et al. (2006), would allow for a fuller understanding of the potential preservation of biosignatures in any materials derived from future Mars sample return missions. In order to obtain a more accurate mineral assemblage within these small fractures (including the absolute proportions of each alteration mineral phase), synchrotron X-Ray diffraction should be carried out; the small beam size of this technique will provide higher precision with which to analyze alteration materials.

It is critical to expand this astrobiological characterization work to all other Martian meteorites currently available to the scientific community. The recently discovered NWA

7034, a volcanic breccia, represents a new type of Martian meteorites. This rock is known to be extremely water-rich and contains diverse clasts, including low-temperature iron oxides (Agee et al., 2013). These qualities make NWA 7034 the most attractive Martian meteorite candidate for further habitability characterization. The chassignites, with their high olivine contents, are also attractive candidates for follow-up investigations similar to those reported here. Similarly, the methodologies for habitability characterization reported here should be expanded to terrestrial samples known to host microbial life, such as samples collected by the integrated ocean drilling program. Such investigations would provide information on the conditions for habitability within known microbial substrates, and can be used as astrobiological control samples on which to test established techniques for potential future Mars sample return.

Many other solar system bodies, such as Europa and Titan, are attractive candidates for future *in situ* astrobiology or sample return missions. Though the volcanic samples studied in this work are not analogous to the surficial materials on those bodies, the methodologies for habitability characterization reported here can be applied to other terrestrial samples (such as sulfates and ice cores) to prepare for the future exploration of the surfaces of these unique astrobiological targets.

Chapter 6.0 References

Adhikari, R.R., Kallmeyer, J., 2010. Detection and quantification of microbial activity in the subsurface. *Chemie der Erde* **70**, 135-143.

Agee, C.B., Wilson, N.V., McCubbin, F.M., Ziegler, K., Polyak, V.J., Sharp, Z.D., Asmerom, Y., Nunn, M.H., Shaheen, R.b, Thiemens, M.H., Steele, A., Fogel, M.L., Bowden, R., Glamoclija, M., Zhang, Z., Elardo, S.M., 2013. Unique meteorite from early Amazonian Mars: Water-rich basaltic breccia Northwest Africa 7034. *Science* **339**, 780-785.

Amend, J.P., Teske, A., 2005. Expanding frontiers in deep subsurface microbiology. *Palaeogeography, Palaeoclimatology, Palaeoecology* **219**, 131-155.

Anthony, J.W., Bideaux, R.A., Bladh, K.W., Nichols, M.C., 1995. Handbook of Mineralogy, Volume II: Silica, Silicates, Part 1. *Mineral Data Publishing*, Tucson, AZ, USA.

Armstrong, J.T., 1995. CITZAFL A package of correction programs for the quantitative electron microbeam X-ray analysis of thick polished materials, thin films, and particles. *Microbeam Analysis* **4**, 177-200.

Artemieva, N., Ivanov, B., 2004. Launch of martian meteorites in oblique impacts. *Icarus* **171**, 84-101.

Arvidson, R.E., Bell II, J.F., Bellutta, P., et al, 2010. Spirit Mars rover mission: Overview and selected results from the northern Home Plate winter haven to the side of Scamander crater. *Journal of Geophysical Research* **115** (E00F03).

Arvidson, R.E., Ashley, J.W., Bell III, J.F., et al, 2011. Opportunity Mars rover mission: Overview and selected results from Purgatory ripple to traverses to Endeavour crater. *Journal of Geophysical Research* **116** (E00F15).

Ashworth, J.R., Hutchison, R., 1975. Water in non-carbonaceous stony meteorites. *Nature* **256**, 714-715.

Bagshaw, E.A., Cockell, C.S., Magan, N., Wadham, J.L., Venugopalan, T., Sun, T., Mowlem, M., Croxford, A.J., 2011. The microbial habitability of weathered volcanic glass inferred from continuous sensing techniques. *Astrobiology* **11** (7), 651-664.

Balme, M., Greeley, R., 2006. Dust devils on Earth and Mars. *Reviews of Geophysics* **44**, RG3003.

Banerjee, N. R., Muehlenbachs, K., 2003. Tuff life: Bioalteration in volcaniclastic rocks from the Ontong Java Plateau, Geochemistry, Geophysics, Geosystems, **4** (4), 1037, doi:10.1029/2002GC000470.

Banerjee, N.R., Furnes, H., Muehlenbachs, K., Staudigel, H., De Wit, M., 2006. Preservation of ~3.4-3.5 Ga microbial biomarkers in pillow lavas and hyaloclastites from the Barberton Greenstone Belt, South Africa. *Earth and Planetary Science Letters* **241**, 707-722.

Banerjee, N.R., Furnes, H., Muehlenbachs, K., Staudigel, H., Mcloughlin, N., Bebout, G, 2008. Biogeochemical tracers of modern and ancient life in seafloor lavas. *Geochimica et Cosmochimica Acta* **71** (2), from 18th Annual V M Goldschmidt Conference (#A51).

Banerjee, N.R., Bridge, N.J., Izawa, M.R.M., Anderson, L.D., Bebout, G.E., Flemming, R.L., 2009. Glassy subaqueous lavas as a habitat for life on Earth, Mars, and elsewhere? *Lunar and Planetary Science Conference XXXII.* Conference abstract #1331.

Banin, A., Clark, B.C., Waenke, H., 1992. Surface Chemistry and Mineralogy, in "Mars", *University of Arizona Press*, Tucson, USA.

Bennett, J., Shostak, S., 2007. Life in the Universe, Second Edition. *Pearson Education, Inc., Addision-Wesley*. San Francisco, CA, USA.

Benzerara, K., Menguy, N., 2009. Looking for traces of life in minerals. *C. R. Palevol* **8**, 617-628.

Bibring, J.-P., Langevin, Y., Mustard, J.F., Poulet, F., Arvidson, R., Gendrin, A., Gondet, B., Mangold, N., the OMEGA Team, 2006. Global mineralogy and aqueous Mars history derived from OMEGA/Mars Express data. *Science* **312**, 400-404.

Blasius, K.R., Cutts, J.A., Guest, J.E., Masursky, H., 1977. Geology of the Valles Marineries: first analysis of imaging from the Viking 1 orbiter primary mission. *Journal of Geophysical Research* **82**, 4067-4091.

Bonch-Osmolovskaya, E.A., 2010. High-temperature deep-subsurface microbial communities as a possible equivalent of ancient ecosystems. *Paleontological Journal* **44** (7), 851-859.

Borg, L.E., Draper, D.S., 2003. A petrogenetic model for the origin and compositional variation of the Martian basaltic meteorites. *Meteoritics & Planetary Science* **38** (12), 1713-1731.

Boston, P.J., Ivanov, M.V., McKay, C.P., 1992. On the possibility of chemosynthetic ecosystems in subsurface habitats on Mars. *Icarus* **95**, 300-308.

Bridges, J.C., Grady, M.M., 2000. Evaporite mineral assemblages in the nakhlite (Martian) meteorites. *Earth and Planetary Science Letters* **176**, 276-279.

Bridges, J.C., Catling, D.C., Saxton, J.M., Swindle, T.D., Lyon, I.C., Grady, M.M., 2001. Alteration assemblages in Martian meteorites: Implications for near-surface processes. *Space Science Reviews* **96**, 365-392.

Bridges, J.C., Warren, P.H., 2006. The SNC meteorites: Basaltic igneous processes on Mars. *Journal of the Geological Society, London* **163**, 229-251.

Bridges, J.C., Schwenzer, S.P., 2012. The nakhlite hydrothermal brine on Mars. *Earth and Planetary Science Letters* **359-360**, 117-123.

Britt, D.T., Consolmagno S.J., G.J., 2003. Stony meteorite porosities and densities: A review of the data through 2001. *Meteoritics & Planetary Science* **38** (8), 1161-1180.

Bunch, T.E., Reid, A.M., 1975. The nakhlites. Part 1: Petrography and mineral chemistry. *Meteoritics* **10**, 303-315.

Cady, S.L., Farmer, J.D., Grotzinger, J.P., Schopf, J.W., Steele, A., 2003. Morphological biosignatures and the search for life on Mars. *Astrobiology* **3** (2), 351-368.

Caldwell, D.R., 2000. Microbial Physiology and Metabolism, Second Edition. *Star Publishing Company*, Belmont, CA, USA.

Cardace, D., Hoehler, T.M., 2009. Serpentinizing fluids craft microbial habitat. *Northeastern Naturalist* **16** (5), 272-284.

Carr, M.H., 1996. "Water on Mars". *Oxford University Press*. New York, USA.

Carr, M.H., 2001. Mars Global Surveyor observations of Martian fretted terrain. *Journal of Geophysical Research* **106**, 23571-23594.

Carr, M.H., 2006. The Surface of Mars. *Cambridge University Press.* Cambridge, UK.

Carr, M.H., Head, J.W., 2010. Geologic history of Mars. *Earth and Planetary Science Letters* **294**, 185-203.

Catling, D.C.,1999. A chemical model for evaporates on early Mars: Possible sedimentary tracers of the early climate and implications for exploration. *Journal of Geophysical Research* **104,** 16453–16469.

Chang, L.L.Y., Howie, R.A., Zussman, J., 1996. Rock-Forming Minerals: Non-silicates: Sulphates, Carbonates, Phosphates, Halides. *Longman Group Limited*. Essex, UK.

Changela, H.G., Bridges, J.C., 2011. Alteration assemblages in the nakhlites: Variation with depth on Mars. *Meteoritics & Planetary Science* **45** (12), 1847-1867.

Chennaoui Aoudjehane, H., Avice, G., Barrat, J.-A., Boudouma, O., Chen, G., Duke, M.J.M., Franchi, I.A>, Gattecceca, J., Grady, M.M., Greenwood, R.C., Herd, C.D.K., Hewins, R., Jambon, A., Marty, B., Rochette, P., Smith, C.L., Sautter, V., Verchovsky, A., Weber, P., Zanda, B., 2012. Tissint Martian meteorite: A fresh look at the interior, surface, and atmosphere of Mars. *Science* **338**, 785-788.

Chevrier, V., Poulet, F., Bibring, J.-P., 2007. Early geochemical environment of Mars as determined from thermodynamics of phyllosilicates. *Nature* **448**, 60-63.

Chi Fru, E., 2009. Iron oxides influence bacterial community structure and the spatial distribution of the aerobic methanotrophs and sulphate reducers in granitic aquifers. *Geomicrobiology Journal* **26**, 415-429.

Clayton, R.N., Onuma, N., Mayeda, T.K., 1976. A classification of meteorites based on oxygen isotopes. *Earth and Planetary Science Letters* **30**, 10-18.

Cockell, C.S., Barlow, N.G., 2002. Impact excavation and the search for subsurface life on Mars. *Icarus* **155**, 340-349.

Cockell, C.S., Osinski, G.R., Lee, P., 2003. The impact crater as a habitat: Effects of impact processing of target materials. *Astrobiology* **3** (1), 181-191.

Cockell, C.S., Raven, J.A., 2004. Zones of photosynthetic potential on Mars and the early Earth. *Icarus* **169**, 300-310.

Cockell, C.S., 2007. Habitability. From "Complete Course in Astrobiology", *WILEY-VCH Verlag GmbH & Co. KGaA,* Weinheim, Germany.

Cockell, C.S., van Calsteren, P., Mosselmans, J.F.W., Franchi, I.A., Gilmour, I., Kelly, L,. Olsson-Francis, K., Johnson, D., JC24 Shipboard scientific party, 2010. Microbial endolithic colonization and the geochemical environment in young seafloor basalts. *Chemical Geology* **279**, 17-30.

Colwell, F.S., Onstott, T.C., Delwiche, M.E., Chandler, D., Fredrickson, J.K., Yao, Q.-J., McKinley, J.P., Boone, D.R., Griffiths, R., Phelps, T.J., Ringelberg, D., White, D.C., LaFreniere, L., Balkwill, D., Lehman, R.M., Konisky, J., Long, P.E., 1997. Microorganisms from deep, high temperature sandstones: Constraints on microbial colonization. *FEMS Microbiology Reviews* **20**, 425-435.

Cowen, J.P., Giovannoni, S.J., Kenig, F., Johnson, H.P., Butterfield, D., Rappe, M.S., Hutnak, M., Lam, P., 2003. Fluids from aging ocean crust that support microbial life. *Science* **299**, 120-123.

Crisp, J., 2004. Volcanoes on Mars: A view from the surface. From "Volcanic worlds: Exploring the solar system's volcanoes. *Praxis Publishing, Ltd.*, Chichester, UK.

Davila, A.F., Skidmore, M., Fairen, A.G., Cockell, C., Schulze-Makuch, D., 2010. New priorities in the robotic exploration of Mars: the case for in situ search for extant life. *Astrobiology* **10** (7), 705-710.

Delvigne, J., Bisdom, E.B.A., Sleeman, J., Stoops, G., 1979. Olivines, their pseudomorphs and secondary products. *Pedologie XXIX* **3**, 247-309.

Delvigne, J., 1998. Atlas of micromorphology of mineral alteration and weathering. *Canadian Mineralogist Special Publication #3*, Mineralogical Association of Canada, Ottawa, 495 pp.

Dohm, J.M., Anderson, R.C., Barlow, N.G., Miyamoto, H., Davies, A.G., Taylor, G.J., Baker, V.R., Boynton, W.V., Keller, J., Kerry, K., Janes, D., Fairen, A.G., Schulze-Makuch, D., Glamoclija, M., Marinangeli, L., Ori, G.G., Strom, R.G., Williams, J.-P., Ferris, J.C., Rodriguez, J.A.P., de Pablo, M.A., Karunatillake, S., 2008. Recent geological and hydrological activity on Mars: The Tharsis/Elysium corridor. *Planetary and Space Science* **56**, 985-1013.

Edwards, K.J., McCollom, T.M., Konishi, H., Buseck, P.R., 2003. Seafloor bioalteration of sulfide minerals: Results from in situ incubation studies. *Geochimica et Cosmochimica Acta* **67** (15), 2843-2856.

Ehlmann, B.L., Mustard, J.F., Murchie, S.L., Bibring, J-P., Meunier, A., Fraeman, A.A., Langevin, Y., 2011. Subsurface water and clay mineral formation during the early history of Mars. *Nature* **479**, 53-60.

Eickmann, B., Bach, W., Kiel, S., Reitner, J., Peckmann, J., 2009. Evidence for cryptoendolithic life in Devonian pillow basalts of Variscan orogens, Germany. *Palaeogeography, Palaeoclimatology, Palaeoecology* **283**, 120-125.

Engelen, B., Zigelmuller, K., Wolf, L., Kopke, B., Gittel, A., Cypionka, H., Treude, T., Nakagawa, S., Inagaki, F., Lever, M.A., Steinsbu, B.O., 2008. Fluids from the oceanic crust support microbial activities within the deep biosphere. *Geomicrobiology Journal* **25**, 56-66.

Ernst, R.E., Grosfils, E.B., Mege, D., 2001. Giant dike swarms: Earth, Venus, and Mars. *Annual Review of Earth and Planetary Sciences* **29**, 489-534.

Eugster, O., Weigel, A., Polnau, E., 1997. Ejection times of Martian meteorites. *Geochimica et Cosmochimica Acta* **61** (13), 2749-2757.

Fairen, A.G., 2010. A cold and wet Mars. *Icarus* **208**, 165-175.

Fisk, M.R., Giovannoni, S.J., 1999. Sources of nutrients and energy for a deep biosphere on Mars. *Journal of Geophysical Research* **104** (E5), 11,805-11,815.

Fisk, M.R., Popa, R., Mason, O.U., Storrie-Lombardi, M.C., Vicenzi, E.P., 2006. Iron-magnesium silicate bioweathering on Earth (and Mars?). *Astrobiology* **6** (1), 48-68.

Flemming, R.L., 2007. Micro X-Ray diffraction (μXRD): A versatile technique for characterization of earth and planetary materials. *Canadian Journal of Earth Sciences* **44** (9), 1333-1346.

Foley, C.N., Wadhwa, M., Borg, L.E., Janney, P.E., Hines, R., Grove, T.L., 2005. The early differentiation history of Mars from ^{182}W-^{142}Nd isotope systematics in the SNC meteorites. *Geochimica et Cosmochimica Acta* **69** (18), 4557-4571.

Formisano, V., Atreya, S., Encrenaz, T., Ignatiev, N., Giuranna, M., 2004. Detection of methane in the atmosphere of Mars. *Science* **306**, 1758-1761.

Friedman-Lentz, R.C., Taylor, G.J., Treiman, A.H., 1999. Formation of a Martian pyroxenite: A comparative study of the nakhlite meteorites and Theo's Flow. *Meteoritics & Planetary Science* **34**, 919–932.

Furnes, H., Banerjee, N.R>, Muehlenbachs, K., Staudigel, H., De Wit, M., 204. Early life recorded in Archean pillow lavas. *Science* **304**, 578-581. science

Furnes, H., Mcloguhlin, N., Staudigel, H., Banerjee, N.R., Fliegel, D., Muehlenbachs, K., Dewit, M., 2009. Pillow lava as microbial habitat for 3.5 billion years: Petrographic signatures of bioalteration. *Geochimica et Cosmochimica Acta* **73** (13), from 19thAnnual V M Goldschmidt Conference (#A404).

Gallagher, C., Balme, M.R., Conway, S.J., Grindrod, P.M., 2011. Sorted clastic stripes, lobes and associated gullies in high-latitude craters on Mars: Landforms indicative of very recent, polycyclic ground-ice thaw and liquid flows. *Icarus* **211**, 458-471.

Ghatan, G.J., Head, J.W., Wilson, L., 2005. Mangala Valles, Mars: assessment of early stages of flooding and downstream flood evolution. *Earth, Moon, Planets* **96**, 1-57.

Gibson, Jr., E.K., McKay, D.S., Thomas-Keprta, K.L., Wentworth, S.J., Westall, F., Steele, A., Romanek, C.S., Bell, M.S., Toporski, J., 2001. Life on mars: Evaluation of the evidence within Martian meteorites ALH84001, Nakhla, and Shergotty. *Precambrian Research* **106**, 15-34.

Glavin, D.P., Bada, J.L., Brinton, K.L.F., McDonald, G.D., 1999. Amino acids in the Martian meteorite Nakhla. *Proceedings of the National Academy of Sciences, USA* **96**, 8835-8838.

Gooding, J.L., Wentworth, S.J., Zolensky, M.E., 1991. Aqueous alteration of the Nakhla meteorite. *Meteoritics* **26**, 135–143.

Grady, M.M., 2000. Catalogue of Meteorites, fifth ed. *Cambridge University Press,* Cambridge, UK. 690 pp.

Grady, M.M., 2007. Astrobiology of the terrestrial planets, with emphasis on Mars. From "Complete Course in Astrobiology", *WILEY-VCH Verlag GmbH & Co. KGaA,* Weinheim, Germany.

Greeley, R., Spudis, P., 1981. Volcanism on Mars. *Reviews of Geophysics and Space Physics* **19**, 13-41.

Grotzinger, J.P., Crisp, J., Vasavada, A.R., et al, 2012. Mars Science Laboratory Mission and Science Investigation. *Space Science Reviews* **170**, 5-56.

Haberle, R.M., McKay, C.P., Schaeffer, J., Cabrol, N.A., Grin, E.A., Zent, A.P., Quinn, R., 2001. On the possibility of liquid water on present-day Mars. *Journal of Geophysical Research* **106** (E10), 23,317-23,326.

Hanesch, M., 2009. Raman spectroscopy of iron oxides and (oxy)hydroxides at low laser power and possible applications in environmental magnetic studies. *Geophysical Journal International* **177**, 941-948.

Harrison, K.P., Chapman, M.G., 2008. Evidence for ponding and catastrophic floods in central Valles Marineries, Mars. *Icarus* **198**, 351-364.

Hartmann, W.K., Neukum, G., 2001. Cratering chronology and the evolution of Mars. *Space Science Reviews* **96**, 165-194.

Harvey, R.P., McSween Jr., H.Y., 1992. The petrogenesis of the nakhlites: Evidence from cumulate mineral zoning. *Geochimica et Cosmochimica Acta* **56**, 1655–1663.

Hauber, E., van Gasselt, S., Ivanov, B., Werner, S., Head, J.W., Neukum, G., Jaumann, R., Greeley, R., Mitchell, K.L., Muller, P., 2005. Discovery of a flank caldera and very young glacial activity at Hecates Tholus, Mars. *Nature* **434**, 356-361.

Herd, C.D.K., 2008. Basalts as probes of planetary interior redox state. *Reviews in Mineralogy & Geochemistry* **68**, 527-553.

Herrera, A., Cockell, C.S., Self, S., Blaxter, M., Reitner, J., Thorsteinsson, T., Arp, G., Drose, W., Tindle, A.G., 2009. A cryptoendolithic community in volcanic glass. *Astrobiology* **9** (4), 369-381.

Herut, B., Starinsky, A., Katz, A., and Bein, A., 1990. The role of seawater freezing in the formation of subsurface brines', *Geochimica et Cosmochimica Acta* **54,** 13–21.
Hoehler T.M., 2007. An energy balance concept for habitability. *Astrobiology* **7,** 824–838.

Hovius, N., Lea-Cox, A., Turowski, J.M., 2008. Recent volcano-ice interaction and outburst flooding in a Mars polar cap re-entrant. *Icarus* **197**, 24-38.

Izawa, M.R.M., Banerjee, N.R., Flemming, R.L., Bridge, N.J., Schultz, C., 2010. Basaltic glass as a habitat for microbial life: Implications for astrobiology and planetary exploration. *Planetary and Space Science* **58** (4), 583-591.

Jakosky, B.M., Westall, F., Brack, A., 2007. Mars. From "Planets and Life: The Emerging Science of Astrobiology", *Cambridge University Press,* Cambridge, UK.

Janecky, D.R., Seyfried, Jr., W.E., 1986. Hydrothermal serpentinization of peridotite within the oceanic crust: Experimental investigations of mineralogy and major element chemistry. *Geochimica et Cosmochimica Acta* **50**, 1357-1378.

Jarosewich, 2002. Smithsonian microbeam standards. *Journal of Research of the National Institute of Standards and Technology* **107** (6), 681-685.

Jepsen, S.M., Priscu, J.C., Grimm, R.E., Bullock, M.A., 2007. The potential for lithoautotrophic life on Mars: Application to shallow interfacial water environments. *Astrobiology* **7** (2), 342-354.

Johnson, C.L., Phillips, R.J., 2005. Evolution of the Tharsis region of Mars: Insights from magnetic field observations. *Earth and Planetary Science Letters* **230**, 241-254.

Jorgensen, B.B., Boetius, A., 2007. Feast and famine – microbial life in the deep-sea bed. *Nature Reviews Microbiology* **5**, 770-781.

Jull, A.J.T., Beck, J.W., Burr, G.S., 2000. Isotopic evidence for extraterrestrial organic material in the Martian meteorite, Nakhla. *Geochimica et Cosmochimica Acta* **64** (21), 3763-3772.

Kasting, J.F., 1991. CO_2 condensation and the climate of early Mars. *Icarus* **94**, 1-13.

Kate, I.L., 2010. Organics on Mars? *Astrobiology* **10** (6), 589-603.

Kerney, K.R., Schuerger, A.C., 2011. Survival of *Bacillus subtilis* endospores on ultraviolet-irradiated rover wheels and Mars regolith under simulated Martian conditions. *Astrobiology* **11** (5), 477-485.

Klein, H.P., 1996. On the search for extant life on Mars. *Icarus* **120**, 431-436.

Lang, N.P., Tornabene, L.L., McSween, Jr., H.Y., Christensen, P.R., 2009. Tharsis-sourced relatively dust-free lavas and their possible relationship to Martian meteorites. *Journal of Volcanology and Geothermal Research* **185**, 103-115.

Lehto, K., 2007. From molecular evolution to cellular life. From "Complete Course in Astrobiology", *WILEY-VCH Verlag GmbH & Co. KGaA,* Weinheim, Germany.

Lentz, R.C.F., McSween, Jr., H.Y., 2000. Crystallization of the basaltic shergottites: Insights from crystal size distribution (CSD) analysis of pyroxenes. *Meteoritics & Planetary Science* **35**, 919-927.

Leshin, L.A., Vicenzi, E., 2006. Aqueous processes recorded by Martian meteorites: Analyzing Martian water on Earth. *Elements* **2**, 157-162.

Liu, D., Dong, H., Bishop, M.E., Zhang, J., Wang, H., Xie, S., Wang, S., Huang, L., Eberl, D.D., 2012. Microbial reduction of structural iron in interstratified illite-smectite

minerals by a sulfate-reducing bacterium. *Geobiology* **10**, 150-162.

Lorand, J.-P., Chevrier, V., Sautter, V., 2005. Sulfide mineralogy and redox conditions in some shergottites. *Meteoritics & Planetary Science* **40** (8), 1257-1272.

Lunine, J.L., 2005. Astrobiology: A Multidisciplinary Approach. *Pearson Addison Wesley*, San Francisco, CA, USA.

Machel, H.G., 2004. Concepts and models of dolomitization: A critical reappraisal. *Geological Society, London, Special Publications* **235**, 7-63.

Macke, R.J., Britt, D.T., Consolmagno, G.J., 2011. Density, porosity, and magnetic susceptibility of achondritic meteorites. *Meteoritics & Planetary Science* **46** (2), 311-326.

Mahaffy, P.R., Webster, C.R., Cabane, M., et al, 2012. The Sample Analysis at Mars investigation and instrument suite. *Space Science Reviews* **170**, 401-478.

Malin, M.C., Edgett, K.S., 2001. Mars Global Surveyor Mars Orbiter Camera: interplanetary cruise through primary mission. *Journal of Geophysical Research* **106**, 23429-23570.

Mangold, N., 2012. Fluvial landforms on fresh impact ejecta on Mars. *Planetary and Space Science* **62**, 69-85.

Marquez, A., Fernandez, C., Anguita, F., Farelo, A., Anguita, J., de la Casa, M.-A., 2004. New evidence for a volcanically, tectonically, and climatically active Mars. *Icarus* **172**, 573-581.

Marinova, M.M., Aharonson, O., Asphaug, E., 2008. Mega-impact formation of the Mars hemispheric dichotomy. *Nature* **453**, 1216-1219.

Martel, J., Young, D., Peng, H.-H, Wu, C.-Y., Young, J.D., 2012. Biomimetic properties of minerals and the search for life in the Martian meteorite ALH84001. *Annual Revieww of Earth & Planetary Sciences* **40**, 167-193.

Marti, K., Kim, J.S., Thakur, A.N., McCoy, T.J., Keil, K., 1995. Signatures of the Martian atmosphere in glass of the Zagami meteorite. *Science* **267**, 1981-1984.

McBride, K.M., Righter, K., 2011. The 100th anniversary of the fall of Nakhla: The subdivision of BM1913,25. Abstract No. 5179, *74th Annual Meteoritical Society Meeting*, London, England, UK.

McCoy, T.J., Taylor, G.J., Keil, K., 1992. Zagami: Product of a two-stage magmatic history. *Geochimica et Cosmochimica Acta* **57**, 3571-3582.

McCoy, T.J., Wadhwa, M., Keil, K., 1999. New lithologies in the Zagami meteorite: Evidence for fractional crystallization of a single magma unit on Mars. *Geochmica et Cosmochimica Acta* **63** (7/8), 1249-1262.

McCoy, T.J., Corrigan, C.M., Herd, C.D.K., 2011. Combining meteorites and missions to explore Mars. *Proceedings of the National Academy of Sciences* **108** (48), 19159-19164.

McKay, C.P., 1986. Exobiology and future Mars missions: The search for Mars' earliest biosphere. *Advances in Space Research* **6** (12), 269-185.

McKay, D.S., Gibson, Jr., E.K., Thomas-Keprta, K.L., Vali, H., Romanek, C.S., Clemett, S.J., Chillier, X.D.F., Maechling, C.R., Zare, R.N., 1996. Search for past life on Mars: Possible relic biogenic activity in Martian meteorite ALH84001. *Science* **273** (5277), 924-930.

McKay, D.S., Wentworth, S.J., Longazo, T.G., Thomas-Keprta, K., Gibson, E.K., 2001. Textures of secondary alteration zones in Nakhla. *Lunar and Planetary Science Conference XXXII.* Conference abstract #2040.

McLennan, S.M., Sephton, M.A., Allen, C., Allwood, A.C., Barbieri, R., Beaty, D.W., Boston, P., Carr, M., Grady, M., Grant, J., Heber, V.S., Herd, C.D.K., Hofmann, B., King, P., Mangold, N., Ori, G.G., Rossi, A.P., Raulin, F., Ruff, S.W., Sherwood Lollar, B., Symes, S., and Wilson, M.G., 2011. Planning for Mars returned sample science: Final report of the MSR End-to-End International Science Analysis Group (E2E-iSAG). *Astrobiology* **12**, 175–230.

McSween, Jr., H.Y., 1984. SNC meteorites: Are they Martian rocks? *Geology* **12**, 3-6.

McSween, Jr., H.Y., 1989. Achondrites and igneous processes on asteroids. *Annual Review of Earth and Planetary Sciences* **17**, 119-140.

McSween, Jr., H.Y., 1994. What we have learned about Mars from SNC meteorites. *Meteoritics* **29**, 757-779.

McSween, Jr., H.Y., 2002. The rocks of Mars. *Meteoritics & Planetary Science* **37**, 7-25.

McSween, Jr., H.Y., Huss, G.R., 2010. Cosmochemistry: Probing the origin and chemical evolution of the solar system, 1st Ed. *University Press,* Cambridge, UK.

McSween, Jr., H.Y., Mittlefehldt, D.W., Beck, A.W., Mayne, R.G., McCoy, T.J., 2011. HED meteorites and their relationship to the geology of Vesta and the Dawn mission. *Space Science Reviews* **163**, 141-174.

Mielke, R.E., Pace, D.L., Porter, T., Southam, G., 2003. A critical stage in the formation of acid mine drainage: colonization of pyrite by *Acidithiobacillus ferrooxidans* under pH-neutral conditions. *Geobiology* **1**, 81-90.

Ming, D.W., Morris, R.V., Clark, B.C., 2008. Aqueous Alteration on Mars. From "They: Composition, Mineralogy, and Physical Properties. *Cambridge University Press*, Cambridge, UK.

Mohlmann, 2005. Adsorption water-related potential chemical and biological processes in the upper Martian surface. *Astrobiology* **5** (6), 770-777.

Mortimer, R.J.G., Coleman, M.L., 1997. Microbial influence on the oxygen isotopic composition of diagenetic siderite. *Geochimica et Cosmochimica Acta* **61** (8), 1705-1711.

Muehlenbachs, K., Furnes, H., De Wit, M., 2009. Thermophile inhabitants of the Archean seafloor basalts. *Geochimica et Cosmochimica Acta* **73** (13), from 19thAnnual V M Goldschmidt Conference (#A911).

Mumma, M.J., Villanueva, G.L., Novak, R.E., Hewagama, T., Bonev, B.P., DiSanti, M.A., Mandell, A.M., Smith, M.D., 2009. Strong release of methane on Mars in Northern Summer 2003. *Science* **323**, 1041-1045.

Mustard, J.F., Poulet, F., Head, J.W., Mangold, N., Bibring, J.-P., Pelkey, S.M., Fassett, C.L., Langevin, Y., Neukum, G., 2007. Mineralogy of Nili Fossae region with OMEGA/Mars Express data: 1. Ancient impact melt in the Isidis Basin and implcations for the transition from the Noachian to Hesperian. *Journal of Geophysical Research* **112**, E08S03.

Navarro-Gonzalez, R., Rainey, F.A., Molina, P., Bagaley, D.R., Hollen, B.J., de la Rosa, J., Small, A.M., Quinn, R.C., Grunthaner, F.J., Caceres, L., Gomez-Silva, B., McKay, C.P., 2003. Mars-like soils in the Atacama desert, Chile, and the dry limit of microbial life. *Science* **302**, 1018-1021.

Nelson, M.J., Newsom, H.E., Draper, D.S., 2005. Incipient hydrothermal alteration of basalts and the origin of martian soil. *Geochimica et Cosmochimica Acta,* **69** (10), 2701-2711.

Neumann, G.A., Zuber, M.T., Wieczorek, M.A., McGovern, P.J., Lemoine, F.G., Smith, D.E., 2004. Crustal structure of Mars from gravity and topography. *Journal of Geophysical Research* **109**, E08002.

Newsom, H.E., Hagerty, J.J., 1997. Chemical components of the Martian soil: Melt degassing, hydrothermal alteration, and chondritic debris. *Journal of Geophysical Research* **102**, 19345-19355.

Newsom, H.E., 2005. Clays in the history of Mars. *Nature* **438**, 570-571.

Nyquist, L.E., Bogard, D.D., Shih, C.-Y., Greshake, A., Stoffler, D., Eugster, O., 2001. Ages and geologic histories of Martian meteorites. *Chronology and Evolution of Mars* **96**, 105-164.

Osinski, G.R., Spray, J.G., Lee, P., 2001. Impact-induced hydrothermal activity within the Haughton impact structure, arctic Canada: Generation of a transient, warm, wet oasis. *Meteoritics & Planetary Science* **36**, 731-745.

Osinski, G.R., 2005. Hydrothermal activity associated with the Ries impact event, Germany. *Geofluids* **5**, 202-220.

Osinski, G.R., Tornabene, L.L., Banerjee, N.R., Cockell, C.S., Flemming, R., Izawa, M.R.M., McCutcheon, J., Parnell, J., Preston, L.J., Pickersgill, A.E., Pontefract, A., Sapers, H.M., Southam, G., 2013. Impact-generated hydrothermal systems on Earth and Mars. *Icarus* **224**, 347-363.

Papike, J.J., Karner, J.M., Shearer, C.K., Burger, P.V., 2009. Silicate mineralogy of martian meteorites. *Geochimica et Cosmochimica Acta* **73**, 7443-7485.

Parnell, J, Boyce, A.J., Blamey, N.J.F., 2010. Follow the methane: The search for a deep biosphere, and the case for sampling serpentinites, on Mars. *International Journal of Astrobiology* **9** (4), 193-200.

Pavlov, A.K., Shelegedin, V.N., Vdovina, M.A., Pavlov, A.A., 2010. Growth of microorganisms in Martian-like shallow subsurface conditions: Laboratory modelling. *International Journal of Astrobiology* **9** (1), 51-58.

Peckmann, J., Bach, W., Behrens, K., Reitner, J., 2008. Putative cryptoendolithic life in Devonian pillow basalt, Rheinisches Schiefergebirge, Germany. *Geobiology* **6**, 125-135.

Pederson, K., 2000. Exploration of deep intraterrestrial microbial life: Current perspectives. *FEMS Microbiology Letters* **185**, 9-16.

Phillips, R.J., Zuber, M.T., Solomon, S.C., Golombek, M.P., Jakosky, B.M., Banerdt, W.B., Smith, D.E., Williams, R.M., Hynek, B.M., Aharonson, O., Hauck II, S.A., 2001. Ancient geodynamics and global scale hydrology on Mars. *Science* **291**, 2587-2591.

Platz, T., Michael, G., 2011. Eruption history of the Elysium Volcanic Province, Mars. *Earth and Planetary Science Letters* **312**, 140-151.

Popa, Ra., Smith, A.R., Popa, Ro, Boone, J., Fisk, M., 2012. Olivine-respiring bacteria isolated from the rock-ice interface in a lava-tube cave, a Mars analog environment. *Astrobiology* **12** (1), 9-18.

Reith, F., 2011. Life in the deep subsurface. *Geology* **39** (3), 287-288.

Robbins, S.J., Di Achille, G., Hynek, B.M., 2011. The volcanic history of Mars; High-resolution crater-based studies of the calders of 20 volcanoes. *Icarus* **211**, 1179-1203.

Ross, K.A., Fisher, R.V., 1986. Biogenic grooving on glass shards. *Geology* **14** (7), 571-573.

Rossi, A.P., van Gesselt, S., 2010. Geology of Mars after the first 40 years of exploration. *Research in Astronomy and Astrophysics* **10** (7), 621-652.

Rost, D., Stephan, T., Greshake, A., Fritz, J., Weber, I., Jessberger, E.K., Stoffler, D., 2009. A combined ToF-SIMS and EMP/SEM study of a three-phase symplectite in the Los Angeles basaltic shergottite. *Meteoritics & Planetary Science* **44** (8), 1225-1237.

Rubin, A.E., Warren, P.H., Greenwood, J.P., Verish, R.S., Leshin, L.A., Hervig, R.L., Clayton, R.N., 2000. Los Angeles: The most differentiated basaltic martian meteorite. *Geology* **28** (11), 1011-1014.

Rull, F., Martinez-Frias, J., Sansano, A., Medina, J., Edwards, H.G.M., 2004. Comparative micro-Raman study of the Nakhla and Vaca Muerta meteorites. *Journal of Raman Spectroscopy* **35**, 497-503.

Schulte, M., Blake, D., Hoehler, T., McCollom, T., 2006. Serpentinization and its implications for life on the early Earth and Mars. *Astrobiology* **6** (2), 364-376.

Schulze-Makuch, D., Fairen, A.G., Davila, A.F., 2008. The case for life on Mars. *International Journal of Astrobiology* **7** (2), 117-141.

Scott, D.H., Carr, M.H., 1978. Geologic map of Mars. *U.S. Geological Survey Misc. Inv.*, Map I-1083.

Scott, D.H., Tanaka, K.L., 1981. Mars: Paleostratigraphic resoration of buried surfaces in Tharsis Montes. *Icarus* **45**, 304-319.

Scott, E.R.D., Wasson, J.T., 1975. Classification and properties of iron meteorites. *Reviews of Geophysics and Space Physics* **13** (4), 527-546.

Sephton, M.A., Wright, I.P., Gilmour, I., de Leeuw, J.W., Grady, M.M., Pinninger, C.T., 2002. High molecular weight organic matter in martian meteorites. *Planetary and Space Science* **50**, 711-716.

Shock, E.L., Schulte, M.D., 1998. Hydrothermal systems as locations of organic synthesis on the early Earth and Mars. *Journal of Geophysical Research*.

Shock, E.L., 2009. Minerals as energy sources for microorganisms. *Economic Geology* **104**, 1235-1248.

Smith, K.L., Milnes, A.R., Eggleton, R.A., 1987. Weathering of basalt: formation of iddingsite. *Clays & Clay Mineralogy* **35**, 418–428.

Staudigel, H., Yayanos, A., Chastain, R., Davis, G., Verdurmen, E.A.Th., Schiffman, P., Bourcier, R., De Baar, H., 1998. Biologically mediated dissolution of volcanic glass in seawater. *Earth and Planetary Science Letters* **164**, 233-244.

Staudigel, H., Furnes, H., McLoughlin, N., Banerjee, N.R., Connell, L.B., Templeton, A., 2008. 3.5 billion years of glass bioalteration: Volcanic rocks as a basis for microbial life? *Earth-Science Reviews* **89**, 156-176.

Stillman, D.E., Grimm, R.E., 2011. Dielectric signatures of adsorbed and salty liquid water at the Phoenix landing site, Mars. *Journal of Geophysical Research* **116**, E09005.

Southam, G., Rothschild, L.J., Westall, F., 2007a. The geology and habitability of terrestrial planets: Fundamental requirements for life. *Space Science Reviews* **129**, 7-34.

Southam, G., Westall, F., 2007b. Geology, life and habitability, *Treatise on Geophysics: Planets and Moons* **10,** 421–438.

Squyres, S.W., Kasting, J.F., 1994. Early Mars: How warm and how wet? *Science* **265**, 744-749.

Stan-Lotter, H., 2007. Extremophiles, the physicochemical limits of life (growth and survival). From "Complete Course in Astrobiology", *WILEY-VCH Verlag GmbH & Co. KGaA,* Weinheim, Germany.

Stetter, K.O., Fiala, G., Huber, G., Huber, R., Segerer, A., 1990. Hyperthermophilic microorganisms. *FEMS Microbiology Reviews* **75**, 117-124.

Stevens, T.O and McKinley, J.P., 1995. Lithoautotrophic microbial ecosystems in deep basalt aquifers. *Science* **270** (5235), 450–454.

Stillman, D.E., Grimm, R.E>, 2011. Dielectric signatures of adsorbed and salty liquid water at the Phoenix landing site, Mars. *Journal of Geophysical Research* **116**, E09005.

Szymanski, A., Brenker, F.E., Palme, H., El Goresy, A., 2010. High oxidation state during formation of Martian nakhlites. *Meteoritics & Planetary Science* **45** (1), 21-31.

Taylor, G.J., McLennan, S.M., McSween, Jr., H.Y., Wyatt, M.B., Lentz, R.C.F., 2008. Implications of observed primary lithologies. From "The: Composition, Mineralogy, and Physical Properties. *Cambridge University Press*, Cambridge, UK.

Taylor, S.R., McLennan, S.M., 2009. *Planetary Crusts: Their Composition, Origin and Evolution.* Cambridge University Press, Cambridge, UK.

Thomas, D.J., Schimel, J.P., 1991. Mars after the Viking missions: Is life still possible? *Icarus* **91**, 199-206.

Thomsen, T.R., Finster, K., Ramsing, N.B., 2001. Biogeochemical and molecular signatures of anaerobic methane oxidation in a marine sediment. *Applied and Environmental Microbiology* **67** (4), 1646-1656.

Thorseth, I.H., Furnes, H., Heldal, M., 1992. The importance of microbiological activity in the alteration of natural basaltic glass. *Geochimica et Cosmochimica Acta* **56**, 845-850.

Thorseth, I.H., Torsvik, T., Torsvik, V., Daae, F.L., Pederson, R.B., Keldysh-98 Scientific Party, 2001. Diversity of life in ocean floor basalt. *Earth and Planetary Science Letters* **194**, 31-37.

Thorseth, I.H., Pederson, R.B., Christie, D.M., 2003. Microbial alteration of 0-30-Ma seafloor and sub-seafloor basaltic glasses from the Australian Antarctic Discordance. *Earth and Planetary Science Letters* **215**, 237-247.

Tornabene, L.L., Moersch, J.E., McSween, Jr., H.Y., McEwen, A.S., Piatek, J.L., Milam, K.A., Christensen, P.R., 2006. Identification of large (2-10 km) rayed craters on Mars in THEMIS thermal infrared images: Implications for possible Martian meteorite source regions. *Journal of Geophysics Research* **111**, E10006.

Tosca, N.J., Milliken, R.E., Michel, F.M., 2008. Smectite formation on early Mars: Experimental constraints. Abstract #7030 at *LPI Workshop on Martian Phyllosilicates: Recorders of Aqueous Processes*. Lunar and Planetary Institute, Houston, USA.

Treiman, A.H., Barrett, R.A., Gooding, J.L., 1993. Preterrestrial aqueous alteration of the Lafayette (SNC) meteorite. *Meteoritics* **28**, 86-97.

Treiman, A.H., 2003. Submicron magnetite grains and carbon compounds in Martian meteorite ALH84001: Inorganic, abiotic formation by shock and thermal metamorphism. *Astrobiology* **3** (1), 369-392.

Treiman, A.H., 2005. The nakhlite meteorites: Augite-rich igneous rocks from Mars. *Chemie der Erde* **65**, 203–270.

Varnes, E.S., Jakosky, B.M., McCollom, T.M., 2003. Biological potential of Martian hydrothermal systems. *Astrobiology* **3** (2), 407-414.

Veronique, D., Doris, B., Phillippe, C., Vinciane, D., Johan, D.K., Emmanuelle, J., Steven, G., Ozgur, K., Tilman, S., Carine, V.A., Frank, V., Tim, V.H., Valerie, W., 2012. From meteorites to evolution and habitability of planets. *Planetary and Space Science* **72**, 3-17.

Vickery, A.M., Melosh, H.J., 1983. The origin of SNC meteorites: An alternative to Mars. *Icarus* **56**, 299-318.

Walton, A.W., 2008. Microtubules in basalt glass from Hawaii Scientific Drilling Project #2 phase 1 core and Hilina slope, Hawaii: Evidence of the occurrence and behavior of endolithic microorganisms. *Geobiology* **6**, 351-364.

Warren, J., 2000. Dolomite: Occurrence, evolution and economically important associations. *Earth-Science Reviews* **52**, 1-81.

Warren, P.H., Greenwood, J.P., Rubin, A.E., 2004. Los Angeles: A tale of two stones. *Meteoritics & Planetary Science* **39** (1), 137-156.

Watters, T.R., 2004. Elastic dislocation modeling of wrinkle ridges on Mars. *Icarus* **171**, 284-294.

Weber, K.A., Achenbach, L.A., Coates, J.D., 2006. Microorganisms pumping iron: Anaerobic microbial iron oxidation and reduction. *Nature Reviews Microbiology* **4**, 752-764.

Weisberg, M.K., McCoy, T.J., Krot, A.N., 2006. Systematics and evaluation of meteorite classification, in Meteoritics and the Early Solar System II. *University of Arizona Press*, Tucson, AZ, USA.

Werner, S.C., 2009. The global martian volcanic evolutionary history. *Icarus* **201**, 44-68.

Werner, S.C., Tanaka, K.L., Skinner, Jr., J.A., 2011. Mars: The evolutionary history of the northern lowlands based on crater counting and geologic mapping. *Planetary and Space Science* **59**, 1143-1165.

Westall, F., 2008. Morphological biosignatures in early terrestrial and extraterrestrial materials. *Space Science Reviews* **135**, 95-114.

Williams, D.A., Greeley, R., Fergason, R.L., Kuzmin, R., McCord, T.B., Combe, J.-P., Head, J.W., Xiao, L., Manfredi, L., Poulet, F., Pinet, P., Baratoux, D., Plaut, J.J., Raitala, J., Neukum, G., HRSC Co-I Team, 2009. The circum-Hellas volcanic province, Mars: Overview. *Planetary and Space Science* **57**, 895-916.

Winter, J.D., 2001. An Introduction to Igneous and Metamorphic Petrology. *Prentice-Hall, Inc.* New Jersey, USA.

Wise, D.U., Golombeck, M.P., McGill, G.E., 1979. Tharsis province of Mars: Geologic sequence, geometry, and a deformation mechanism. *Icarus* **38**, 456-472.

Xirouchakis, D., Draper, D.S., Schwandt, C.S., Lanzirotti, A., 2002. Crystallization conditions of Los Angeles, a basaltic Martian meteorite. *Geochimica et Cosmochimica Acta* **66** (10), 1867-1880.

Appendix A: Sample XRD Patterns

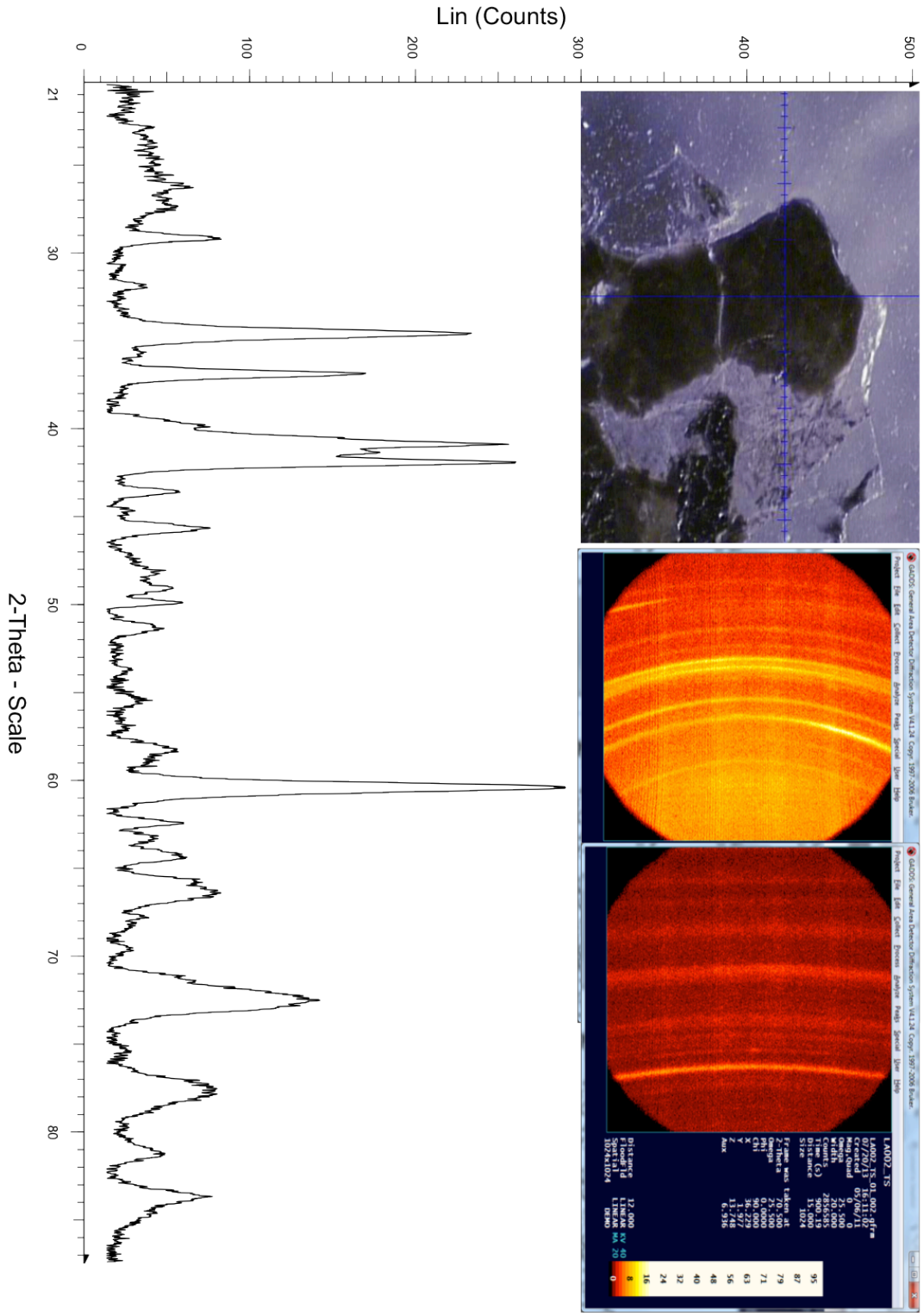

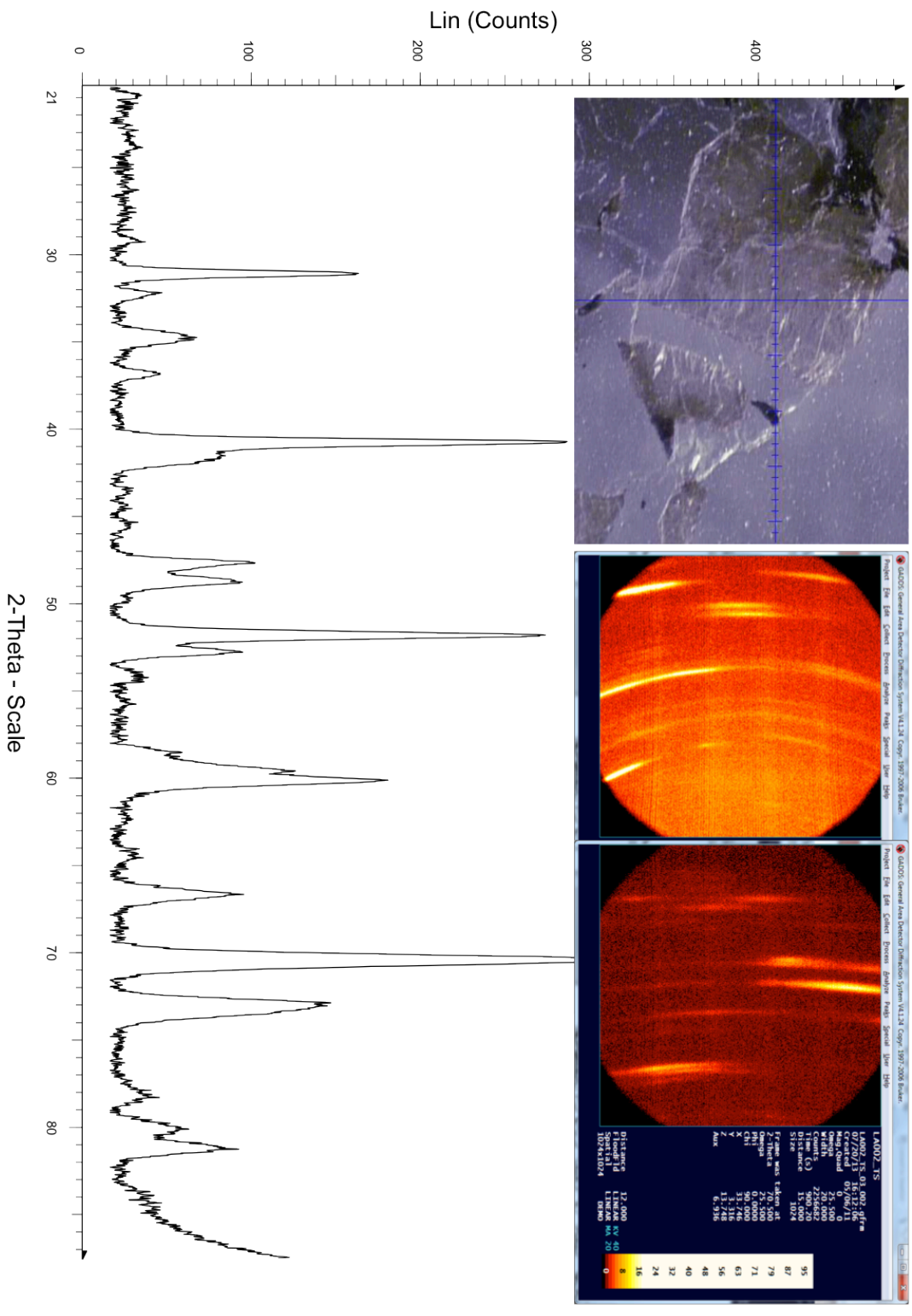
LA002_TS_03
Lin (Counts)
2-Theta - Scale

LA002_TS_07

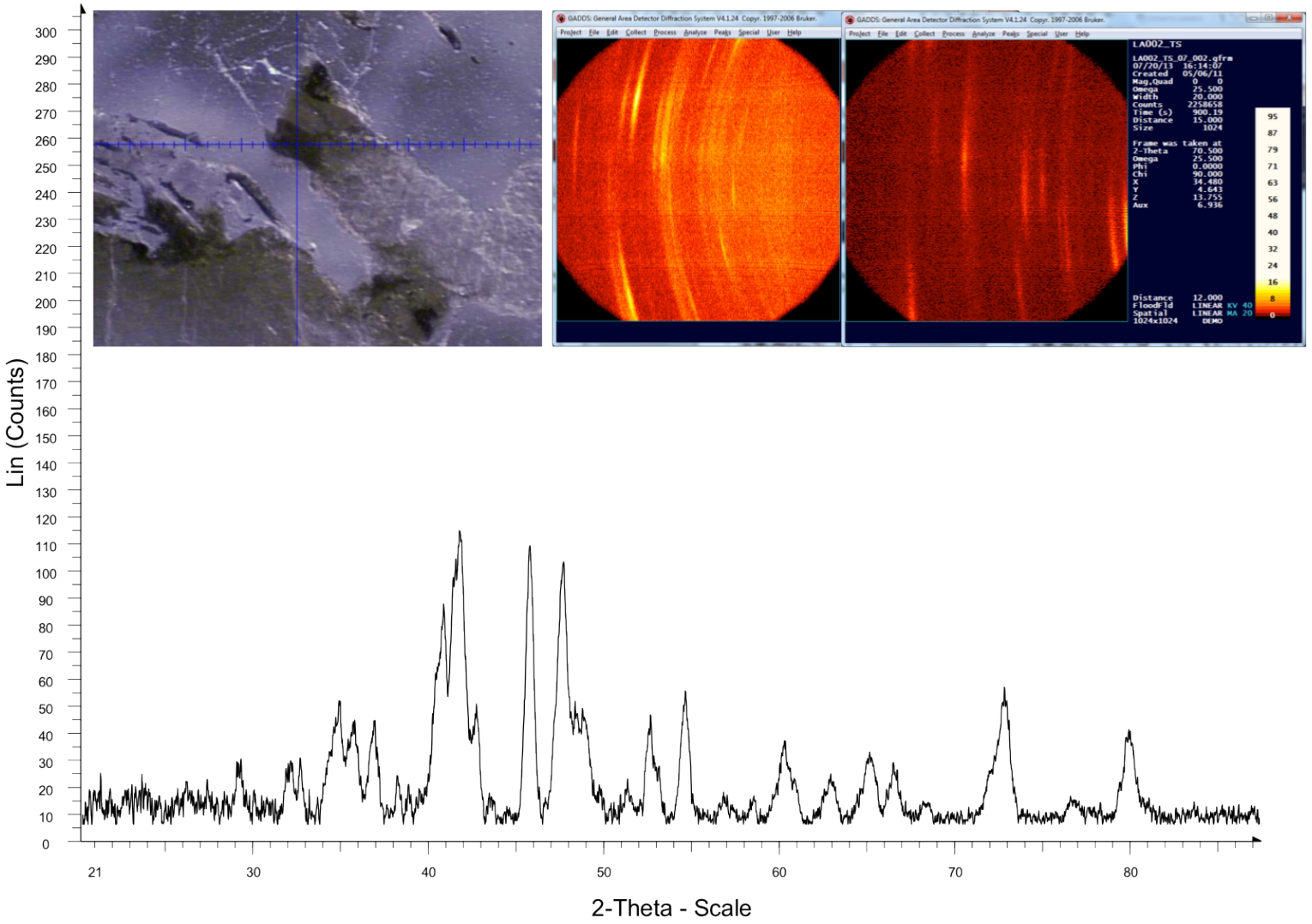
Lin (Counts)
2-Theta - Scale
0
10
20
30
40
50
60
70
80
90
100
110
120
130
140
150
160
170
180
190
200
210
220
230
240
250
260
270
280
290
300
21
30
40
50
60
70
80
LA002_TS
LA002_TS_07_002.gfrm
07/20/13 16:14:07
Created 05/06/11
Mag,Quad 0 0
Omega 25.500
Width 20.000
Counts 2258658
Time (s) 900.19
Distance 15.000
Size 1024
Frame was taken at
2-Theta 70.500
Omega 25.500
Phi 0.0000
Chi 90.000
X 34.480
Y 4.643
Z 13.755
Aux 6.936
Distance 12.000
FloodFld LINEAR KV 40
Spatial LINEAR MA 20
1024x1024 DEMO

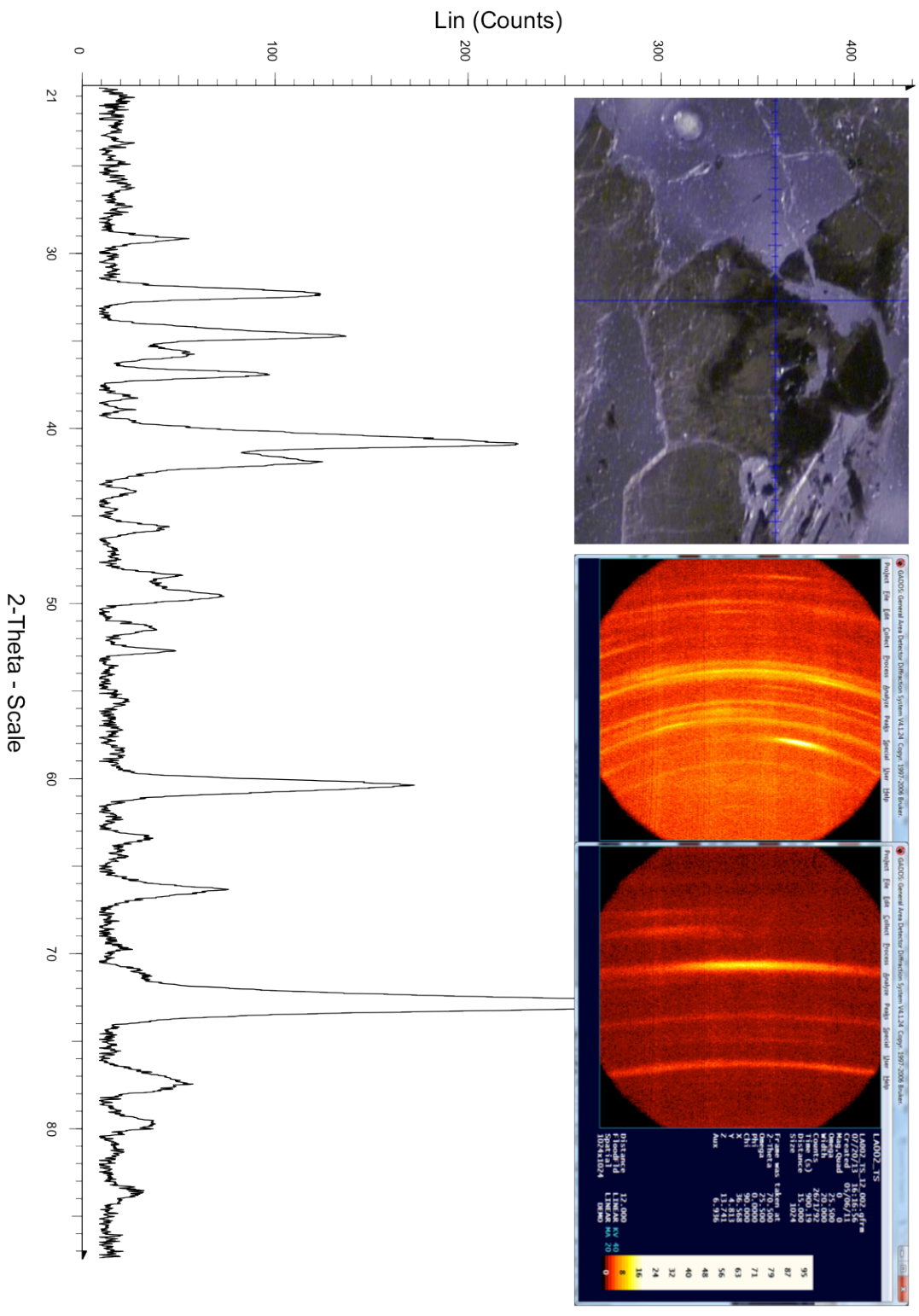
LA002_TS_12
Lin (Counts)
0
100
200
300
400
2-Theta - Scale
21
30
40
50
60
70
80

LA002_TS_22

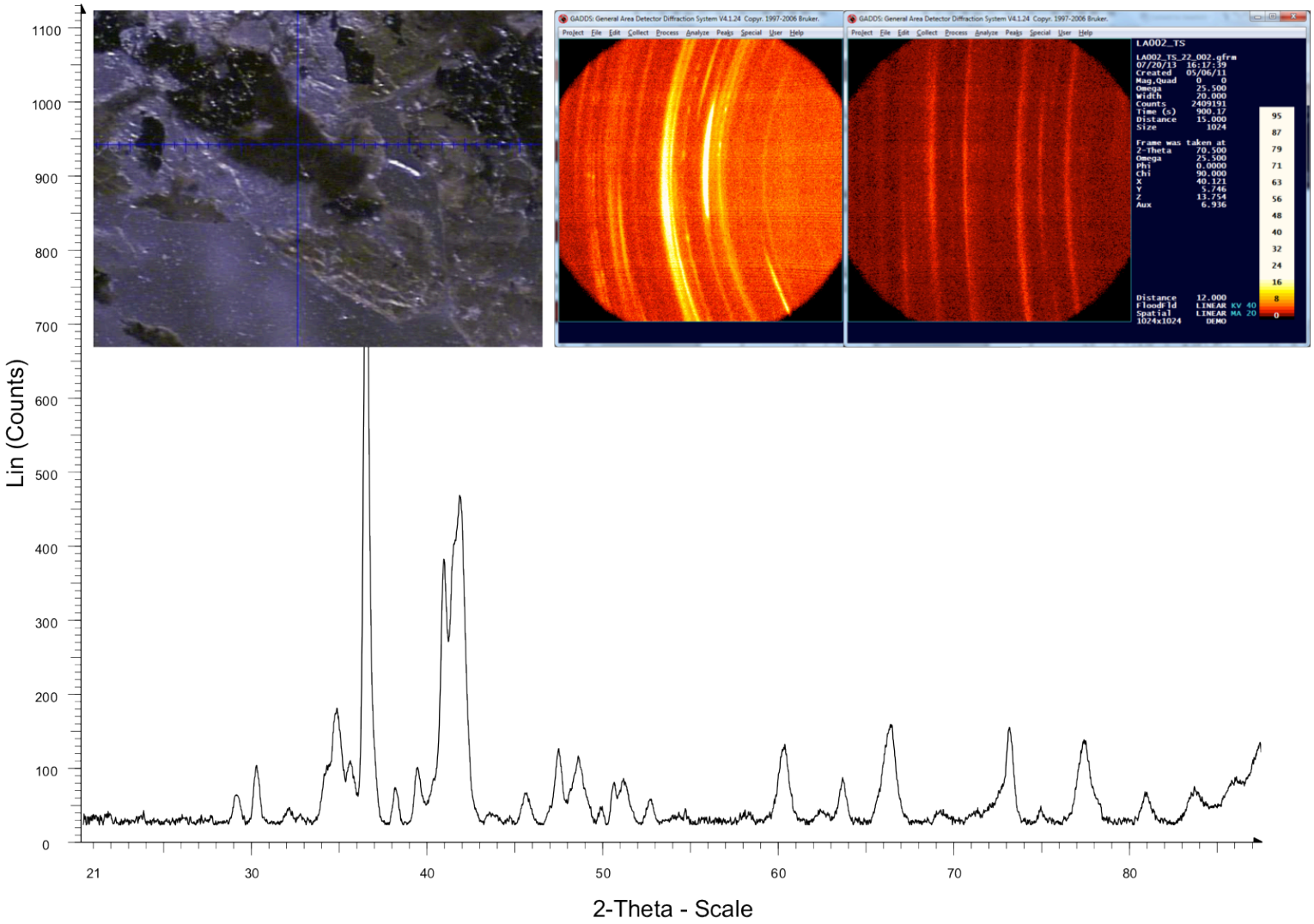
Lin (Counts)
2-Theta - Scale
0
100
200
300
400
500
600
700
800
900
1000
1100
21
30
40
50
60
70
80
LA002_TS
LA002_TS_22_002.gfrm
07/20/13 16:17:39
Created 05/06/11
Mag,Quad 0 0
Omega 25.500
Width 20.000
Counts 2409191
Time (s) 900.17
Distance 15.000
Size 1024
Frame was taken at
2-Theta 70.500
Omega 25.500
Phi 0.0000
Chi 90.000
X 40.121
Y 5.746
Z 13.754
Aux 6.936
Distance 12.000
FloodId LINEAR KV 40
Spatial LINEAR MA 20
1024x1024 DEMO

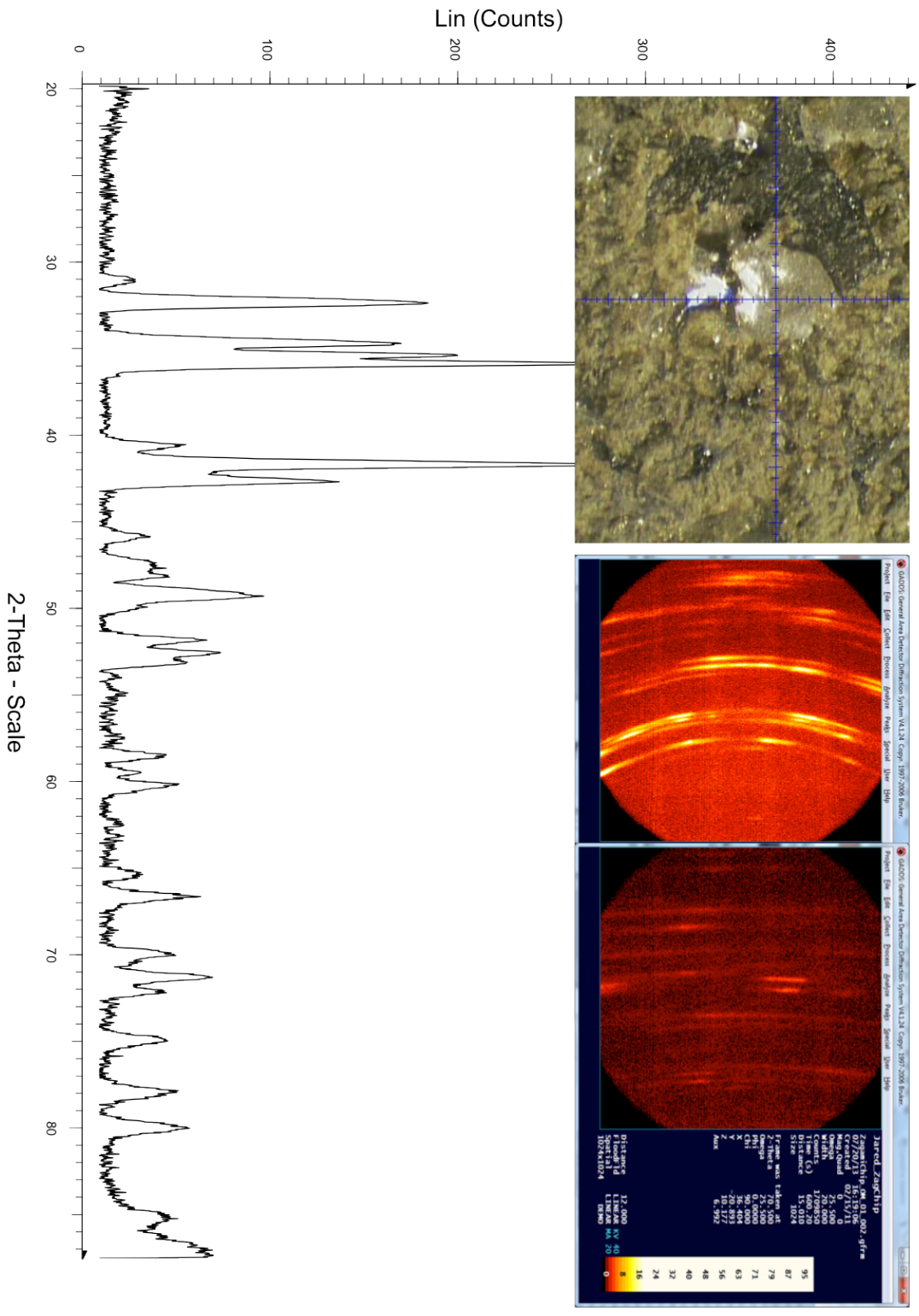
ZagamiChip_OM_01
Lin (Counts)
2-Theta - Scale

ZagamiChip_OM_04

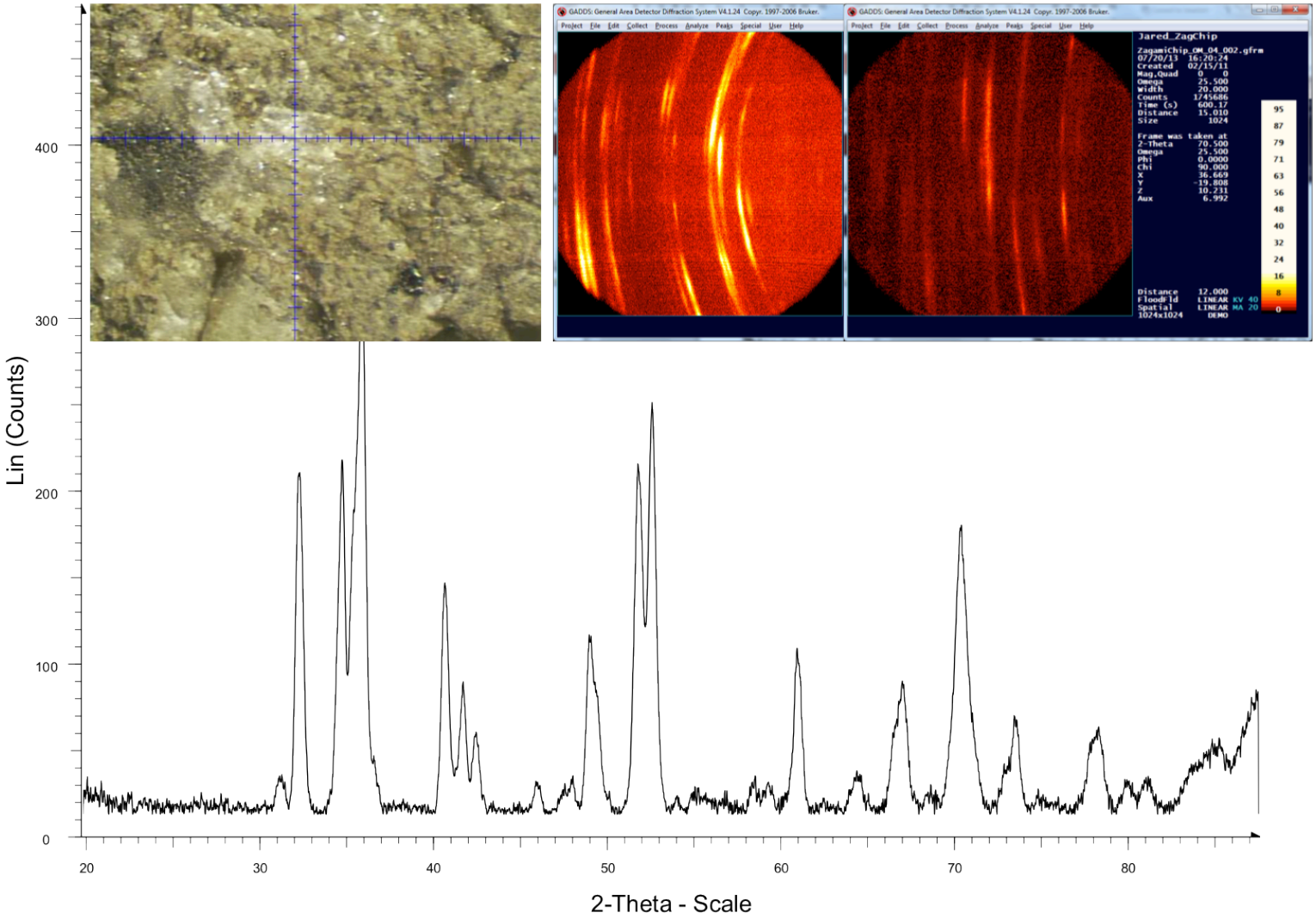

ZagamiChip_OM_05

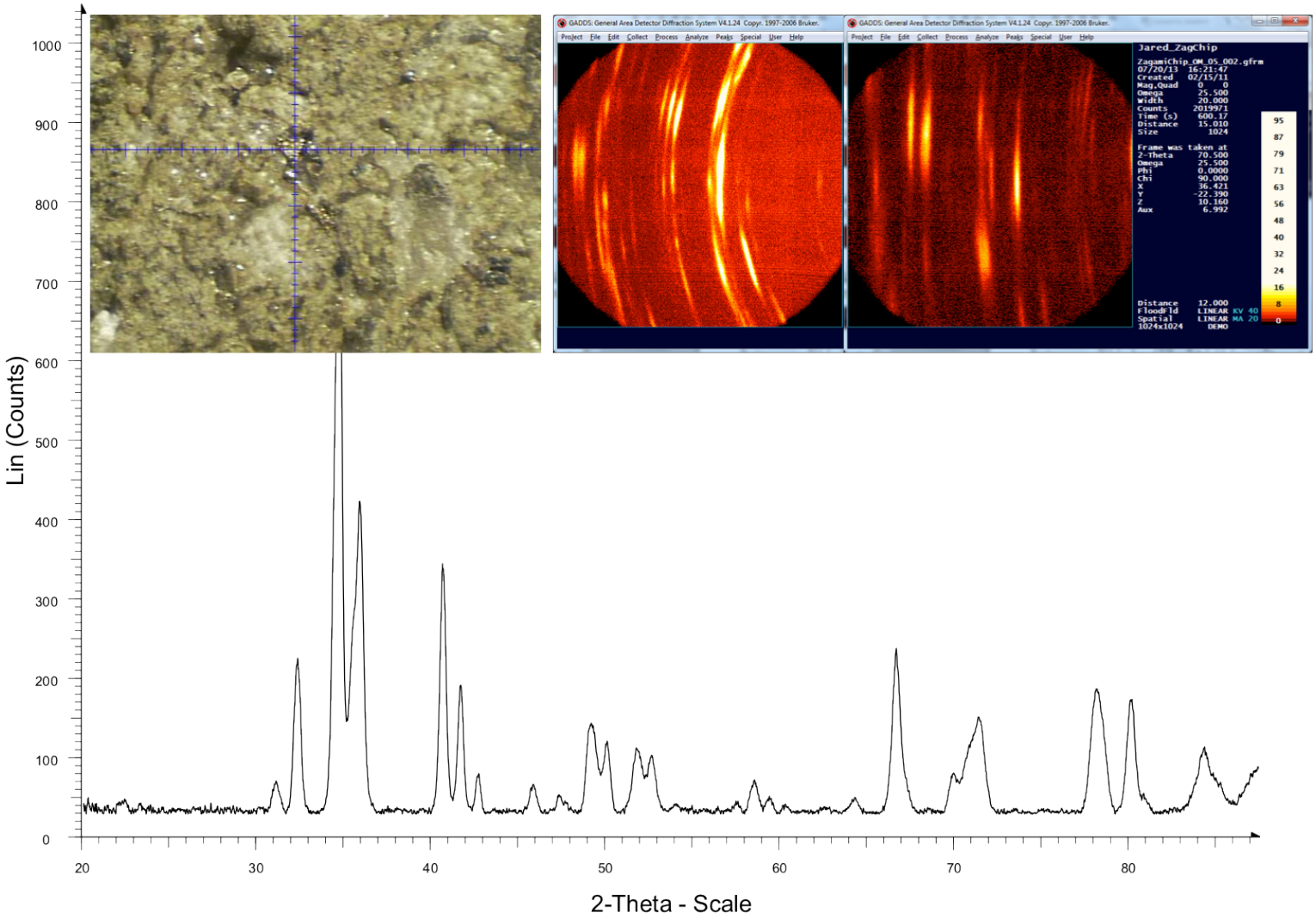

ZagamiChip_OM_07

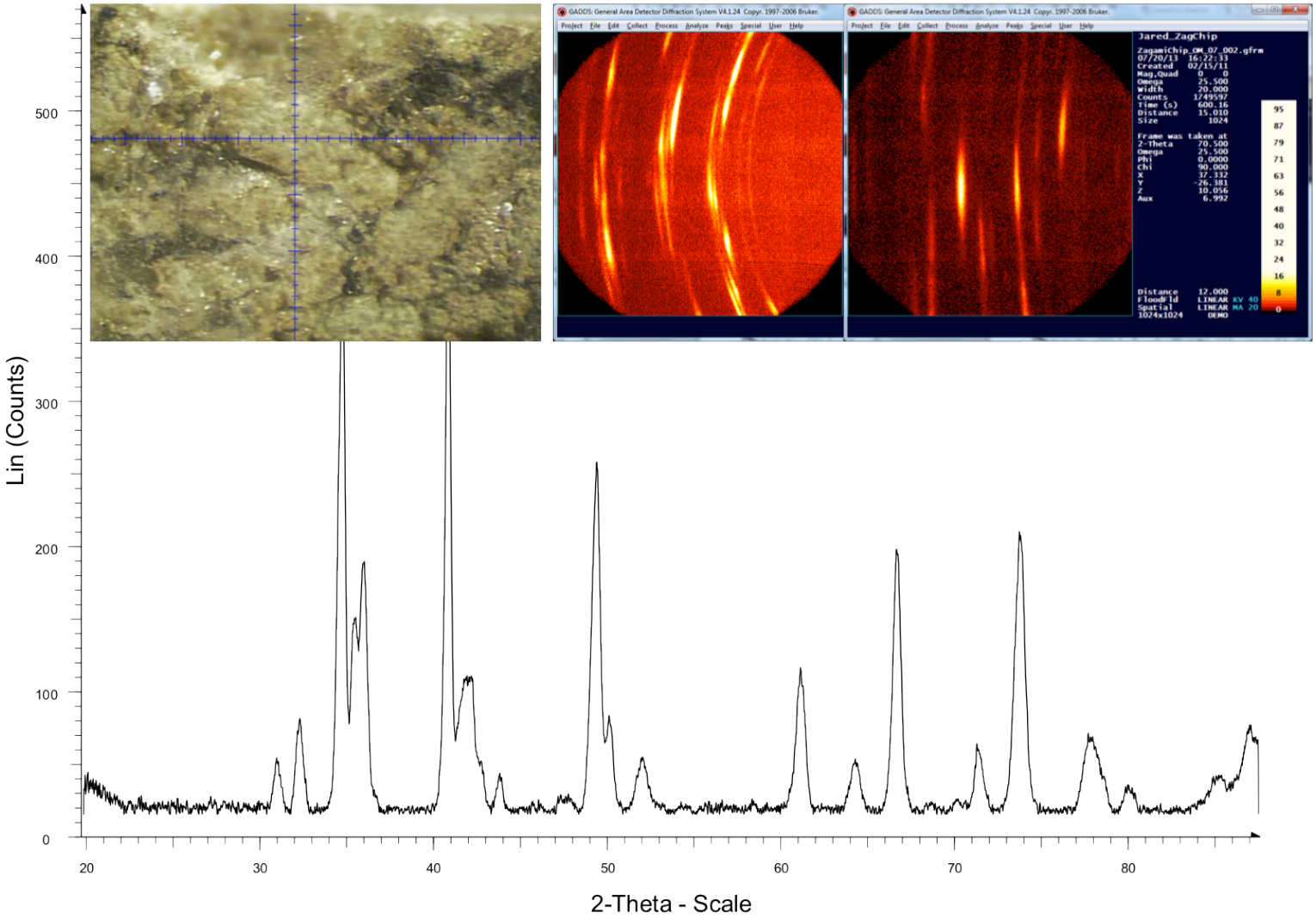

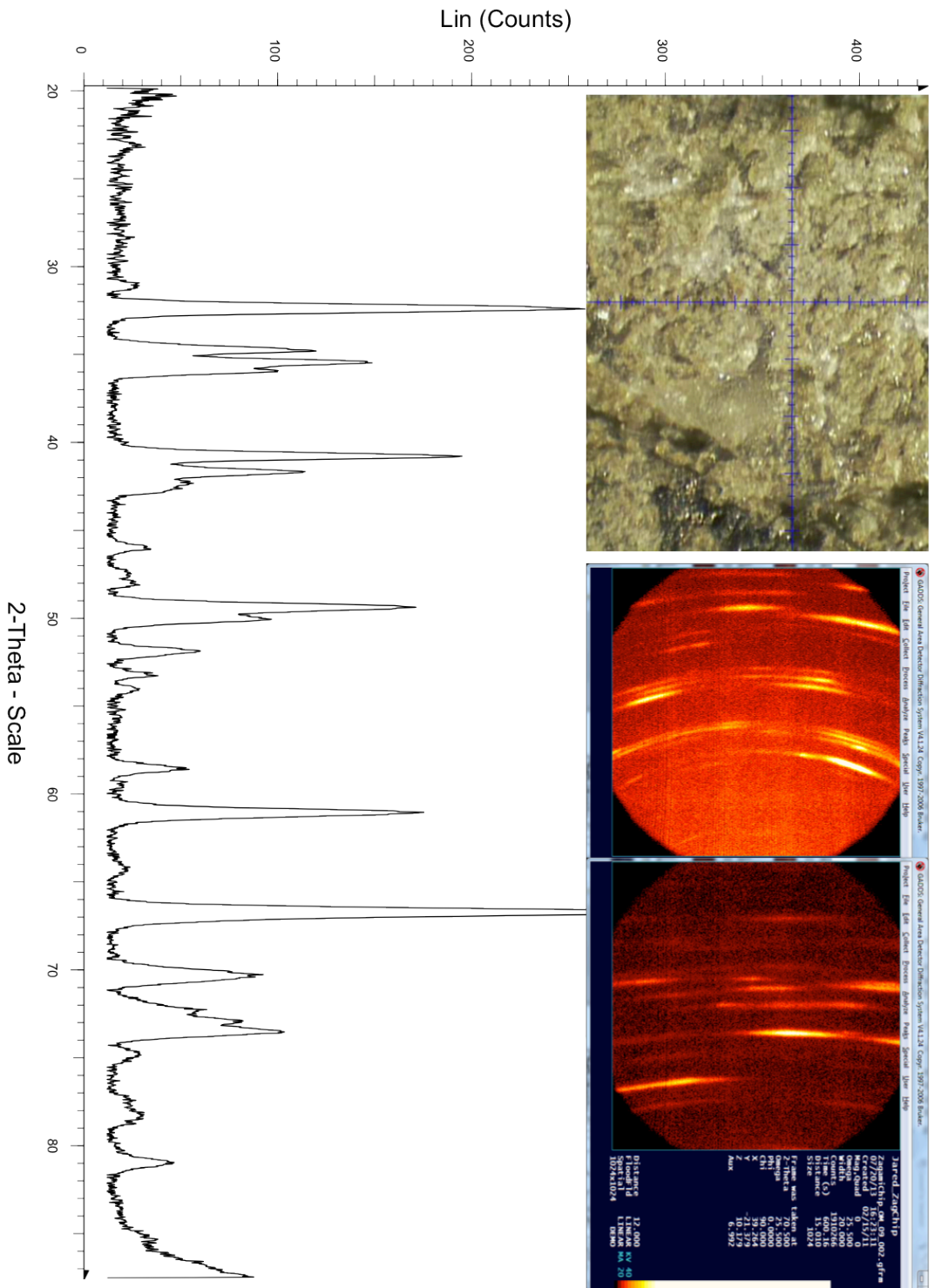
ZagamiChip_OM_09
Lin (Counts)
2-Theta - Scale

Jared_Nakhla_augfay_01

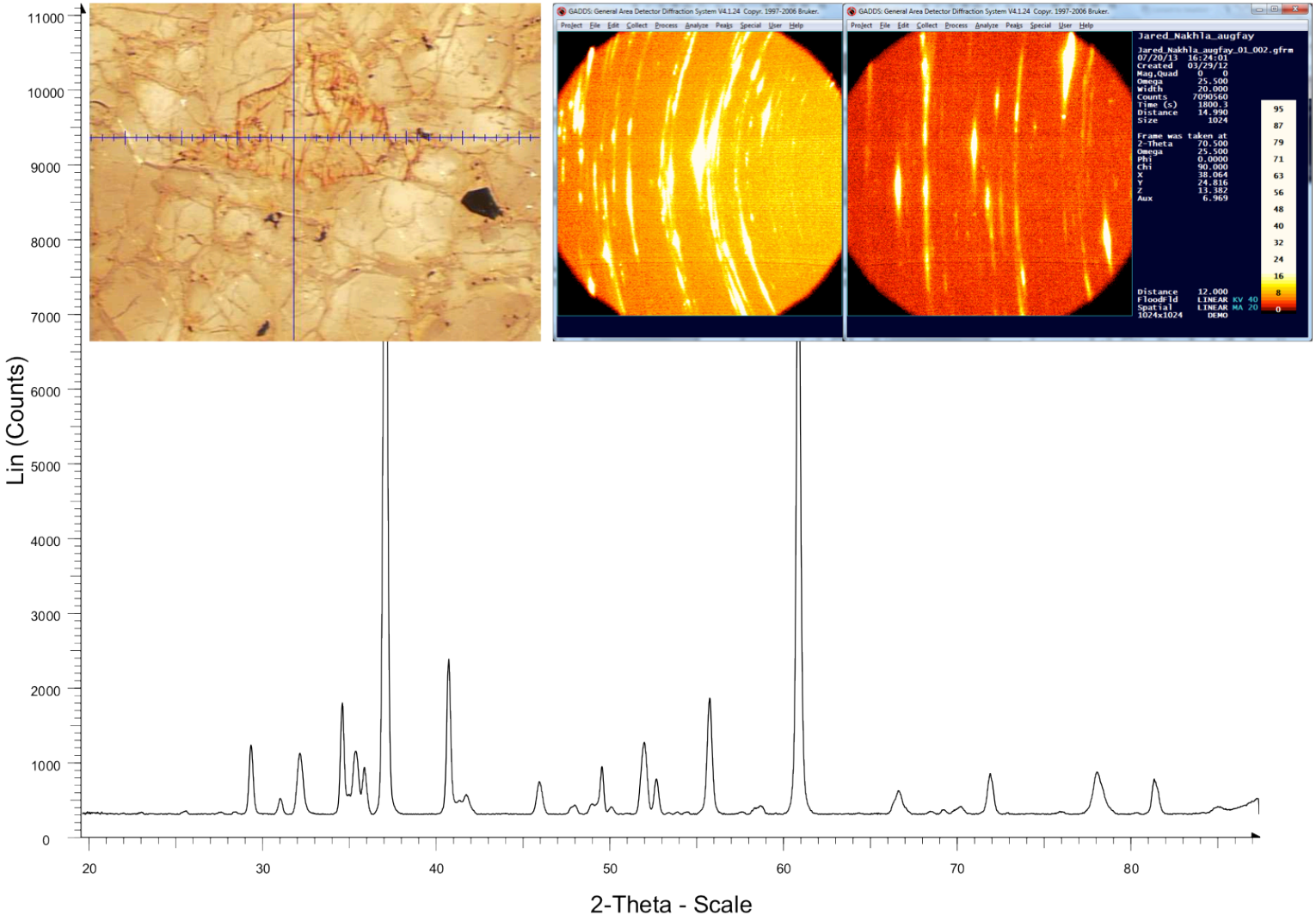

Jared_Nakhla_augfay_02

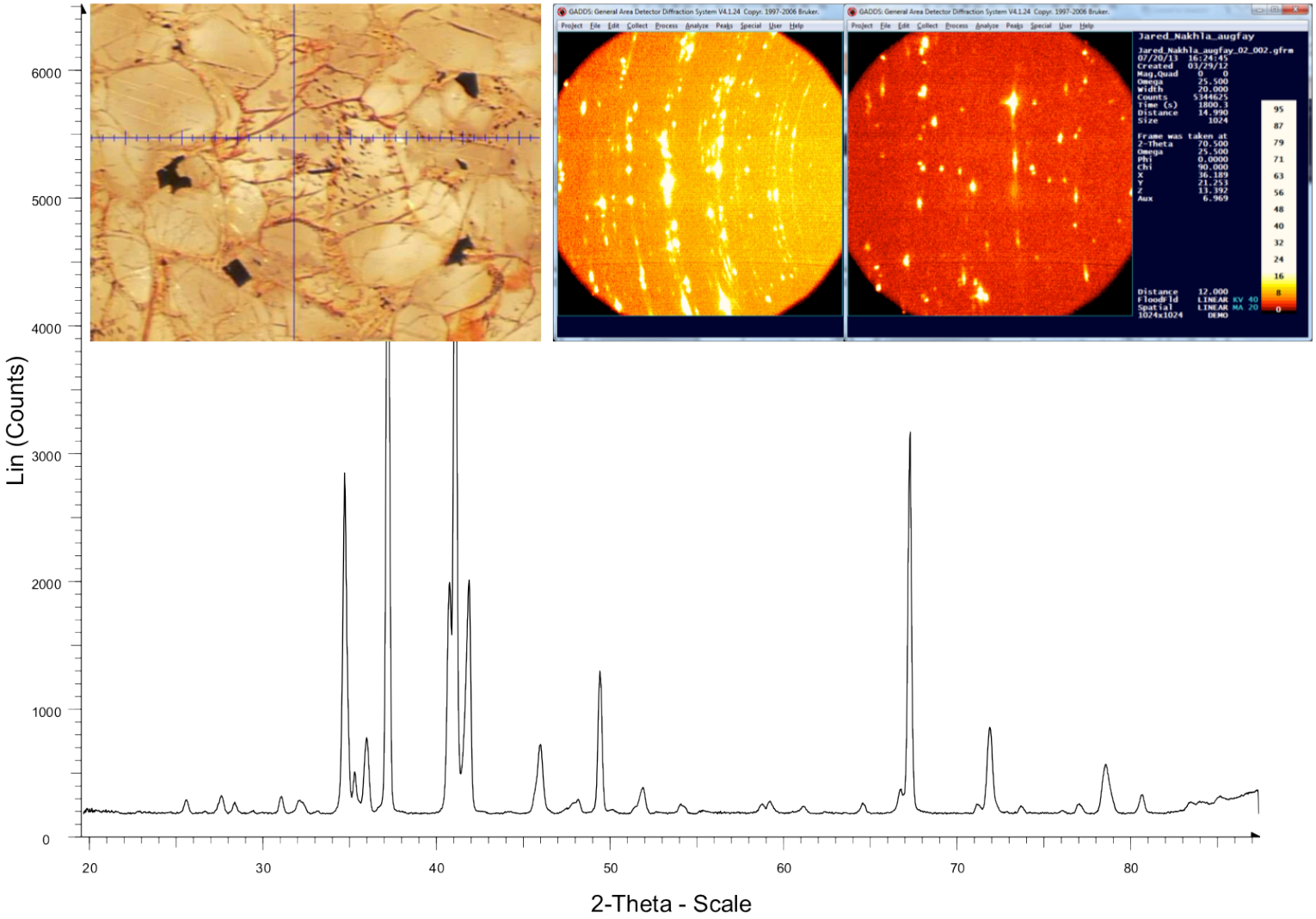

Jared_Nakhla_augfay_04

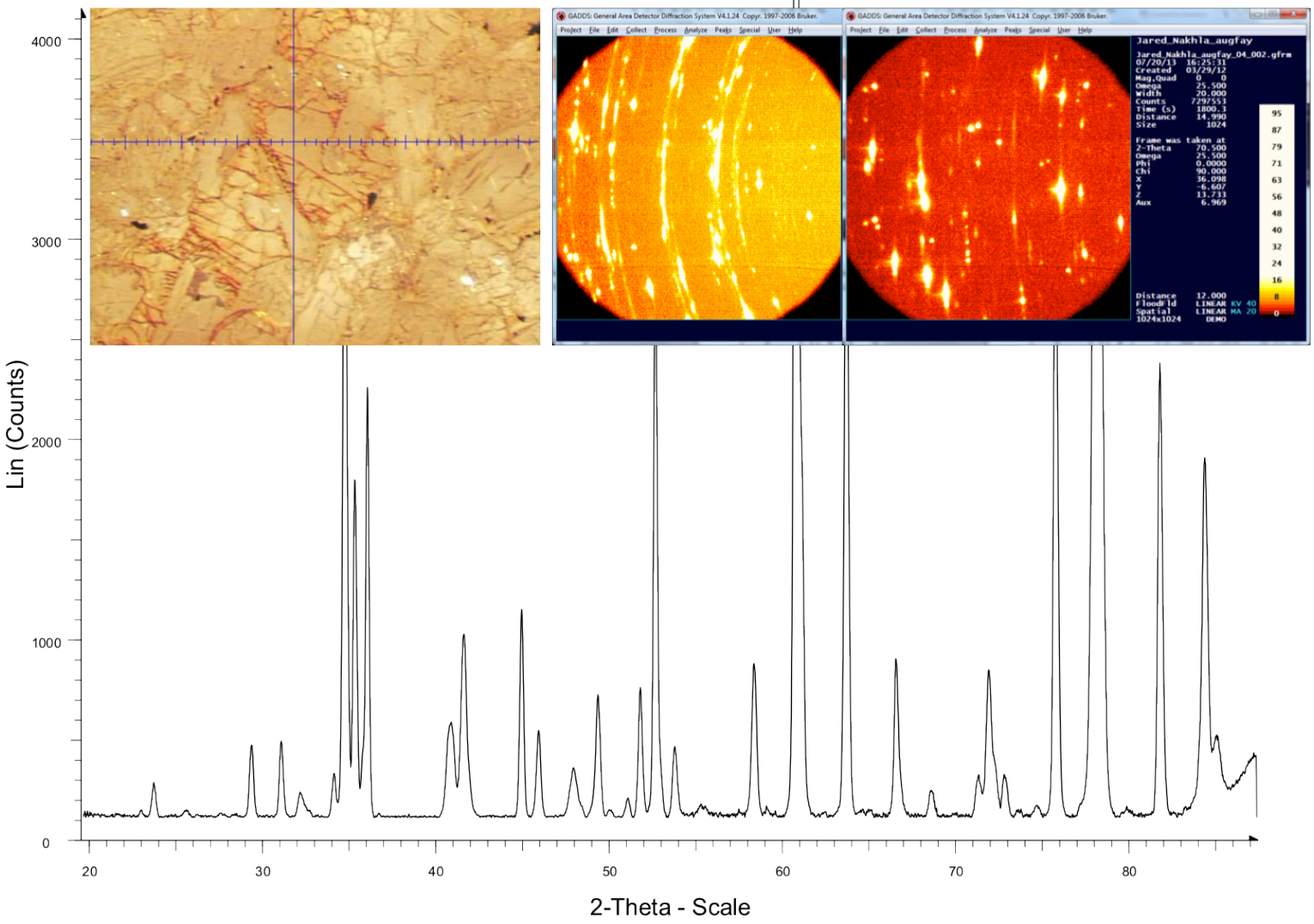

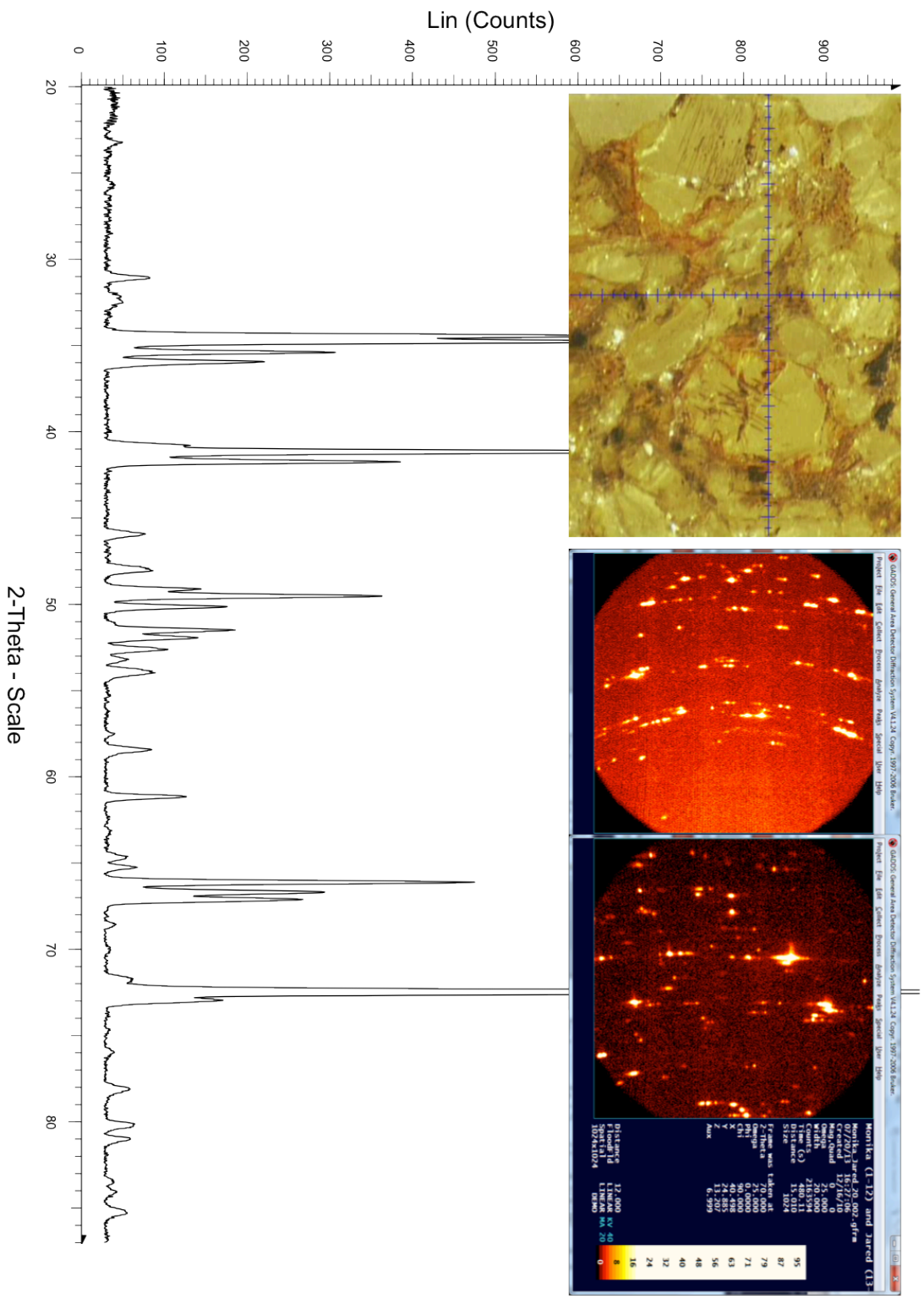
Monika_Jared_20
Lin (Counts)
2-Theta - Scale

Monika_Jared_21

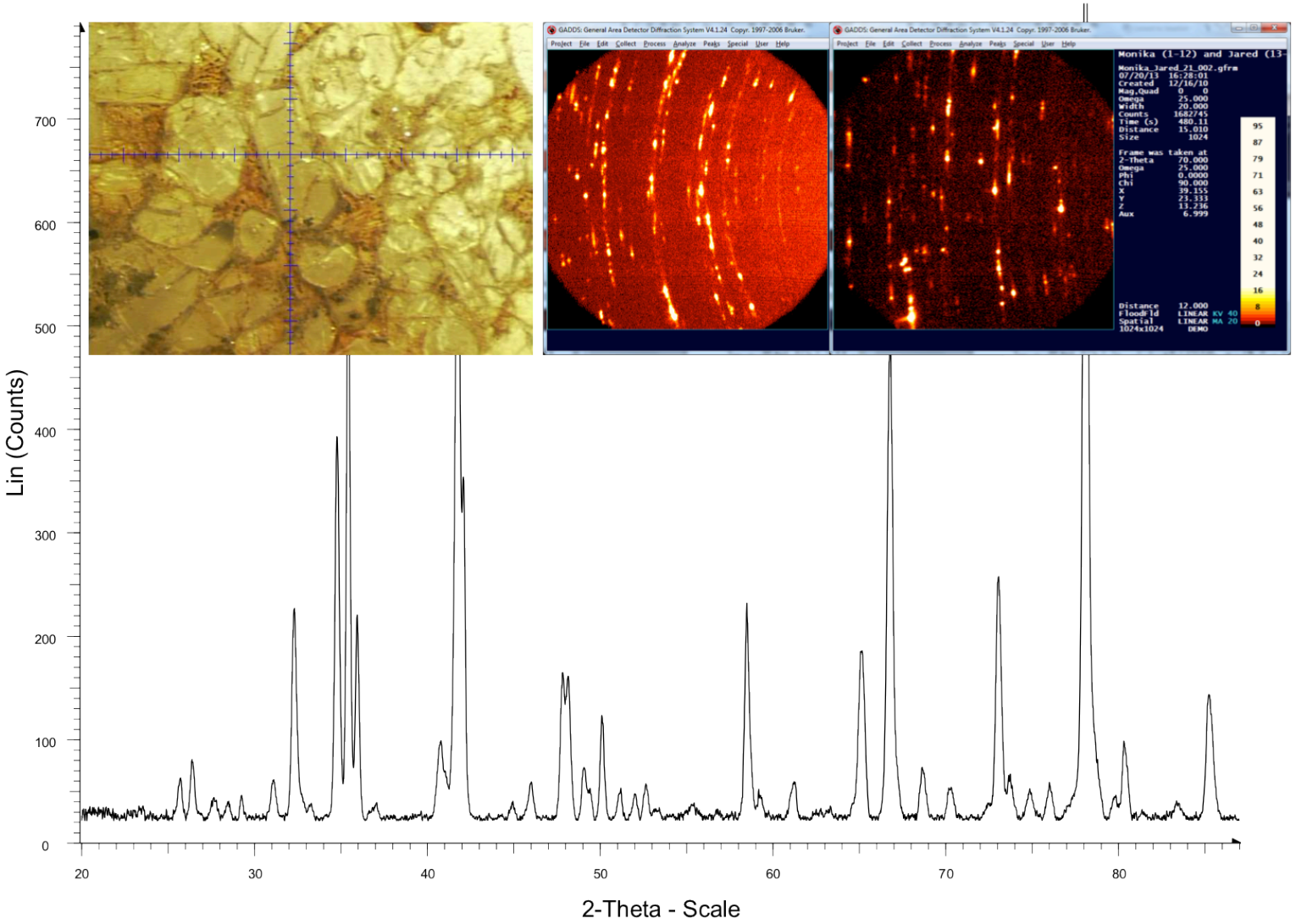

Appendix B: BSE Images

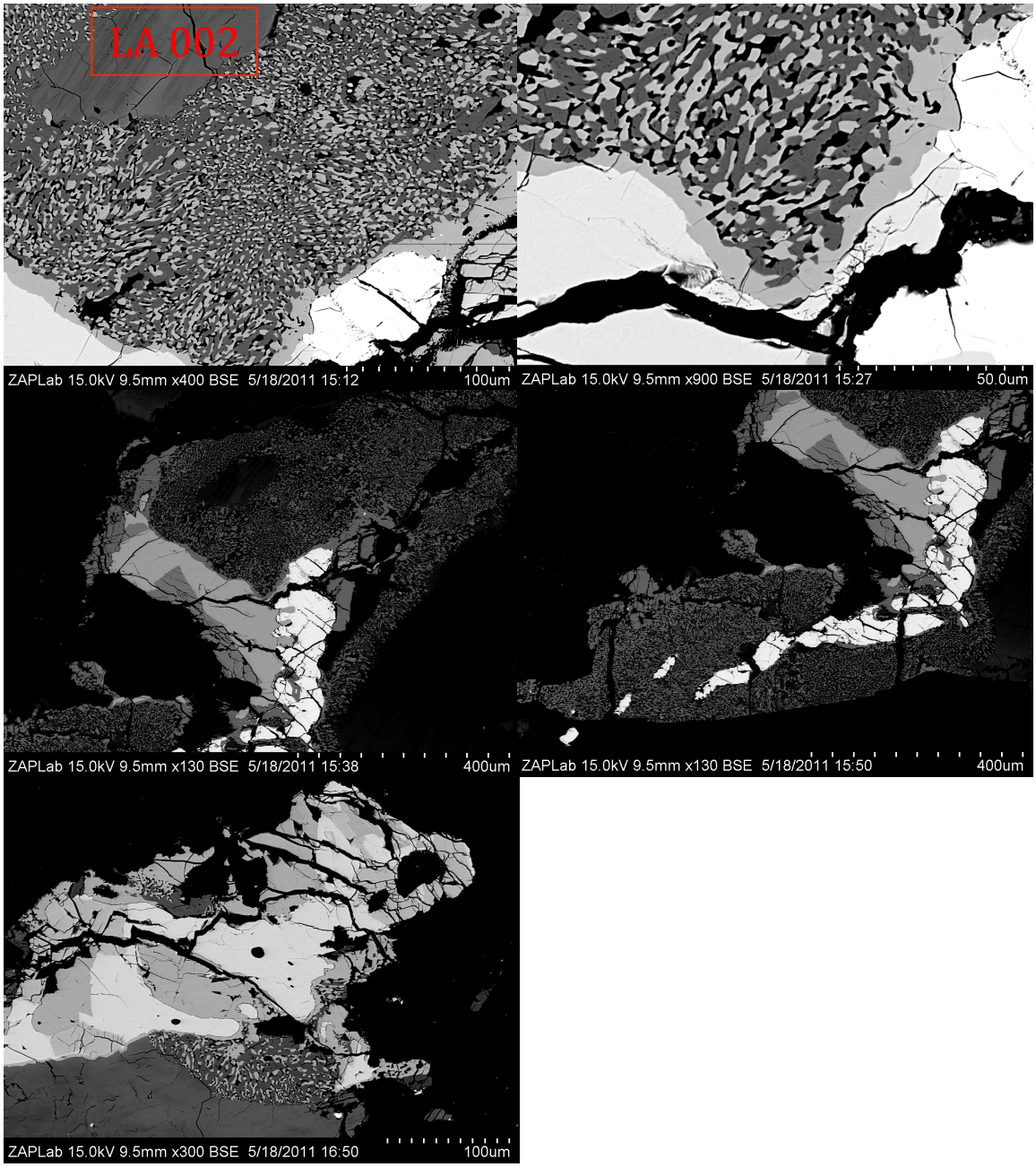

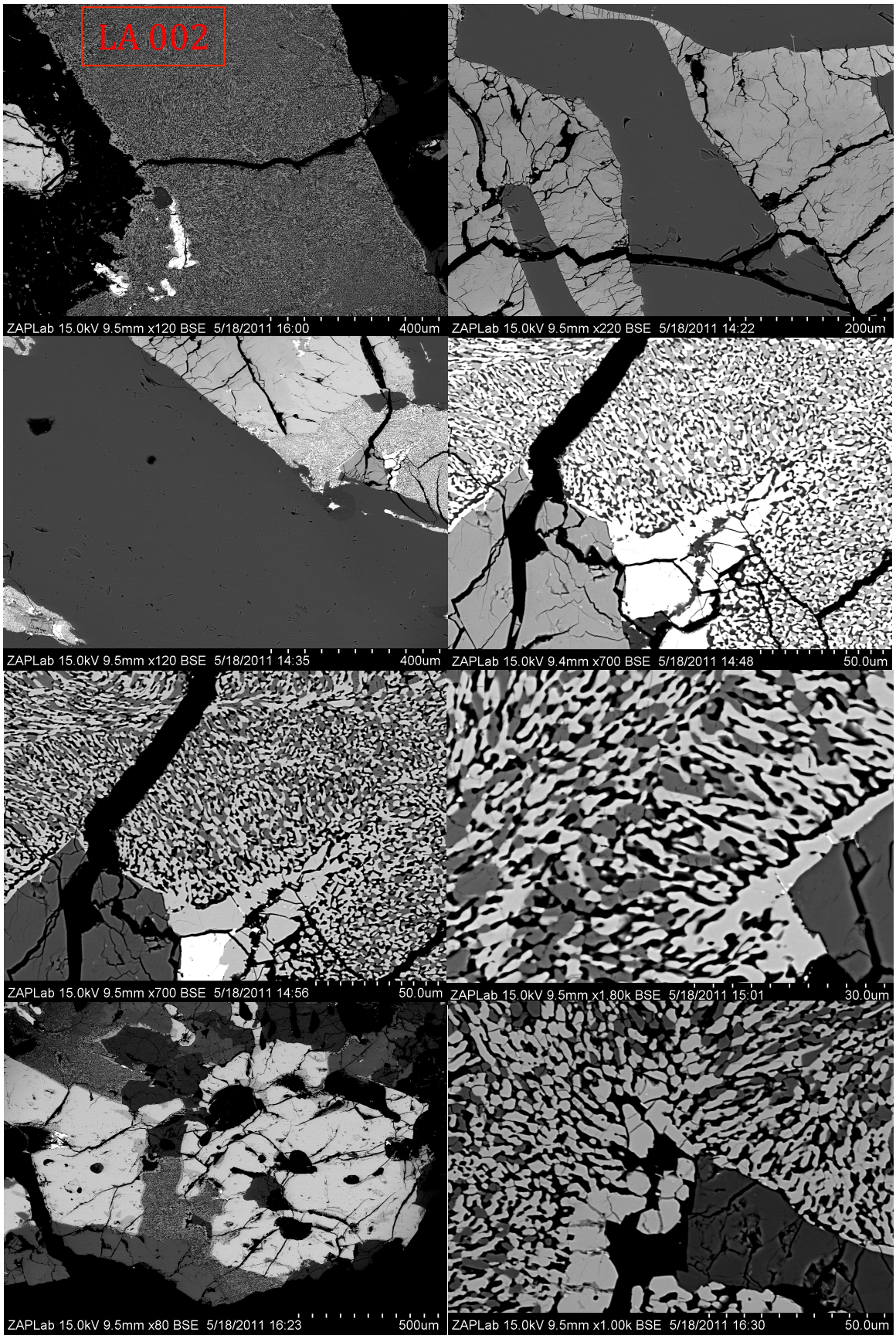
LA 002
ZAPLab 15.0kV 9.5mm x120 BSE 5/18/2011 16:00 400um
ZAPLab 15.0kV 9.5mm x220 BSE 5/18/2011 14:22 200um
ZAPLab 15.0kV 9.5mm x120 BSE 5/18/2011 14:35 400um
ZAPLab 15.0kV 9.4mm x700 BSE 5/18/2011 14:48 50.0um
ZAPLab 15.0kV 9.5mm x700 BSE 5/18/2011 14:56 50.0um
ZAPLab 15.0kV 9.5mm x1.80k BSE 5/18/2011 15:01 30.0um
ZAPLab 15.0kV 9.5mm x80 BSE 5/18/2011 16:23 500um
ZAPLab 15.0kV 9.5mm x1.00k BSE 5/18/2011 16:30 50.0um

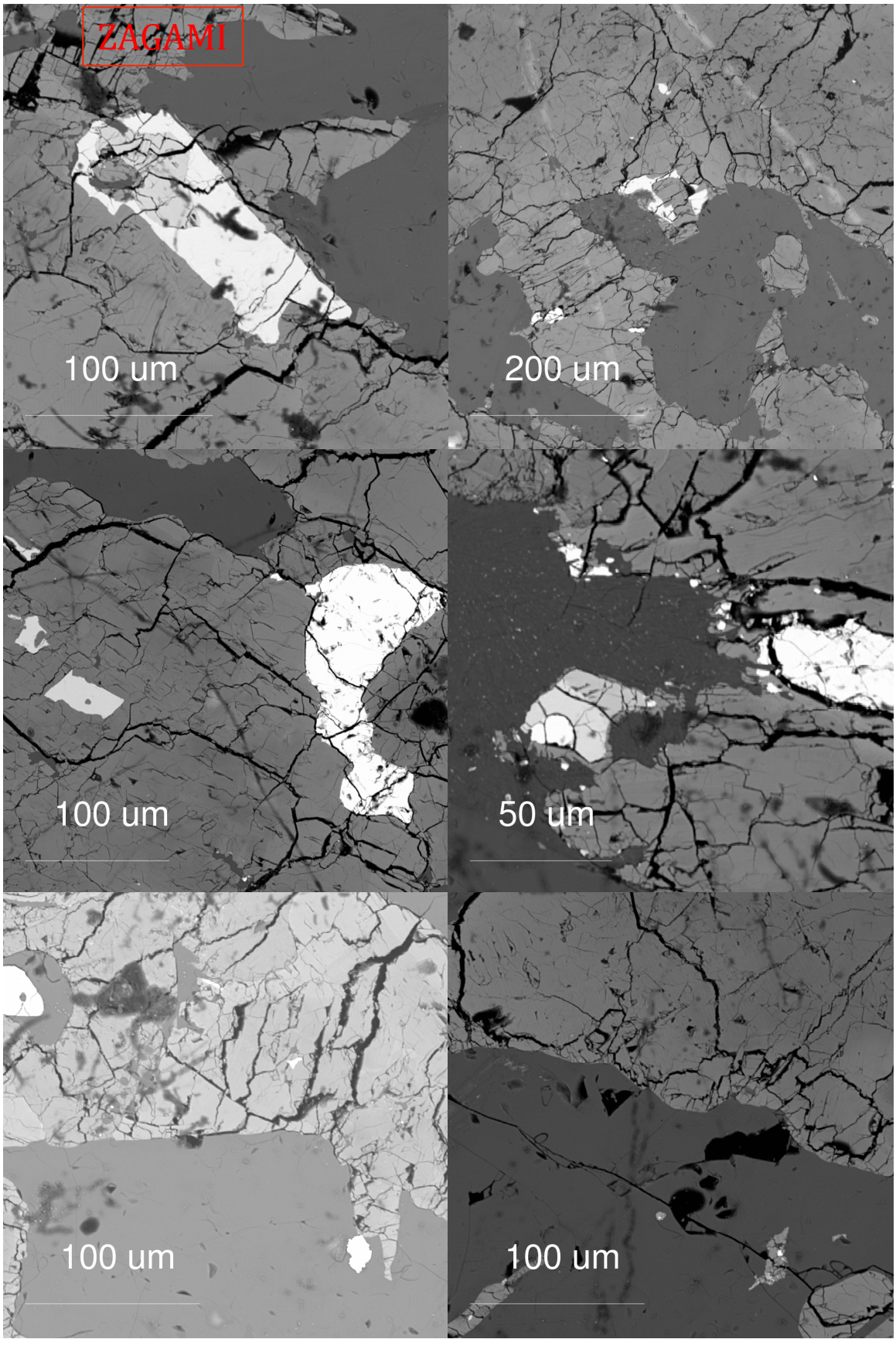
ZAGAMI
100 um
200 um
100 um
50 um
100 um
100 um

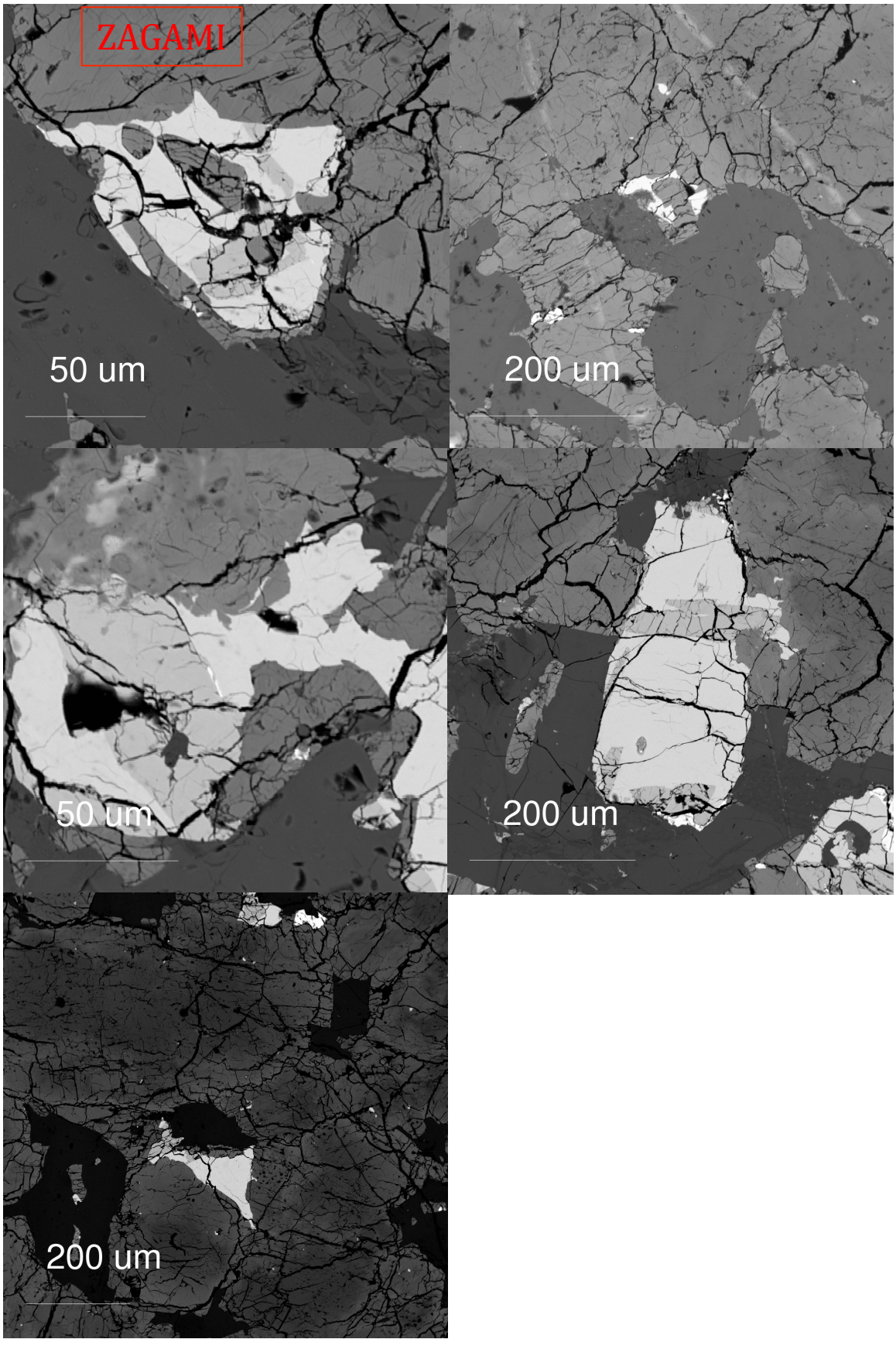
ZAGAMI
50 um
200 um
50 um
200 um
200 um

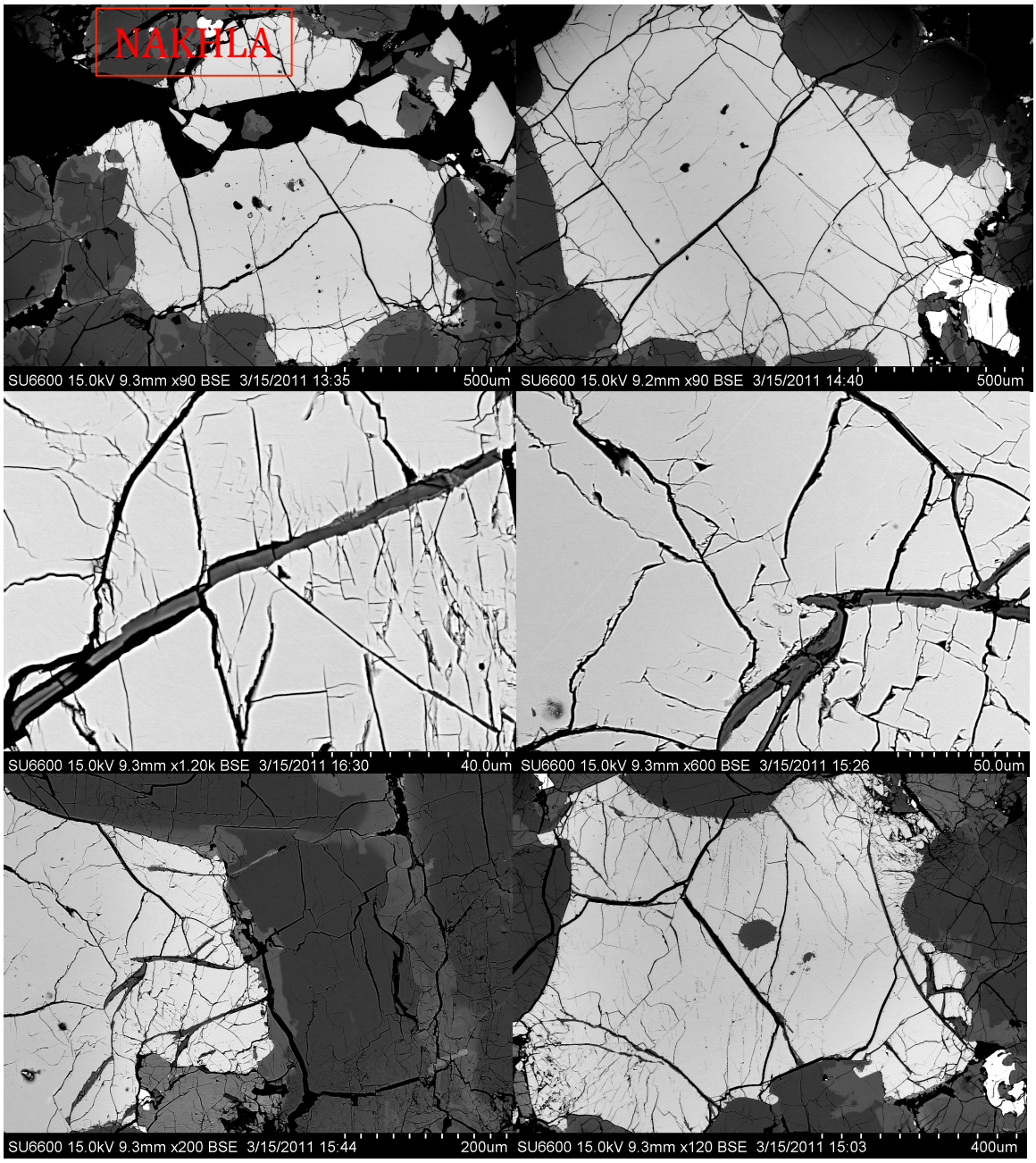
NAKHLA
SU6600 15.0kV 9.3mm x90 BSE 3/15/2011 13:35 500um
SU6600 15.0kV 9.2mm x90 BSE 3/15/2011 14:40 500um
SU6600 15.0kV 9.3mm x1.20k BSE 3/15/2011 16:30 40.0um
SU6600 15.0kV 9.3mm x600 BSE 3/15/2011 15:26 50.0um
SU6600 15.0kV 9.3mm x200 BSE 3/15/2011 15:44 200um
SU6600 15.0kV 9.3mm x120 BSE 3/15/2011 15:03 400um

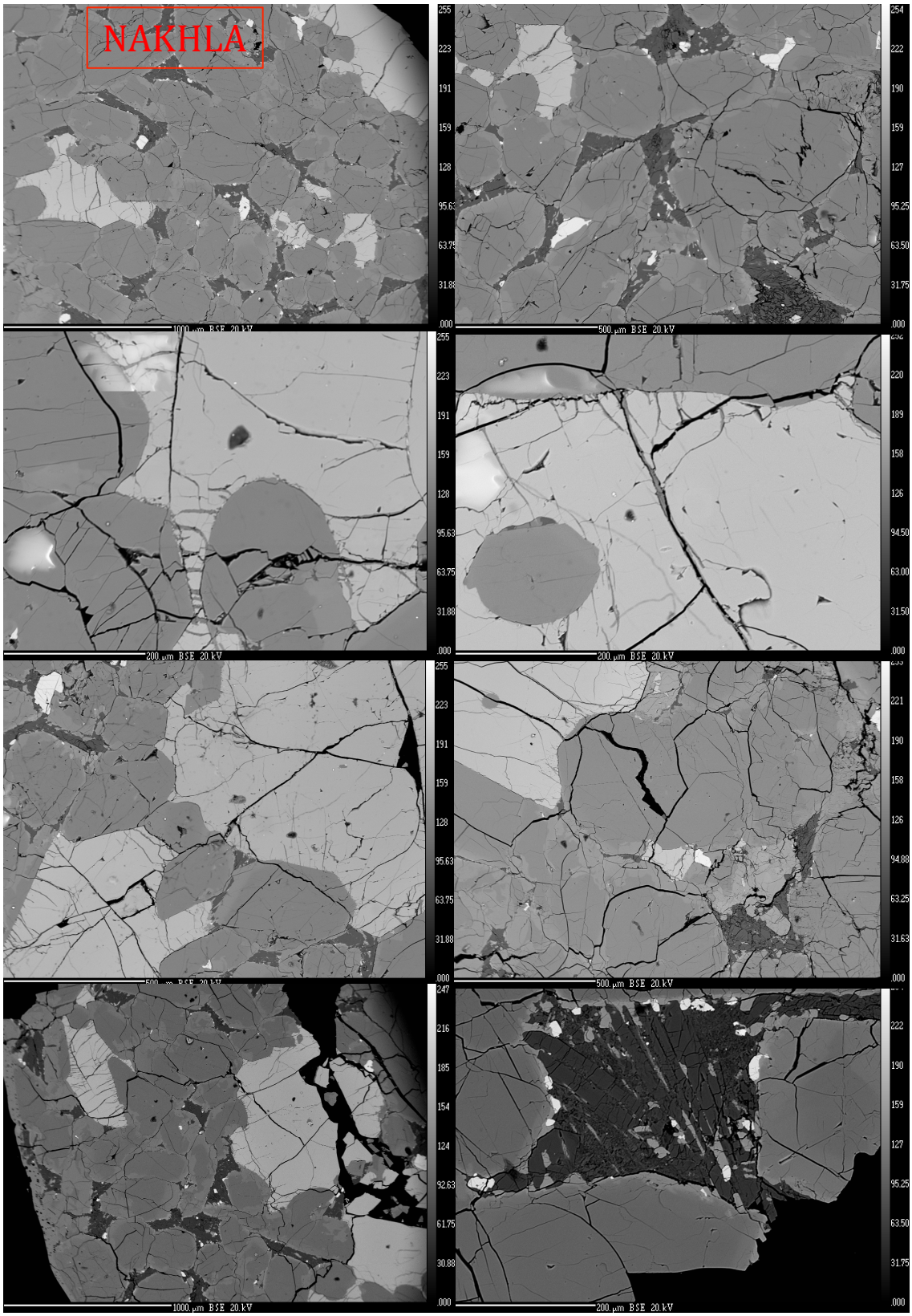
NAKHLA
1000 µm BSE 20 kV
500 µm BSE 20 kV
200 µm BSE 20 kV
200 µm BSE 20 kV
500 µm BSE 20 kV
1000 µm BSE 20 kV
200 µm BSE 20 kV

Appendix C: EPMA Data

Comment	Mineral Phase	Na_2O	MgO	Al_2O_3	SiO_2	CaO	TiO_2	MnO	FeO	NiO	Cr_2O_3	K_2O	P_2O_5	Total
LA 002 1-6	Maskelynite	4.858	0.079	28.082	54.506	10.967	0.042	0.004	0.564	-0.004	-0.006	0.182	0.004	99.279
LA 002 1-15	Maskelynite	2.914	0.099	27.147	55.650	10.693	0.035	0.008	0.553	0.002	-0.006	0.204	0.026	97.322
LA 002 3-1	Maskelynite	4.570	0.054	26.717	58.135	8.961	0.048	0.014	0.638	0.004	0.001	0.371	0.031	99.545
LA 002 3-23	Maskelynite	4.264	0.004	23.846	55.488	6.664	0.028	0.006	0.648	0.006	0.026	3.998	0.016	94.992
LA 002 3-28	Maskelynite	1.511	0.019	24.901	57.472	8.011	0.054	-0.001	0.635	0.010	-0.005	0.544	-0.017	93.131
LA 002 3-33	Maskelynite	5.197	0.005	24.836	58.980	7.479	0.034	-0.012	0.593	-0.002	0.000	0.815	0.021	97.947
LA 002 4-8	Maskelynite	5.165	0.071	27.046	52.884	10.137	0.046	-0.013	0.545	-0.008	0.035	0.290	-0.006	96.191
LA 002 4-9	Maskelynite	2.477	1.078	13.682	49.717	9.693	0.630	0.403	17.151	-0.030	0.015	0.570	2.049	97.435
LA 002 4-10	Maskelynite	3.235	0.958	14.269	50.038	9.101	0.531	0.370	17.106	-0.005	0.023	0.547	2.015	98.188
LA 002 4-11	Maskelynite	2.678	0.072	26.702	53.820	10.158	0.029	0.015	0.600	-0.013	0.007	0.243	-0.016	94.296
LA 002 4-22	Maskelynite	4.865	0.053	27.886	53.618	10.738	0.035	0.009	0.611	0.003	0.000	0.327	0.029	98.175
LA 002 Mis1	Maskelynite	3.010	0.111	28.334	55.158	11.274	0.035	0.004	0.539	0.017	0.001	0.135	0.027	98.644
LA 002 Mis2	Maskelynite	2.937	0.119	27.982	54.098	11.710	0.037	0.018	0.537	0.006	0.012	0.115	0.039	97.608
LA 002 1-4	Merrillite	1.318	0.978	0.026	0.097	46.219	-0.011	0.157	4.933	-0.001	-0.020	0.076	46.378	100.148
LA 002 1-5	Merrillite	1.275	0.964	0.041	0.092	46.438	-0.013	0.178	5.052	0.000	-0.012	0.068	46.612	100.695
LA 002 1-25	Merrillite	1.460	1.481	0.042	0.098	53.786	0.028	0.164	5.596	0.003	0.011	0.081	53.730	116.481
LA 002 3-3	Merrillite	1.161	0.831	0.041	0.091	46.336	0.017	0.164	5.141	0.011	0.006	0.065	46.137	100.002
LA 002 3-7	Merrillite	1.213	0.797	0.058	0.112	46.299	0.004	0.172	5.167	0.008	-0.006	0.060	46.606	100.491
LA 002 3-12	Merrillite	0.010	0.029	0.044	0.428	53.460	0.080	0.098	0.942	0.000	-0.013	0.003	42.535	97.615
LA 002 3-14	Merrillite	1.150	0.916	0.032	0.074	46.264	-0.013	0.163	5.075	0.005	0.004	0.054	46.459	100.183
LA 002 3-24	Merrillite	1.246	0.984	0.053	0.079	46.077	0.018	0.185	4.934	-0.013	0.009	0.075	46.169	99.815
LA 002 3-31	Merrillite	1.215	0.940	0.065	0.087	46.045	-0.002	0.164	5.170	-0.007	-0.026	0.065	46.369	100.086
LA 002 3-32	Merrillite	1.179	0.782	0.027	0.094	46.053	0.000	0.214	5.233	0.006	-0.007	0.064	46.786	100.430
LA 002 4-1	Merrillite	1.212	0.992	0.045	0.071	46.226	0.002	0.205	4.921	-0.016	-0.001	0.063	46.430	100.148
LA 002 4-21	Merrillite	1.226	0.878	0.042	0.101	46.495	0.033	0.166	5.167	-0.007	-0.012	0.073	45.645	99.807
LA 002 2-3	Merrillite	1.177	0.805	0.072	0.092	46.621	0.027	0.172	5.291	-0.005	0.001	0.071	46.686	101.008
LA 002 1-12	Mesostasis	0.272	-0.002	2.025	95.788	0.290	0.196	0.018	0.462	0.001	-0.006	0.739	0.025	99.806
LA 002 1-14	Mesostasis	0.581	-0.007	3.334	92.368	0.576	0.217	0.011	0.689	0.001	-0.018	1.083	0.023	98.859
LA 002 3-4	Mesostasis	0.668	-0.006	7.243	86.081	1.505	0.219	0.023	0.520	-0.002	0.009	1.330	-0.004	97.587
LA 002 3-8	Mesostasis	1.022	0.005	11.802	76.125	0.495	0.275	-0.002	0.721	0.007	0.018	6.443	0.059	96.969
LA 002 3-10	Mesostasis	1.398	0.000	12.123	75.276	0.927	0.242	0.015	0.441	-0.001	-0.005	6.287	0.485	97.189
LA 002 4-15	Mesostasis	1.246	0.005	12.425	75.297	0.722	0.197	0.027	0.539	-0.007	-0.008	4.830	0.117	95.390
LA 002 4-18	Mesostasis	2.297	0.012	12.917	74.465	1.275	0.459	0.011	1.269	0.001	-0.035	4.896	0.079	97.646
LA 002 2-15	Mesostasis	1.849	0.016	12.754	76.375	1.023	0.152	0.042	1.459	0.005	0.025	4.495	0.055	98.250
LA 002 2-27	Mesostasis	0.203	0.002	1.396	97.121	0.190	0.112	0.016	1.016	-0.010	-0.001	0.437	-0.012	100.469
LA 002 1-2	Pyroxene	0.170	9.484	0.808	48.966	8.997	0.426	0.858	31.386	0.004	0.013	0.016	0.033	101.161
LA 002 1-8	Pyroxene	0.164	2.334	0.668	46.514	7.542	0.674	0.973	42.550	0.008	-0.011	0.019	0.037	101.472
LA 002 1-10	Pyroxene	0.226	6.916	0.789	48.605	10.779	0.611	0.846	32.533	0.000	-0.011	0.025	0.011	101.331

LA 002 1-11	Pyroxene	0.171	10.410	0.797	50.110	11.825	0.427	0.767	26.195	0.012	0.027	0.015	0.024	100.781
LA 002 1-17	Pyroxene	0.159	3.993	0.634	47.779	8.477	0.560	0.963	39.132	0.003	-0.017	0.013	-0.013	101.684
LA 002 3-2	Pyroxene	0.088	6.135	0.514	47.660	6.525	0.432	0.956	38.089	-0.006	-0.007	0.006	-0.034	100.358
LA 002 3-9	Pyroxene	0.121	1.951	0.716	47.066	11.176	0.520	0.814	38.669	0.017	0.038	0.006	-0.002	101.093
LA 002 3-16	Pyroxene	0.083	8.778	0.598	46.432	6.922	0.388	0.861	33.850	0.013	0.009	0.008	-0.015	97.924
LA 002 3-19	Pyroxene	0.088	2.157	0.658	44.144	10.883	0.528	0.811	37.629	0.000	0.009	0.004	0.039	96.949
LA 002 3-30	Pyroxene	0.059	2.275	0.489	46.004	6.844	0.465	1.002	42.664	-0.001	-0.022	0.005	0.005	99.789
LA 002 3-34	Pyroxene	0.015	1.602	0.286	46.297	5.967	0.283	1.216	44.535	0.004	0.038	0.013	0.032	100.287
LA 002 4-3	Pyroxene	0.095	4.027	0.655	47.010	8.667	0.555	0.958	38.271	0.009	0.009	0.021	-0.005	100.272
LA 002 4-5	Pyroxene	0.083	1.710	0.281	45.150	5.365	0.246	1.382	45.044	0.013	0.013	0.019	0.021	99.326
LA 002 4-12	Pyroxene	0.138	3.063	0.778	46.845	9.303	0.454	0.905	37.195	0.005	-0.010	0.057	0.072	98.804
LA 002 4-13	Pyroxene	0.129	3.718	0.565	46.578	7.707	0.456	0.989	40.294	0.002	-0.014	0.010	-0.029	100.405
LA 002 4-14	Pyroxene	0.127	14.568	0.866	50.404	8.337	0.274	0.737	25.053	0.019	0.038	0.014	0.018	100.456
LA 002 4-16	Pyroxene	0.120	9.759	0.611	48.060	6.608	0.360	0.876	33.062	-0.004	-0.009	0.016	0.018	99.477
LA 002 4-24	Pyroxene	0.051	1.736	0.247	45.925	5.509	0.287	1.169	45.185	-0.013	0.005	0.012	-0.004	100.107
LA 002 2-17	Pyroxene	0.030	1.627	0.305	46.379	5.661	0.247	1.136	45.393	0.007	0.027	-0.005	0.037	100.843
LA 002 2-19	Pyroxene	0.052	2.362	1.202	47.605	5.398	0.211	1.655	42.130	-0.021	0.013	0.004	0.022	100.633
LA 002 2-22	Pyroxene	0.023	1.986	0.331	46.251	5.504	0.189	1.443	44.589	-0.003	0.001	0.008	0.002	100.324
LA 002 2-23	Pyroxene	0.096	1.531	0.619	52.690	8.806	0.376	0.755	34.238	-0.005	0.008	0.055	0.235	99.403
LA 002 2-30	Pyroxene	0.050	1.851	0.313	46.497	5.647	0.276	1.376	44.879	-0.021	-0.028	0.012	0.009	100.862
LA 002 Mis2	Pyroxene	0.103	13.414	0.750	51.189	6.372	0.263	0.825	28.902	0.002	0.058	0.006	-0.004	101.879
LA 002 Mis4	Pyroxene	0.174	10.545	1.084	50.522	14.468	0.425	0.663	23.009	0.010	0.018	0.015	0.009	100.942
LA 002 1-7	Pyroxferroite	0.112	1.020	0.124	31.922	1.258	0.098	1.238	67.436	-0.020	0.002	0.016	0.066	103.271
LA 002 3-5	Pyroxferroite	0.085	1.406	0.247	49.422	4.294	0.249	1.116	44.698	0.023	0.002	0.016	0.025	101.583
LA 002 3-22	Pyroxferroite	0.066	2.106	0.431	41.993	9.665	0.341	0.880	39.318	0.005	0.022	0.014	0.018	94.858
LA 002 4-2	Pyroxferroite	0.064	1.953	0.077	31.002	0.500	0.079	1.432	65.148	0.004	-0.004	0.011	0.037	100.302
LA 002 4-6	Pyroxferroite	0.063	1.922	0.297	40.001	9.628	0.313	1.206	46.717	0.009	-0.009	0.001	0.019	100.166
LA 002 4-7	Pyroxferroite	0.136	1.975	0.302	44.826	6.505	0.212	1.009	44.928	0.003	-0.019	0.017	0.041	99.934
LA 002 4-20	Pyroxferroite	0.101	1.420	0.323	48.378	8.503	0.285	0.785	38.940	-0.011	0.010	0.010	-0.002	98.743
LA 002 4-23	Pyroxferroite	0.074	1.678	0.268	46.041	7.604	0.275	1.088	43.305	-0.002	-0.007	0.011	0.020	100.354
LA 002 2-13	Pxf black	0.085	1.347	0.315	53.887	3.209	0.141	0.888	44.761	-0.004	0.001	0.010	0.016	104.657
LA 002 Mis9	Pxf black	0.124	1.185	7.771	48.250	1.843	0.138	0.936	45.556	-0.012	0.001	0.040	0.017	105.849
LA 002Mis10	Pxf black	0.211	1.413	3.731	57.326	14.038	0.463	0.591	26.068	0.007	-0.023	0.046	0.024	103.893
LA 002 2-11	Pxf grey	0.099	2.068	0.499	42.734	9.667	0.313	0.994	47.860	0.017	0.004	0.013	0.004	104.272
LA 002 2-29	Pxf grey	0.064	1.633	0.161	33.954	1.517	0.529	1.263	63.030	0.010	0.009	0.021	0.016	102.206
LA 002 2-31	Pxf grey	0.116	1.728	0.571	48.317	8.467	0.240	0.744	39.719	0.010	-0.014	0.017	0.036	99.951
LA 002 Mis7	Pxf grey	0.202	1.756	0.799	48.135	18.161	0.733	0.618	30.746	-0.004	0.006	0.016	0.016	101.184
LA 002 Mis8	Pxf grey	0.164	1.773	0.604	57.444	10.564	0.557	0.511	25.351	0.024	-0.003	0.051	0.041	97.081
LA 002 2-12	Pxf white	0.021	1.419	0.075	33.190	0.441	0.045	1.227	61.896	0.002	-0.006	0.009	0.010	98.328
LA 002 2-16	Pxf white	0.031	0.810	0.247	47.397	0.483	0.067	1.001	49.499	0.005	-0.018	0.067	0.031	99.618
LA 002 2-18	Pxf white	0.039	1.620	0.136	36.538	1.612	0.091	1.172	56.748	0.004	-0.013	-0.001	0.014	97.959

LA 002 2-20	Pxf white	0.178	2.014	0.516	32.898	0.335	0.072	1.310	64.729	-0.005	-0.002	0.116	0.058	102.218
LA 002 2-25	Pxf white	0.085	1.711	0.835	47.076	7.807	0.303	0.775	37.821	0.009	-0.004	0.035	0.004	96.457
LA 002 Mis6	Pxf white	0.121	1.397	0.474	50.700	10.515	0.414	0.649	29.453	-0.006	0.011	0.044	0.000	93.771
LA 002 Mis6	Pxf white	0.100	1.511	0.062	31.163	0.483	0.067	1.304	66.698	-0.004	-0.006	0.009	0.002	101.389
LA 002 1-16	Pyrrhotite	0.120	0.007	0.049	0.048	0.026	0.004	0.019	81.881	0.075	0.021	0.006	0.041	82.296
LA 002 1-18	Pyrrhotite	0.098	-0.016	0.035	0.042	0.024	0.009	0.022	83.452	0.071	0.009	0.017	-0.010	83.751
LA 002 1-19	Pyrrhotite	0.189	-0.005	0.034	0.016	0.055	-0.004	0.015	83.329	0.088	0.006	0.016	0.020	83.759
LA 002 1-20	Pyrrhotite	0.132	0.002	0.062	0.034	0.022	-0.007	0.005	83.488	0.063	0.014	0.015	-0.031	83.798
LA 002 1-22	Pyrrhotite	0.140	0.002	0.023	0.033	0.013	0.001	0.017	83.974	0.084	0.002	0.017	-0.019	84.285
LA 002 1-23	Pyrrhotite	0.086	0.003	0.041	0.078	0.090	0.019	0.017	84.016	0.050	0.006	0.011	-0.002	84.413
LA 002 3-25	Pyrrhotite	0.004	-0.013	0.015	-0.010	0.034	-0.006	0.027	79.676	0.057	0.005	0.001	-0.002	79.788
LA 002 3-26	Pyrrhotite	-0.004	-0.001	0.027	0.037	0.038	-0.003	0.042	82.044	0.048	0.006	0.005	0.019	82.257
LA 002 3-27	Pyrrhotite	0.022	-0.008	0.085	0.042	0.033	-0.008	0.040	81.935	0.054	-0.009	0.001	0.015	82.200
LA 002 3-29	Pyrrhotite	-0.007	0.016	0.015	0.026	0.029	0.020	0.032	82.942	0.049	-0.015	0.003	0.006	83.117
LA 002 3-36	Pyrrhotite	0.016	0.002	0.099	0.030	-0.003	0.729	0.046	81.434	0.043	-0.009	0.007	0.005	82.399
LA 002 3-37	Pyrrhotite	-0.020	-0.015	0.036	0.032	0.004	0.613	0.031	81.706	0.037	-0.008	0.006	0.032	82.453
LA 002 4-4	Pyrrhotite	0.055	0.008	0.908	0.206	0.062	-0.008	0.022	78.429	0.048	-0.002	0.014	0.019	79.763
LA 002 4-25	Pyrrhotite	0.061	-0.006	0.050	0.027	0.028	-0.016	0.031	82.218	0.055	0.023	0.018	-0.003	82.486
LA 002 1-1	Titanomagnetite	0.126	0.167	2.052	0.092	0.018	28.213	0.650	81.219	0.002	0.085	0.015	-0.013	112.626
LA 002 1-3	Titanomagnetite	0.086	0.117	1.524	0.066	0.010	25.173	0.494	72.500	-0.016	0.040	0.015	-0.005	100.005
LA 002 1-9	Titanomagnetite	0.100	0.170	1.663	0.067	0.015	26.211	0.475	70.902	0.017	0.072	0.005	-0.003	99.692
LA 002 1-13	Titanomagnetite	0.083	0.154	1.658	0.076	0.001	25.416	0.520	71.792	0.008	0.043	0.011	-0.013	99.748
LA 002 1-21	Titanomagnetite	0.075	0.256	0.111	0.015	0.004	52.384	0.576	48.218	-0.003	0.008	0.013	-0.004	101.651
LA 002 1-24	Titanomagnetite	0.085	0.178	1.740	0.096	0.012	25.558	0.510	71.342	0.012	0.054	0.020	-0.028	99.577
LA 002 3-6	Titanomagnetite	0.017	0.106	1.689	0.107	0.005	25.501	0.522	71.427	0.007	0.015	0.005	-0.024	99.377
LA 002 3-11	Titanomagnetite	0.021	0.099	1.813	0.130	-0.003	25.362	0.519	71.703	0.016	0.027	0.004	0.008	99.698
LA 002 3-13	Titanomagnetite	0.041	0.095	1.737	0.075	0.031	25.123	0.526	71.307	0.011	0.036	0.011	-0.026	98.966
LA 002 3-15	Titanomagnetite	0.010	0.106	1.607	0.065	-0.002	25.574	0.504	70.454	-0.019	0.007	0.002	0.008	98.314
LA 002 3-17	Titanomagnetite	0.022	0.143	1.848	0.078	0.000	25.849	0.532	70.007	0.003	0.038	0.003	0.020	98.543
LA 002 3-18	Titanomagnetite	0.011	0.152	1.740	0.105	0.001	26.154	0.512	69.807	-0.008	0.038	0.005	-0.034	98.482
LA 002 3-20	Titanomagnetite	0.009	0.153	1.738	0.077	-0.003	25.949	0.517	69.801	-0.004	0.000	0.010	0.024	98.271
LA 002 3-21	Titanomagnetite	-0.011	0.152	1.472	0.073	0.011	25.617	0.574	69.971	0.008	0.033	0.010	-0.014	97.896
LA 002 3-35	Titanomagnetite	0.085	0.062	1.725	0.091	0.023	23.517	0.623	72.000	0.020	0.006	0.012	0.013	98.176
LA 002 4-17	Titanomagnetite	0.041	0.092	1.655	0.077	-0.001	24.922	0.469	71.674	0.025	0.014	0.007	0.011	98.986
LA 002 4-19	Titanomagnetite	0.061	0.124	0.131	0.137	0.047	49.229	0.666	47.209	-0.010	-0.002	0.022	0.039	97.651
LA 002 2-2	Titanomagnetite	0.037	0.071	1.706	0.110	0.069	23.885	0.549	71.125	0.015	-0.006	0.012	0.012	97.583
LA 002 2-24	Titanomagnetite	1.266	0.249	7.130	11.937	1.751	19.134	0.595	57.963	0.011	0.017	0.227	-0.032	100.247
LA 002 2-1	Fayalite	0.043	1.607	0.046	29.801	0.297	0.488	1.322	66.583	0.012	0.031	0.018	-0.007	100.239
LA 002 2-4	Fayalite	0.033	1.534	0.044	29.488	0.425	0.067	1.329	67.158	0.010	0.014	0.012	0.193	100.307
LA 002 2-5	Fayalite	0.349	1.517	1.193	30.162	0.583	0.261	1.319	65.961	0.023	-0.011	0.048	0.014	101.418
LA 002 2-6	Fayalite	0.031	1.547	0.049	29.978	0.275	0.052	1.375	67.028	-0.017	0.008	0.019	0.014	100.358

LA 002 2-7	Fayalite	0.063	0.877	0.234	46.371	0.553	0.075	0.946	49.430	-0.019	-0.008	0.031	0.033	98.586
LA 002 2-8	Fayalite	0.026	1.251	0.044	21.092	0.232	0.030	0.922	72.388	0.020	-0.006	0.010	0.085	96.093
LA 002 2-9	Fayalite	0.002	0.244	0.185	3.404	0.100	0.024	0.116	81.029	0.030	0.011	0.010	0.015	85.169
LA 002 2-10	Fayalite	0.069	1.131	0.234	46.119	1.424	0.104	0.988	50.661	-0.004	0.007	0.010	0.083	100.824
LA 002 2-14	Fayalite	0.005	1.494	0.039	30.103	0.304	0.070	1.336	67.843	0.002	0.000	0.006	0.019	101.221
LA 002 2-21	Fayalite	0.219	1.385	1.564	39.312	0.465	0.082	1.212	62.022	0.004	-0.016	0.161	0.064	106.472
LA 002 2-26	Fayalite	0.042	1.573	0.040	29.491	0.312	0.250	1.343	67.058	-0.017	-0.020	0.009	0.007	100.085
LA 002 2-28	Fayalite	0.066	1.657	0.041	30.428	0.523	0.419	1.306	66.813	-0.013	0.008	0.020	0.057	101.325

Comment	Mineral Phase	K_2O	Na_2O	CaO	SiO_2	FeO	TiO_2	MgO	P_2O_5	Al_2O_3	MnO	Cr_2O_3	Total
Zagami Site 1-1	Maskelynite	0.335	5.020	10.140	53.680	0.652	0.059	0.103	0.010	26.460	0.009	0.000	96.468
Zagami Site 2-1	Maskelynite	0.529	5.080	9.210	56.910	0.647	0.039	0.091	0.036	26.410	0.041	0.000	99.019
Zagami Site 5-2	Maskelynite	0.381	4.920	10.450	55.380	0.685	0.080	0.081	0.059	27.320	0.000	0.025	99.404
Zagami Site 6-1	Maskelynite	0.284	4.900	10.960	55.870	0.657	0.061	0.110	0.059	28.440	0.000	0.000	101.364
Zagami Site 7-4	Maskelynite	0.303	4.700	11.150	55.680	0.753	0.100	0.090	0.024	28.420	0.034	0.022	101.28
Zagami Site 8-5	Maskelynite	0.646	5.120	9.140	57.120	0.720	0.066	0.073	0.000	26.410	0.023	0.028	99.355
Zagami Site 8-7	Maskelynite	0.295	5.070	8.680	58.070	1.037	0.034	0.038	0.035	25.960	0.007	0.000	99.227
Zagami Site 9-2	Maskelynite	0.333	4.750	10.650	55.850	0.744	0.063	0.062	0.047	28.030	0.000	0.039	100.568
Zagami Site 9-7	Maskelynite	0.441	4.890	10.340	56.780	1.001	0.040	0.054	0.054	27.760	0.036	0.000	101.396
Zagami Site10-1	Maskelynite	0.518	5.400	8.730	57.300	0.557	0.062	0.067	0.014	25.870	0.010	0.008	98.576
Zagami Site10-8	Maskelynite	0.518	5.240	9.220	58.590	1.253	0.154	0.077	0.036	27.040	0.000	0.026	102.163
ZagamiSite 1012	Maskelynite	0.294	5.040	10.550	55.960	0.930	0.012	0.103	0.042	27.640	0.016	0.019	100.621
ZagamiSite 11-7	Maskelynite	0.732	5.280	8.670	57.890	0.725	0.089	0.026	0.046	26.250	0.018	0.000	99.727
ZagamiSite 12-4	Maskelynite	0.394	4.950	10.500	56.640	0.949	0.022	0.086	0.026	28.160	0.032	0.000	101.78
ZagamiSite 12-5	Maskelynite	0.261	5.010	10.930	55.660	0.899	0.062	0.128	0.098	28.220	0.019	0.000	101.288
ZagamiSite 12-8	Maskelynite	0.456	4.770	10.670	56.060	1.168	0.068	0.116	0.080	27.750	0.000	0.000	101.143
ZagamiSite 1210	Maskelynite	0.463	4.790	11.110	55.280	0.781	0.037	0.062	0.050	28.380	0.016	0.010	100.978
ZagamiSite 13-4	Maskelynite	0.298	4.890	10.760	56.050	0.819	0.032	0.096	0.034	28.150	0.012	0.000	101.147
ZagamiSite 13-6	Maskelynite	0.306	4.920	10.510	55.700	0.827	0.049	0.069	0.000	27.380	0.000	0.041	99.803
ZagamiSite 13-9	Maskelynite	0.472	4.790	10.480	55.570	0.927	0.070	0.091	0.060	27.300	0.009	0.061	99.837
Zagami Site 5-5	Merrillite	0.085	1.630	46.710	0.115	3.220	0.000	2.140	44.500	0.034	0.129	0.034	102.165
Zagami Site 8-4	Merrillite	0.106	1.680	46.870	0.108	2.530	0.063	2.620	45.120	0.026	0.114	0.043	102.779
Zagami Site 8-6	Merrillite	0.106	1.440	47.310	0.117	2.880	0.101	2.710	44.720	0.032	0.146	0.067	103.428
Zagami Site 4-1	Mesostasis	0.177	1.850	2.050	87.310	0.321	0.312	0.023	0.045	8.490	0.000	0.000	100.584
Zagami Site 5-4	Mesostasis	5.750	1.380	1.060	76.920	0.831	0.401	0.022	0.073	11.630	0.023	0.010	98.127
Zagami Site 9-4	Mesostasis	6.760	1.490	0.100	75.130	1.142	0.302	0.038	0.134	12.680	0.036	0.014	97.869
ZagamiSite 10-3	Mesostasis	6.340	1.510	0.991	77.960	0.491	0.327	0.033	0.067	11.870	0.039	0.012	99.675
ZagamiSite 10-5	Mesostasis	5.710	1.223	1.191	77.110	0.740	0.631	0.051	0.076	11.910	0.030	0.000	98.684
ZagamiSite 10-6	Mesostasis	5.840	1.312	1.308	76.760	0.828	0.561	0.029	0.069	12.300	0.056	0.000	99.071

ZagamiSite 10-7	Mesostasis	0.437	2.360	3.160	80.510	0.430	0.202	0.040	0.016	12.970	0.023	0.008	100.162
ZagamiSite 1010	Mesostasis	7.880	1.780	0.123	72.000	1.690	0.304	0.051	0.080	15.110	0.031	0.000	99.153
ZagamiSite 1011	Mesostasis	7.520	2.970	2.430	66.610	1.157	0.228	0.040	0.115	20.140	0.011	0.000	101.253
ZagamiSite 11-8	Mesostasis	0.221	1.950	1.560	88.460	0.269	0.211	0.027	0.000	6.230	0.000	0.000	98.936
ZagamiSite 11-9	Mesostasis	6.170	1.500	0.144	72.040	1.170	0.238	0.027	0.193	11.720	0.021	0.010	93.255
Zagami Day 2 5	Mesostasis	0.074	1.043	2.220	80.509	16.898	1.091	0.609	0.955	3.877	0.448	0.025	107.757
Zagami Day 2 6	Mesostasis	0.007	0.145	0.172	98.916	0.194	0.210	-0.011	-0.010	1.757	0.009	0.023	101.421
Zagami Day 2 7	Mesostasis	0.006	0.573	0.139	98.570	0.128	0.249	0.006	-0.029	1.444	0.004	-0.027	101.062
Zagami Site 1-2	Pyroxene	0.038	0.243	6.020	47.200	31.290	0.421	10.820	0.026	0.520	0.815	0.000	97.401
Zagami Site 2-3	Pyroxene	0.032	0.260	6.310	49.960	30.500	0.455	11.970	0.000	0.776	0.866	0.149	101.29
Zagami Site 3-2	Pyroxene	0.020	0.224	6.100	49.510	32.130	0.493	11.310	0.030	0.555	0.815	0.000	101.187
Zagami Site 3-5	Pyroxene	0.028	0.325	14.140	50.670	20.830	0.473	12.150	0.010	1.288	0.635	0.418	100.999
Zagami Site 4-5	Pyroxene	0.014	0.270	6.250	49.060	31.940	0.531	11.080	0.010	0.587	0.814	0.077	100.652
Zagami Site 5-6	Pyroxene	0.037	0.209	7.360	49.060	31.950	0.540	10.120	0.000	0.611	0.857	0.077	100.833
Zagami Site 6-2	Pyroxene	0.036	0.226	6.070	50.500	27.050	0.294	14.840	0.015	0.855	0.772	0.203	100.86
Zagami Site 7-1	Pyroxene	0.034	0.203	7.360	50.100	27.810	0.465	13.140	0.028	0.883	0.769	0.226	101.049
Zagami Site 7-2	Pyroxene	0.054	0.260	6.510	49.020	33.520	1.073	9.840	0.000	0.774	0.880	0.072	102.004
Zagami Site 7-5	Pyroxene	0.026	0.243	5.860	48.780	33.040	1.052	9.840	0.027	0.652	0.878	0.142	100.542
Zagami Site 7-7	Pyroxene	0.071	0.342	6.180	48.330	33.100	1.406	9.140	0.037	0.599	0.823	0.113	100.142
Zagami Site 8-8	Pyroxene	0.027	0.291	4.450	49.060	36.040	0.642	9.750	0.023	0.498	0.859	0.060	101.701
Zagami Site 9-1	Pyroxene	0.027	0.282	9.750	50.240	26.830	0.439	12.010	0.010	0.776	0.691	0.266	101.32
Zagami Site 9-8	Pyroxene	0.010	0.215	5.560	50.460	29.650	0.364	13.720	0.000	0.712	0.824	0.176	101.704
ZagamiSite 10-2	Pyroxene	0.026	0.306	15.980	50.290	20.730	0.599	10.990	0.016	1.087	0.551	0.319	100.91
ZagamiSite 10-4	Pyroxene	0.036	0.444	13.390	49.420	23.060	0.501	11.440	0.020	0.891	0.686	0.248	100.141
ZagamiSite 11-1	Pyroxene	0.017	0.255	14.170	49.690	23.340	0.619	10.600	0.000	0.867	0.659	0.206	100.421
ZagamiSite 11-4	Pyroxene	0.010	0.189	6.060	50.660	26.430	0.296	15.630	0.000	0.834	0.789	0.362	101.28
ZagamiSite 11-5	Pyroxene	0.012	0.244	12.730	45.860	30.430	0.824	5.480	0.042	0.788	0.867	0.043	97.358
ZagamiSite 12-1	Pyroxene	0.000	0.366	10.950	49.070	27.980	0.634	10.050	0.032	0.722	0.706	0.039	100.548
ZagamiSite 12-3	Pyroxene	0.011	0.348	15.530	49.680	22.630	0.659	10.090	0.062	0.984	0.553	0.166	100.711
ZagamiSite 12-6	Pyroxene	0.035	0.233	6.370	49.630	32.450	0.432	10.870	0.025	0.526	0.864	0.066	101.505
ZagamiSite 12-9	Pyroxene	0.000	0.207	6.470	51.970	18.780	0.139	20.610	0.010	0.800	0.645	0.497	100.15
ZagamiSite 13-1	Pyroxene	0.030	0.215	4.510	52.700	19.270	0.119	21.890	0.000	0.570	0.621	0.451	100.381
ZagamiSite 13-2	Pyroxene	0.023	0.225	6.850	50.380	28.290	0.496	13.140	0.000	0.698	0.712	0.187	101.018
ZagamiSite 13-5	Pyroxene	0.000	0.134	6.130	50.130	29.560	0.375	13.150	0.019	0.783	0.807	0.233	101.336
ZagamiSite 13-7	Pyroxene	0.000	0.234	6.010	49.610	28.070	0.334	14.050	0.024	0.821	0.782	0.293	100.254
ZagamiSite 13-8	Pyroxene	0.026	0.194	4.690	52.450	20.080	0.137	21.630	0.010	0.631	0.664	0.366	100.878
ZagamiSite1311	Pyroxene	0.018	0.186	5.390	51.610	19.180	0.152	21.390	0.010	0.677	0.663	0.425	99.701
ZagamiSite1312	Pyroxene	0.009	0.308	16.120	50.440	13.840	0.207	15.230	0.000	0.963	0.476	0.682	98.293
ZagamiSite 1313	Pyroxene	0.019	0.208	6.280	50.270	25.920	0.194	15.540	0.022	0.752	0.744	0.171	100.127
Zagami Site 1-3	Pyrrhotite	0.048	0.526	0.109	0.139	82.470	0.025	0.058	0.024	0.025	0.070	0.000	83.494
Zagami Site 3-1	Pyrrhotite	0.041	0.309	0.058	0.081	82.700	0.033	0.000	0.013	0.022	0.054	0.000	83.312

Zagami Site 4-2	Pyrrhotite	0.050	0.570	0.120	0.166	81.890	0.287	0.022	0.016	0.019	0.031	0.023	83.203
Zagami Site 4-4	Pyrrhotite	0.044	0.504	0.097	0.098	82.330	0.000	0.049	0.040	0.024	0.078	0.058	83.366
Zagami Site 9-5	Pyrrhotite	0.025	0.380	0.014	0.139	82.820	0.132	0.055	0.000	0.020	0.023	0.000	83.622
Zagami Site 1-4	Titanomagnetite	0.051	0.195	0.068	0.142	71.950	22.280	0.427	0.026	1.764	0.526	1.253	98.681
Zagami Site 2-2	Titanomagnetite	0.006	0.164	0.075	0.044	48.000	51.390	0.823	0.015	0.070	0.548	0.138	101.293
Zagami Site 2-4	Titanomagnetite	0.019	0.227	0.030	0.116	71.600	22.830	0.482	0.000	2.010	0.515	1.388	99.248
Zagami Site 3-3	Titanomagnetite	0.017	0.174	0.139	0.078	61.070	21.730	1.660	0.023	4.000	0.540	9.630	99.075
Zagami Site 3-4	Titanomagnetite	0.007	0.081	1.089	1.901	60.120	20.530	1.680	0.000	4.010	0.532	8.790	98.75
Zagami Site 4-3	Titanomagnetite	0.009	0.183	0.118	0.128	47.280	50.120	0.496	0.000	0.082	0.688	0.055	99.168
Zagami Site 5-3	Titanomagnetite	0.039	0.348	0.267	0.128	72.790	21.120	0.348	0.075	2.040	0.578	0.743	98.489
Zagami Site 7-3	Titanomagnetite	0.000	0.131	0.071	0.113	71.910	21.660	0.423	0.010	2.180	0.496	1.460	98.476
Zagami Site 7-6	Titanomagnetite	0.034	0.359	0.071	0.144	46.680	49.600	0.718	0.000	0.073	0.524	0.179	98.443
Zagami Site 8-1	Titanomagnetite	0.029	0.317	0.116	0.125	67.440	21.340	0.516	0.032	2.300	0.517	6.240	98.98
Zagami Site 8-2	Titanomagnetite	0.022	0.350	0.075	0.069	47.190	51.540	0.804	0.013	0.056	0.604	0.227	100.95
Zagami Site 8-3	Titanomagnetite	0.022	0.141	0.324	0.111	68.040	22.500	0.513	0.000	2.030	0.542	4.590	98.825
Zagami Site 9-3	Titanomagnetite	0.016	0.126	0.012	0.042	47.990	50.860	0.731	0.000	0.093	0.701	0.047	100.646
Zagami Site 9-6	Titanomagnetite	0.000	0.064	0.000	0.164	73.040	22.910	0.396	0.000	1.886	0.622	0.581	99.67
ZagamiSite 10-9	Titanomagnetite	0.017	0.165	0.078	0.191	71.480	21.580	0.535	0.013	2.200	0.518	1.780	98.557
ZagamiSite 11-2	Titanomagnetite	0.015	0.079	0.000	0.099	73.470	22.240	0.279	0.000	2.040	0.481	0.868	99.61
ZagamiSite 11-3	Titanomagnetite	0.013	0.074	0.010	0.086	48.300	51.110	0.463	0.000	0.087	0.605	0.123	100.908
ZagamiSite 11-6	Titanomagnetite	0.000	0.018	0.022	0.116	72.340	23.550	0.336	0.000	1.681	0.488	0.638	99.214
ZagamiSite1110	Titanomagnetite	0.008	0.115	0.010	0.107	72.620	22.820	0.403	0.000	1.881	0.593	0.585	99.167
ZagamiSite 1111	Titanomagnetite	0.007	0.143	0.000	0.152	72.770	23.080	0.250	0.010	1.867	0.515	0.662	99.455
Zagami Site 122	Titanomagnetite	0.009	0.256	0.027	0.144	72.120	22.980	0.589	0.000	1.835	0.484	1.148	99.635
ZagamiSite 12-7	Titanomagnetite	0.000	0.236	0.023	0.115	71.300	25.090	0.412	0.000	1.606	0.470	0.555	99.815
ZagamiSite 13-3	Titanomagnetite	0.000	0.118	0.057	0.117	72.010	21.450	0.448	0.000	2.210	0.534	2.040	99.007
ZagamiSite1310	Titanomagnetite	0.025	0.313	0.024	0.131	69.890	23.150	0.641	0.000	1.868	0.483	3.110	99.646

Comment	Mineral Phase	Na_2O	MgO	Al_2O_3	SiO_2	CaO	TiO_2	MnO	FeO	NiO	Cr_2O_3	K_2O	Total
Nakhla D-1 1	Augite	0.196	13.217	0.764	52.099	18.554	0.187	0.437	14.482	0.026	0.405	0.004	100.367
Nakhla D-1 2	Augite	0.258	13.335	0.613	52.473	18.115	0.140	0.449	14.407	0.009	0.427	0.009	100.205
Nakhla D-1 7	Augite	0.194	13.376	0.508	52.401	18.290	0.125	0.471	14.622	0.008	0.443	-0.004	100.441
Nakhla D-1 9	Augite	0.243	12.665	1.109	51.972	18.733	0.340	0.419	14.817	0.011	0.421	0.006	100.717
Nakhla D-1 15	Augite	0.212	13.235	0.532	52.298	18.325	0.162	0.442	14.502	0.010	0.407	0.004	100.139
Nakhla D-1 21	Augite	0.216	13.275	0.522	52.000	18.193	0.129	0.461	14.412	0.001	0.394	0.010	99.645
Nakhla 426-6 6	Augite	0.218	13.179	0.921	50.471	18.798	0.311	0.429	14.084	0.011	0.411	0.001	98.834
Nakhla 426-6 7	Augite	0.208	13.482	0.633	51.431	18.592	0.167	0.425	14.065	0.018	0.358	0.007	99.386
Nakhla 426-6 8	Augite	0.259	13.076	1.204	50.994	18.691	0.293	0.444	14.410	0.011	0.364	0.011	99.757
Nakhla 426-6 9	Augite	0.197	12.425	0.564	49.507	16.938	0.150	0.454	15.003	-0.002	0.367	0.011	95.615
Nakhla 426-6 10	Augite	0.222	11.766	0.746	50.371	18.095	0.184	0.505	17.208	0.030	0.212	0.006	99.346

Nakhla 426-6 11	Augite	0.255	9.447	1.465	49.062	17.749	0.395	0.552	20.183	0.008	0.094	0.008	99.218
Nakhla 426-6 24	Augite	0.170	13.476	0.584	52.691	18.380	0.151	0.437	14.521	0.007	0.411	0.004	100.831
Nakhla 426-6 25	Augite	0.277	8.659	1.974	49.933	17.158	0.546	0.576	21.975	-0.018	0.123	0.010	101.211
Nakhla 426-6 31	Augite	0.255	9.888	1.422	51.301	17.758	0.326	0.531	19.829	-0.003	0.243	0.008	101.558
Nakhla 426-6 35	Augite	0.201	13.377	0.872	51.920	18.470	0.297	0.424	14.773	0.012	0.480	0.000	100.828
Nakhla 426-6 37	Augite	0.225	11.419	0.918	51.062	17.984	0.228	0.510	17.883	0.023	0.244	0.004	100.498
Nakhla 426-6 46	Augite	0.186	13.367	0.831	52.393	18.478	0.179	0.454	14.418	0.000	0.434	0.008	100.748
Nakhla 426-6 66	Augite	0.183	12.470	0.737	39.124	15.803	0.181	0.423	14.551	-0.006	0.374	0.003	83.843
Nakhla 426-6 75	Augite	0.192	13.386	0.750	52.371	18.441	0.194	0.459	14.497	0.008	0.453	-0.002	100.749
Nakhla 426-6 78	Augite	0.203	13.365	0.949	51.908	18.838	0.251	0.385	13.688	0.020	0.423	0.009	100.037
Nakhla 426-6 84	Augite	0.781	11.819	4.057	50.851	16.244	0.731	0.507	16.837	0.005	0.215	0.022	102.069
Nakhla 426-6 87	Augite	0.258	10.015	1.213	50.747	17.765	0.326	0.543	19.912	0.013	0.258	0.006	101.056
Nakhla 426-2 4	Augite	0.183	12.959	0.765	51.113	17.912	0.199	0.447	14.718	0.001	0.410	-0.001	98.706
Nakhla 426-2 6	Augite	0.187	13.097	0.755	50.638	17.747	0.203	0.439	14.378	0.008	0.415	0.006	97.873
Nakhla 426-2 11	Augite	0.161	12.887	0.527	49.317	17.164	0.144	0.432	14.828	-0.010	0.397	0.004	95.850
Nakhla 426-2 15	Augite	0.177	12.698	0.805	41.282	15.478	0.117	0.484	14.838	0.012	0.355	0.005	86.250
Nakhla 426-2 16	Augite	0.204	12.111	0.748	38.998	15.469	0.279	0.414	15.005	0.007	0.357	0.002	83.593
Nakhla 426-2 17	Augite	0.226	12.201	0.619	39.658	16.037	0.288	0.458	14.682	0.011	0.334	-0.001	84.512
Nakhla 426-2 18	Augite	0.282	8.251	2.056	35.432	14.199	0.324	0.543	20.067	0.013	0.160	0.009	81.334
Nakhla 426-2 19	Augite	0.244	8.112	1.255	37.571	14.391	0.394	0.578	22.221	-0.002	0.103	0.010	84.876
Nakhla 426-2 20	Augite	0.208	10.893	0.595	39.425	14.951	0.168	0.493	17.716	0.019	0.311	-0.002	84.775
Nakhla 426-2 33	Augite	0.196	12.935	0.445	43.689	16.356	0.103	0.455	14.736	0.015	0.399	-0.002	89.326
Nakhla 426-2 37	Augite	0.179	12.548	0.751	39.897	15.878	0.247	0.406	14.398	0.010	0.368	0.009	84.690
Nakhla 426-2 48	Augite	0.223	12.241	0.512	37.999	15.379	0.141	0.440	14.862	-0.007	0.341	0.004	82.133
Nakhla 426-2 49	Augite	0.243	8.373	1.175	36.290	14.439	0.395	0.557	21.547	-0.003	0.054	0.006	83.077
Nakhla426-2 50	Augite	0.250	7.443	1.394	35.885	14.080	0.470	0.572	22.809	0.014	0.077	0.010	83.003
Nakhla 426-2 55	Augite	0.170	13.011	0.539	49.870	17.460	0.170	0.448	14.788	0.010	0.413	-0.001	96.879
Nakhla 426-2 57	Augite	0.212	13.703	0.467	52.451	17.715	0.122	0.426	14.331	0.012	0.419	0.008	99.867
Nakhla 426-2 66	Augite	0.179	12.840	0.718	48.742	17.687	0.219	0.439	14.448	0.022	0.398	0.008	95.699
Nakhla 426-2 67	Augite	0.212	13.427	0.459	49.723	17.132	0.123	0.439	14.366	0.023	0.430	0.010	96.343
Nakhla 426-2 72	Augite	0.225	12.488	0.760	46.716	17.299	0.266	0.430	14.470	0.005	0.371	0.001	93.030
Nakhla 426-2 76	Augite	0.240	10.250	0.900	45.103	16.093	0.238	0.543	19.799	0.021	0.179	-0.005	93.361
Nakhla 426-2 77	Augite	0.282	9.707	1.140	44.584	15.828	0.311	0.554	20.507	-0.008	0.295	0.003	93.203
Nakhla 426-2 79	Augite	0.207	12.902	0.541	46.312	16.582	0.155	0.440	14.802	0.000	0.360	0.007	92.308
Nakhla D-1 3	Fayalite	0.026	17.199	0.017	33.682	0.456	0.011	0.984	49.159	0.041	0.005	0.002	101.664
Nakhla D-1 6	Fayalite	0.016	14.101	0.056	32.880	0.485	0.009	1.010	52.706	0.023	0.014	0.005	101.320
Nakhla D-1 10	Fayalite	0.024	12.208	0.023	32.379	0.265	0.034	1.128	55.115	0.012	0.019	0.012	101.213
Nakhla D-1 11	Fayalite	0.016	14.225	0.035	32.805	0.396	0.023	1.048	53.038	0.023	0.011	0.008	101.693
Nakhla D-1 17	Fayalite	0.018	13.525	0.048	32.925	0.169	0.022	1.058	53.432	0.018	0.008	0.001	101.267
Nakhla D-1 19	Fayalite	0.027	13.656	0.035	32.828	0.483	0.013	1.037	52.847	0.008	0.009	0.004	101.016
Nakhla D-1 20	Fayalite	0.019	17.636	0.037	33.431	0.562	0.018	0.949	47.830	0.034	0.038	0.011	100.594

Nakhla D-1 22	Fayalite	0.023	13.549	0.035	32.598	0.466	0.021	1.022	52.602	0.022	-0.002	0.007	100.356
Nakhla D-1 24	Fayalite	0.019	13.673	0.026	32.532	0.448	-0.006	1.058	52.418	0.008	-0.023	0.001	100.201
Nakhla D-1 25	Fayalite	0.037	12.660	0.029	32.100	0.184	0.030	1.065	53.966	0.022	0.018	0.013	100.203
Nakhla D-1 26	Fayalite	0.008	14.600	0.032	33.059	0.213	0.038	1.033	51.999	0.025	0.011	0.002	101.054
Nakhla 426-6 1	Fayalite	-0.002	17.272	0.016	33.223	0.443	0.000	0.971	48.942	0.019	-0.004	0.003	100.883
Nakhla 426-6 3	Fayalite	0.004	15.362	0.012	32.825	0.369	0.026	0.996	50.887	0.031	0.009	0.004	100.523
Nakhla 426-6 4	Fayalite	0.004	13.109	0.024	32.101	0.365	-0.002	1.073	53.505	0.008	0.012	0.003	100.202
Nakhla 426-6 5	Fayalite	0.003	14.981	0.042	32.585	0.418	0.003	0.987	51.346	0.014	0.029	-0.004	100.404
Nakhla 426-6 12	Fayalite	-0.001	17.091	0.010	34.001	0.427	0.004	0.941	49.348	0.020	-0.002	0.001	101.839
Nakhla 426-6 13	Fayalite	0.009	15.261	0.019	33.292	0.357	0.017	1.021	51.699	0.017	0.022	0.002	101.714
Nakhla 426-6 34	Fayalite	0.006	17.327	0.020	33.754	0.351	0.005	0.942	49.403	0.010	0.005	0.005	101.827
Nakhla 426-6 56	Fayalite	-0.005	12.067	0.022	32.499	0.151	0.047	0.985	56.183	0.016	0.002	0.005	101.972
Nakhla 426-6 57	Fayalite	-0.002	13.325	0.056	23.668	0.430	0.003	1.022	54.298	0.016	-0.010	0.009	92.813
Nakhla 426-6 79	Fayalite	0.010	16.069	0.027	33.192	0.474	0.035	0.976	50.471	0.027	0.010	0.001	101.291
Nakhla 426-6 93	Fayalite	0.137	9.478	0.075	35.349	0.251	0.071	0.818	45.558	0.014	0.024	0.294	92.068
Nakhla 426-2 3	Fayalite	-0.009	12.946	0.021	30.908	0.421	0.008	1.017	54.950	0.011	0.021	0.003	100.296
Nakhla 426-2 10	Fayalite	0.008	15.265	0.078	30.067	1.090	0.027	0.967	51.586	0.002	0.109	0.011	99.209
Nakhla 426-2 12	Fayalite	-0.008	12.861	0.007	23.810	0.276	0.021	1.054	54.900	0.018	0.029	0.006	92.973
Nakhla 426-2 13	Fayalite	0.008	15.140	0.010	23.610	0.399	0.028	0.963	51.661	0.016	0.006	0.002	91.844
Nakhla 426-2 14	Fayalite	0.004	11.305	0.019	22.719	0.224	0.019	1.070	55.159	0.003	-0.031	0.001	90.493
Nakhla 426-2 26	Fayalite	0.017	15.594	0.023	23.561	0.365	0.023	0.984	51.377	0.036	0.004	0.009	91.992
Nakhla 426-2 31	Fayalite	0.003	14.840	0.018	27.039	0.428	0.025	1.029	52.710	0.027	0.010	0.009	96.139
Nakhla 426-2 36	Fayalite	-0.011	16.773	0.025	25.240	0.337	0.010	0.941	49.662	0.026	0.014	0.003	93.018
Nakhla 426-2 47	Fayalite	-0.018	11.752	0.011	23.779	0.227	0.020	1.088	56.048	0.018	0.022	-0.002	92.945
Nakhla 426-2 54	Fayalite	0.016	12.855	0.039	30.830	0.427	0.014	1.040	55.031	0.017	0.020	0.007	100.295
Nakhla 426-2 56	Fayalite	0.137	14.800	0.405	32.264	0.510	0.014	1.016	51.494	0.031	0.009	0.016	100.697
Nakhla 426-2 70	Fayalite	0.007	17.429	0.029	28.064	0.368	0.019	0.943	49.408	0.031	0.000	0.000	96.297
Nakhla 426-2 71	Fayalite	0.006	15.623	0.030	29.079	0.395	0.003	1.053	51.871	0.016	0.004	0.007	98.085
Nakhla 426-2 78	Fayalite	0.053	14.637	-0.002	28.484	0.278	0.018	1.090	53.694	0.013	-0.007	0.013	98.272
Nakhla D-1 4	Mesostasis	7.458	0.243	24.038	59.486	6.713	0.057	0.012	1.100	0.003	-0.012	0.612	99.797
Nakhla D-1 5	Mesostasis	5.819	0.580	23.110	61.316	6.106	0.054	0.019	1.405	0.002	-0.013	0.886	99.343
Nakhla D-1 8	Mesostasis	7.051	0.101	24.168	61.104	6.468	0.067	0.011	0.930	-0.005	0.023	1.272	101.214
Nakhla D-1 12	Mesostasis	8.795	0.229	27.542	67.779	7.557	0.071	-0.002	0.911	0.019	-0.013	0.787	113.773
Nakhla D-1 13	Mesostasis	3.914	0.590	20.201	60.996	3.079	0.022	0.044	1.465	0.009	-0.018	5.793	96.124
Nakhla D-1 14	Mesostasis	7.291	0.993	23.207	58.811	6.646	0.081	0.010	1.080	-0.004	-0.001	0.702	98.878
Nakhla D-1 16	Mesostasis	1.723	4.701	7.450	70.839	0.372	0.174	0.097	4.933	0.019	-0.018	4.012	94.296
Nakhla D-1 18	Mesostasis	6.688	0.674	18.985	66.137	3.907	0.104	0.013	1.344	-0.004	-0.001	1.807	99.713
Nakhla D-1 23	Mesostasis	6.461	0.540	24.173	58.858	6.368	0.080	0.018	1.265	0.005	0.001	0.742	98.558
Nakhla 426-6 2	Mesostasis	6.367	0.121	18.815	54.989	2.381	0.023	0.013	0.765	-0.004	-0.012	2.926	86.384
Nakhla 426-6 17	Mesostasis	6.965	0.040	23.841	59.680	6.137	0.007	-0.002	0.680	0.000	0.030	0.607	97.985
Nakhla 426-6 18	Mesostasis	7.784	0.145	22.792	62.581	4.239	0.034	-0.013	0.972	-0.007	0.002	0.925	99.454

Nakhla 426-6 19	Mesostasis	7.286	0.044	24.331	59.131	8.012	0.056	0.008	0.881	0.002	0.002	0.523	100.277
Nakhla 426-6 20	Mesostasis	7.717	0.019	24.256	60.674	6.601	0.064	0.007	0.928	0.000	-0.005	0.670	100.931
Nakhla 426-6 21	Mesostasis	7.422	0.030	24.054	60.759	6.497	0.044	0.012	0.848	-0.008	0.013	0.754	100.425
Nakhla 426-6 22	Mesostasis	1.991	1.246	12.084	65.890	0.261	0.096	0.040	3.738	-0.003	-0.017	7.778	93.105
Nakhla 426-6 23	Mesostasis	1.580	0.463	10.161	76.328	0.250	0.137	0.017	1.730	-0.004	0.007	5.845	96.514
Nakhla 426-6 29	Mesostasis	8.054	0.043	29.250	70.070	8.232	0.035	-0.005	1.071	0.002	0.004	0.834	117.590
Nakhla 426-6 38	Mesostasis	7.189	0.051	23.201	57.448	6.205	0.027	0.005	0.944	0.006	0.017	0.741	95.833
Nakhla 426-6 48	Mesostasis	6.045	0.257	20.863	50.557	5.560	0.040	0.020	1.939	-0.004	-0.017	0.456	85.715
Nakhla 426-6 67	Mesostasis	2.004	0.853	7.150	31.244	15.790	0.063	0.100	3.538	0.004	-0.001	3.617	64.360
Nakhla 426-6 76	Mesostasis	6.088	1.616	20.572	56.133	5.552	0.035	0.048	5.734	0.000	-0.024	0.587	96.341
Nakhla 426-6 77	Mesostasis	5.388	0.720	20.580	58.092	5.562	0.021	0.039	1.882	-0.013	0.002	0.820	93.092
Nakhla 426-6 88	Mesostasis	7.701	0.033	24.716	60.574	6.592	0.066	0.005	1.002	-0.019	0.004	0.661	101.334
Nakhla 426-2 5	Mesostasis	1.574	1.090	13.147	55.828	0.553	0.313	0.065	3.913	-0.010	0.007	5.717	82.196
Nakhla 426-2 21	Mesostasis	1.444	2.099	10.084	44.759	0.415	0.123	0.095	12.017	0.016	0.006	4.559	75.617
Nakhla 426-2 22	Mesostasis	1.984	0.551	7.002	63.655	0.265	0.107	0.035	2.162	0.002	-0.006	3.430	79.187
Nakhla 426-2 23	Mesostasis	4.020	0.352	14.764	53.265	3.214	0.081	0.019	1.840	0.016	-0.012	1.554	79.113
Nakhla 426-2 64	Mesostasis	7.864	0.053	21.253	53.937	6.058	0.060	-0.001	0.932	-0.001	0.013	0.542	90.711
Nakhla 426-2 65	Mesostasis	5.248	1.813	11.847	37.567	3.865	1.471	0.068	8.602	0.003	0.323	0.452	71.259
Nakhla 426-2 73	Mesostasis	6.639	0.080	21.575	53.093	6.465	0.033	0.001	1.210	-0.001	0.000	0.564	89.658
Nakhla 426-2 74	Mesostasis	7.665	0.026	20.409	55.065	5.239	0.060	0.011	0.883	0.000	0.026	0.680	90.065
Nakhla 426-6 14	Titanomagnetite	-0.003	0.391	1.691	0.068	0.013	15.061	0.410	78.527	-0.004	0.791	0.010	96.954
Nakhla 426-6 15	Titanomagnetite	0.004	0.404	0.944	0.051	0.070	21.547	0.467	73.156	0.008	1.216	0.001	97.867
Nakhla 426-6 16	Titanomagnetite	0.000	0.287	1.168	0.085	0.033	16.776	0.452	76.747	0.017	0.925	0.011	96.500
Nakhla 426-2 24	Titanomagnetite	0.023	0.202	0.765	0.078	0.056	11.590	0.341	82.958	0.013	0.423	0.008	96.458
Nakhla 426-2 44	Titanomagnetite	0.034	0.275	0.884	0.042	0.061	12.557	0.399	81.032	0.009	0.815	0.010	96.117
Nakhla 426-2 45	Titanomagnetite	0.005	0.387	0.931	0.051	0.072	15.974	0.468	77.316	-0.005	1.138	0.001	96.337
Nakhla 426-2 62	Titanomagnetite	0.089	1.579	1.526	4.018	0.272	11.251	0.416	70.217	-0.010	3.917	0.137	93.412
Nakhla 426-2 63	Titanomagnetite	-0.002	0.402	1.507	0.033	0.086	16.606	0.490	73.449	0.005	6.002	0.006	98.582

Appendix D: Raman Spectra

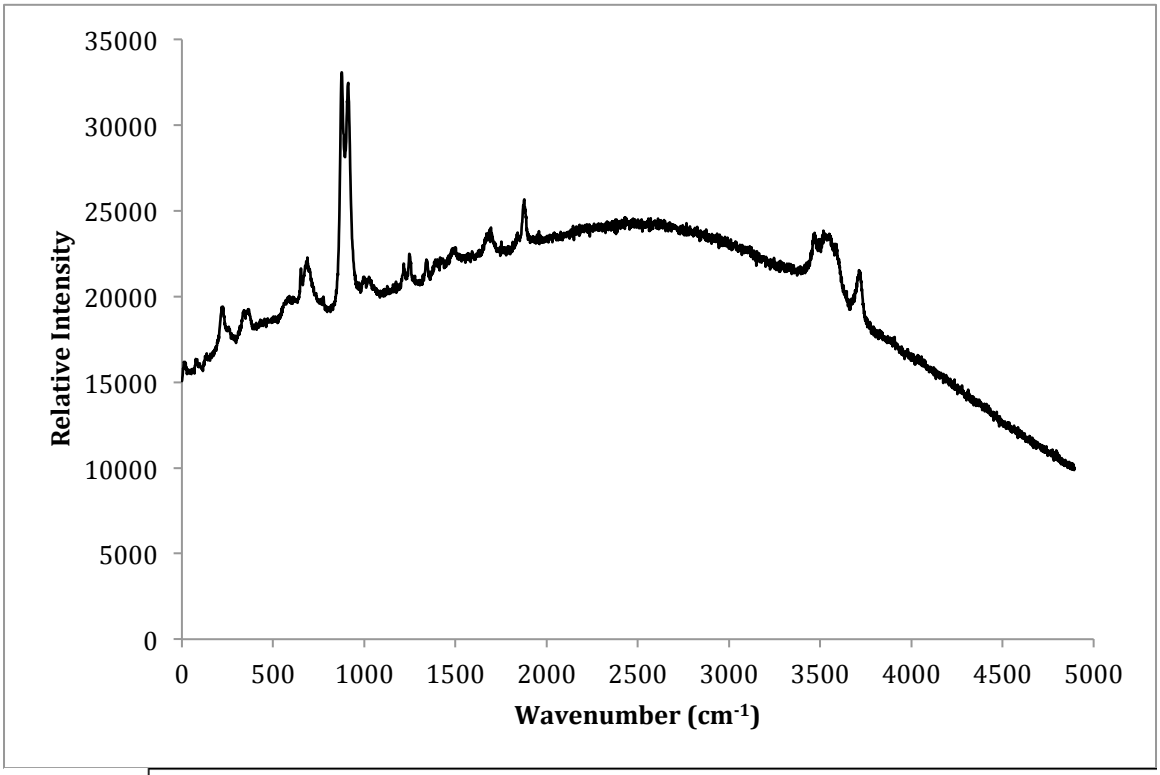

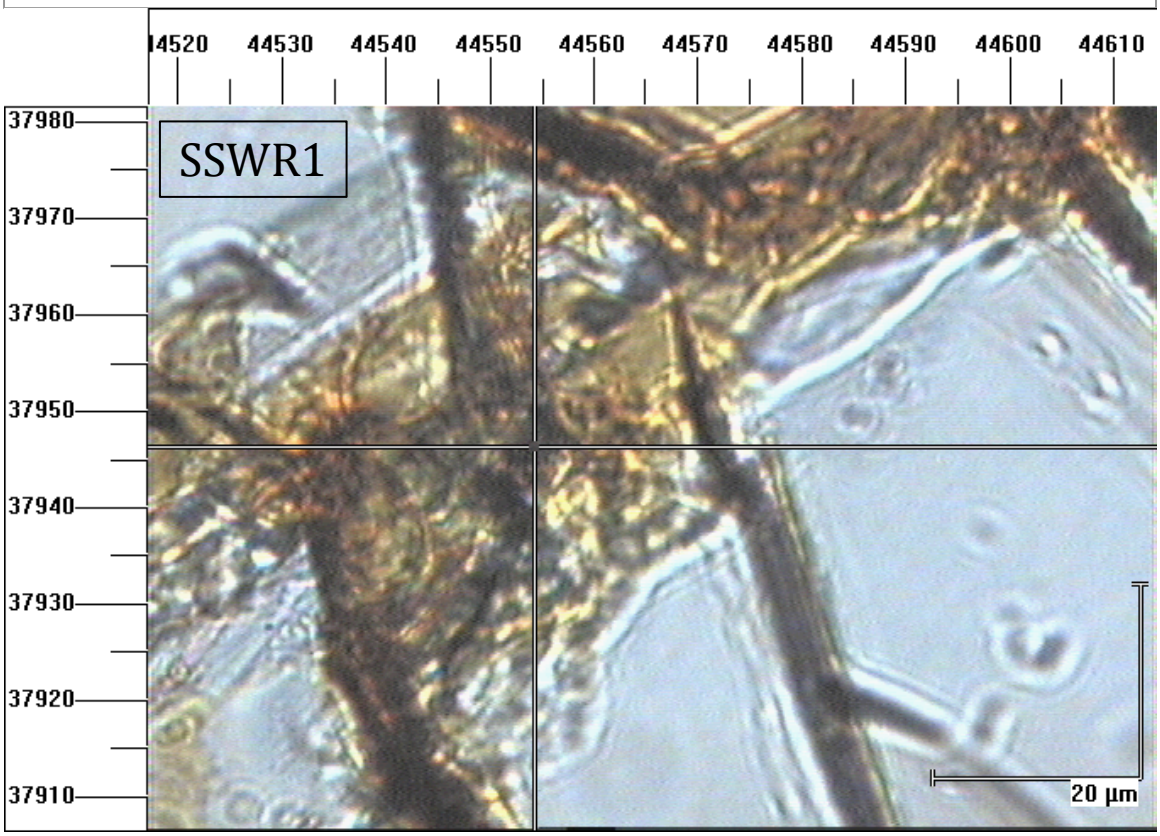

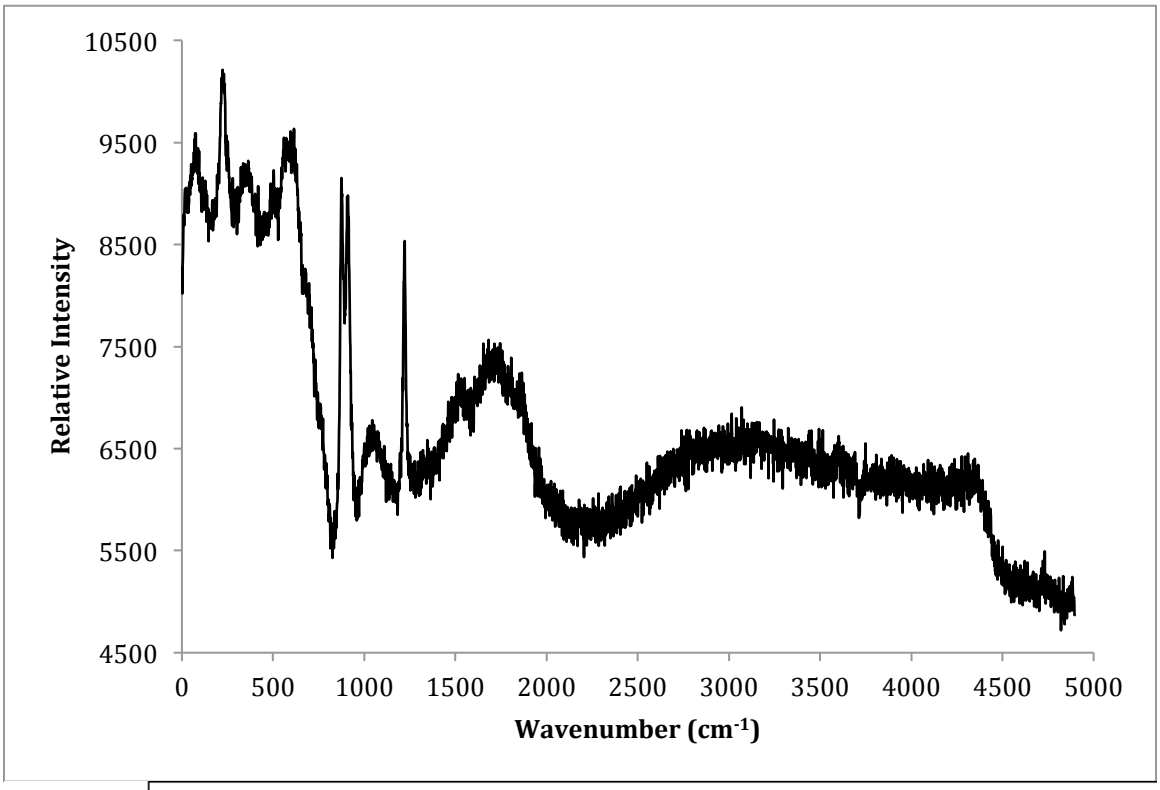
10500
9500
8500
7500
6500
5500
4500
Relative Intensity
0
500
1000
1500
2000
2500
3000
3500
4000
4500
5000
Wavenumber (cm-1)

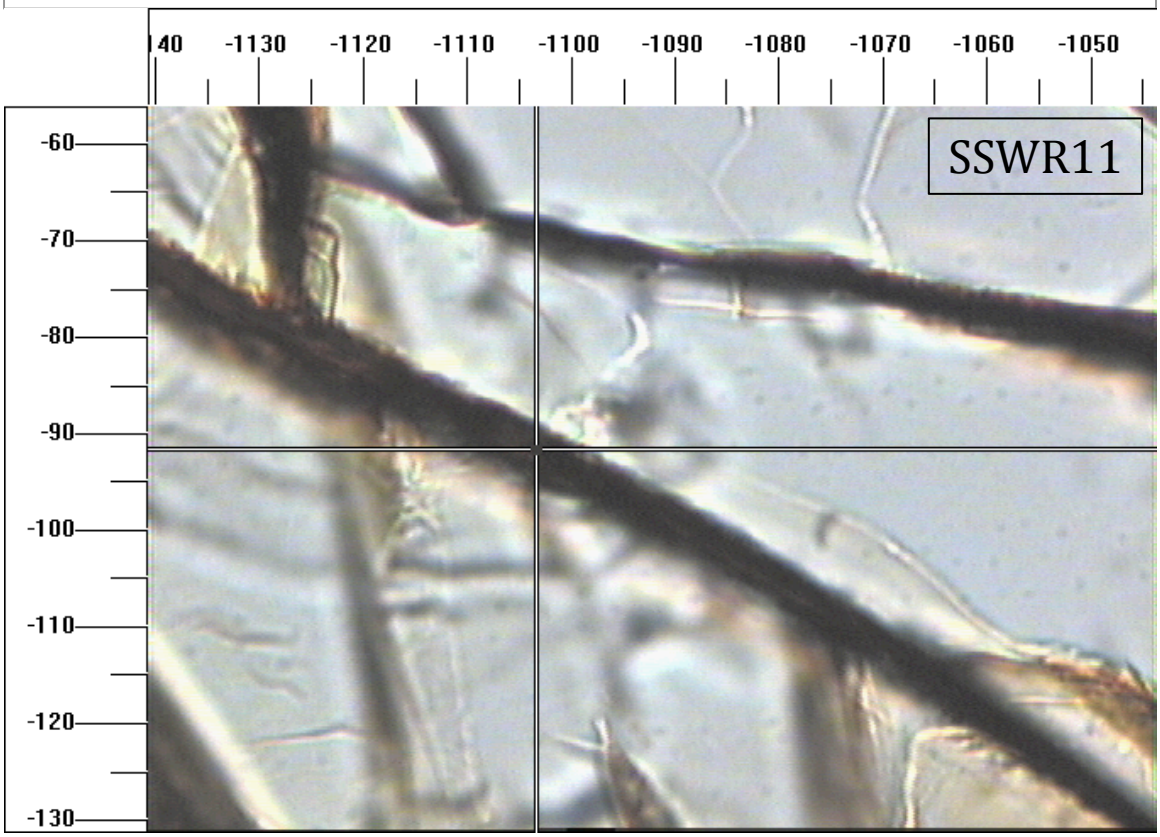
140
-1130
-1120
-1110
-1100
-1090
-1080
-1070
-1060
-1050
-60
-70
-80
-90
-100
-110
-120
-130
SSWR11

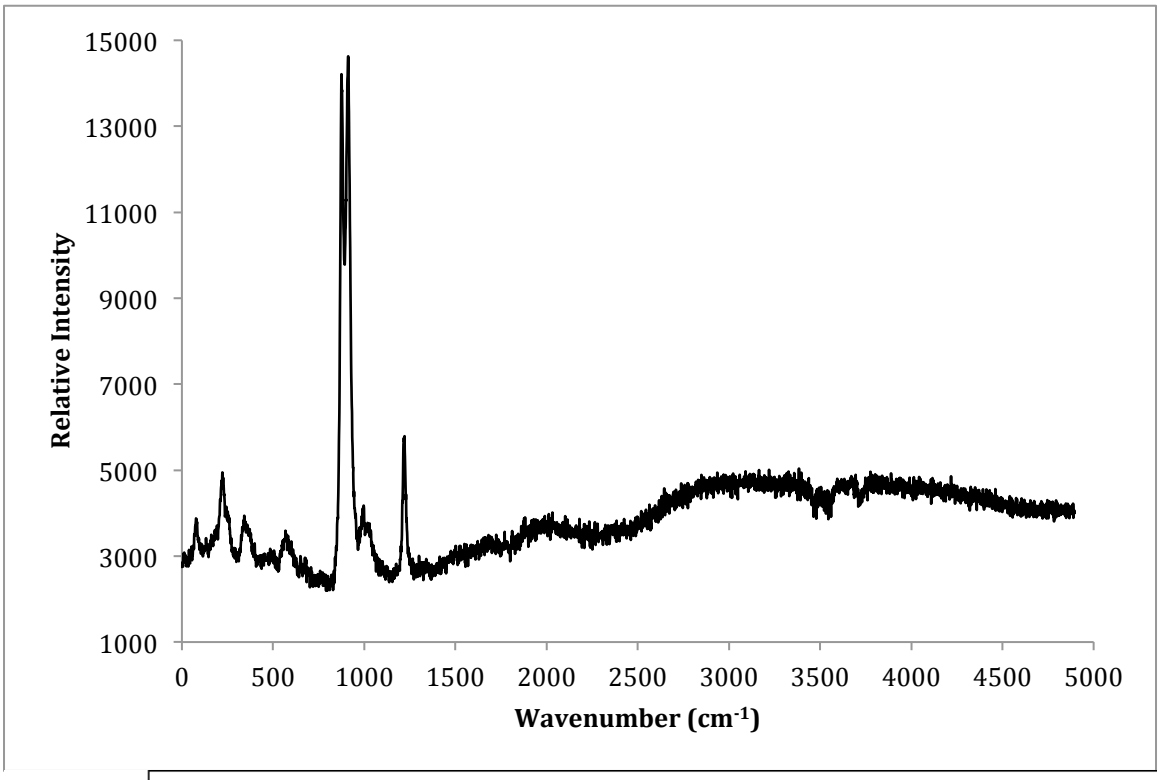
15000
13000
11000
9000
7000
5000
3000
1000
Relative Intensity
0
500
1000
1500
2000
2500
3000
3500
4000
4500
5000
Wavenumber (cm-1)

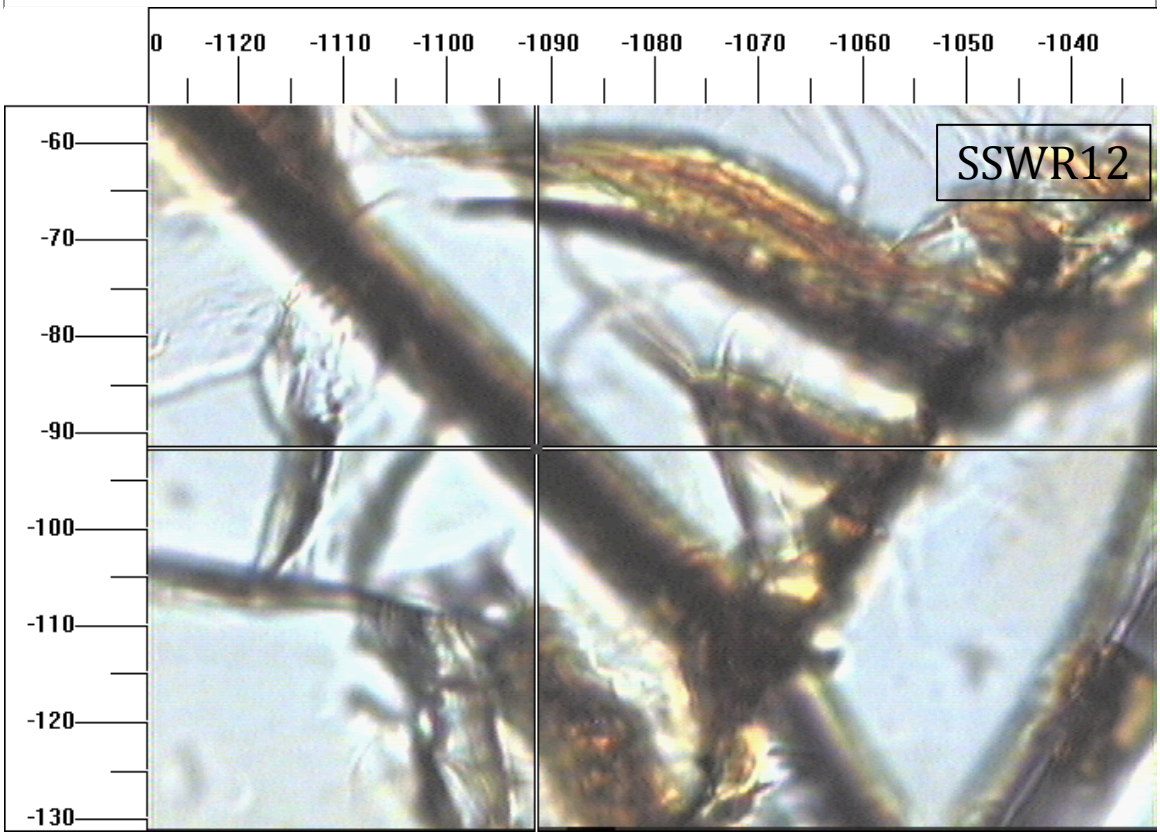
0
-1120
-1110
-1100
-1090
-1080
-1070
-1060
-1050
-1040
-60
-70
-80
-90
-100
-110
-120
-130
SSWR12

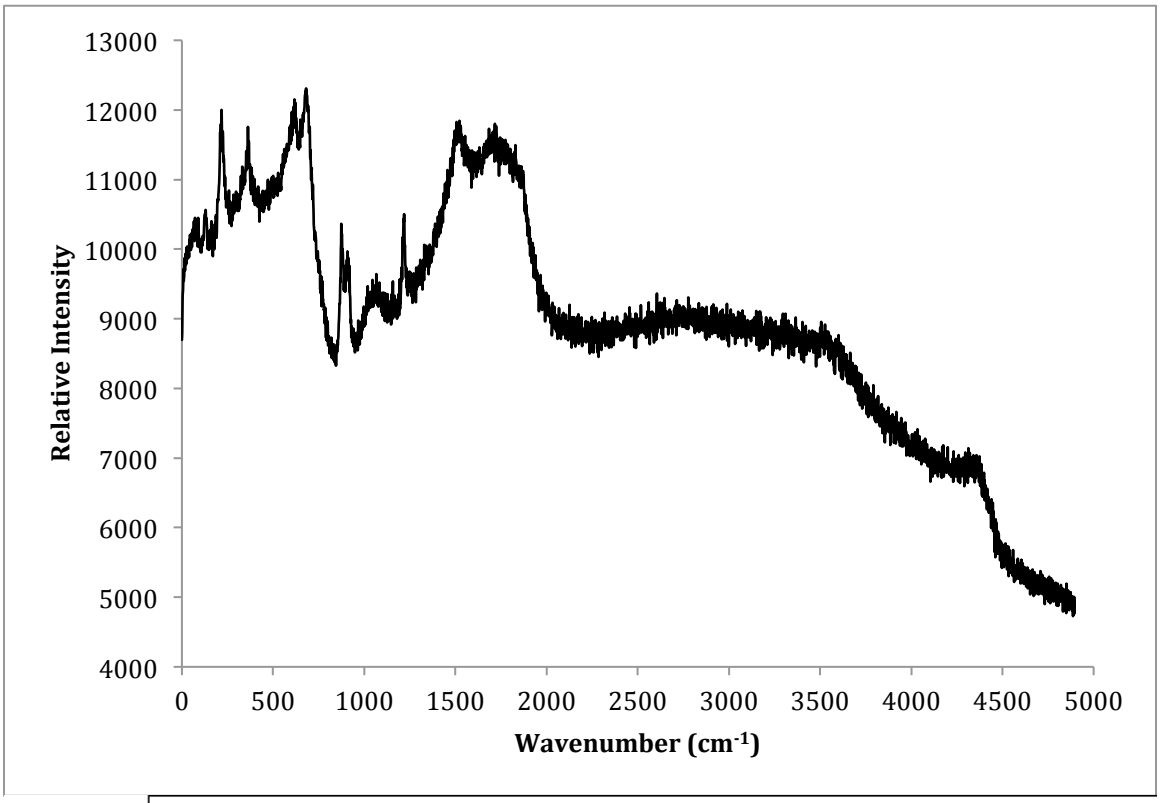
13000
12000
11000
10000
9000
8000
7000
6000
5000
4000
Relative Intensity
0
500
1000
1500
2000
2500
3000
3500
4000
4500
5000
Wavenumber (cm-1)

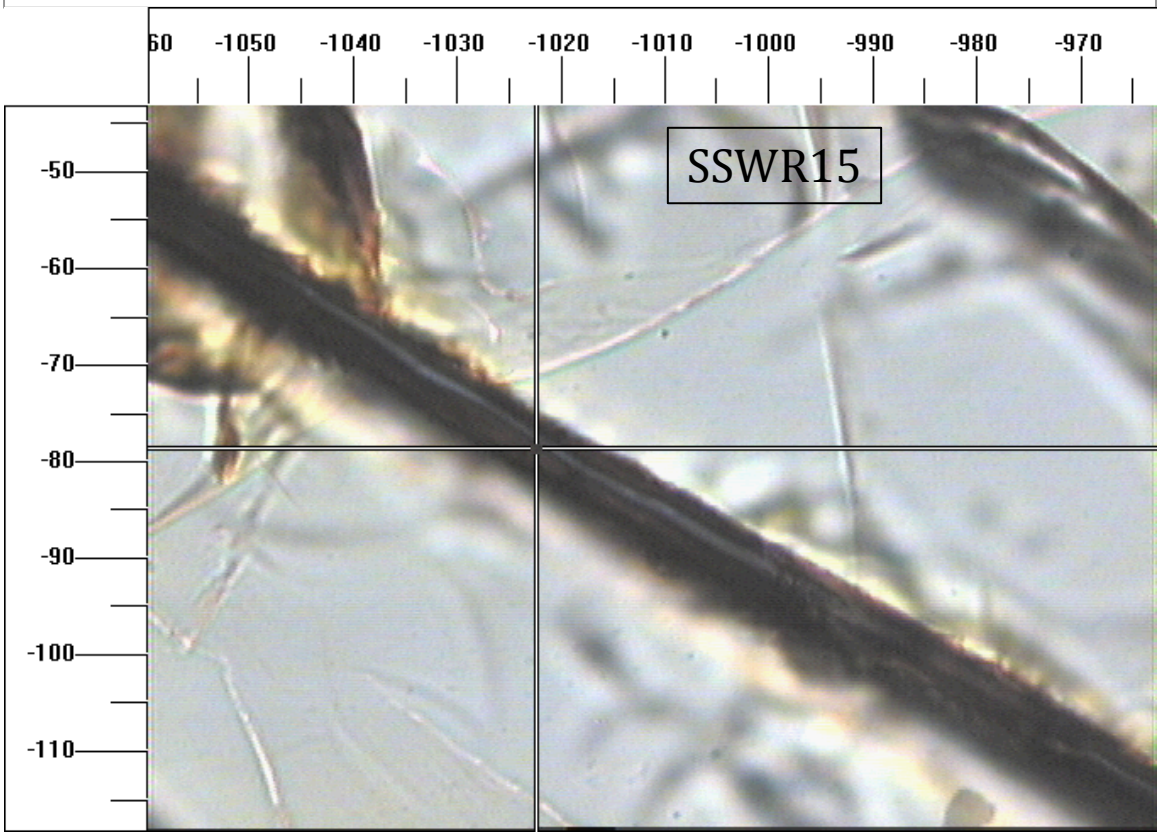
60
-1050
-1040
-1030
-1020
-1010
-1000
-990
-980
-970
-50
-60
-70
-80
-90
-100
-110
SSWR15

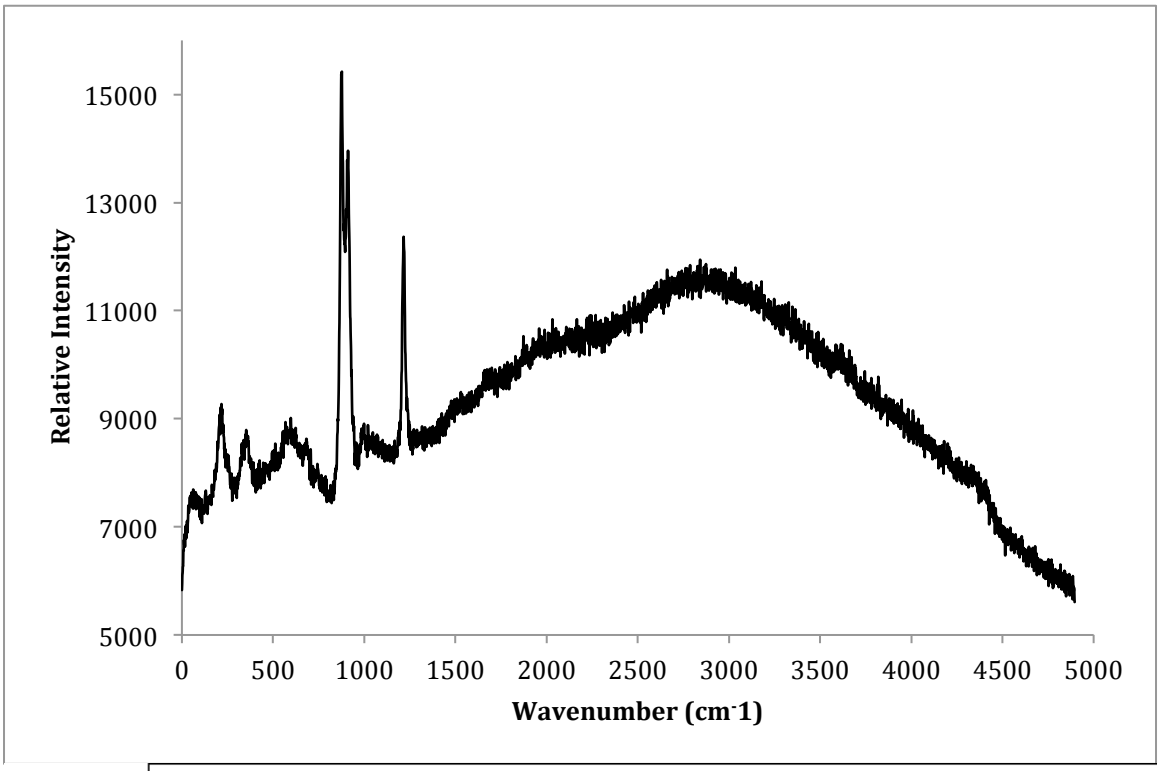
15000
13000
11000
9000
7000
5000
Relative Intensity
0
500
1000
1500
2000
2500
3000
3500
4000
4500
5000
Wavenumber (cm-1)

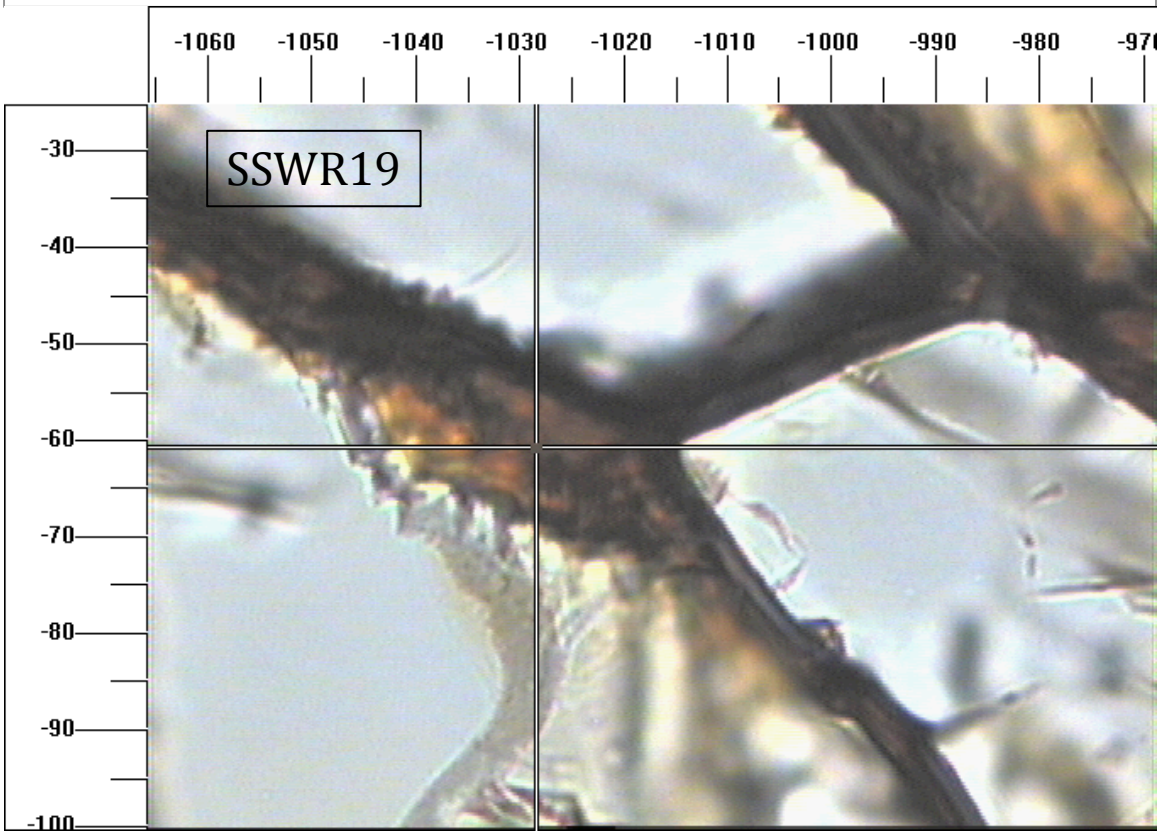
-1060
-1050
-1040
-1030
-1020
-1010
-1000
-990
-980
-30
-40
-50
-60
-70
-80
-90
-100
SSWR19

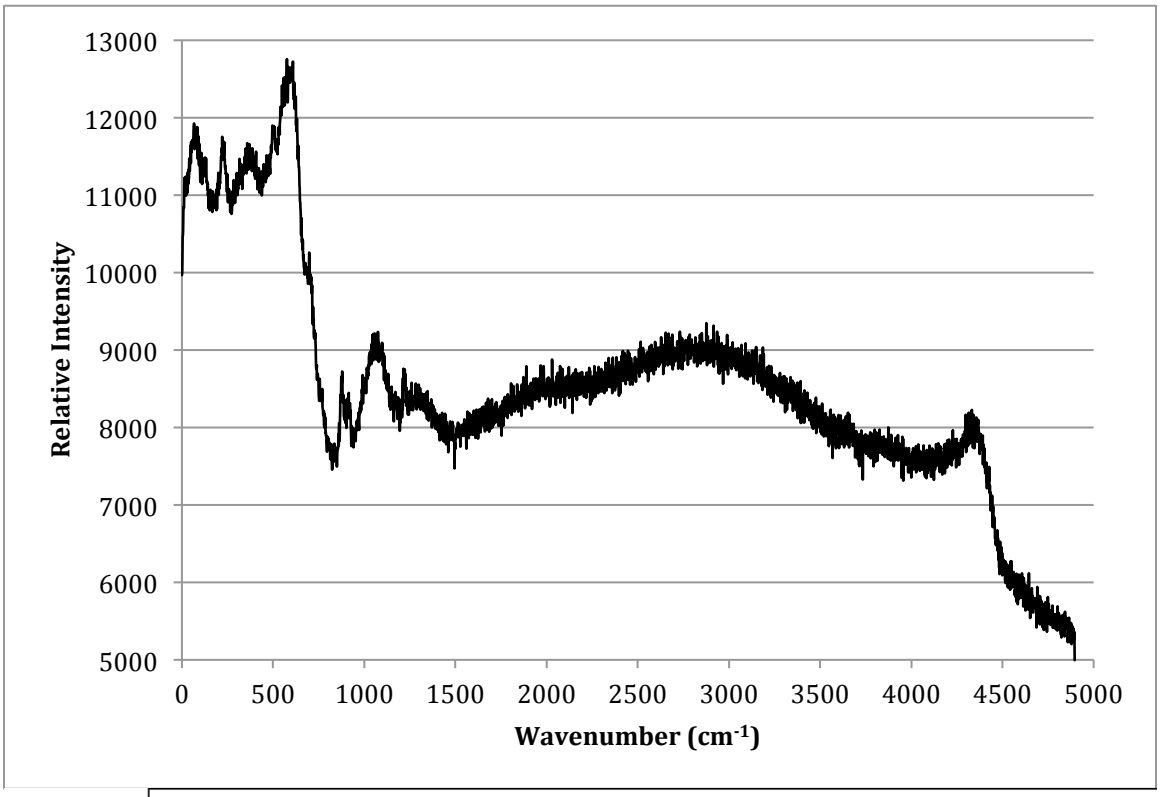
13000
12000
11000
10000
9000
8000
7000
6000
5000
Relative Intensity
0
500
1000
1500
2000
2500
3000
3500
4000
4500
5000
Wavenumber (cm-1)

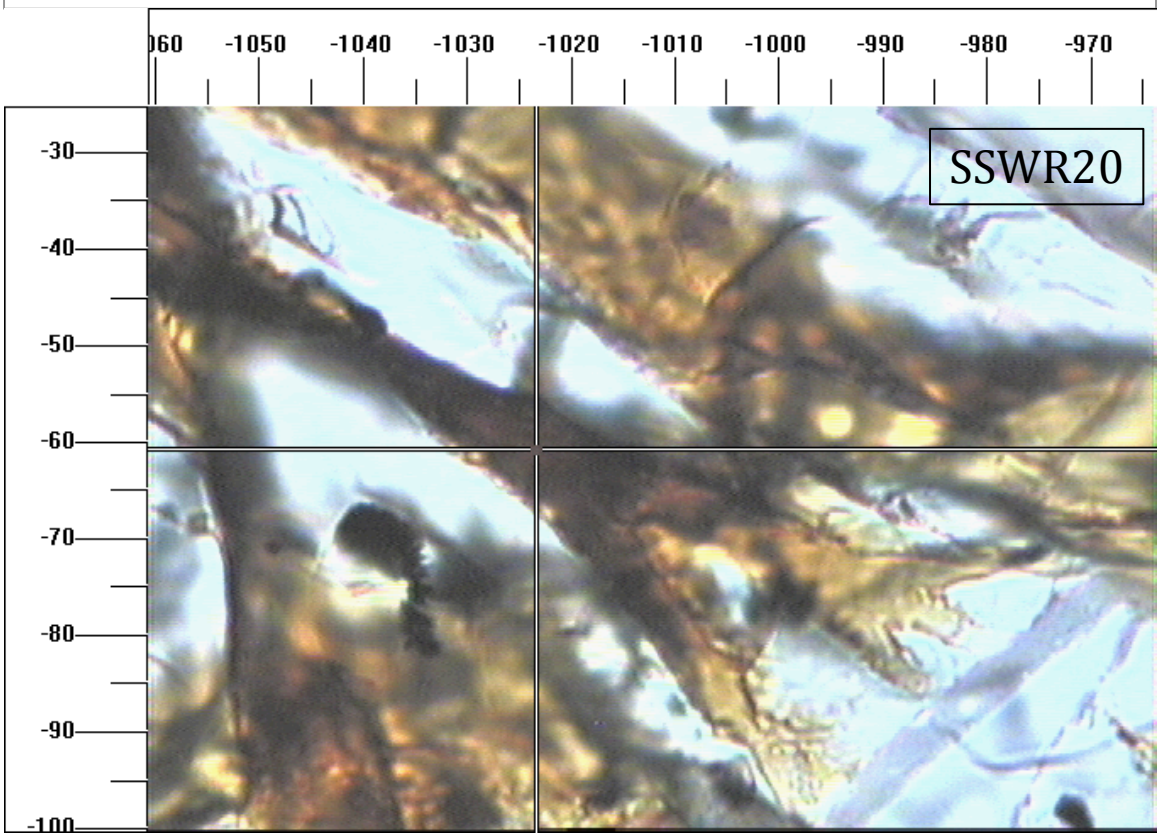
-1050
-1040
-1030
-1020
-1010
-1000
-990
-980
-970
-30
-40
-50
-60
-70
-80
-90
-100
SSWR20

Curriculum Vitae

Name:	Jared Shivak
Post-secondary Education and Degrees:	Queen's University Kingston, Ontario, Canada 2006-2010, B.Sc. (Geological Engineering) The University of Western Ontario London, Ontario, Canada 2010-2013, M.Sc. (Geology & Planetary Science)
Honours and Awards:	Barringer Award: Travel to 2013 Meteoritical Society Meeting Best Oral Presentation Award (Astrobiology): AESRC 2013 NSERC CREATE Canadian Astrobiology Training Program Graduate Fellowship, 2010-2013 NASA/CSA Grant in Support of Research, 2011 Western Graduate Research Scholarship, 2010
Related Work Experience	Graduate Teaching Assistant, 2010-2013 Department of Earth Sciences The University of Western Ontario Visiting Researcher, 2011 NASA Academy NASA Goddard Space Flight Center

Selected Publications, Oral Presentations, and Poster Presentations:

Shivak, J.N.*, Pavlov, A.A., 2013. *Liquid Water in the Extremely Shallow Martian Subsurface.* Astrobiology. *In Prep;* Journal Article.

Shivak, J.N., Banerjee, N.R., Flemming, R.L., 2013. *Habitability of the Martian Subsurface Constrained by SNC Meteorites*. 2013 Annual Meeting of the Meteoritical Society, Edmonton, Alberta; Conference Oral Presentation.

Shivak, J.N.*, Banerjee, N.R., Flemming, R.L., 2012, *Aqueous Alteration of Nakhla: Implications for Habitability of Martian Rocks*. NASA Astrobiology Science Conference 2012, Atlanta, Georgia; Poster Presentation.

Shivak, J.N.*, Flemming, R.L., Banerjee, N.R., 2011, *Looking for Life in Los Angeles: Astrobiological Characterization of the LA 002 Martian Meteorite*. Geological Association of Canada & Mineralogical Association of Canada Joint Annual Meeting 2011, Ottawa, Ontario; Conference Oral Presentation.